Joint analysis of neutrino oscillations using data from T2K and reactor experiments

Thesis submitted for the Degree of Doctor of Philosophy

Author:

Maria Antonova

Directors:

Dr. Anselmo Cervera Villanueva

Dr. Pau Novella Garijo

Universitat de València

3126 Programa Oficial de Doctorado en Física

Instituto de Física Corpuscular, Departamento de Física Experimental

Universitat de València – Consejo Superior de Investigaciones Científicas

May of 2023

To my beloved grandmother Dr. Natalia Vesenina. You has been and will always be in my heart, as my closest friend, a role model I've been always fascinated by and a great scientist. I love you.

Моей бабушке, кандидату биологических наук, Весениной Наталии Ефимовне. Ты всегда была, есть и будешь для меня самым близким другом, примером для подражания,прекрасным ученым и просто Бусей. Люблю тебя.

Abstract

This doctoral thesis presents studies on neutrino oscillations phenomenon with the T2K experiment, located in Japan. Neutrino oscillations are a crucial phenomenon in particle physics that have been extensively studied over the past few decades, providing valuable insights into the fundamental properties of neutrinos.

The work presented here includes two separate studies in the context of the T2K. The first, more physics oriented, consists in exploring the use of Daya Bay reactor neutrino experiment data as a constraint for the T2K measurements, which being an accelerator-based neutrino experiment uses a complementary technique. The Daya Bay experiment, located in China, measures the oscillation of neutrinos emitted from nuclear reactors. T2K has historically used a constraint on $\sin^2\theta_{13}$ obtained from reactor experiments. However, this constraint has always been introduced assuming a symmetric systematic error and neglecting the sensitivity of those experiments to Δm^2_{32} . The present work investigates the impact of using a two-dimensional $\sin^2\theta_{13}$ - Δm^2_{32} likelihood surface from Daya Bay as a constraint for the T2K oscillation analysis.

The second study, hardware oriented, focuses on plastic scintillator ageing. This effect, being never a primary interest of researchers in neutrino experiments, have not been thoroughly explored in the past. However, plastic scintillators are extensively used in those experiments, which usually run for more than a decade. Now, in the high precision era, it is important to perfect our understanding of those components and the overall detector behavior. This thesis presents a comprehensive study of the impact of ageing on the performance of plastic scintillator detectors, and their consequences in the context of accelerator neutrino oscillation measurements.

Resumen

Esta tesis doctoral presenta un estudio sobre oscilaciones de neutrinos empleando datos del experimento T2K, ubicado en Japón. Las oscilaciones de neutrinos constituyen un fenómeno crucial en física de partículas, que ha sido ampliamente estudiado durante las últimas décadas, proporcionando información valiosa sobre las propiedades fundamentales de los neutrinos. El trabajo presentado aquí incluye dos estudios separados en el contexto de T2K. El primero, más orientado a la física, consiste en explorar el uso de los datos del experimento de neutrinos del reactor de Daya Bay como restricción para las mediciones llevadas a cabo por T2K, que al ser un experimento de aceleradores usa una técnica complementaria. Daya Bay, ubicado en China, mide la oscilación de neutrinos emitidos por varios reactores nucleares. Históricamente, T2K ha utilizado la medida de $\sin^2\theta_{13}$ obtenida de los experimentos de reactores como restricción en sus análisis. Sin embargo, siempre se ha hecho asumiendo un error sistemático simétrico, y despreciando la sensibilidad de esos experimentos a Δm^2_{32} . En este trabajo se estudia el impacto en la sensibilidad de T2K a los parámetros de la oscilación del uso de una restricción bi- dimensional de Daya Bay, usando una superficie de probabilidad en $\sin^2\theta_{13}$ - Δm^2_{32} . El segundo estudio investiga el envejecimiento de los centelleadores plásticos. Este efecto, no siendo nunca de interés primario para los investigadores en experimentos con neutrinos, no ha sido explorado a fondo. Sin embargo, los centelladores plásticos se utilizan ampliamente en experimentos de neutrinos, cuya vida útil se extiende mas allá de una década. En la era de alta precisión en la que nos encontramos, es importante perfeccionar nuestra comprensión del comportamiento de estos componentes. Esta tesis presenta un estudio exhaustivo del impacto del envejecimiento en el rendimiento de los detectores de centelleo de plástico, así como su consecuencias en el contexto de los experimentos de oscilaciones de neutrinos.

Acknowledgements

This chapter is probably the easiest one to write. First of all I'd like to acknowledge help of my supervisors Pau Novella and Anselmo Cervera, without your patience and wise advice this work won't be possible. Also I'd like to thank Yuri Kudenko and Alexander Izmaylov, for giving me a great start in science and guiding through my very first steps in academia. As well I highly appreciate help of T2K oscillation analysis working group, Patrick Dune, Lukas Berns, Ed Atkin and other analyzers

Francis Bench, working with you as VALOR team was one of the best parts of my PhD journey. Thank you so much for your time dedicated to in answer my endless questions, help with tons of code bugs and nice talks over the bowl of ramen. Jaiden Parlone, my partner in code, you are an awesome person and working with you over VALOR (better say constantly trying to make it working) was a great experience, I always knew you are there in case of any doubts, for a brainstorm or just a friendly chit-chat.

Thanks to my colleagues from IFIC: el Rincon de IATA and all related folks. You guys made my stay in Valencia unforgettable. Migue, well, I love you much but will write more in a later version, please, don't be mad. Joking, it is the final version. Thanks a lot, jovencita, it is a big luck of mine to have a friend like you. Yo me parto la camisa como camarón. Judith Plenter, special thanks goes to you, glad to had you as my friend through these tough PhD years and La Caixa trainings. To my future wife, Tatiana Ovsiannikova thanks for saving my sanity countless numbers of times, supporting me in the darkest time and celebrating the happiest. Sergey Suvorov, thanks a lot, my friend, for patience, advice, quiz games and coffee calls, maybe it was not a big deal for you, it means the world to me.

To my family and all other friends all over the world. Love you guys. Мама, папа, Мася, Савва, бабушка Аля и бабушка Наташа. Вы были моей опорой и поддержкой в течении всего этого долгого пути. Спасибо большое! Без вас мне было бы гораздо сложнее. Очень вас люблю.

This work has been supported by funds from "la Caixa" Foundation (ID 100010434, fellowship code LCF/BQ/IN17/11620050), the European Union's Horizon 2020 Research and Innovation programme under the Marie Skłodowska-Curie grant agreement no. 713673

Contents

List of Figures

List of Tables

Introduction

Neutrino oscillations have revolutionized our understanding of neutrinos, revealing their unique properties and providing insights into the fundamental forces of nature. The experimental investigation of neutrino oscillations has been one of the most exciting and challenging endeavors in particle physics, involving cutting-edge technology, innovative techniques, and complex data analysis. This doctoral thesis focuses on experimental studies of neutrino oscillations, including the design, construction, and operation of detectors and experiments, as well as the analysis and interpretation of data.

After more than two decades of intense research, the combined result of a number of experiments with solar, atmospheric, reactor and accelerator-produced neutrinos has demonstrated that neutrinos have mass and oscillate, providing the first (and, so far, only) direct evidence for physics beyond the Standard Model of Particle Physics. The discovery of non-zero neutrino masses in the late 1990s has brought the field of neutrino studies to the forefront of research in experimental and theoretical particle physics. Experimentalists have made enormous progress in measuring neutrino properties. The field has been data-driven, with unexpected results frequently producing paradigm shifts in our common wisdom about neutrinos. Theorists have been able to explain most of the data with simple models, such as the three-flavor framework to explain neutrino oscillation results, and have established the profound implications that neutrinos have on our understanding of elementary particle physics theories and of the Universe. Barring additional unexpected results, experimental and theoretical progress in neutrino physics has narrowed the fundamental questions about neutrinos that are yet to be answered to the following list:

- Neutrino nature: is the neutrino its own antiparticle?
- Neutrino mass scale: what is the absolute scale of neutrino masses?
- Neutrino mass spectrum: how are the three neutrino mass states ordered from lightest to heaviest (neutrino "mass ordering")? Is it similar or "opposite" to quarks?
- Neutrino mixing: is the CP symmetry violated in the neutrino sector? This question is of at most interest since the presence of CP-violation is one of the so-called Sakharov conditions to explain the matter-antimatter asymmetry in the Universe.
- Neutrino species: are there sterile neutrino species in addition to the three active ones participating in the weak interactions?

Neutrino oscillations consist in the transformation in flight from one neutrino flavor to another. This mechanism is described by two mass squared differences (Δm^2_{12}, Δm^2_{32}) and by the PMNS mixing matrix (analogous to the CKM matrix of the quark sector), which contains three angles (θ_{12},θ_{23},θ_{13}) and one CP-violating phase, δ_{CP} . The PMNS matrix establishes the connection between the "flavor" neutrino states (that suffer weak interactions) and the "mass" states (with defined mass values) governing their transformations in flight.

The discovery and further study of the so-called atmospheric and solar oscillation modes have allowed the determination of the parameters (θ_{12}, Δm^2_{12}) and (θ_{23}, Δm^2_{32}), respectively. The Super-Kamiokande (SK) experiment is recognized as the one that discovered neutrino oscillations in 1998, being the first to unambiguously observe the atmospheric transition. A few years later (2001), the SNO experiment confirmed the solar oscillation mode. Both discoveries were awarded the 2015 Nobel Prize in Physics (T. Kajita and A. McDonald). SK played and still plays a major role in neutrino oscillation physics as the far detector of the T2K experiment, in Japan. These accelerator-based long-baseline experiments (hereafter LBL) confirmed neutrino oscillations by means of man-made neutrino sources. In particular, T2K (taking data since 2010) was the first experiment observing a clear indication of a non-zero θ_{13}, as published in 2011 [20]. Double Chooz also provided in 2011 the first indication of a non-zero value of θ_{13} with a reactor-based experiment [21]. This mixing angle, which represents the connection between the atmospheric and solar oscillation modes, was finally measured with very good precision by the reactor experiments Daya Bay, RENO and Double Chooz [19, 22, 23]. Independent confirmation of the non-zero value of θ_{13} was provided by T2K in 2014, with the observation of the ν_e appearance in a ν_μ beam with a 7.3σ significance [24]. Now that the paradigm of the 3-flavor neutrino oscillation is demonstrated, the accelerator-based experiments arise as a critical component in the program to further probe the neutrino nature, and in particular, the questions 3 and 4 mentioned earlier. LBL experiments provide the only known practical way to measure the neutrino CP-violating phase δ_{CP} . Once a relatively large and non-zero θ_{13} was measured, this is the main goal for the current generation of LBL experiments, T2K and NOνA. They are already providing valuable information about the CP-violating phase demonstrating that, in combination with reactor experiments, some values of δ_{CP} can already be excluded at 90$\%$ C.L. However, their sensitivity to δ_{CP} is limited and there is a general consensus in the community that more sensitive neutrino facilities will be necessary to make a definitive claim on the existence of CP violation. Two long-baseline neutrino projects are proposed: the DUNE experiment [25] in the US and the HK experiment [26] in Japan. With different strategies and detector technologies, both DUNE and HK will have improved sensitivity to the CP-violating phase and the mass ordering.

The T2K (Tokai to Kamioka) experiment is a leading international research project aimed at studying neutrino oscillations. The experiment is located in Japan and involves a powerful accelerator that produces a beam of muon neutrinos, which is then detected 295 kilometers away by a Super Kamiokande detector located in the Kamioka Observatory. The T2K experiment uses state-of-the-art detectors and analytical techniques to study neutrino oscillations and investigate the fundamental properties of neutrinos. The project is a collaboration between over 60 institutions from around the world, including Japan, the United States, and Europe. The T2K experiment has produced groundbreaking results and continues to push the boundaries of our understanding of neutrino oscillations.

The thesis presents a detailed description of the experimental methods used to study neutrino oscillations, including accelerator-based and reactor-based experiments, and the latest results and discoveries in the field. The thesis also addresses the challenges and limitations of experimental studies of neutrino oscillations and discusses the future prospects for improving our understanding of these elusive particles. One of the studies presented in this work explores an effect on T2K's sensitivity to oscillation parameters directly using a likelihood surface from a reactor experiment (Daya Bay in this case, as it dominates the field at the moment).

Another focus of this thesis lies in hardware plane: the ageing of scintillator detectors and its impact on measurement accuracy. Nowadays plastic scintillator counters are widely used in neutrino experiments and as most of these experiments are long run projects, in modern era of high-precision measurements, it is crucial to perfect our understanding of such detectors performance.

Chapter 1 provides an overview of the history of neutrino physics, tracing its origins and development from the early discoveries of beta decay to the modern understanding of neutrino oscillations. The chapter describes the key theoretical concepts underlying the phenomenon of neutrino oscillations and provides a comprehensive review of the experimental efforts that have been made to study this phenomenon.

The T2K experiment, which is the focus of this work, is described in detail in Chapter 2. This chapter provides a thorough description of the experimental setup, including the accelerator complex, the neutrino beamline, and the near and far detectors. The chapter also discusses the various sources of systematic errors that can affect the experiment and outlines the strategies employed to minimize these errors.

Chapters 3 and 4 present the inputs and implementation choices for the oscillation analysis performed using the VALOR neutrino fitting software. This study explores possible ways to enhance the accuracy and precision of the oscillation analysis machinery. The options that were probed included an alternative way to constrain some of the oscillation parameters using data from other experiments. The chapter also describes the methods used to evaluate the sensitivity of the analysis to changes in these input parameters.

Finally, Chapter 5 provides a summary of the findings of this work and presents the results of the oscillation analysis. The chapter discusses the implications of these results for improving the accuracy and precision of future neutrino oscillation measurements. It also highlights the potential of complementary experiments, such as reactor neutrino experiments, to constrain the uncertainties in the T2K measurements.

The Chapter 6 is dedicated to the investigation of a scintillator detector ageing, one of the impactful systematic errors for T2K near detector, as it is mainly composed of plastic scintillator bars of various shapes and origins. T2K, which as collected data more than a decade, constitutes the ideal framework for such a study

1 — History of neutrinos

1.1 — Prediction and discovery of neutrino

1.1.1 — The first encounter: prediction

There were no signs of neutrino existence until the middle of 20th century. First hint arrived when in 1914 James Chadwick performed a study [27] of a process known as beta-decay. He believed the process to be as follows:

$$ {}^{A}_{Z}N \rightarrow {}^{A}_{Z+1}N' + e^{-} \tag{1.1} $$

A transformation of a nucleus N to a daughter nucleus N' with an increase of atomic number Z by one, unchanged atomic mass A and an emission of an electron (Eq. (1.1)). Or in a modern interpretation:

$$ n \rightarrow p + e^{-} \tag{1.2} $$

Radioactive nucleus of Radium were meant to emit electrons of a discrete energy spectra, preserving both conservation laws of angular momentum, lepton number and, the most important, the conservation of energy (from Eq. (1.2)). However the obtained result was exactly the contrary of the expected: a continuous spectra. Later this finding was confirmed by Ellis and Wooster [1] (Fig. 1.1) .

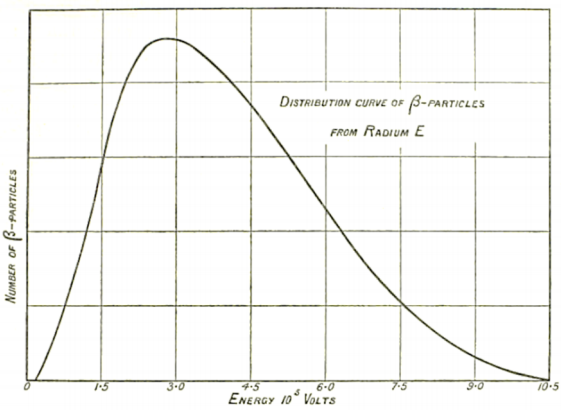

Figure 1.1: Energy spectrum of electrons, emitted during beta decay of Radium [1].

In 1933, according to his own words, Wolfgang Pauli [28] did a "terrible thing": he postulated a particle

that cannot be detected, but which solves inconsistency in beta-decay spectra. The particle, originally called neutron for not having an electric charge, was said to have a spin $-\frac{1}{2}$ and be massless. After a discovery of what we now know as neutron, it was re-baptized as a little neutron — neutrino.

1.1.2 — The first encounter: detection

Even though Pauli was convinced that neutrinos were impossible to detect, Frederick Reines and Clyde Cowan started to work towards finding these ghosty particles. In order to detect a neutrino one obviously needed a very intense source, like the reactor core of a nuclear powerplant. An enormous flux of electron anti-neutrinos, $\sim 2 \times 10^{20}$ $\bar{\nu}_e$ per second per GWth of thermal power, is getting produced as a side-product of nuclear fusion. In 1956 at Savannah River nuclear powerplant, Reines and Cowan installed a detector full of liquid scintillator with PMTs to look for a signal coming from neutrons produced in an inverse beta-decay reaction (Eq. (1.3)) and then being absorbed by Cd with emission of a delayed γ (Eq. (1.4)):

$$\bar{\nu}_e \ + p \rightarrow n + e^+ \tag{1.3}$$

$$n + {}^{108}Cd \rightarrow {}^{109}Cd* \rightarrow {}^{109}Cd + \gamma \tag{1.4}$$

The presence of this delayed gamma signal arrived as an experimental confirmation of neutrino's existence.

However, this was a proof of existence only for the case of the electron (anti)neutrino. In 1936 Anderson and Neddermeyer [29] discovered a next generation lepton - a muon. All together that motivated scientists to look for the muon neutrino which was successfully detected in Brookheaven National laboratory just 6 years after such a study was proposed. In the experiment by Lederman, Schwartz and Steinberger [30] a beam of protons accelerated at an alternating gradient synchrotron (ASG) were collided at a Beryllium target, resulting in the production of a π meson shower. Then in a decay volume the mesons were converting into neutrinos and muons (Eq. (1.5)), right before hitting a 5,000 ton steel wall to filter out the latter and let only neutrinos pass through.

$$\pi^{\pm} \rightarrow \mu^{\pm} + (\nu_\mu \ / \bar{\nu}_\mu \ ) \tag{1.5}$$

Then neutrinos were interacting in neon-filled spark chamber, where the spark trails of daughter-muons would be photographed as a proof of ν_μ existence.

The discovery of a second neutrino flavour raised an obvious question: how many neutrino are predicted by the Standard Model? The number of light active neutrinos could be predicted via studying of the Z^0 boson decay (Eq. (1.6)). The width of the decay is proportional to the number of neutrino flavours, i.e. the wider the decay is the more neutrinos flavours were expected to be found.

$$Z^0 \rightarrow \nu_l \bar{\nu}_{\ l} \tag{1.6}$$

In the 90's experiments at LEP successfully measured the number of light - active neutrinos which couple with electroweak force to be $N_\nu = 2.984 \pm 0.008$ [31]. This, together with a discovery of τ boson in 1998, were

a strong suggestion of the existence of a third neutrino. In 2001, the DONUT collaboration announced the discovery of ν_τ [32]. The experiment was conducted using the neutrino beam produced at Fermilab. ν_τ 's were produced using a technique similar to te one used for the ν_μ discovery: protons accelerated to 800MeV hitting a tungsten target and creating Ds mesons, which in their turn were decaying into ν_τ / $\bar{\nu}_\tau$. After passing a filter, a beam of neutrinos was arriving to a detector composed of photoemulsion planes sandwiched with iron layers. τ particles, produced on the ν_τ interactions (Eq. (1.8)) were leaving a $\sim$ 1mm trace before decaying into a signal muon event and corresponding neutrinos.

$$\nu_\tau + n \rightarrow \tau^- + p \tag{1.7}$$

$$\bar{\nu}_\tau + p \rightarrow \tau^+ + n \tag{1.8}$$

1.1.3 — Solar neutrino problem

The discovery of three neutrino flavors was calling to a further deepening of the knowledge of these particles. One of the most interesting to study and also promising sources of neutrinos is the Sun. Observation of solar neutrino allows to directly probe modes of thermonuclear reaction happening in the core of the star. And neutrinos are a very unique tool, as electromagnetic radiation from such reactions is getting deformed due to scattering as it is passing through the layers of matter towards the surface of the star. Even then, it requires photons 10^7 years to reach the surface. Thus, neutrinos constitute our only source of information about the Sun's interior. According to the Standard Solar Model (SSM) [3], for a star like the Sun, most of the energy is getting generated through the so called proton-proton (pp) chain where hydrogen transforms directly into helium. There are various types of branches which lead to a production of one or two ν_e 's (Fig. 1.2).

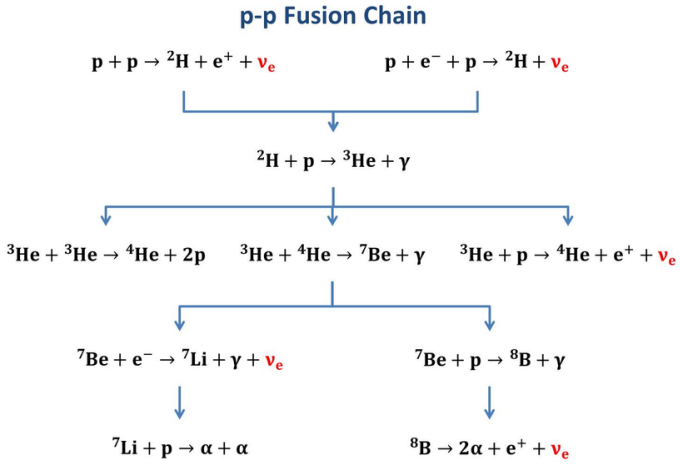

Figure 1.2: Solar reactions in the Sun: pp chain. Reproduced from [2].

The sun produces about 2×10^{38} neutrinos per second. However, despite being an intensive flux, detecting solar neutrinos is hard due to their extremely small cross-section ($\sigma \approx 10^{-43} cm^2$). Knowing the energy for

the pp chains, one can predict the spectra of solar neutrinos (Fig. 1.3). Most neutrinos are concentrated at energies below 1 MeV. These will play a crucial role for solar neutrino experiments.

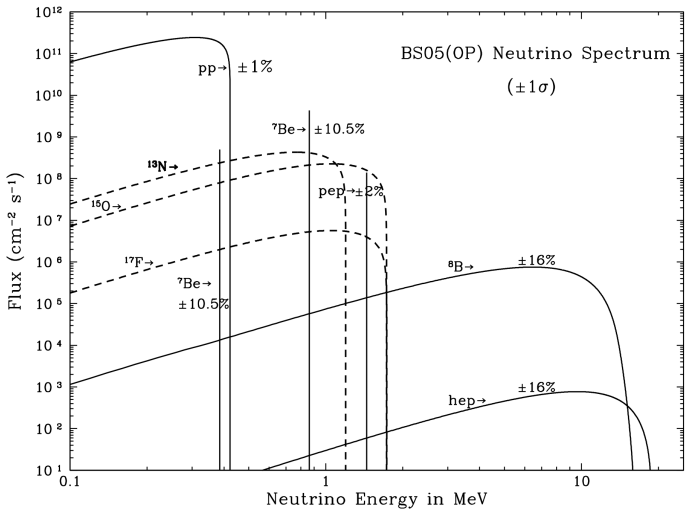

Figure 1.3: Solar neutrino energy spectrum [3].

The first experiment of this type, lead by Ray Davis, was constructed in the Homestake mine and started operation in 1967. The flux of solar neutrinos was measured through the following reaction:

$$\nu_e \ + {}^{37}Cl \rightarrow {}^{37}Ar + e^- \tag{1.9}$$

In this inverse β decay reaction, neutrinos interact with atoms of chloride filling the detector, producing argon atoms. Which in their turn would be from time to time chemically extracted from the tank and counted [33]. The number of captured neutrinos was only one third of what the SSM was predicting [34]. This reaction, however, requires energies higher than 0.8 MeV, i.e. such experiment is sensitive to "pp" neutrinos coming from the ${}^8B$ branch (Fig. 1.2). This came as a limiting factor of the Homestake experiment,which would be possible to overcome using Gallium as an active target. That was done in SAGE [35] and GALLEX [36], detecting neutrinos through:

$${}^{71}Ga + \nu_e \ \rightarrow {}^{71}Ge + e^- \tag{1.10}$$

The reaction in Eq. (1.10) has a threshold of only 0.2 MeV, that allowed to track wider spectra of neutrinos. And yet the deficit was confirmed again. This problem has been called the Solar Neutrino Problem (SNP).

1.1.4 — Atmospheric neutrino problem

Another anomaly has been observed detecting neutrinos produced in the atmosphere of our planet. They are a result of cosmic rays interacting with nuclei of the upper layers, producing hadron showers consisting of kaons and pions. Which in their turn decay into leptons subsequently originating neutrinos in a wide energy range from MeV to TeV.

As it is illustrated at the Fig. 1.4, most of the atmospheric neutrinos are produced in $\pi \rightarrow \mu$ decay chain, so it was expected to detect roughly twice more muon neutrinos than electrons. Nonetheless, in order to com-

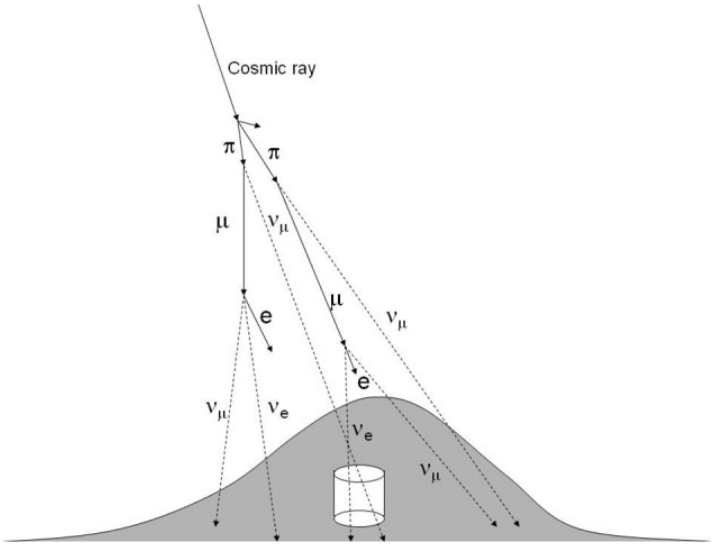

Figure 1.4: Atmospheric neutrinos production scheme. Reproduced from [4].

pare results of various experiments, such as Kamiokande, Super-Kamiokande, IMB and Soudan-2, it became more convenient to use a double ratio (Eq. (1.11)), which allowed to cancel out uncertainties related to the corresponding flux and cross-section.

$$R = \frac{(\mu/e)_{data}}{(\mu/e)_{MC}} \tag{1.11}$$

This ratio was expected to be equal to 1 and the neutrino flux studies [37] were prognosed uncertainty on the double ratio (Eq. (1.11)) below 5%. However, the experimental result was below that (Fig. 1.5). This effect has been called atmospheric neutrino anomaly (ANA).

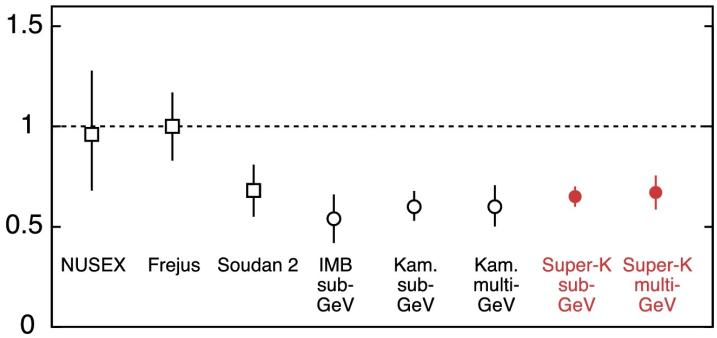

Figure 1.5: Double ratio for atmospheric μ and e fluxes in comparison of data to MC prediction. Reproduced from [5]

1.1.5 — Discovery of neutrino oscillations

Both SNP and ANA could be explained by the hypothesis of neutrino oscillations: a conversion of neutrino's flavor state as the particle propagates through space. Even though at that time there were other concurring hypothesis, they are out of the scope of interest of present thesis and thus will not be discussed here.

The proof of neutrino oscillations standing behind the solar neutrino problem came from SNO experiment in 2002 [38]. The Cherenkov detector with 400 tonnes heavy water target was able to detect all three flavours

of ^8B neutrinos coming from the Sun via charged current (CC), neutral current (NC) and elastic scattering (ES):

$$\nu_e + d \rightarrow p + p + e^- \tag{1.12}$$

$$\nu_\alpha + d \rightarrow p + n + \nu_\alpha \tag{1.13}$$

$$\nu_\alpha + e^- \rightarrow \nu_\alpha + e^- \tag{1.14}$$

where d stands for deuteron and $\alpha = e, \mu, \tau$. While the CC interaction (Eq. (1.12)) provides information only on the ν_e flux (similar to Homestake experiment discussed earlier), the NC (Eq. (1.13)) and the ES (Eq. (1.14)) interaction channels are sensitive to all flavours which allows measuring the total solar neutrino flux. The flux

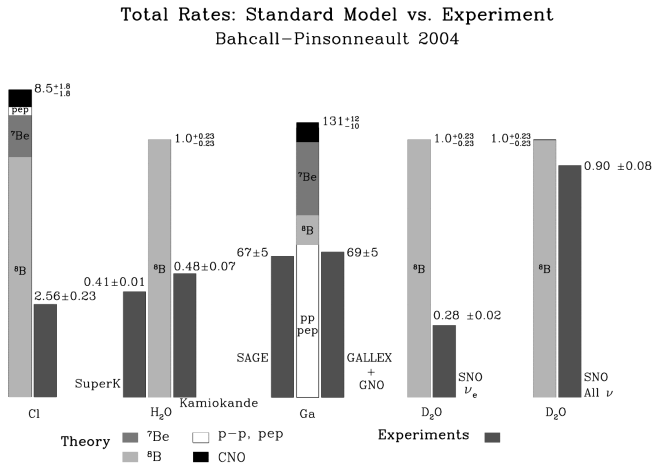

Figure 1.6: Theory versus experiment. The figure compares the predictions of the standard Solar Model plus the standard model of electroweak interactions with the measured rates in all solar neutrino experiments. Reproduced from [3].

of ν_e observed by SNO was approximately one third of the one predicted by the SSM, but the total flux was in a good agreement with the model (Fig. 1.6), probe of its validity. This discovery arrived as both a solution for SNP and a proof for an existence of neutrino oscillations.

A resolution for the ANA came from data accumulated by another experiment: Super-Kamiokande [6], a successor of Kamiokande. Super-Kamiokande, also a Cherenkov detector, however filled with ultra pure water, with 40kt of active volume. If ANA could be explained with neutrino oscillations, then the flux of muon neutrinos traversing Earth would be smaller than the one passing the detector from the opposite side i.e. flux should depend on zenith angle. Also, the flux was expected to show dependency on neutrino energy. This was exactly the result observed by Super-Kamiokande (Fig. 1.7).

The results of both experiments showed that neutrinos can undergo a similar flavor oscillations which were previously demonstrated in case of kaons [39]. A theoretical explanation of this process will be presented in more detailed in the next section.

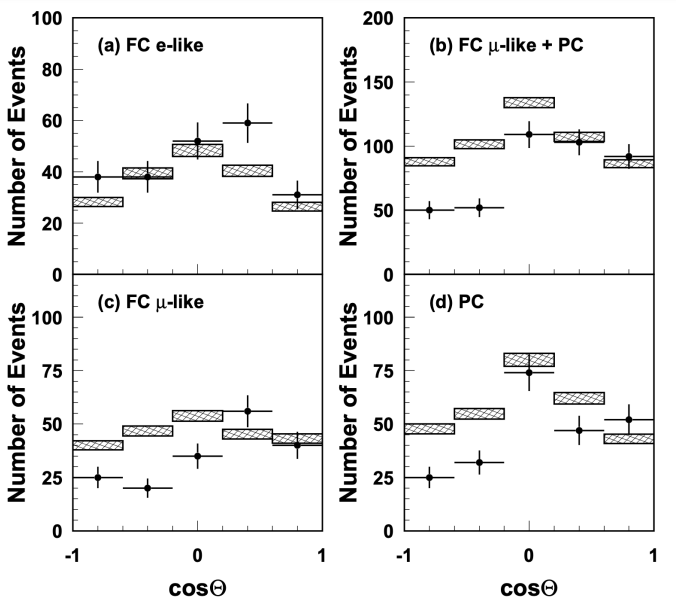

Figure 1.7: Observed (points) and expected (shaded blocks) number of neutrino events with respect to zenith angle. Predictions calculated assuming no oscillations. Reproduced from [6].

1.2 — The theory of neutrino oscillations

Neutrino oscillations can be described in terms of the flavor eigenstates $\nu_\alpha(\alpha = e, \mu, \tau)$, produced through electroweak interaction, and mass eigenstates (m_1, m_2, m_3) of these particles. ν_α can be described as a linear combination of mass eigenstates:

$$|\nu_\alpha\rangle = \sum_k U^*_{\alpha k} |\nu_k\rangle \tag{1.15}$$

where U is a unitary 3×3 matrix called Ponetecorvo-Maki-Nakagawa-Sakata (PMNS) matrix [40, 41], which can be presented as follows:

$$U = \begin{pmatrix} U_{e1} & U_{\mu 1} & U_{\tau 1} \\ U_{e2} & U_{\mu 2} & U_{\tau 2} \\ U_{e3} & U_{\mu 3} & U_{\tau 3} \end{pmatrix} \tag{1.16}$$

Or in a parametrized view:

$$U = \begin{pmatrix} c_{12}c_{23} & s_{12}c_{13} & s_{13}e^{-i\delta_{CP}} \\ -s_{12}c_{23} - c_{12}s_{23}s_{13}e^{i\delta_{CP}} & c12c_{23} - s12s_{23}s_{13}e^{i\delta_{CP}} & s_{23}c_{13} \\ s_{12}s_{23} - c_{12}c_{23}s_{13}e^{i\delta_{CP}} & -c12s_{23} - s12c_{23}s_{13}e^{i\delta_{CP}} & c_{23}c_{13} \end{pmatrix} \tag{1.17}$$

where $c_{ij} = cos\theta_{ij}$ and $s_{ij} = sin\theta_{ij}$ are trigonometric functions of the three mixing angles and δ_{CP} is the Charge-Parity (CP) symmetry violating complex phase. This is the most general way to parametrize a three generation mixing matrix (same parametrization can be used in case of CKM quark mixing matrix [42–44]) This parametrization will be used further through out the present thesis.

In order to obtain the probability of the transition $\nu_\alpha \rightarrow \nu_\beta$ as a function of time, one should start by describing the evolution of the mass states with time. Given that massive neutrinos are eigenstates of the Hamiltonian:

$$H|\nu_k\rangle = E_k|\nu_k\rangle \tag{1.18}$$

with eigenvalues $E_k = \sqrt{\vec{p}^2 + m_k^2}$. Then the time evolution is presented through time-dependent Shrödinger equation

$$i\frac{d}{dt}|\nu_k(t)\rangle = H|\nu_k\rangle \tag{1.19}$$

and massive neutrino states evolution can be approximated with a plane wave.

$$|\nu_k(t)\rangle = e^{-iE_k t}|\nu_k\rangle \tag{1.20}$$

From Eq. (1.15) and Eq. (1.20), a time evolution of a flavour state of neutrino, produced with a flavour α at time $t = 0$, can be presented as:

$$|\nu_\alpha(t)\rangle = \sum_k U^*_{\alpha k} e^{-iE_k t}|\nu_k\rangle \tag{1.21}$$

As the matrix U is unitary, massive states ν_k can be presented similarly to Eq. (1.15). Substituting this expression to Eq. (1.21), if the PMNS matrix (Eq. (1.17)) is not diagonal (i.e. it contains non-zero mixing angles), a neutrino created with a well-defined flavour eigenstate can evolve in time to become a superposition of flavour eigenstates.

$$|\nu_\alpha(t)\rangle = \sum_{\beta=e,\mu,\tau} (\sum_k U^*_{\alpha k} e^{-iE_k t}) U_{\beta k}|\nu_\beta\rangle \tag{1.22}$$

Therefore the oscillation probability of $\nu_\alpha \rightarrow \nu_\beta$ can be written as follows:

$$P_{\nu_\alpha \rightarrow \nu_\beta}(t) = |\langle\nu_\beta|\nu_\alpha(t)\rangle|^2 = \sum_{k,j} U^*_{\alpha k} U_{\beta k} U_{\alpha j} U^*_{\beta j} e^{-i(E_k - E_j)t} \tag{1.23}$$

An ultra-relativistic limit applies in the case of neutrinos and it is possible to use an approximation of $E_k - E_j \simeq \frac{\Delta m^2_{kj}}{2E}$, where $\Delta m^2_{kj} = m^2_k - m^2_j$ and $E = |\vec{p}|$ (neutrino energy, neglecting neutrino mass). Again, in the ultra-relativistic limit, $t = L$, where L is the distance between the source and the detector. Thus, substituting in Eq. (1.23), the oscillation probability can be shown as a function of neutrino energy and the baseline length

$$P_{\nu_\alpha \rightarrow \nu_\beta}(L, E) = |\langle\nu_\beta|\nu_\alpha(t)\rangle|^2 = \sum_{k,j} U^*_{\alpha k} U_{\beta k} U_{\alpha j} U^*_{\beta j} e^{-i\frac{\Delta m^2_{kj} L}{2E}} \tag{1.24}$$

In Eq. (1.24), the transition probability is expressed through U matrices, therefore through the mixing angles and CP the violating phase, squared mass differences, baseline length and particle's energy. The amplitude of neutrino oscillations is determined by the mixing matrix U. And separating real and imaginary part in the equation Eq. (1.24),

$$\begin{aligned} P_{\nu_\alpha \rightarrow \nu_\beta}(L, E) = \delta_{\alpha\beta} - 4\sum_{k>j} \mathrm{Re}\left[U^*_{\alpha k} U_{\beta k} U_{\alpha j} U^*_{\beta j}\right] \sin^2\left(\frac{\Delta m^2_{kj} L}{4E}\right) \\ +2\sum_{k>j} \mathrm{Im}\left[U^*_{\alpha k} U_{\beta k} U_{\alpha j} U^*_{\beta j}\right] \sin\left(\frac{\Delta m^2_{kj} L}{2E}\right) \end{aligned} \tag{1.25}$$

where $\delta_{\alpha,\beta}$ is the Kronecker delta, it is visible that $\Delta m_{kj} \neq 0$ is required for neutrino oscillations to take place. Therefore, at least one of the neutrinos must be massive and at least one of the neutrinos must have mass different from others. Thus if there are oscillations, then neutrinos must have mass.

1.2.1 — Neutrino mass

As it has been shown in Eq. (1.24), the probability of neutrino oscillations depends not directly on the neutrino mass but on the neutrino mass difference squared. This way experiments dedicated to study the oscillation process cannot directly measure neutrino mass. Instead what is measured are Δm^2_{21} and $|\Delta m^2_{31}|$, although the sign of the latter remains unknown [45]. Because of this fact, there are two possible hierarchies of the neutrino masses: $m_1 < m_2 < m_3$ (normal mass ordering, or NO) and $m_3 < m_1 < m_2$ (inverted mass ordering, or IO) (Fig. 1.8).

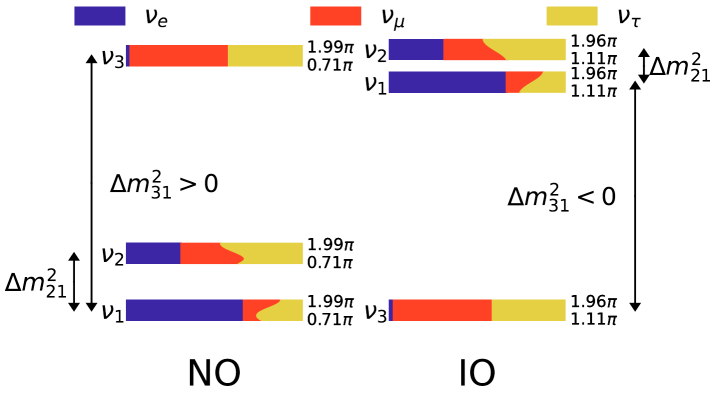

Figure 1.8: Illustration of normal and inverted neutrino mass ordering. Reproduced from [7].

There are experiments focused on direct mass measurements, but these experiments so far have only set upper limits on the mass values. Also, constraints of the sum of neutrino masses are coming from cosmological bounds or neutrinoless double beta decay experiments [46, 47]. Global fit [48, 49] of these experiments yields a constraint:

$$\sum m_\nu^{NO} \gtrsim 0.06eV$$
$$\text{and} \sum m_\nu^{IO} \gtrsim 0.01eV$$

1.2.2 — Neutrino oscillations in matter

The mathematical formalism presented above assumes oscillations in vacuum. However, the in case of an accelerator experiment, T2K in particular, the mixing of neutrinos is happening while they are propagating through the matter of the Earth. Therefore it is important to understand how this difference would affect the transition probability. In 1979 L.Wolfstein [50] suggested that the characteristics of neutrino oscillations in matter should be different from the one in vacuum and then S.Mikheyev and A.Smirnov [51], in 1985 showed the dependency of the neutrino oscillation probability on the density of the matter.

When neutrinos travel through a dense medium, they experience forward scattering from particles they encounter along the way. The interaction potential in the case of the CC chanel can be written as follows:

$$V_{CC} = \sqrt{2} G_F N_e, \tag{1.26}$$

and for the NC channel:

$$V_{NC} = -\frac{1}{2}\sqrt{2} G_F N_n, \tag{1.27}$$

where G_F is the Fermi constant and N_e (N_n) is the density number of the electrons (neutrons) in matter. If matter is neutral then for NC channel the effect from protons and electrons cancels out. Also, the contribution to the NC potential for all three ν flavours is the same, thus there is no effect on the oscillation probability coming from this interaction channel. There will be then a contribution to the Hamiltonian from a potential proportional to the density of electrons (CC channel):

$$\mathcal{H} = -\frac{1}{2E}\left(U M^2 U^\dagger + A_{CC}\right) \tag{1.28}$$

where

$$M^2 = \begin{bmatrix} 0 & 0 & 0 \\ 0 & \Delta m^2_{21} & 0 \\ 0 & 0 & \Delta m^2_{31} \end{bmatrix}, \tag{1.29}$$

$$A_{CC} = 2EV_{CC} \begin{bmatrix} 1 & 0 & 0 \\ 0 & 0 & 0 \\ 0 & 0 & 0 \end{bmatrix} \tag{1.30}$$

In order to simplify the calculation, the two-flavour approximation will be used for further steps. In case of two flavor oscillations the neutrino mixing matrix U in vacuum (Eq. (1.31)) for convenience is defined positive.

$$U = \begin{bmatrix} \cos\theta & \sin\theta \\ -\sin\theta & \cos\theta \end{bmatrix} \tag{1.31}$$

where θ is a single mixing angle and $\Delta m^2 = m_2^2 - m_1^2$ is a single mass-squared difference. Then the oscillation probability $\nu_\alpha \to \nu_\beta$:

$$P_{\nu_\alpha \to \nu_\beta}(L, E) = \sin^2(2\theta)\sin^2\left(\frac{\Delta m^2 L}{4E}\right), \tag{1.32}$$

where Δm^2 is a single mass squared difference. Using Eq. (1.28) and Eq. (1.31) Hamiltonian in flavour basis can be written as:

$$\mathcal{H}_F = \frac{1}{4E}\begin{bmatrix} -\Delta m^2 \cos 2\theta + A_{CC} & \Delta m^2 \sin 2\theta \\ \Delta m^2 \sin 2\theta & \Delta m^2 \cos 2\theta - A_{CC} \end{bmatrix} \tag{1.33}$$

The effective Hamiltonian in mass basis can be derived through diagonalization of the effective mixing matrix U_M in matter, such that:

$$\mathcal{H}_M = U_M^T \mathcal{H}_F U_M = \frac{1}{4E} \begin{bmatrix} -\Delta m_M^2 & 0 \\ 0 & \Delta m_M^2 \end{bmatrix}, \tag{1.34}$$

where

$$U_M = \begin{bmatrix} \cos\theta_M & \sin\theta_M \\ -\sin\theta_M & \cos\theta_M \end{bmatrix} \tag{1.35}$$

$$\begin{aligned} \Delta m_M^2 &= \sqrt{\left(\Delta m^2 \cos 2\theta - A_{CC}\right)^2 + \left(\Delta m^2 \sin 2\theta\right)^2} \\ \sin 2\theta_M &= \frac{\Delta m^2 \sin 2\theta}{\Delta m_M^2} \end{aligned} \tag{1.36}$$

Then if the matter density is constant, then the oscillation probability $\nu_\alpha \to \nu_\beta$ can be presented as follows:

$$P_{\nu_\alpha \to \nu_\beta}(L, E) = \sin^2(2\theta_M) \sin^2\left(\frac{\Delta m_M^2 L}{4E}\right) \tag{1.37}$$

The structure of the Eq. (1.37) is the same as for Eq. (1.32), however the mixing angle and squared mass difference are replaced by corresponding effective values in matter. The electron density number relevant in case of T2K is $N_e \sim 1.7 \times 10^{30} m^{-3}$ [52], $A_{CC} \sim 1.5 \times 10^{-4} eV^2$ for $E = 600$MeV (peak oscillation energy of neutrinos in T2K [53]). Assuming $\Delta m^2 = 2.45 \times 10^{-3} eV^2$ and $\theta = 46.5°$ [53], then effective mixing parameters would be: $\Delta m_M^2 \sim 2.5 \times 10^{-3} eV^2$ and $\theta = 42°$. As it can be seen, these parameters, in case of T2K, are not getting significant changes from the matter effect, mainly due to having relatively short baseline.

1.3 — Modern neutrino oscillation experiments

Even though the historical introduction may give an impression that we know much about neutrino oscillations, there are still a lot of open questions. Is $\Delta m_{32}^2 > 0$? This would define if mass states are in NO or IO (Fig. 1.8). Is CP symmetry violated? What is the value of δ_{CP}? Answer to these question can lit the light to the origin of matter-antimatter asymmetry in our Universe. Is value of θ_{23} is equal, more or less than 45°? These three questions are some of the most interesting directions for modern experiments measuring oscillation parameters. In the following section there will be discussed the current status of the field and prospects of the future experiments.

1.3.1 — $\theta_{12}, \Delta m_{21}^2$

Measurements of so-called "solar" parameters θ_{12}, Δm_{21}^2 were initially a subject of the setups dedicated to study of solar flux through ν_e disappearance channel.

The latest measurement of θ_{12} and Δm_{21}^2 are coming from SK and SNO [54] atmospheric experiments as well as reactor experiment KamLAND [55]. All three experiments give consistent results for θ_{12} (Fig. 1.9), with an averaged value of $\theta_{12} = 0.307 \pm 0.013$ [54]. However, for Δm_{21}^2, there is a tension and a combined fit of SK+SNO disfavors KamLAND bets fit value at $\sim 1.4\sigma$ (Fig. 1.9). A joined fit suggests $\Delta m_{21}^2 = (7.53 \pm 0.18) \times 10^{-5} eV^2$ [54].

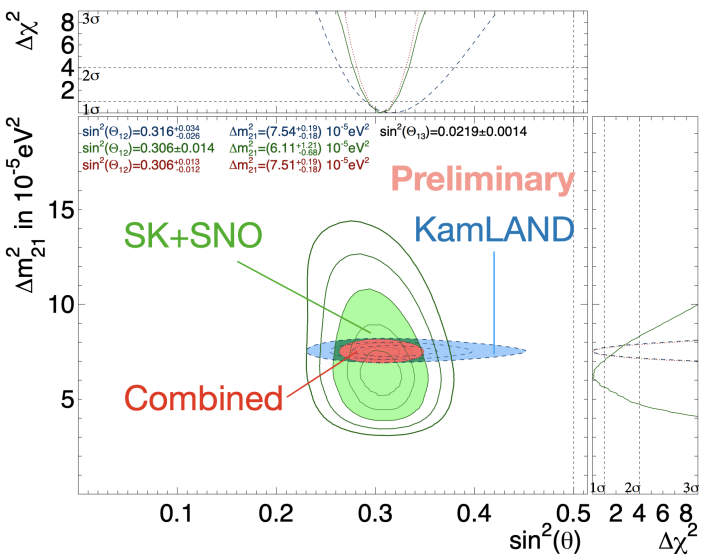

Figure 1.9: Allowed regions for solar parameters from SK+SNo and KamLand experiments and a combined one. Reproduced from [7].

A future experiment, JUNO will be monitoring a reactor neutrino flux from two sites, located 53 km away and containing, in total, 10 nuclear reactors. Also, JUNO has a potential to measure a flux of solar ^8B neutrinos and together with reactor $\bar{\nu}_e$ surviving data the experiment is aiming to achieve a sub-percent precision on both solar parameters [56]. Moreover a comparison between solar and reactor measurements made at the same setup may lite the light of present discrepancy between KamLAND [55] and solar experiments [54] results on Δm^2_{21} [57].

1.3.2 — θ_{13}

Even though this mixing angle is quite often refereed as "reactor" one, it can also be measured with some accelerator experiments. The T2K experiment (it will be described in details in the following chapter) is sensitive to θ_{13} thorough ν_e appearance channel:

$$P\left(v_\mu \rightarrow v_e\right) \approx \sin^2\theta_{23}\left(\sin^2 2\theta_{13}\sin^2\left(\frac{\Delta m^2_{32}L}{4E_v}\right)\left(1+\frac{2a}{\Delta m^2_{31}}\left(1-2\sin^2\theta_{13}\right)\right)\right.$$
$$\left. -\sin 2\theta_{12}\sin 2\theta_{23}\left(\sin 2\theta_{13}\right)\cos\theta_{13}\sin\delta\sin^2\left(\frac{\Delta m^2_{32}L}{4E_v}\right)\sin\left(\frac{\Delta m^2_{21}L}{4E_v}\right)\right. \tag{1.38}$$

And the latest measurement yields $\theta_{13} = (2.54 \pm 0.39) \times 10^{-2}$ [58].

These result is consistent with measurements coming from reactor experiments. Such experiments deal with an intense flux of $\bar{\nu}_e$ with energies around 4 MeV, produced in fusion and fission processes in the core of nuclear powerplants and captured via inverse beta-decay reaction:

$$\bar{\nu}_e + p \rightarrow e^+ + n \tag{1.39}$$

The probability of $\bar{\nu}_e$ disappearance process, typical for reactor experiments:

$$\begin{aligned} P\left(\bar{\nu}_e \to \bar{\nu}_e\right) = 1 &- \cos^4\left(\theta_{13}\right)\sin^2\left(2\theta_{12}\right)\sin^2\left(\Delta m^2_{21}L/4E\right) \\ &- \cos^2\left(\theta_{12}\right)\sin^2\left(2\theta_{13}\right)\sin^2\left(\Delta m^2_{31}L/4E\right) \\ &- \sin^2\left(\theta_{12}\right)\sin^2\left(2\theta_{13}\right)\sin^2\left(\Delta m^2_{32}L/4E\right) \end{aligned} \tag{1.40}$$

Particle Data Group (PDG) averages the best fit value of θ_{13} based on data from several experiments. Double Chooz, an liquid scintillator detector located near a nuclear power plant in France, $\sin^2\theta_{13} = (2.70 \pm 0.37) \times 10^{-2}$ [59]. RENO experiment has been collecting data from Hanbit Nuclear Power Plant (Korea) since August 2011. Two identical liquid scintillator detectors are looking for neutrino events from interactions on free protons, followed by neutron capture on hydrogen. The latest result on θ_{13} is $\sin^2\theta_{13} = (2.22 \pm 0.21_{stat} \pm 0.37_{syst}) \times 10^{-2}$ [60]. Daya Bay is reactor neutrino experiment located in the south of China between Hong Kong and Shenzhen. In three underground halls eight detectors are catching antineutrinos from six cores (grouped by two) of water pressure power plants. The experiment started data taking in 2012 and finished operating at the end of this year. This experiment provides a world-leading precise result, $\theta_{13} = (2.189 \pm 0.076) \times 10^{-2}$ [19].

1.3.3 — CP violation phase δ

δ_{CP} can be measured only in case if mixing angles are not equal to zero. After in 2011 T2K discovered non-zero value of the last unknown angle θ_{13} in 2011 and then, later in 2012 the discovery has been made by DayaBay experiment, confirming the indication. It open the door to a new and now very promising challenge: the search for CP violation in leptonic sector.

For a direct study of CP asymmetry it is crucial to compare the oscillation probability for neutrinos, $P(\nu_\alpha \to \nu_\beta)$, and antineutrinos $P(\bar{\nu}_\alpha \to \bar{\nu}_\beta)$. This makes accelerator experiments the best tool to measure δ_{CP}. Nowadays the world-leading result is coming from the T2K experiment [58] excluding CP conservation at $\sim 2\sigma$ level for both mass orderings. And excluding $\delta_{CP} = 0$ at 3σ level while still having $\delta_{CP} = \pm\pi$ inside the confidence interval in case of NO.

Other competing experiment NOνA [61] in contrary disfavors CP violating combinations:

$$\delta_{CP} = \pi/2 \text{ excluded at } > 3\sigma \text{ for IO}$$
$$\delta_{CP} = 3\pi/2 \text{ disfavored at } 2\sigma \text{ level for NO}$$

Confirming or rejecting CP violation at 5σ level is one of the goals of the next generation's accelerator experiments: HyperKamiokande (HK) and DUNE. HyperKamiokande, a bigger reincarnation of water Cherenkov detector SuperKamiokande (260kt instead of 50kt respectively of fiducial volume), will be using high intensity and purity neutrino beam produced in J-PARC, this way being an upgrade of currently running T2K experiment. As one can see at Fig. 1.10 HK expects to achieve 3σ sensitivity to CP violation for 80% of δ_{CP} values and close to 5σ for 57%, both after 10 years of data taking. However it should be able to exclude CP conservation ($\delta_{CP} = 0$) if CP violation will be found maximal (i.e. $\delta_{CP} = -\pi/2$).

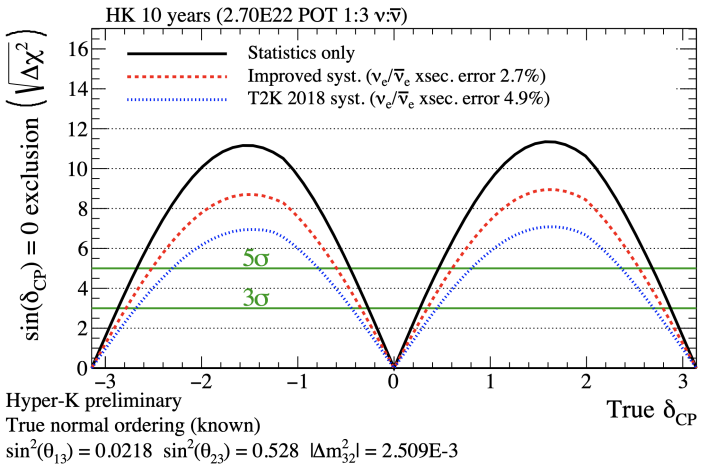

Figure 1.10: Sensitivity to exclude CP conservation with respect to true δ_{CP} values for 10 years of statistic accumulation in HK. Assumed true normal mass ordering. Reproduced from [8]

Another experiment DUNE will be using a novel at such scales liquid Argon technology. Far detector, is design to be a 4 liquid Argon TPC's with total fiducial volume of 40kt. This technology provides high-precision reconstruction and after of 13 years of running DUNE should be able to determine CP violation for 75% of CP values at 3σ level.

1.3.4 — $|\Delta m^2_{32}|, \theta_{23}$ and mass ordering

The newest results on the "atmospheric" parameters $|\Delta m^2_{32}|, \theta_{23}$ are coming from both atmospheric and long baseline accelerator experiments

$$\sin^2\theta_{23} = 0.57^{+0.003}_{-0.04}$$

for NOνA experiment [61] and

$$\sin^2\theta_{23} = 0.53^{+0.003}_{-0.04}$$

for T2K [58].

Both NOνA and T2K latest fits give slight preference to NO of neutrino mass states.

The most promising results are expected from the upcoming experiments. Perviously mentioned JUNO will bee able to discriminate between neutrino mass ordering hypothesis at the 3σ level. While DUNE experiment, thanks to long baseline (1300km) will be utmost sensitive to mass ordering. It will provide a 5σ level sensitivity to mass ordering for all of CP values (Fig. 1.11). Finally HyperKamiokande, with a combination of accelerator and atmospheric data can determine mas ordering with sensitivity of (4-6)σ.

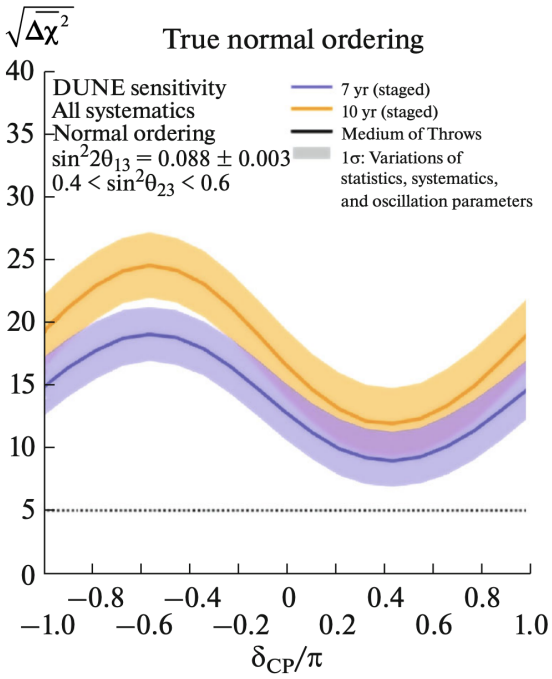

Figure 1.11: Sensitivity to mass hierarchy with respect to true δ_{CP} values for 7 and 10 years of statistic accumulation in DUNE. Assumed true normal mass ordering. Reproduced from [9].

2 — T2K experiment

T2K (Tokai to Kamioka) is a long baseline accelerator neutrino experiment located in Japan. Originally, it was proposed in early 2000's to lit the light on the neutrino oscillation parameters θ_{13} and δ_{CP}, looking for the appearance of the ν_e in the beam of ν_μ (see Fig. 2.1a). Also, the experiment was designed to provide a precise measurements of the atmospheric oscillation parameters mixing angle θ_{23} and the mass splitting term Δm^2 through the measurements of the disappearance of the ν_μ in the ν_μ beam (see Fig. 2.1b).

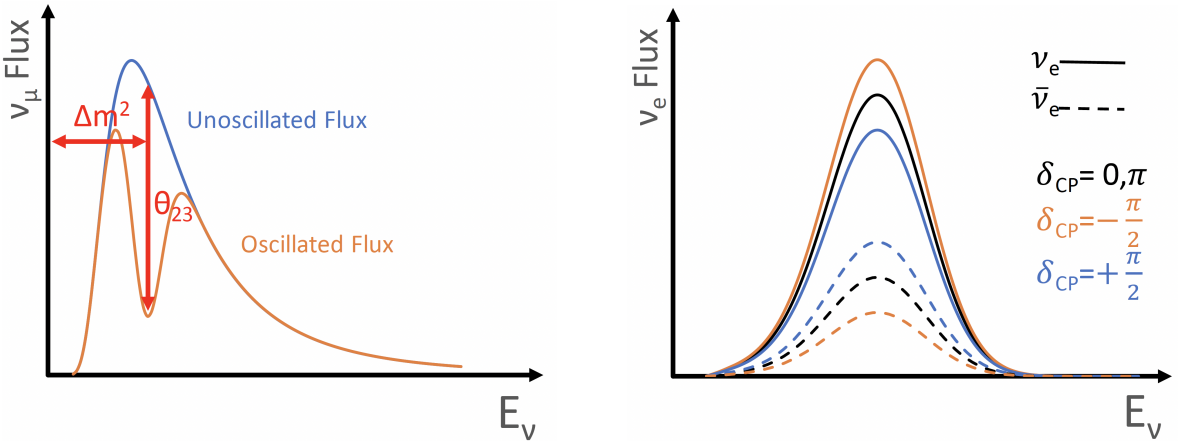

(a) (b)

Figure 2.1: T2K event distribution with respect to energy. (a) shows the distribution for the case of ν_μ disappearance and (b) for the case of ν_e appearance in the ν_μ beam

Aside from the main program, T2K aims to measure neutrino cross-sections on active water targets, carbon scintillator bars and iron plates. Today, T2K consistently provides ones of the world-leading results for neutrino oscillation parameters on both neutrino appearance and disappearance ([53, 62–65]). The experiment consists of J-PARC proton accelerator facility, located on the eastern coast of Japan (Tokai), a neutrino beamline, a pair of near detectors and a far detector, based on the opposite, western, coast in a mine near Kamioka. A proton beam hits the target and creates hadrons, which in their turn decay producing neutrinos, which are the only particles meant to cross the filter wall and be detected twice: first time 280m away from the target by near detectors INGRID and ND280 and then, after traveling 295km through the Earth's surface, by a far detector Super Kamiokande (SK) (see Fig. 2.2). At 2019 near detector site has been equipped with a WAGASCI-BabyMIND [66, 67] complex. However at the present moment this data is not yet used in T2K

analyses.

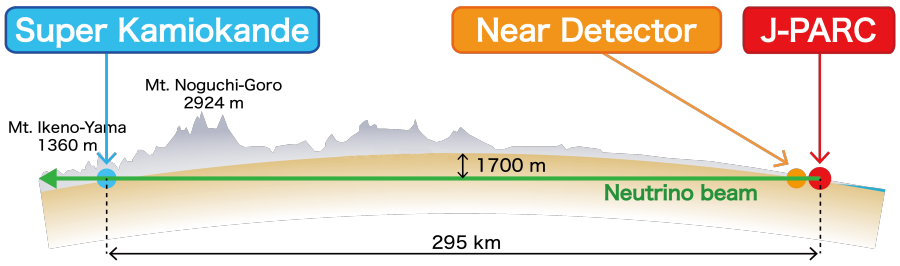

Figure 2.2: Simplified scheme of the main parts of the T2K experiment

This chapter is dedicated to a description of the mentioned detectors, performance and reconstruction specifics. Also, as a part of this work, has been conducted a separate study on the scintillator detectors ageing.

2.1 — Neutrino beam

J-PARC accelerator complex, located near the city of Tokai (Ibaraki, Japan) is made out of three main parts: a linear accelerator (LINAC), a rapid-cycling synchrotron (RSC) and the main ring synchrotron (MR) (see Fig. 2.3). Neutrino beam starts with a H^- ions dumped to LINEAC and accelerated up to 400 MeV. At the moment of injection to RCS these are stripped of electrons and converted to protons (H^+), which are accelerated up to 3 GeV. In RCS there are two bunches per cycle which, over multiple cycles, are supplied to the MR. In MR protons, formed in up to 8 bunches, are accelerated up to 30 GeV (maximum beam power up to 2021 522.6 kW) before being fast extracted via a set of five kicker magnets into a neutrino beamline. Time synchronization between extracted proton beam and signals in near and far detectors is crucial for discriminating various background-like, for instance, cosmic rays or neutrinos produced in the interactions in the surrounding materials. Therefore every beam spill is extracted in a very narrow time window of $5\ \mu$s which is synchronized through a custom made GPS based system with other parts of the experiments at the scale of O(50 ns) [20].

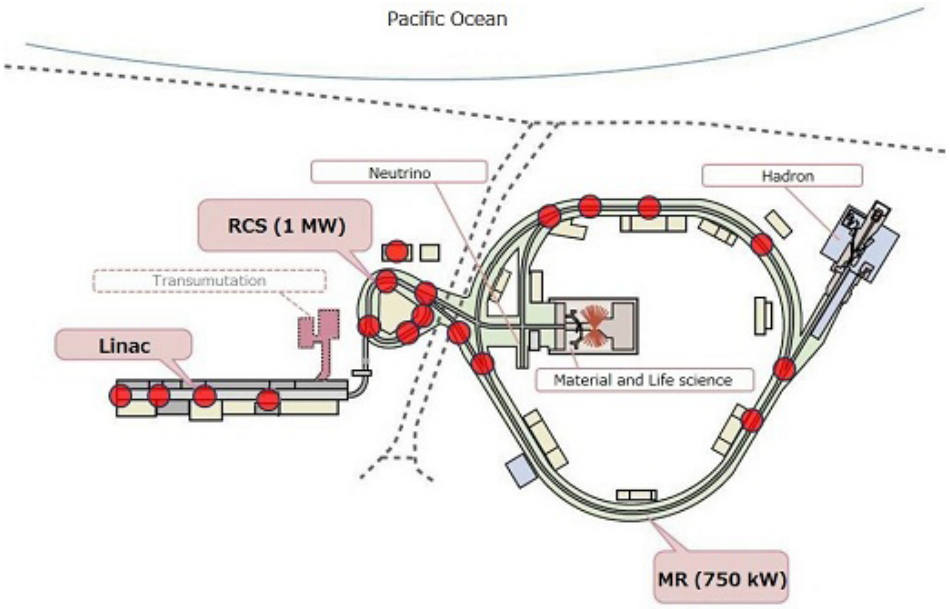

Figure 2.3: Schematic view of the J-PARC accelerator facility

Once a beam spill of eight bunches is extracted it has to travel through a neutrino beamline, that consists of two sections: primary and secondary beam lines (see Fig. 2.4).

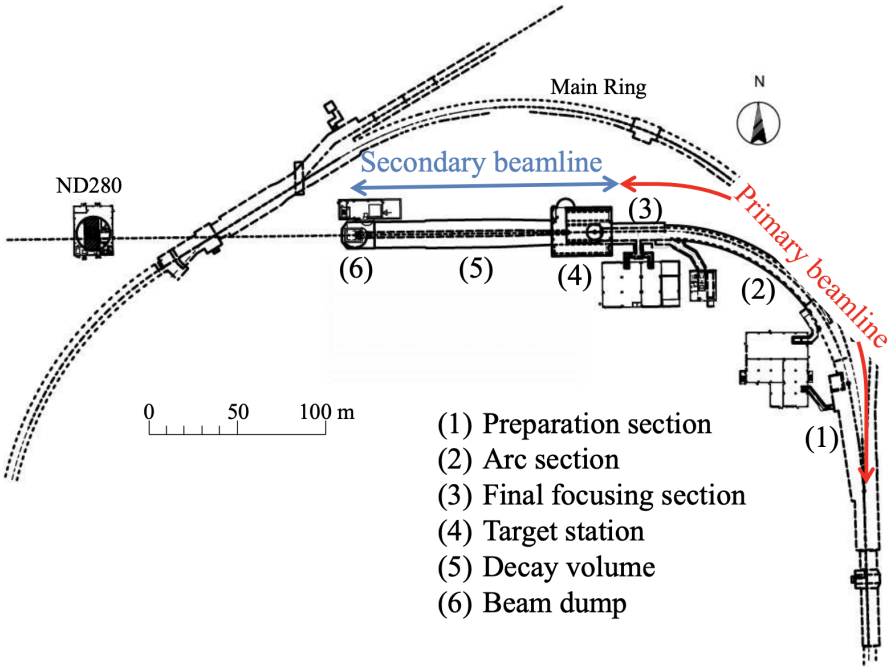

Figure 2.4: Plot of J-PARC's neutrino beam line

The former one, composed of normal and superconducting magnets, bends the beam directing it toward Kamioka along with setting an off-axis angle in the range from 2.0° (minimum) to 2.5° (maximum, current setup). The off-axis concept allows T2K to have a narrow energy band neutrino beam with great suppression

of high energy tails. Off-axis beam spectra has the peak at 0.6 GeV that falls at the first oscillation maximum at 295km (exactly where the T2K's far detector, Super Kamiokande, is), allowing to have lower wrong-sign neutrino background contamination as well as maximizing the effect of the oscillations (see Fig. 2.5).

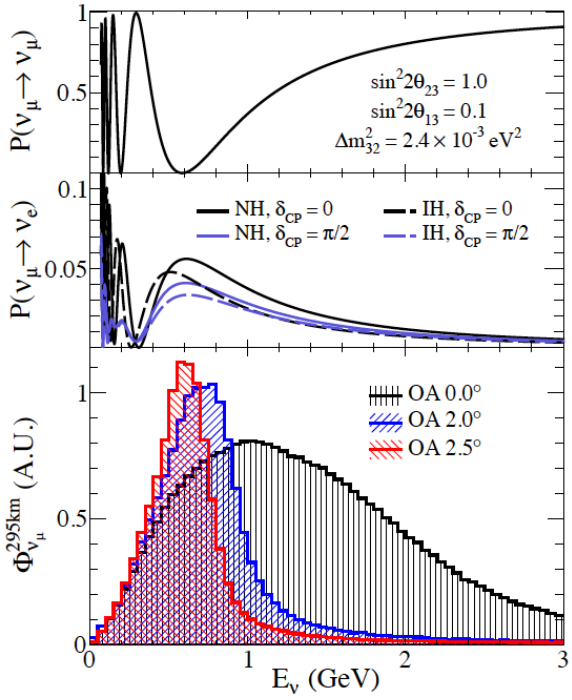

Figure 2.5: Neutrino energy spectra for different off-axis angles

Beam section hosts a number of subsystems to monitor beam's position, angle and profile stability as well as losses. Secondary beamline is sequential to primary and consists of target station, decay volume and a beam dump. Inside the target station there are a graphite target and three focusing magnetic horns. As the beam hits the 91.4 cm target rod, proton interactions produce charged secondary hadrons. Then magnetic horns, depending on the current direction, i.e. so called forward horn current (FHC) or reverse horn current (RHC), are focusing hadrons of only one charge. That allows to have a beam mainly composed of only neutrinos (in case of FHC) or anti neutrinos (RHC). Selected pions and kaons travel through the decay volume producing neutrinos and muons. Apart from neutrinos, which are then used in the experiment, only muons of energy above 5 GeV are able to pass through the target. They are later used to characterize neutrino beam.

Right after the neutrino beam leaves the primary beamline its intensity is measured to derive an expected number of protons to hit the target (POT = Proton On Target), which is one of the main ways to quantify the accumulated data (see

Fig. 2.6).

Table 2.1: Dates of T2K Run periods.

T2K Run	Data Taking Period
Run 1	March 2010 – June 2010
Run 2	November 2010 – March 2011
Run 3	February 2012 – June 2012
Run 4	October 2012 – May 2013
Run 5	May 2014 – June 2014
Run 6	November 2014 – June 2015
Run 7	February 2016 – May 2016
Run 8	October 2016 – April 2017
Run 9	October 2017 – May 2018
Run10	November 2019 – February 2020
Run11	March 2021 – April 2021

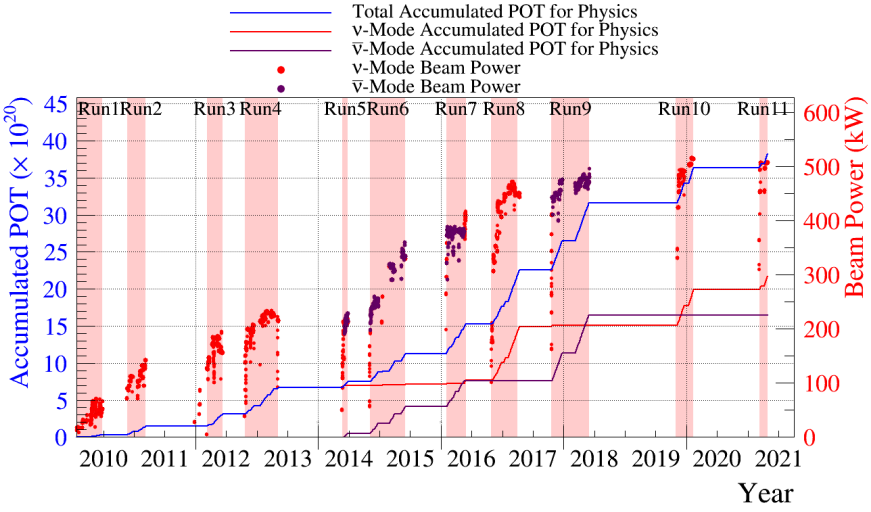

Figure 2.6: Data taking summary since 2010 in terms of instantaneous beam power and accumulated POT.

2.2 — Near detectors

As it was mentioned before, in the T2K experiment the neutrino beam is being detected twice at different distances from the target therefore giving information of the beam content at different L/E points.

First neutrinos encounter a near detector complex, located 280 meters away from the target station. Here the flux is meant to contain mainly not yet oscillated neutrinos. The INGRID detector is standing straight at the beam axis line, while ND280 complex is shifted 2.5°. WAGASCI-BabyMIND is located in the same pit as other near detectors 1.5 °off the beam axis.

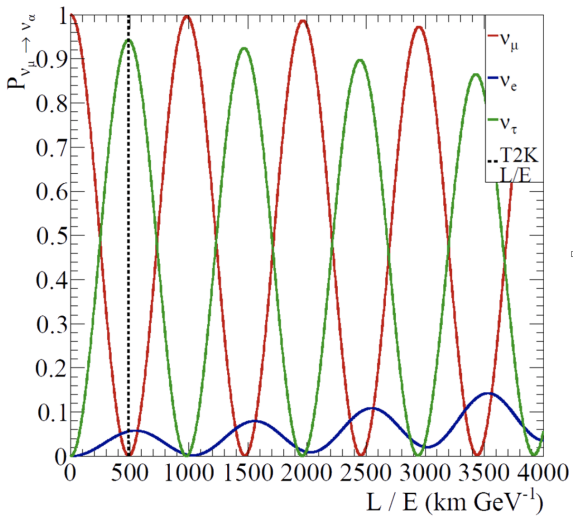

Figure 2.7: The neutrino oscillation probability as a function of the L/E ratio. The dash line marks the location of the T2K's far detector Super Kamiokande. For the near detector the ratio is very close to zero.

2.2.1 — INGRID

INGRID is situated exactly on the T2K's beam axis and is crucial for direct beam rate and stability monitoring along with measuring neutrino interaction cross-sections on iron and scintillator targets. The detector itself consists of 14 sandwich-like modules of iron and scintillator plates surrounded by veto panels (Fig. 2.9). Ingrid modules form a cross (Fig. 2.8), centred on the beam axis with 0.4 mrad precision. Side modules are used to measure beam asymmetry.

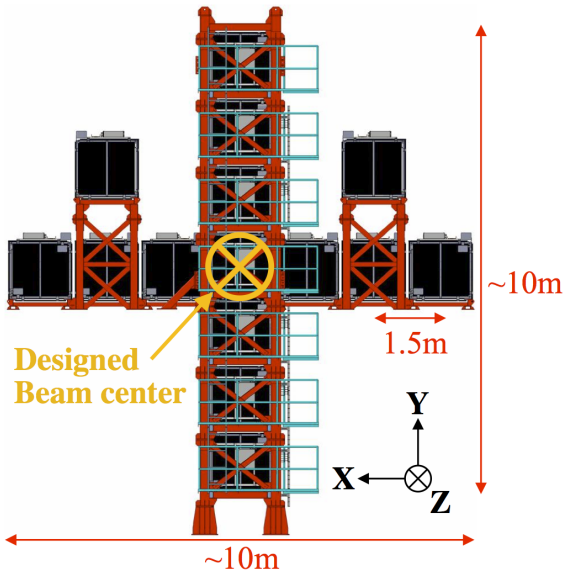

Figure 2.8: Structure of the INGRID detector

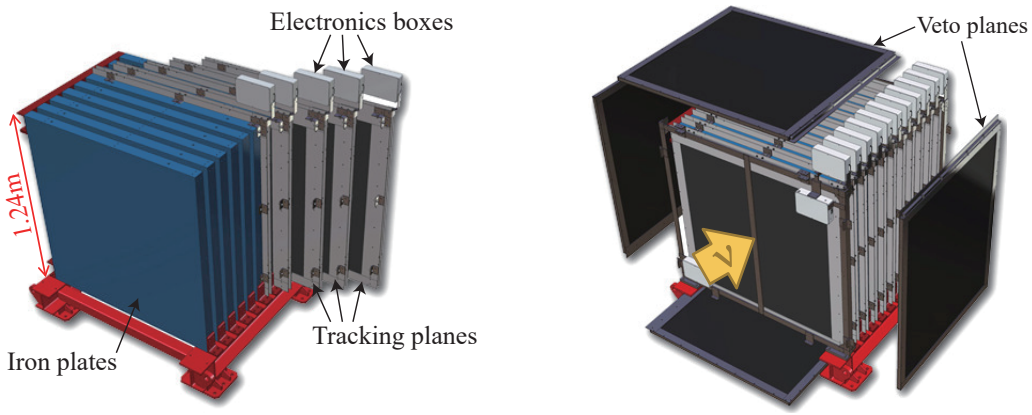

Figure 2.9: INGRID module structure: (a) scintillator and iron plates inside the module, (b) a module surrounded by veto panels

INGRID extruded scintillator bars were made in 2007-2008 in Fermilab of DowStyron 663 W polystyrene doped with 1% PPO and 0.03% POPOP. Each bar is coated with a layer of TiO_2 for diffuse reflection of the scintillator light. A wavelength shifting fibre (WLS) Kuraray Y11 passes through the centre of the bar and collects light to deliver it towards a Hammamtsu MPPC readout on not mirrored end of the bar (see Fig. 2.10).

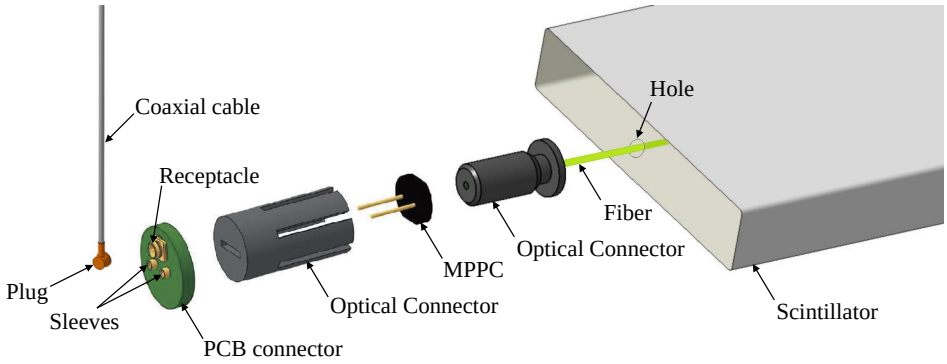

Figure 2.10: Schematic view of INGRID readout

2.2.2 — ND280

The off-axis near detector is located 280 meters away from the target and 2.5° degrees with respect to the beam axis. ND280 measures the flux and spectrum for the different neutrino species in the beam prior to oscillation, as well as several neutrino interaction cross-sections with the target materials of the detector, e.g. water and carbon. A precise knowledge of the initial neutrino beam is crucial to predict the neutrino flux and spectrum at the far detector, and hence to determine the neutrino oscillation parameters. Also, measuring of the ν_μ cross-section provides a great constraint on the backgrounds for ν_e appearance search.

Figure Fig. 2.11 shows an exploded view of ND280 with its different sub-detectors. A neutral pion detector (PØD), three time projection chambers (TPC) and two fine grained detectors (FGD) compose the core, so

called ”tracker” part of ND280. The tracker is surrounded by electro-magnetic calorimeters (ECaL) and then by a magnet, re-used after UA1 [68] and NOMAD experiments. Air gaps of the magnet are equipped with the side muon range detector (SMRD). The magnet provides the magnetic field of 0.2T that is crucial to distinguish positive and negative charged particles.

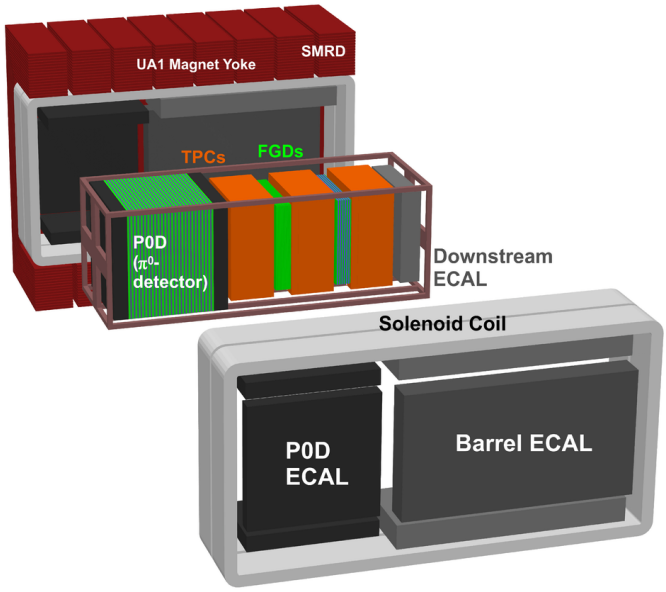

Figure 2.11: ND280 detector complex sub subsystems

Apart from the TPCs (its operation specifics will be discussed in section Section 2.2.2), all of the ND280's sub systems have scintillator bars as an active detecting material. When a particle traverses these detectors, it excites valence electrons of the bar material's atoms and when these electrons are falling back to the ground state, they emit photons with a typical wavelength of $\sim$ 420 nm. Typically, in order to convert scintillation light into a signal, one would use a set of photon multiplying tubes (PMTs), but the presence of the magnetic field makes their operation impossible. Instead, ND280 detectors use multi pixel photon counters (MPPC) to readout the signals. As the MPPC are sensitive to a longer wavelengths, all the scintillator bars have Kuraray Y-11 wave length shifting fibre (WLS) to deliver photons to MPPCs counters, changing their wavelength from blue to green. PØD, ECaL and FGD extruded plastic scintillator bars have the same composition as bars produced for INGRID detector and to the ones used in MINOS experiment [69]. PØD and ECaL counters were also produced at FNAL whereas FGSs are a product of Celco Plastics Ltd. Surrey, British Columbia. Unlike others, for scintillator bars used in the SMRD detector, polystyrene is doped with 1.5% PTP and 0.001% POPOP with reflecting coating being chemically etched instead of extrusion method. These bars were produced by Uniplast company in Vladimir, Russia. ND280's scintillator detectors were manufactured between 2006 and 2009. This subsection is dedicated to ND280 sub-detectors and their main features in the light of T2K oscillation analysis (chapter Chapter 4) as well as scintillator ageing study (chapter Chapter 6).

PØD

The π^0 detector is located in the most upstream (closest to the target) part of ND280. It was designed to measure the neutrino-nucleus interactions with water target with neutral pions production (NC π^0). This is one of the most important backgrounds in SK for the ν_e appearance measurements.

PØD bears a water target surrounded by orthogonal layers of triangular shaped scintillator bars. This detector can run with or without water, therefore via comparing the data accumulated in both modes one can subtract an interaction rate on water for the cross-section studies.

The bars were produced at Fermi National Accelerator Laboratory (FNAL) between 2007 and 2008 and are identical to the ones of the MINERνA experiment. The detector consists of 40 so-called PØDules - modules containing two layers of scintillator bars covered by brass panels. These modules are placed perpendicular to the beam line. All modules are grouped into four Super-PØDules [10]. These units are used for the further analysis described in chapter Chapter 6.

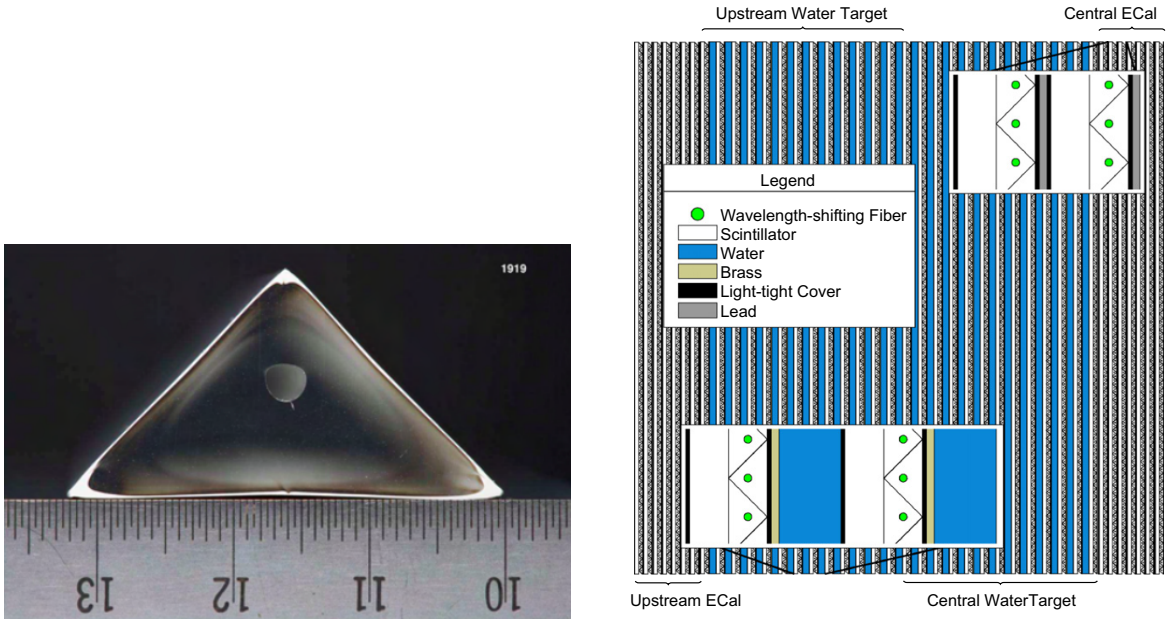

(a) (b)

Figure 2.12: PØD bar view Fig. 2.12a and assembled construction view Fig. 2.12b. Reproduced from [10].

FGD

In ND280 there are two FGDs. The first and the most upstream one has only a scintillator target while the second contains a water target. As for PØD, comparison of the interaction rates with and without water target allows to derive neutrino cross-section on water, that is crucial to constrain systematic uncertainties of the model used to predict the neutrino flux in water Cherenkov far detector. FGDs are the main active target of the ND280 detector, their design provides high spatial resolution, important for an accurate vertex reconstruction. At the same time detectors are thin enough so that most of the secondary particles, escaping from the interaction vertex, will exit FGD and their properties will be measured by surrounding TPCs. Shorter

particle tracks, such as tracks of the recoil protons, are fully measured in FGD. Ability to reconstruct the direction of recoil protons as well as ability to distinguish protons from pions and muons (see Fig. 2.13) is crucial to measure neutrino charge current quasi-elastic (CCQE) interaction and distinguish from a resonant pion production. CCQE is the most dominant neutrino interaction mode at the T2K's peak energies and produces a recoil proton along the lepton, while resonant pion production sits slightly about 0.6 GeV and is a serious background for CCQE [11].

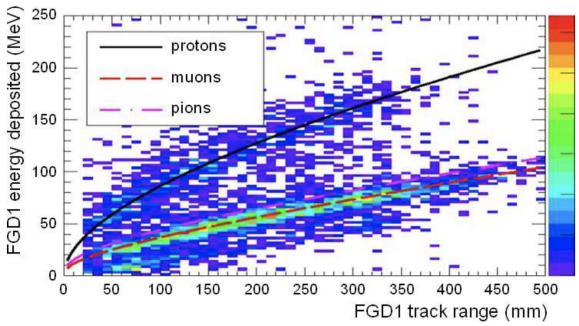

Figure 2.13: Deposited energy vs range for particles stopping in FGD1. The scatterplot shows stopping particles in neutrino beam data, while the curves represent the MC expectations for protons, muons, and pions. Reproduced from [11].

Also similarly to PØD, FGDs consist of orthogonal "XY" layers, which are placed perpendicular to the beam direction. In each bar the signal is read out through one end only having the opposite one mirrored. WLS fibre is coupled to the scintillator through an air gap surrounding it. In FGD fibre extends a few centimeters from the bar and delivers photons to MPPC through a custom made connector.

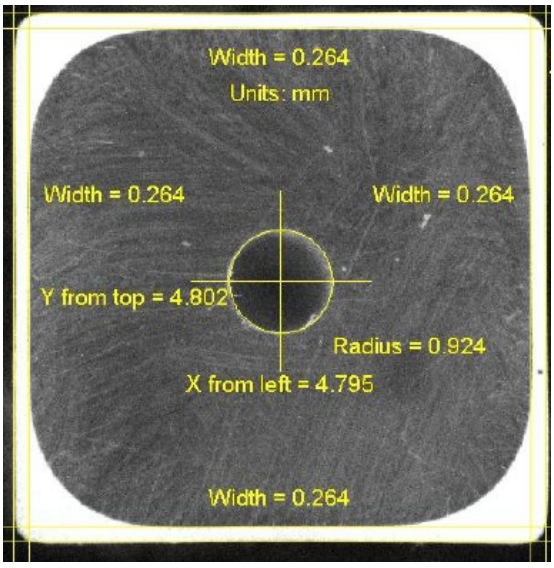

(a)

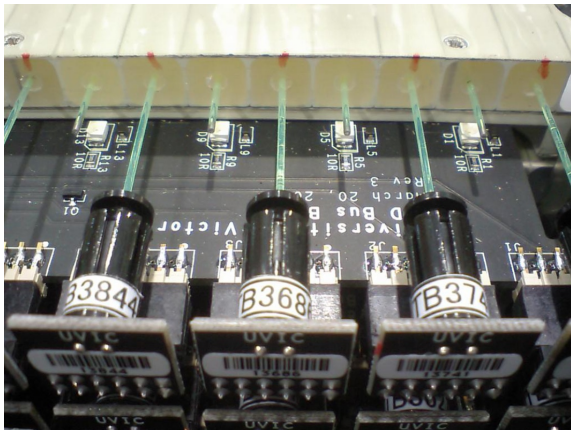

(b)

Figure 2.14: FGD bar view Fig. 2.14a and a view of FGD scintillator layer with WLS fibres connected to MPPC Fig. 2.14b. Reproduced from [11].

TPC

Along with FGDs, ECaL and PØD, a set of two Time Projection Chambers make the tracker part of the ND80 complex. The TPCs are two rectangular boxes with outer dimensions of 2.3 m × 2.4 m × 1.0 m [12]. The volume is divided into two parts: an insulating layer filled with CO_2 and a drift volume containing an argon based gas mixture ($Ar : CF_4 : iC_4H_{10}$ (95:3:2)). When a charged particle traverses the inner volume of the detector it causes the ionization of the gas particles so that created electrons are drifting in the direction of the readout panes away from the central high voltage (HV) cathode (see Fig. 2.15).

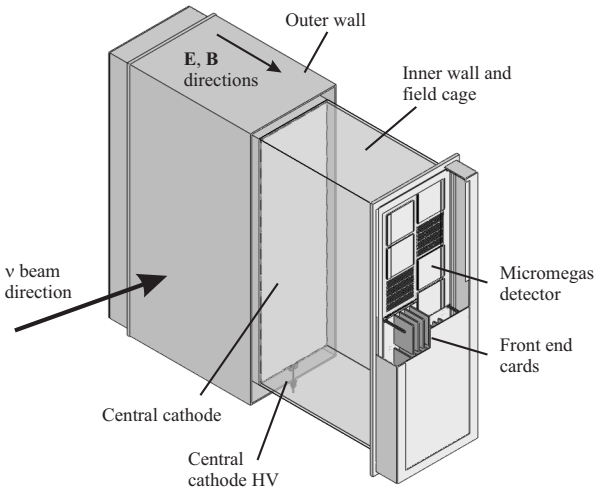

Figure 2.15: Structure of the TPC detector. Reproduced from [12].

TPCs are crucial for the particle identification, providing information on the particle charge, momentum and the track structure. Both chambers are located in between the FGDs that improves the reconstructions of the long tracks, i.e. with vertexes in FGD and continuation in TPC. Such tracks are usually produced buy muons or pions which are the main products of the CCQE neutrino interactions, the predominant mode at the T2K. TPCs operate with an energy resolution of $7.8 \pm 0.2\%$ for minimum ionization particles, that allows to distinguish muons from electrons. Fig. 2.16 illustrates a high separation level: the probability of the particle misidentification takes only 0.2% at the T2K peak energies.

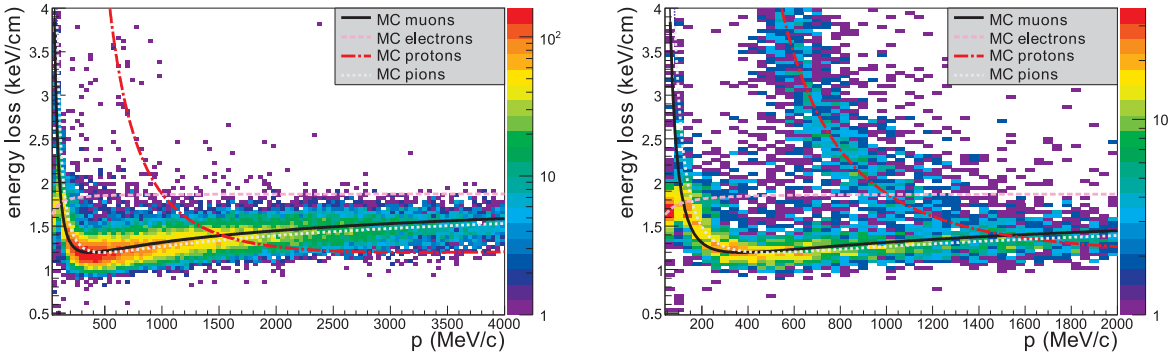

(a) (b)

Figure 2.16: Distribution of the energy loss as a function of the momentum for negatively (Fig. 2.16a) and positively (Fig. 2.16b) charged particles produced in neutrino interactions, compared to the expected curves for muons, electrons, protons and pions. Reproduced from [12].

ECaL

An electromagnetic calorimeter system is surrounding the tracker part of ND280. Its primary goal is to aid identification of the particles, leaving the tracker. Especially, ECaL is important to detect photons from resonant π_0 production, and distinguish these from long muon tracks.

Layers of active scintillator bars in ECaL are separated by lead absorber sheets. Its placement allows to ensure that almost any particle leaving the tracker area will be detected. Track information gathered via ECaL is also crucial in the reconstruction of π^0 produced in the interactions occurring in TPC, FGD and PØD [13]. ECaL shows an energy resolution $\sim 7.5\%$, providing great discrimination of muons from electrons (see Fig. 2.17).

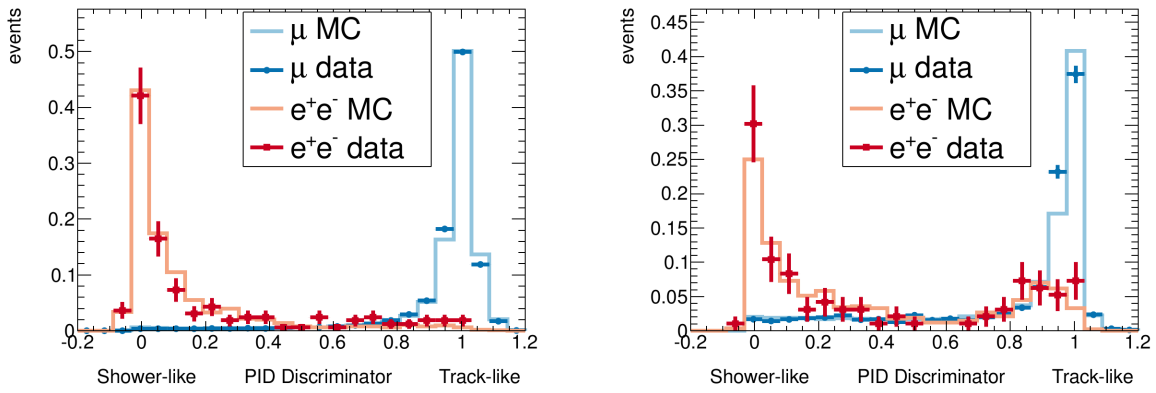

(a) (b)

Figure 2.17: Particle identification (PID) discriminator distribution between track-like (muon-like) and shower-like (electron-like) events for data and MC for Downstream (a) and Barrel ECaL (b). Reproduced from .

ECaL's scintillator bars have a rectangular cross-section of $40 \times 10\text{mm}^2$ and as for the rest of the detectors,

already described in this section, the WLS fibre is passing through the bar, coupled to it via an air gap (see Fig. 2.18). ECaL consists of Downstream and Barrel modules, located around TPCs and FGDs, and a PØD ECaL module. In these modules bars are of a different lengths and types of connection. This way Downstream and Barrel Z modules have MPPC connected to the fibre at both ends of the bar while Barrel X and Y have read out system only at one end with the second one mirrored.

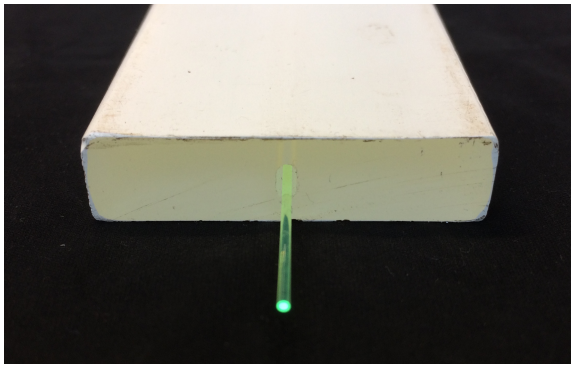

(a)

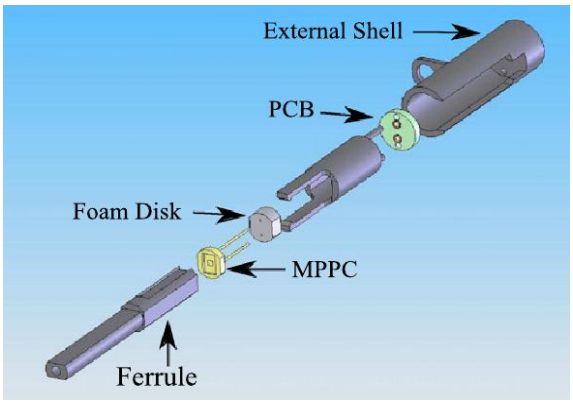

(b)

Figure 2.18: ECaL bar view Fig. 2.18a and a view of ECaL counter connector to MPPCs Fig. 2.18b. Reproduced from [13].

SMRD

SMRD is located in the air gaps of the magnet's yokes. The detector consists of scintillator bars grouped in the modules by 4 or 5. The size of a bar is different depending on whether it is horizontal or vertical. The SMRD bars, unlike others, have a WLS fibres bent in S shape form ($\varnothing = 58mm$) and glued into the groves with BC600 Bicron glue. Such design allows to have a more uniform response through the bar surface and reduces the amount of read out channels to one at the each side of the bar. The collected light is read via MPPC, coupled to the wire through a foam spring [14].

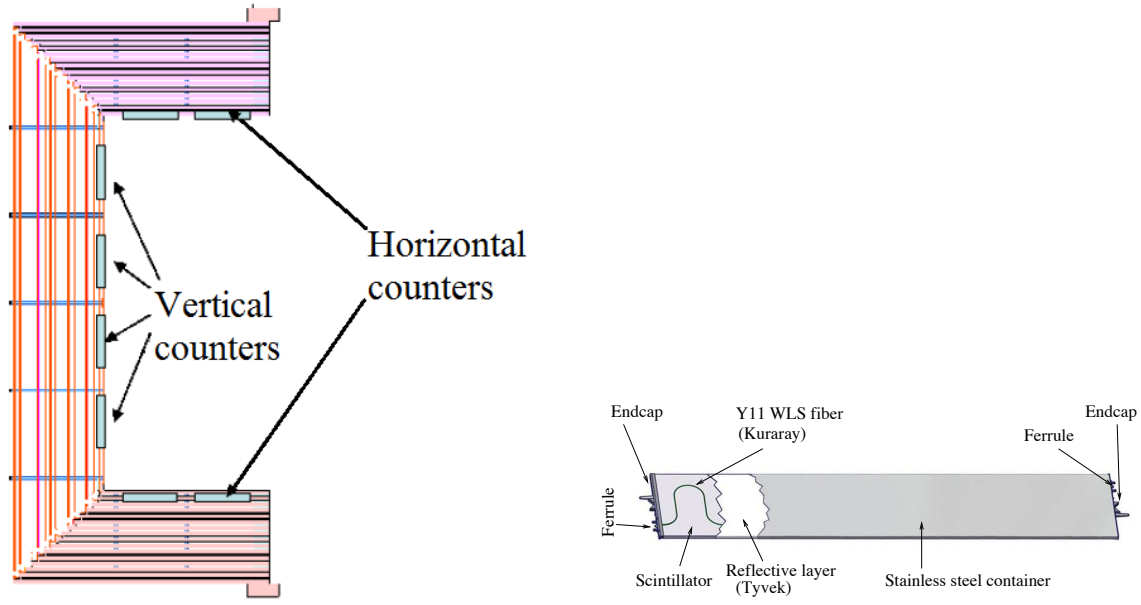

(a) (b)

Figure 2.19: SMRD bar view Fig. 2.19b and a view of SMRD bars located in the yoke of the magnet Fig. 2.19a. Reproduced from [14].

Although SMRD is located outside of the tracker zone, still it is crucial for the analysis as a part of the cosmic trigger, veto system to tell beam events from so called ”sand muons” i.e. muons, produced in neutrino interactions of the walls of detector pit, and also to track and measure the momentum of muons leaving the inner part of ND280.

2.3 — Far detector

Super Kamiokande is one of the biggest water Cherenkov detector with artificially created water volume. The detector is located 295 km away from the point of neutrino production 1km down under the peak of mountain Ikeno. It is a gigantic cylinder filled with 50 kt of very pure water watched by 13.000 PMTs. The detector has been in operation long before T2K started to take data: first events were seen in Super-Kamiokande in 1996 and ever since it has provided one of the world leading limits on the proton decay, measurements of solar, atmospheric and neutrino flavour mixing parameters. Furthermore in 2015 Takaaki Kajita as a head of SK experiment together with McDonald (from SNO) were awarded a Noble Prize for discovery of neutrino oscillations.

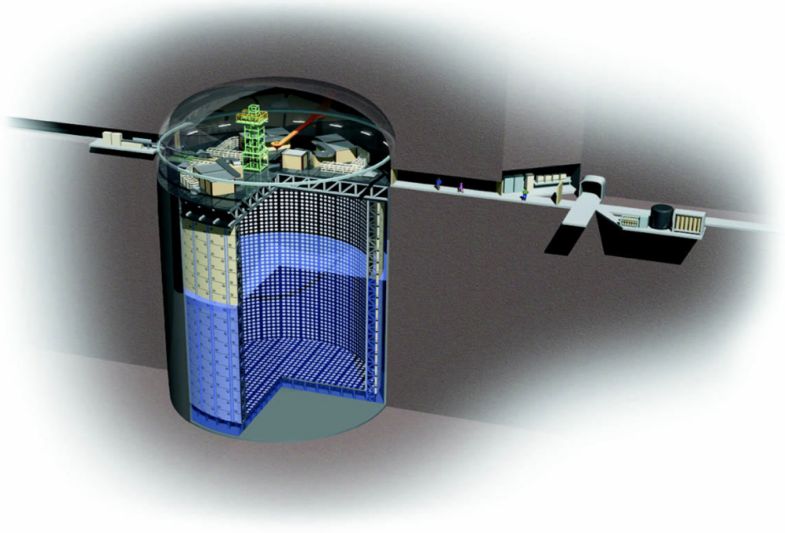

Figure 2.20: A sketch view of the Super Kamiokande detector

Super Kamiokande volume is divided between so-called inner and outer detectors (ID and OD respectively) as one can see at the Fig. 2.20. OD is separated via a wall which hosts both 11,129 50cm diameter PMTs facing ID and 1,885 20 cm diameter PMTs looking at OD. The spaces between PMTs in the ID are covered with a black plastic sheets to better absorb the light and minimize the scattering, whereas on the outer side there is Tyvek material serving exactly the opposite purpose:thanks to its very high reflective property it helps to minimize losses from OD construction features and increase photon rate.

The Super Kamiokande provides a great separation between different neutrino events based on Cherenkov radiation of these particles. Charged particles, produced in neutrino interactions, are crossing the detector faster than the speed of light in water and create Cherenkov radiation cones (see Fig. 2.21a, Fig. 2.21b). That results in characteristic ring-like patterns (see Fig. 2.21c, Fig. 2.21d) of the ignited PMTs on the wall of the SK tank. It is easy to see that muons, being more massive, traverse the detector without scattering and thus produce well-shaped ring. On the contrary, electron scattering creates electromagnetic showers that leads to "fuzzy" edges of the signal ring. Thanks to these differences along with Cherenkov opening angle SK provides an excellent separation of the single lepton events. Apart from only muon or electron like events, produced in CCQE interactions, reconstruction algorithm allows to identify events from resonant pion production. Such events are characterized with either a delayed additional prompt electron event coming from a muon decay (ν_e interactions) or more complicated multiple rings pattern in case of ν_μ interactions: two rings from muon and pion followed by one or two decay electrons.

SK has angular and momentum resolution of 3.0° and $0.6\% + 2.6\%/\sqrt{P[GeV/c]}$ for a single electron events and 1.8° and $1.7\% + 0.7\%/\sqrt{P[GeV/c]}$ for a single muon events. The misidentification rate for single lepton CCQE event is less than 1% at T2K's energies.

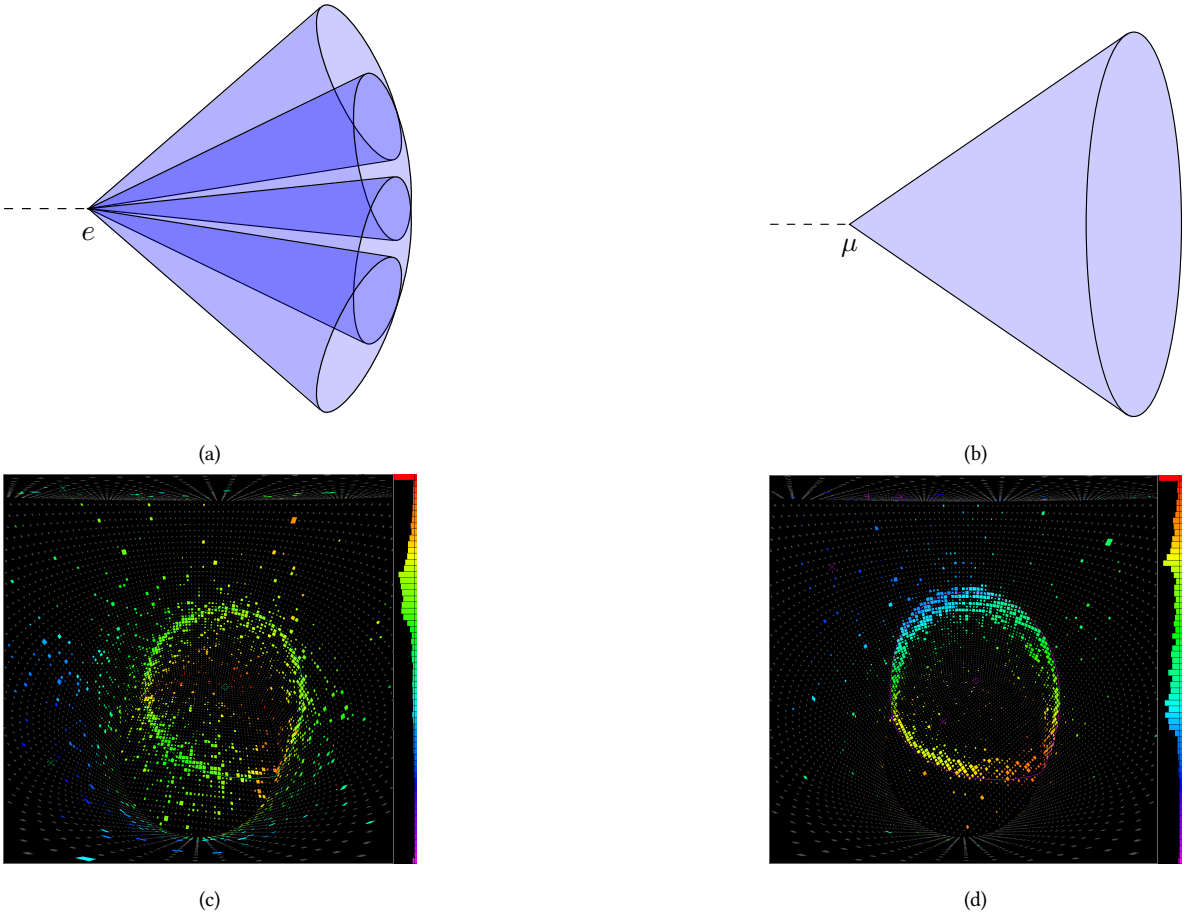

Figure 2.21: Schematic view and an illustration of a signal in the detector for an electron-like event Fig. 2.21a, Fig. 2.21c and from a muon-like event Fig. 2.21b, Fig. 2.21d

3 — Oscillation analysis inputs

One of the main objectives of this thesis is to test the three-flavor oscillation model (see sec.1.2 and determine the parameters that govern its behavior. This involves various analyses that rely on different inputs, illustrated in fig. 3.1. The simulation of the J-PARC proton beam, its interaction with the target, and the resulting neutrino flux are discussed in Section 3.1. The neutrino interaction cross-section model is described in Section 3.2. The observed data at ND280 are used to refine the flux and cross-section model parameters and their uncertainties and correlations, which are discussed in Section 3.3. The criteria for selecting event samples at Super-K are outlined in Section 3.3.4, and the simulation of detector effects in Super-K is explained in Section 3.4.

The analysis presented in Chapter 5 aims to constrain the three-flavor neutrino oscillation parameters using the full T2K Run 1-10 data and explores the potential improvements in sensitivity to oscillation parameters with the addition of an external reactor constraint. This chapter will primarily focus on the changes made compared to the T2K analysis conducted in 2020 and the methodology used for this analysis.

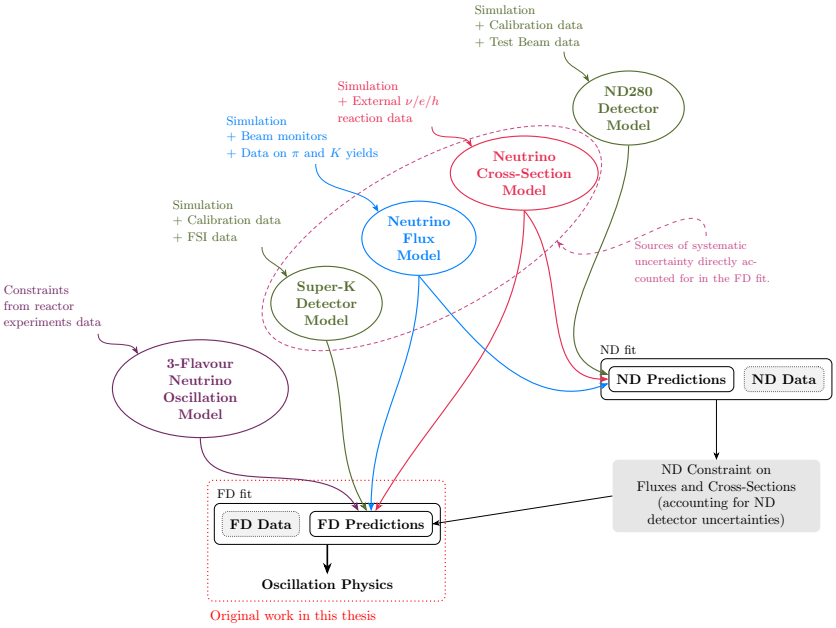

Figure 3.1: An overview of the T2K oscillation analysis

3.1 — Neutrino flux prediction

This section focuses on explaining the multi-stage process used to predict the T2K neutrino flux. The process begins with the use of FLUKA v2011.2x.6 [70], a software tool, to simulate the propagation and interactions of protons in the target material (graphite). GCALOR 1.05/04 [71] is then employed to forecast any interactions that occur outside of the beam target. As mentioned in section 2.1, when protons interact with the target, hadrons are formed, which subsequently decay into leptons and propagate towards the near and far detectors.

To simulate these processes, such as the production of multiple hadrons and their energy spectra, the kinematic output from FLUKA is transferred to JNUBEAM v13av7 [72], a Monte Carlo simulator based on GEANT3 [73]. Additionally, experimental data from the NA61/SHiNE experiment [74] is utilized for fine-tuning the hadron multiplicity.

The NA61/SHiNE experiment covers a significant portion of the phase space relevant to T2K. Fig. 3.2 illustrates the superimposed predictions made with FLUKA, depicting the areas of coverage by the experiment.

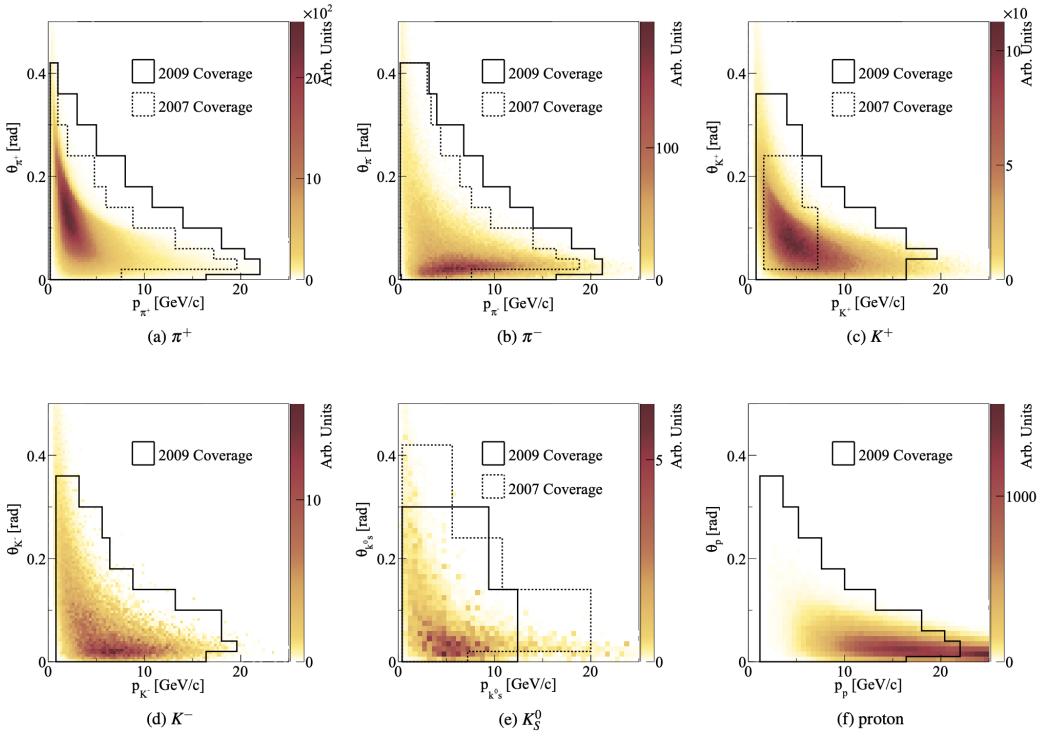

Figure 3.2: Predicted phase space of hadrons π^+, π^-, p, K^+, K^0 and K^0_S contributing to the predicted neutrino flux at SK (coloured histograms), superimposed on areas of space covered by NA61/SHINE (contours). Reproduced from [15].

The flow setting within the analysis involves two main steps. Firstly, each interaction is assigned a weight based on its probability, which is calculated as a ratio of the observed data in the NA61 experiment. This weight is used to simulate the differential multiplicities in FLUKA.

Secondly, for all other particles and non-target events, a weight is determined based on the probability of propagating hadrons entering into further interactions with other target nuclei and forming secondary hadrons. This weight is calculated by multiplying the observables (from various studies, including thin and target data replicas) and estimated cross sections for each interaction with the probability of hadrons propagating without additional interactions.

Fig. 3.3 illustrates the impact of this tuning on the SK flux prediction by showing the ratio between the tuned and untuned results. In both the neutrino and antineutrino beams, event rates for ν_μ and ν_e improve at all energies, while event rates for $\bar{\nu}_\mu$ and $\bar{\nu}_e$ increase at peak energies and are suppressed for the high-energy tail.

The final flux prediction for SK is depicted in fig. 3.4.

3.2 — Neutrino Interaction Modelling

Since neutrinos do not have an electric charge, their detection relies on indirect methods through their interaction with substances inside the detector. Therefore, accurately modeling these interactions is crucial for predicting the velocity and kinematics distributions of neutrino events in both the near and far detectors.

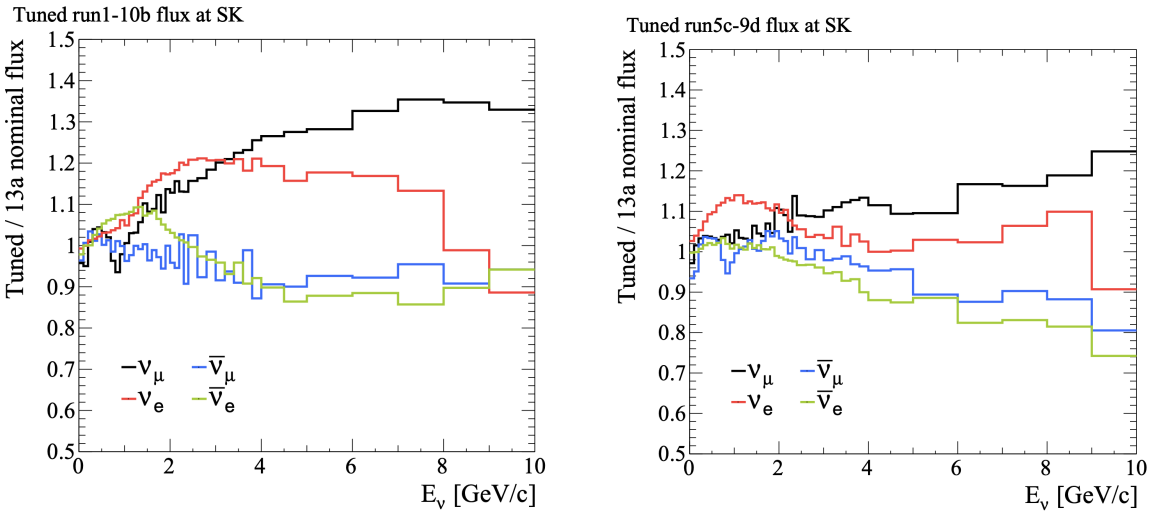

Figure 3.3: Ration between tuned and untuned neutrino flux at SK for neutrino (left) and antineutrino (right) beam modes. Reproduced from [16].

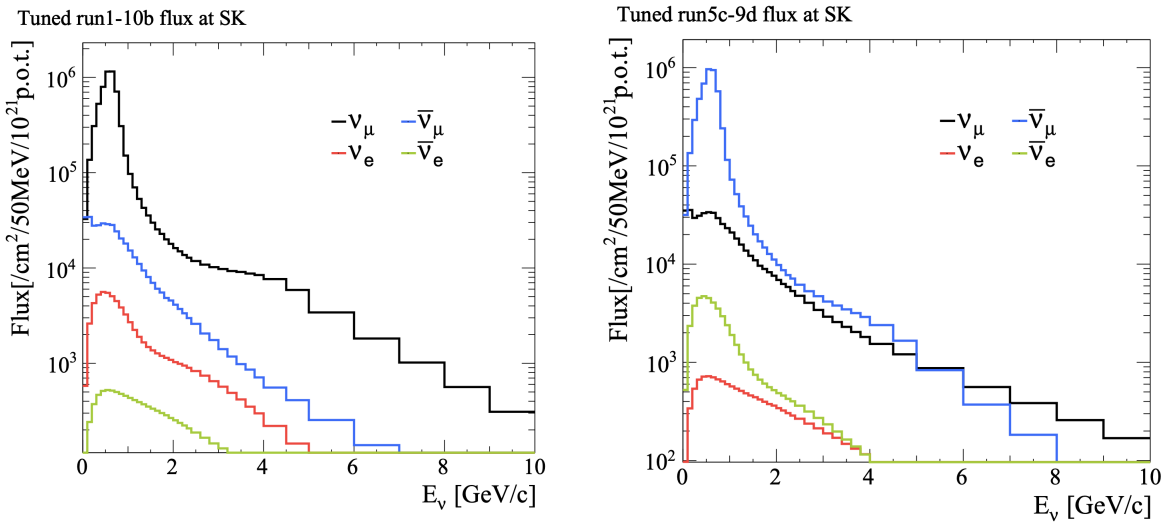

Figure 3.4: Reproduced from [15].

The NEUT Monte Carlo generator version 5.4.0 is used to simulate these interactions for all detectors and processes.

Fig. 3.5 presents the cross sections, which provide information on the likelihood of different interaction processes occurring. Near the peak energy of the T2K flux, quasi-elastic (QE-like) interactions are the predominant processes, while baryon resonances (RES) and deep inelastic scattering (DIS) processes become increasingly important at higher energies.

This section describes the nominal interaction model, also referred to as the "cross section model" used in T2K, compiled from [75] and [76]. It explains how the initial state of the nucleus and each interaction process are modeled and discusses how the associated uncertainties are incorporated into the fluctuation analysis. The uncertainties are summarized in tables A.3 and A.4 in theA application, and their correlations are shown in Fig. 3.13.

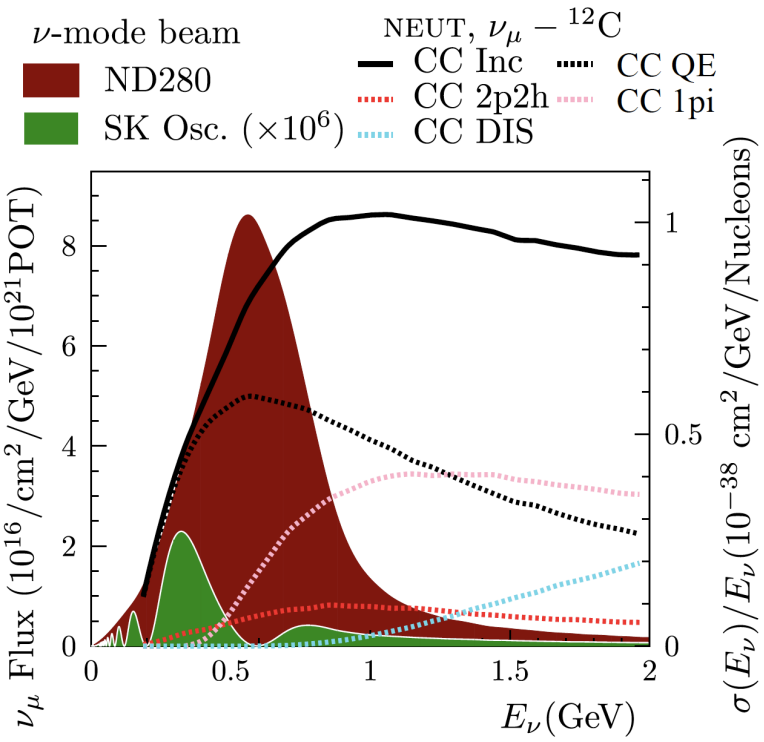

Figure 3.5: The predicted neutrino CC cross sections of per nucleon depending on neutrino energy superimposed on predicted fluxes at ND280 FDG1 and Super-K (with oscillations applied according to Ref. [77] value settings). Forecasts are generated by the NEUT MC generator CC Inc, broken down by flavor type. Adapted from references [78].

3.2.1 — Nuclear Model

To predict the cross sections for neutrino-nucleus interactions, it is necessary to understand the initial state of the affected nucleus. This includes the distribution of nucleon kinematics, the energy required to remove nucleons from the nucleus, and the changes in the outgoing particle's kinematics due to the nuclear potential. Two different models are used to describe the initial state: the Benhar Spectral Function [79] for quasi-elastic

(QE) interactions and the relativistic Fermi gas (RFG) model for all other interactions.

The Benhar Spectral Function incorporates a sophisticated and realistic description of the nucleus's ground state, considering correlations between nucleons and their momentum and removal energy distributions. It provides a more accurate representation than the RFG model, especially in electron scattering. The spectral function is derived from data on electron scattering [80] and exclusive measurements of neutrino cross-sections [81–83]. However, it is important to note that these measurements assume a two-body interaction and are tuned to electron scattering data, which may not hold true for non-QE interactions. An example of a spectral function for ^{16}O is shown in Fig. 3.6.

The one-nucleon contribution to the spectral function is determined from measurements of missing energy and momentum in scattering experiments involving ^{12}C [84] and ^{16}O nuclei [85], accounting for detector effects, final state interactions (FSI), and radiative effects. The contribution of correlated pairs of nucleons is obtained from theoretical calculations in infinite nuclear matter, as the finite size effects of the nucleus are small [79]. This contribution represents about 20% of the spectral function's strength and becomes relevant only for large momentum and removal energy.

On the other hand, the RFG model characterizes the initial state of the nucleus as a sphere with a constant density. In this model, nucleon momenta follow a quadratic distribution up to a maximum value determined by the Fermi momentum, which depends on the number of nucleons. Unlike the spectral function, the RFG model assigns a single value of nucleon removal energy for each nucleon momentum. The characteristics of the RFG model are illustrated in Fig. 3.6 [76].

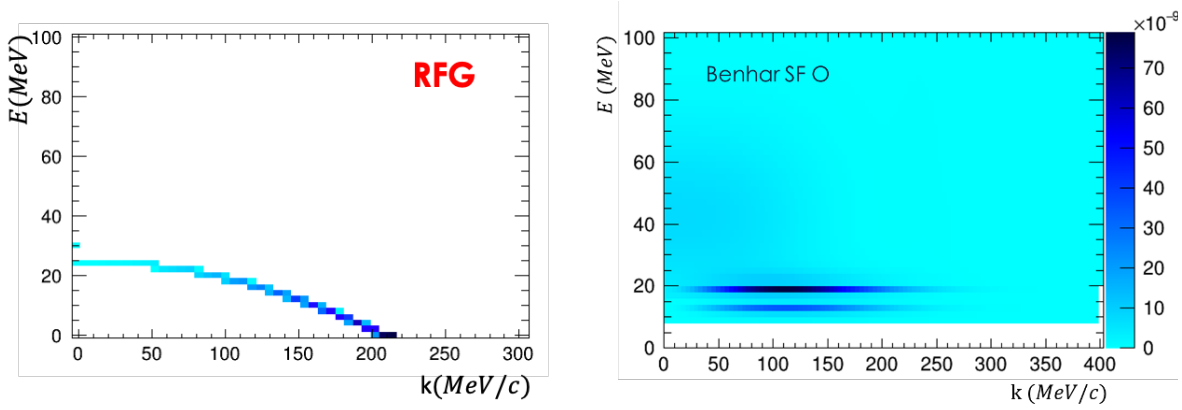

Figure 3.6: The relativistic Fermi gas model (left) and the Benhar spectral function (right) describing the ground state of the nucleus for ^{16}O as a function of the initial momentum of the nucleon, k, and the removal energy, E, as implemented in the NEUT MC generator. For the spectral function, the nuclear shells $1p_{1/2}$ and $1p_{3/2}$ are visible as well-defined lines at about 12 and 18 MeV, respectively, and the nuclear shell $1s_{1/2}$ much wider, covering a wide range of removal energies. Reproduced from link [75].

Both the spectral function and the RFG models are based on the "plane wave momentum approximation," where the neutrino interacts with a single non-relativistic nucleon (or a pair of nucleons in the case of 2p2h interactions). This allows the neutrino-nucleus interaction cross section to be expressed as an incoherent sum over all neutrino-nucleon interaction cross sections.

After modeling the initial state of the nucleus, several effects are considered:

- The primary neutrino-nucleon interaction is simulated, taking into account various interaction types such as CCQE (charged-current quasi-elastic), 2p2h (two-particle, two-hole), resonant and non-resonant pion production, and DIS (deep inelastic scattering). These interaction types are described in detail in Sections 3.2.2 to 3.2.5.
- For CCQE interactions, the nucleon removal energy is subtracted from the available energy of the final state.
- Particles produced during the neutrino-nucleus interaction can further interact with the remaining nucleus, potentially altering the set of observable particles. If not properly accounted for, this can lead to a shift in the reconstructed neutrino energy. The modeling of these interactions and the associated uncertainties are detailed in Section 3.2.6 dedicated to final state interactions (FSI).
- The electrostatic Coulomb potential of the nuclear remnant causes a decrease (increase) in the momentum of the emitted negatively (positively) charged lepton. Measurements of electron and positron scattering in the QE [86] peak have determined the size of this effect. Interestingly, it has been found that the momentum shift is independent of the kinematics of the unshifted lepton. Therefore, a constant momentum shift of -4.3 MeV (+3.3 MeV) is applied to negatively (positively) charged leptons.

These effects and their detailed descriptions are covered in the following sections.

3.2.2 — Charged Current Quasi-Elastic (CCQE) Interactions

The dominant interactions around the peak of the T2K neutrino flux are CCQE interactions, as depicted in Fig. 3.5. These interactions play a crucial role in determining the sensitivity of the T2K experiment to oscillation parameters. In CCQE interactions, neutrinos (or antineutrinos) of flavor l interact with a neutron (or proton) in the nucleus, resulting in the production of a proton (or neutron) and a negatively (or positively) charged flavor lepton l, as illustrated in Fig. 3.7.

The cross section for single-nucleon CCQE interactions is calculated using the Llewellyn Smith model [87]. It depends on various factors, including the energy of the neutrino, the masses of the nucleon and lepton, and the transfer of four-momentum to the nucleus, denoted as Q^2. The Q^2 dependence is described by several shape coefficients, with one of the most significant uncertainties arising from the weak axial form factor F_A [88]. Other shape coefficients either have limited constraints from electron scattering experiments or have minor effects on the overall cross section uncertainty. These uncertainties are discussed further in Section 3.2.7.

The weak axial form factor F_A is modeled by a dipole function, as shown in Eq. (3.1), where $F_A(0)$ is well determined from beta decay experiments, and the axial mass M_A^{QE} is constrained by neutrino scattering experiments [89]. The uncertainty associated with M_A^{QE} is taken into account in the oscillation analysis. However, no uncertainty is assigned to M_A^{QE} for interactions with hydrogen nuclei (i.e., free protons) since nuclear effects are not expected, and the experimental uncertainties in these measurements are negligible [76].

$$F_A(Q^2) = \frac{F_A(0)}{\left(1 + Q^2 / \left[M_A^{QE}\right]^2\right)^2} \tag{3.1}$$

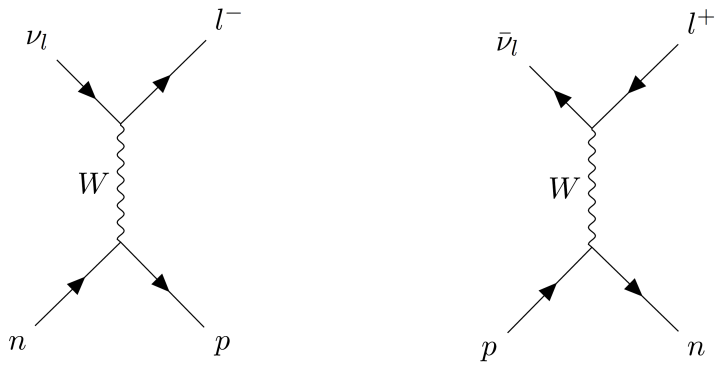

(a) Neutrino.

(b) Antineutrino.

Figure 3.7: Feynman diagrams for CCQE interactions. Reproduced from Ref. [90].

In CCQE interactions involving neutrinos, the energy of the incoming neutrino can be inferred by measuring the energy E_l, momentum p_l, and angle θ_l of the primary outgoing lepton. This can be achieved using Eq. (3.2), under the assumption that the struck nucleon is initially at rest. The equation takes into account the masses of the proton (m_p), neutron (m_n), and lepton (m_l), as well as the nucleon removal energy (E_b).

For antineutrino CCQE events, the same equation can be used, but with the masses of the neutron and exchanged proton. However, at T2K, the difference between the reconstructed energies of neutrinos and antineutrinos is negligible.

$$E_{\text{rec}} = \frac{m_p^2 - (m_n - E_b)^2 - m_l^2 + 2(m_n - E_b)E_l}{2(m_n - E_b - E_l + p_l \cos\theta_l)} \tag{3.2}$$

While the spectral function model is generally successful in predicting neutrino interaction cross sections [91, 92], it has limitations when it comes to accurately predicting cross sections at low values of Q^2, as depicted in Fig. 3.8. This discrepancy at low momentum transfer ($\lesssim 400$ MeV/c) is expected due to the assumptions of the impulse approximation used in the spectral function model, and such shortcomings have been observed previously [75, 93].

To address these issues and improve the predictions of the spectral function model at low Q^2 values, five specific shape uncertainties have been introduced. These uncertainties are incorporated into the oscillation analysis by scaling the CCQE cross sections in the range of 0.05 GeV^2 for $Q^2 \in [0, 2.5]$ GeV^2. These parameters have been carefully selected to improve the agreement between data and the spectral function predictions, particularly for a number of ND280 and MINERvA CC0π datasets [75].

The dipole form factor F_A used in NEUT has been a commonly employed choice historically, but its motivation has not always been well-founded [94–97]. Furthermore, it has underestimated the uncertainties in the $Q^2 \gtrsim 1$ GeV^2 region, where neutrino scattering data were used to constrain its shape. In order to address this limitation and provide additional flexibility to the dipole form factor model, three ad hoc shape uncertainties

Figure 3.8: A comparison of three different spectral function model predictions to observations from the MINERvA experiment [91] as a function of four-momentum transfer, Q^2. The red histogram corresponds to the nominal prediction, with M_A^{QE} fixed to 1.03 GeV and no Q^2-dependent scaling applied. The green histogram corresponds to predictions after applying the Q^2-dependent scaling parameters (fit to ND280 and MINERvA CC0π datasets) and the blue histogram also includes the effect of fitting M_A^{QE}. Reproduced from Ref. [75].

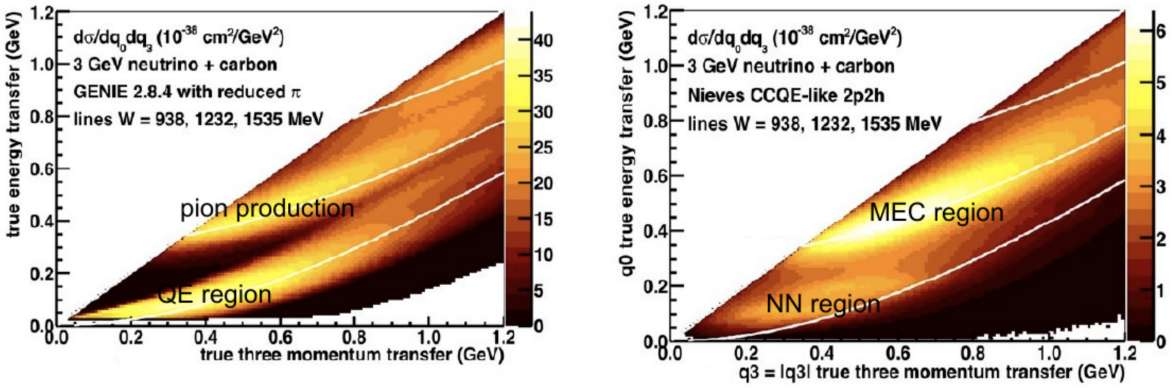

Figure 3.9: Cross-sections for 3 GeV neutrinos incident on ^{12}C. The left panel shows the total cross-section, with the QE and pion production dominated regions indicated. The right panel shows the 2p2h contribution to the total cross-section, with the NN and MEC dominated regions indicated. Note the different colour-axis scales between the two panels. Reproduced from Ref. [76].

have been introduced. These uncertainties are incorporated into the oscillation analysis by scaling the CCQE cross sections in specific Q^2 regions: $[0.25, 0.5]$ GeV^2, $[0.5, 1.0]$ GeV^2, and > 1.0 GeV^2. Alternative form factor parameterizations, such as the 3-component or z-extension shapes, have been fitted to the neutrino scattering data and are being considered for future analyses. A comprehensive summary of these uncertainties, along with other uncertainties associated with the interaction model, can be found in Tables A.3 and A.4.

3.2.3 — Multi-nucleon (2p2h) Interactions

The 2p2h (two particles with two holes) process involves the interaction of a neutrino with two nucleons, potentially resulting in the ejection of both nucleons. NEUT models this process using the Nieves 2p2h [98] model, which includes three types of interactions: meson exchange currents (MEC), nucleon-nucleon correlations (NN), and interference between MEC and NN. Among these interactions, the contributions from NN and MEC occupy a significant portion of the phase space region, overlapping with QE (quasi-elastic) and RES (resonant) interactions, as depicted in Fig. 3.9. The 2p2h interactions bridge the gap between the cross sections of QE and RES interactions, partially filling in the missing cross-section relative to true energy transfer.

Due to the similarities in the final state between 2p2h interactions and CCQE interactions, they are often indistinguishable from each other in the Super-K detector and are commonly referred to as "CCQE-like" events. However, 2p2h events do not exhibit the exact kinematics of CCQE interactions, which can lead to biased results when using the standard formula for reconstructing the neutrino energy (Eq. (3.2)).

The 2p2h process is not well-constrained, and there are several valid models, such as Nieves [98], Martini [99], and SuSAv2 [100, 101], which predict the 2p2h contribution to be between 10-20% of the total cross section for CCQE-like interactions. Due to the uncertain nature of this process, several uncertainties are implemented in the oscillation analysis:

- Two uncorrelated normalization errors for the total cross sections of ν and $\bar{\nu}$ 2p2h interactions.
- Normalization uncertainty for controlling the relative cross sections of 2p2h interactions in ^{12}C and ^{16}O nuclei, with a 100% correlation between ν and $\bar{\nu}$ interactions.
- Shape uncertainty of the 2p2h cross section for ^{16}O, considering the freedom within the Nieves model to modify the poorly constrained relative contributions of meson exchange currents (MEC) and nucleon-nucleon correlations (NN) to the total 2p2h cross section.
- Four uncorrelated energy-dependent shape uncertainties that account for the differences in cross section predictions among the Nieves, Martini, and SuSAv2 models. Two uncertainties are applied to ν interactions, and the other two are applied to $\bar{\nu}$ interactions, with a separation around 600 MeV in order to cover different energy ranges. These uncertainties are not applicable to near detectors since they are insensitive to model differences, and they are propagated to far detectors without restrictions.

3.2.4 — Single pion production

Interactions resulting in the production of a single pion in the final state serve as both the primary background for CCQE event selections and an important component of the T2K signal (refer to Section 3.3.4). The production of pions predominantly occurs through the resonant production of the $\Delta(1232)$ baryon, which subsequently decays into a pion and a nucleon. However, other resonances, coherent interactions with the entire nucleus, or multipion processes can also contribute. Due to pion final-state interactions, some of these processes may appear to only produce a single observable pion in the final state, even though they involve the presence of multiple pions initially. Examples illustrating these interactions can be found in Fig. 3.10. In NEUT, the production of a single pion is modeled using the Rhine-Segal model [102], which incorporates

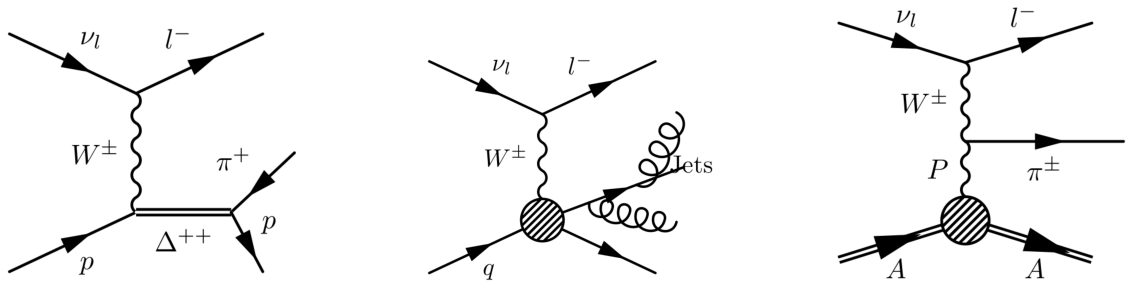

(a) Resonance excitation. (b) Multi-pion processes. (c) Coherent production.

Figure 3.10: Feynman diagram examples for various processes that result in a single-pion being detected in the final state. Reproduced from Ref. [76].

various resonances (including their interference) up to a hadron-invariant mass of $W = 2$ GeV. Above this

threshold, events are treated as deep inelastic scattering. The Rhine-Segal model does not account for the lepton mass, but corrections are introduced based on references [103–105] to accommodate it. Additionally, modifications to the Rhine-Segal form factors have been made to match the electromagnetic production of the $\Delta(1232)$ resonance [106, 107].

As discussed in Section 3.3.4, Super-K has a sample of events that specifically selects for ν_e events associated with the production of a positive pion. The equation used to reconstruct the neutrino energy in the case of single pion production is given by Eq. (3.3) [108], where m_Δ represents the mass associated with the Δ resonance. Notably, this equation does not account for the nucleon removal energy due to limited knowledge of nuclear effects in pion formation, particularly in relation to the propagation of the Δ resonance within the nuclear medium [109].

$$E_{\text{rec}} = \frac{m_p E_l - \frac{1}{2}(m_\Delta^2 - m_l^2 - m_p^2)}{m_l - E_l + p_l \cos\theta_l} \tag{3.3}$$

Similar to CCQE interactions, the cross section dependence of resonant pion production events on Q^2 is described by several form factors. Most of these form factors are well-constrained by electron scattering data or make minor contributions. However, for the axial form factor term in CCQE, the value of the form factor at $Q^2 = 0$, C_5^A, is poorly bounded. Therefore, uncertainties associated with M_A^{RES} (indefinite axial mass) and C_5^A are included in the analysis to account for fluctuations.

A small non-resonant background contribution, where pions are formed without an intermediate resonant state, is also modeled for the dominant isospin-1/2 interaction ($I_{1/2}$) [110,111], following the recommendations of Rein and Segal [102]. In the oscillation analysis, the strength of this background is scaled as a function of energy. The parameters M_A^{RES}, C_5^A, and the scaling for the non-resonant background are set based on ANL, BNL [112], and MiniBooNE [113] neutrino mode datasets [75]. Since there are no antineutrino mode datasets available to tune this background and there is a tendency for charged pion events with momentum $\lesssim 200$ MeV/c to be misidentified as CCQE-like, an additional conservative 100% uncertainty is applied to these events to account for such effects. For future analyses, an alternative pion production model [114], which explains the interference between resonant and non-resonant amplitudes, is being considered.

In pion-producing coherent interactions, the neutrino scatters off the nucleus to produce a pion, transferring only a small amount of energy to the nucleus without exciting it. NEUT models such interactions using the coherent Rhine-Segal model [115]. However, the results from the MINERvA experiment (see Fig. 3.11) indicate that this model overestimates both neutrino and antineutrino coherent cross sections [116]. The later Berger-Segall model [117] shows better agreement with the MINERvA data. Until this model can be fully implemented in NEUT, predictions are reweighted in an ad hoc manner by comparing them to the MINERvA data. Additionally, conservative uncorrelated normalization errors are assigned to the CC and NC coherent cross sections in the analysis [75]. NEUT also accounts for the contribution of diffractive pion production using the Rein model [118]. This process is similar to coherent pion production, but instead of interacting with a nucleus composed of multiple nucleons, it involves the interaction with a single nucleon, specifically hydrogen nuclei. The cross section of this process is extremely small, contributing much less than 0.1% to the total cross section at 1 GeV [75]. However, due to the lack of precise constraints on this process, a nor-

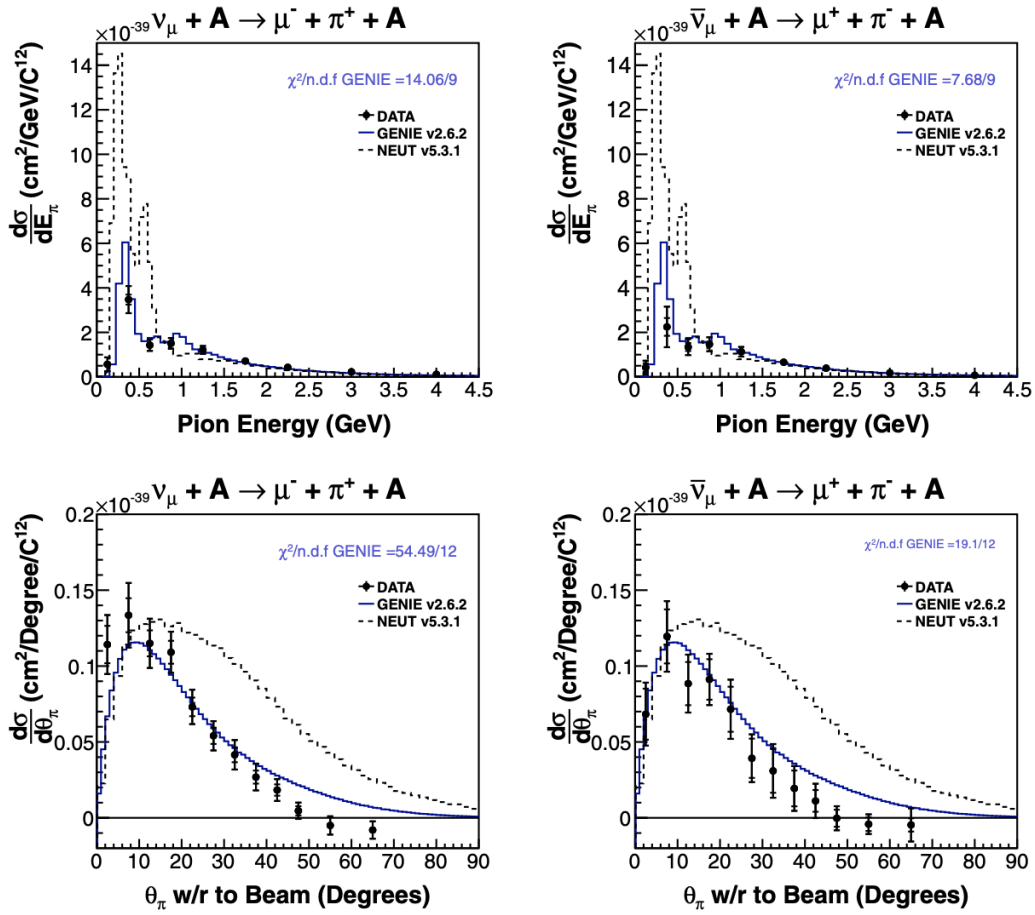

Figure 3.11: Coherent pion production differential cross-sections observed by the MINERvA experiment and compared to predictions from the NEUT and GENIE MC generators. Reproduced from Ref. [116].

malization uncertainty of 100% is assigned. This uncertainty is included as part of the "CC misc" cumulative uncertainties, which will be further discussed in Section 3.2.7.

3.2.5 — Deep Inelastic Scattering (DIS) and Multiple Pion (MPi) Production

At higher energies, when a neutrino interacts with a nucleon, it can transfer enough energy to break apart the nucleon, resulting in the production of various hadrons. This process is known as deep inelastic scattering (DIS) and becomes dominant for neutrino energies around 5 GeV. Although these events are not directly considered as signal or backgrounds in Super-K selections due to the low T2K flux and oscillation probabilities at these energies, accurately characterizing the effects of DIS on the final state kinematics is crucial for constraining flux and pion final state interaction (FSI) uncertainties, which do have significant impacts on oscillation analyses.

In NEUT, the cross sections for DIS interactions are calculated using the GRV98 parton distribution functions (PDFs) [119]. These PDFs describe the probability of finding a quark of a specific type as a function of the momentum carried by the struck quark within the nucleon. However, a known issue with these PDFs is that the perturbative QCD techniques used to model them break down at low values of Q^2 [75]. To address

this, corrections from Bodek and Yang [120] are applied to allow the use of PDFs at the typical Q^2 values encountered in T2K.

Depending on the hadronic invariant mass, W, associated with the interaction, NEUT employs two different models:

- For $1.3 < W < 2$ GeV, a custom multi-pion model is used. The kinematics of the hadrons and the lepton are randomly sampled based on the differential cross sections derived from the PDFs mentioned earlier. The pion multiplicity is then randomized using a multiplicity model that has been tuned to neutrino scattering data [121]. To avoid double-counting with single pion events, only events producing at least two pions are allowed. An oscillation analysis incorporates a shape uncertainty to account for differences in pion multiplicities between two valid multiplicity models: the NEUT default and the AGKY [122] models.
- For $W > 2$ GeV, DIS events are simulated using an external Monte Carlo generator, PYTHIA v5.72 [123]. PYTHIA employs a Lund string model to simulate the fragmentation of quarks and the resulting production of particles.

For both multi-pion and DIS events, the oscillation analyses incorporate the differences between predictions generated with and without Bodek-Yang corrections as conservative shape uncertainties. Additionally, separate normalization uncertainties for neutrinos and antineutrinos are assigned to the full multi-pion plus DIS cross-section to account for differences between the NEUT prediction and the PDG world-average measurements [124].

3.2.6 — Final State Interactions (FSI), Secondary Interactions (SI) and Photonuclear (PN) Interactions

Particles generated during the interaction between neutrinos and the nucleus can interact with the nuclear remnant, potentially changing the composition of observable particles and introducing a bias in the reconstructed neutrino energy if not properly considered. These interactions are referred to as ”final state interactions” (FSI). Similarly, once particles have left the nuclear remnant, they undergo ”secondary interactions” (SI) within the detector material before being detected. The treatment of hadrons and leptons differs in the following ways.

In NEUT, hadronic FSI and SI are implemented using the ”waterfall” model. In this model, particles are treated as classical entities and undergo a series of independent scattering interactions as they traverse the nuclear remnant (starting from a randomly determined position based on the Woods-Saxon potential distribution [125]) or the detector. Each scattering interaction conserves energy and momentum. The mean free path for these scattering events considers the effects of the nuclear environment or detector materials and is adjusted based on measurements of free scattering of particles and nucleons.

An important source of uncertainty in oscillation analyses arises from pion FSI. If a pion is produced but goes undetected due to FSI, it can distort the reconstructed neutrino energy. When pions travel through

nuclear matter, the main interactions they experience include elastic/inelastic pion scattering, pion absorption, and charge exchange. These processes are illustrated in Fig. 3.12. Charge exchange processes can not only lead to a reconstructed energy offset but also impact the production rate of π^0, which is a significant background when searching for ν_e events. The cross sections for each of these processes are primarily determined from experiments such as DUET [126] and others mentioned in Ref. [127]. The associated uncertainties in the form of fluctuations are incorporated into the analysis to account for the scaling of the probability of each process occurring.

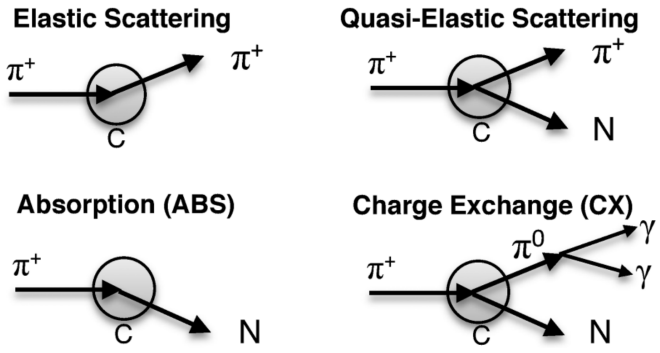

Figure 3.12: Illustration of the dominant types of π^+ FSI and SI with the nucleus, C. 'N' represents any number of nucleons leaving the nucleus. Adapted from Ref. [126].

For π^0 particles, there are additional considerations. Firstly, the lifetime of these particles outside the nucleus is negligible, so they are not subject to secondary interactions [128]. Secondly, the photons produced from the decay of $\pi^0 \to \gamma\gamma$ can be absorbed by the detector before they can be detected. This phenomenon is known as the photonuclear (PN) effect. The PN effect reduces the efficiency of detecting π^0 events, particularly for photons with energies less than 150 MeV. The uncertainties associated with both secondary interactions (SI) and the PN effect are not directly corrected for in the near detector (due to limited sensitivity) and are not directly included in the oscillation analysis. However, these uncertainties are taken into account, along with detector effects, by constructing the Super-K covariance matrix, as described in Section 3.4.

3.2.7 — Additional Sources of Uncertainty in the Cross-Section Model

The cross-sectional model incorporates several additional uncertainties that do not fall into the previously mentioned categories or are applicable to multiple categories simultaneously. These uncertainties will be briefly discussed in this section.

The shape factors for CCQE and CC1π interactions were determined through fitting bubble chamber neutrino scattering data, as described in Sections 3.2.2 and 3.2.4. However, there is a lack of corresponding data in the relevant energy range for antineutrinos [129]. This raises the possibility that there could be differences in the shape factors between neutrinos and antineutrinos. This discrepancy is supported by measurements from the MINERvA experiment on CC1π production, where the predictions are inconsistent with both neutrino and antineutrino datasets [130]. Another source of neutrino-antineutrino differences arises from the

Coulomb correction applied to the outgoing lepton momentum (as discussed in Section 3.2.1). This correction has a different magnitude and sign for neutrino and antineutrino events. Therefore, to account for the uncertainties in the relative cross sections of neutrinos and antineutrinos resulting from both form factors and the Coulomb correction, two 100% anticorrelated normalization errors are included in the oscillation analysis. One error scales the overall neutrino cross section, while the other scales the antineutrino cross section.

First, the radiative corrections for the CCQE process at the tree level are taken into consideration. Although a complete estimate of these modifications is currently unavailable in NEUT, calculations have been performed for the outgoing lepton branch of CCQE interactions in Ref. [131]. These corrections, which have an order of $\alpha_{EM} \ln(Q^2/m_l^2)$ (where α_{EM} represents the fine structure constant), are stronger for ν_e interactions compared to ν_μ . Additionally, uncertainties in form factors and changes in kinematics due to the outgoing lepton mass introduce further uncertainty in the cross sections [131]. The combined effects of these factors are accounted for by employing two 50% anti-correlated normalization uncertainties. One uncertainty is associated with scaling the relative cross sections of ν_μ and ν_e CC interactions, while the other pertains to antineutrinos. These parameters are not constrained by the near detector due to insufficient sensitivity.

The NC1γ process plays a small but significant role in the identification of ν_e and $\bar{\nu}_e$ in Super-K. According to Ref. [132], the NEUT-predicted cross section for this process is approximately half of that calculated using the Alvarez-Ruso model [133]. In the absence of external data or constraints from ND280, the discrepancy between these different models is addressed in the fluctuation analysis through a 100% normalization uncertainty [134].

Several relatively rare CC and NC processes are known to occur, but they do not contribute significantly to the direct background or signal samples. These processes include CC/NC1K, CC/NC1η, CC1γ, and CC pion production by diffraction. Due to the limited knowledge of uncertainties associated with these processes, two conservative 100% normalization uncertainties are assigned—one for CC processes and another for NC processes. The latter is not constrained in the near detector configuration due to a lack of sensitivity.

3.3 — Constraints on the systematic parameters from near detector

The systematic parameters related to the flux and cross section are constrained by fitting the near detector data, which is discussed in ch.3.1 for the flux and ch.3.2 for the cross section. To ensure robustness, two different approaches are employed in the T2K analysis, allowing for cross-checking of the results.

The first approach is the BANFF framework (Beam and ND280 Flux Extrapolation Task Force), which is the more commonly used method. It involves fitting the parameters to the near detector data and extrapolating them to the far detector.

The second approach, called MaCh3, is a Bayesian Markov chain Monte Carlo method. While it is not extensively discussed in detail in the current analysis, it serves as an alternative method for parameter estimation.

3.3.1 — Near detector event samples

In order to constrain the flux and cross section parameters, the data collected by the ND280 detector needs to be categorized into relevant samples. As discussed inSection 2.2, the ND280 detector is magnetized, allowing for the separation of positively and negatively charged leptons and the selection of neutrinos and antineutrinos separately. However, due to its short distance of 280 m from the beam target, it can only measure the non-oscillated $\bar{\nu}_\mu$ flux.

Each sample is organized based on the muon momentum within the corresponding range defined by T2K, $p_\mu \in [0, 30]$ GeV, and the opening angle of the muon with respect to the nominal beam direction across the full range of angles, $\cos\theta_\mu \in [-1, 1]$. The samples are selected exclusively for CC events and are further categorized based on pion multiplicity. However, there are differences in sample selection between different beam modes, as follows:

- ν-mode samples: ν_μ CC 0π, ν_μ CC $1\pi^+$, and ν_μ CC other
- $\bar{\nu}$-mode samples: $\bar{\nu}_\mu$ CC 0π, $\bar{\nu}_\mu$ CC $1\pi^-$, $\bar{\nu}_\mu$ CC other, ν_μ CC 0π, ν_μ CC $1\pi^+$, and ν_μ CC other

The process of event selection and classification into the aforementioned samples involves three main steps, as detailed in [135]:

1. First, a CC-inclusive sample is selected by identifying the primary μ^- or μ^+ and ensuring that the events meet certain quality criteria. These criteria include:
   (a) **Event Quality**: Events must occur within the time window of each spill and are handled independently if they occur in different groups within the same spill, described in Section 2.1.
   (b) **Total Multiplicity**: At least one track crossing the Time Projection Chamber (TPC) must be reconstructable.
   (c) **Track Volume and Quality**: The track vertex should be within the trusted volume of the Fine-Grained Detectors (FGD), and at least one track should be reconstructable in the FGD with a minimum of 18 TPC hit groups.
   (d) **Background Ascending Veto**: Rejecting tracks that start at the same subdetector and show significant scatter before reaching the FGD, as well as rejecting events with parent track vertices in FGD2 and child track vertices in FGD1.
   (e) **Broken Tracks**: Handling cases where a track is split into two components, with one being a standalone FGD track and the other starting in later FGD layers and transitioning to the TPC.
   (f) **Muon identification** - The particle type associated with the primary track is determined by comparing the track curvature and measured energy deposition along the distance in the Time Projection Chamber (TPC) with simulated data for muons, electrons, and protons. Only negatively charged muons are considered for selection in the ν-mode sample, while both positively and negatively charged muons are eligible for selection in the $\bar{\nu}$-mode sample.

2. Secondary particles are identified by applying selection criteria to all tracks except the muon candidate. Two selection paths are available:

   - Standard Case: For particles created in the FGD with sufficient momentum and a small enough angle to enter the TPC, the criteria include:

     (a) **Vertex position and time** - The vertices of the child track must be in the same time group and is located in the same FGD reference volume as the candidate muon.

     (b) **Fiducial volume and track quality** - Same as Item 1c above.

     (c) **Particle identification** - The energy release measured at a distance is compared to the simulation to determine if the clue corresponds to a pion, a positron, or a proton if the particle has a positive charge, or a pion or an electron if it has a negative charge. Neutral pions are indirectly identified by the presence of an electron and a positron as a result of their decay.

   - Finally, with the primary muon and any secondary particles identified, the event is assigned to a specific sample based on the following criteria:

     (a) If no charged pions, electrons, or positrons are identified, the event is assigned to the corresponding CC 0π sample based on the beam mode and muon charge.

     (b) If only a single charged pion is reconstructed (either directly or via Michel decay), the event is assigned to the CC 1π sample based on the beam mode and muon charge.

     (c) If none of the above criteria are met, the event is assigned to the CC other sample based on the beam mode and muon charge.

3.3.2 — Near Detector Fit Methodology

The near-detector approximation aims to minimize the negative logarithm of the binary likelihood function, denoted as λ, described in Eq. (3.4) [136, 137]. This approximation incorporates the observations from all samples and considers the impact of limited Monte Carlo (MC) statistics, as well as prior constraints on flow ($\vec{f}$), cross section ($\vec{x}$), and ND280 detector ($\vec{d}$) systematic parameters.

$$
\begin{aligned}
-2\ln\lambda = 2\sum_{s}^{\text{samples}}\sum_{r}^{\text{bins}}\left[N_{r,s}^{\text{obs}}\cdot\ln\left(\frac{N_{r,s}^{\text{obs}}}{N_{r,s}^{\text{exp}}}\right)+N_{r,s}^{\text{exp}}-N_{r,s}^{\text{obs}}\right] \\
+2\sum_{s}^{\text{samples}}\sum_{r}^{\text{bins}}\frac{\left(\beta_{r,s}-1\right)^{2}}{2\sigma_{\beta_{r,s}}^{2}} \\
+\sum_{i,j}^{\text{flux pars.}}\Delta f_i\left(V_f^{-1}\right)_{i,j}\Delta f_j \\
+\sum_{i,j}^{\text{xsec pars.}}\Delta x_i\left(V_x^{-1}\right)_{i,j}\Delta x_j \\
+\sum_{i,j}^{\text{det. pars.}}\Delta d_i\left(V_d^{-1}\right)_{i,j}\Delta d_j
\end{aligned}
\tag{3.4}
$$

The first term in Eq. (3.4) is derived from the ordinary Poisson probability and represents the likelihood of the observed data given the statistical fluctuations in the prediction. In this term, s denotes a sample of the ND280 event, r represents the bin in the reconstructed space $(p_\mu, \cos\theta_\mu)$, $N^{\text{obs}}_{r,s}$ is the number of events observed in a specific bin and sample, and $N^{\text{exp}}_{r,s} \equiv N^{\text{exp}}_{r,s}(\vec{f}, \vec{x}, \vec{d})$ is the expected number of events in the same bin, taking into account the flow, cross section, and ND280 detector systematic parameters.

The second term in Eq. (3.4) is designed to incorporate the impact of limited Monte Carlo (MC) statistics on the $(p_\mu, \cos\theta_\mu)$ distributions. Following the approach introduced by Barlow and Beeston [138], this term quantifies the logarithm of the probability of the generated prediction, considering the statistical fluctuations that would arise if an infinite amount of MC statistics were available. To account for this, a scale parameter, denoted as $\beta_{r,s}$, is introduced for each bin, which scales the number of expected events generated in the MC simulation to approximate what would be generated with infinite MC statistics. Since the MC statistics are 10-20 times larger than the observed POT (Protons On Target) [137], the values of $\beta_{r,s}$ are assumed to follow a Gaussian distribution [139], and the analytical solution for each $\beta_{r,s}$ is obtained using Eq. (3.5), where $\sigma_{\beta_{r,s}}$ represents the relative statistical uncertainty of the prediction within a given interval [137].

$$\beta^2_{r,s} + (N^{\text{exp}}_{r,s}\sigma^2_{\beta_{r,s}} - 1)\beta_{r,s} - N^{\text{obs}}_{r,s}\sigma^2_{\beta_{r,s}} = 0 \tag{3.5}$$

The remaining terms in Eq. (3.4) contribute to the log-likelihood penalty based on variations in the flow parameters (Δf), cross section parameters (Δx), and detector parameters (Δd). These parameters represent the deviations from their nominal values according to prior constraints, and their uncertainties are represented by the covariance matrices V_f, V_x, and V_d.

To incorporate the uncertainties related to the ND280 detectors, each bin in the $(p_\mu, \cos\theta_\mu)$ distribution is assigned a normalization parameter. These parameters account for uncertainties arising from particle tracking and identification efficiency, as well as uncertainties in the beam and momentum measurements [140]. Such uncertainties can cause event migrations between bins or affect the predicted event rates. To quantify these effects, the detector uncertainties are randomly varied 2×10^3 times according to their respective covariances. This procedure generates a distribution of predicted event rates in each bin, from which the mean and covariance are determined and assigned to the normalization parameters in $\vec{d}$ and V_d [137].

3.3.3 — Results of the Near Detector Fit

Based on the T2K tests 2-9 data, the near detector setup produces the following results, as reported in T2K Technical Note 395 [137]. The flux and cross section covariance matrix after the fitting process is presented in Fig. 3.13. For clarity, the flux and cross section components are shown separately in Figs. A.1 and A.2, respectively. The best-fit values for these parameters, along with their uncertainties before and after the fit, are listed in Tables A.1 to A.4. The values of the parameters before and after the fit, as well as their uncertainties, are also depicted in Figs. 3.14 and 3.15.

The agreement between the $(p_\mu, \cos\theta_\mu)$ distributions modeled after the fitting process and the observed data from ND280 is found to be good. Examples of these distributions, projected onto p_μ, are shown in Fig. 3.16.

To fully assess the compatibility of the data with the post-fit model, a set of predictions is generated by randomly sampling values of the flow, cross section, and detector parameters. These predictions are then used to calculate the distribution of $-2 \ln \lambda$ values, which are compared to the corresponding value obtained from the data set. The proportion of predictions with $-2 \ln \lambda$ values larger than that of the data (i.e., less likely than the data) yields a p-value of 0.74. This indicates excellent compatibility between the data and the post-fit model.

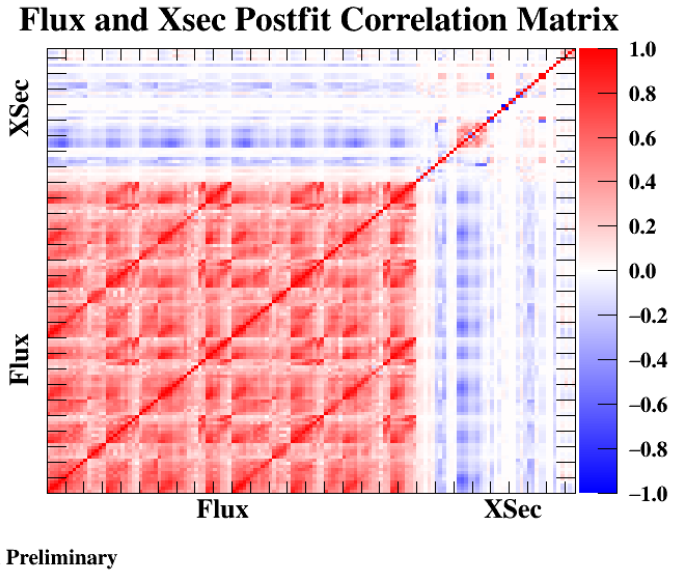

Figure 3.13: The flux and cross-section covariance matrix resulting from the near detector fit.

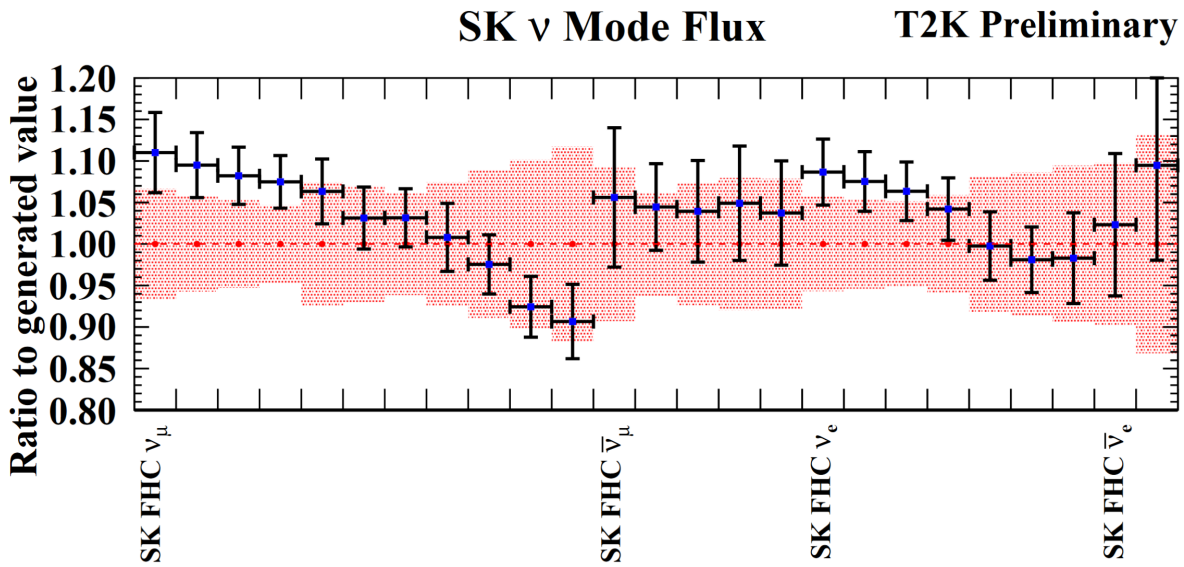

(a) ν-mode flux parameters.

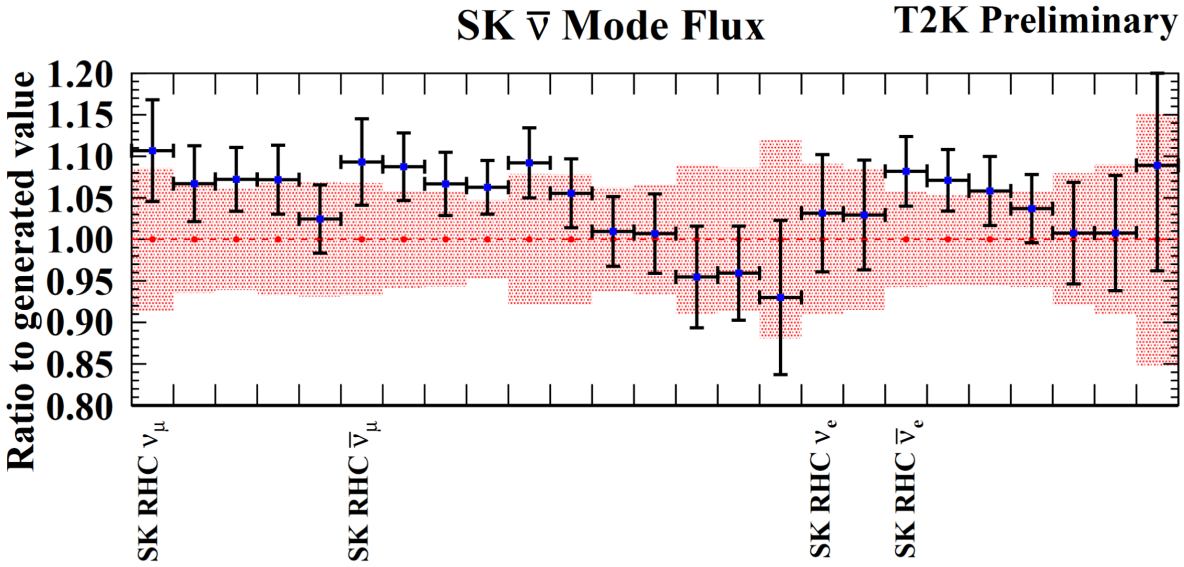

(b) $\bar{\nu}$-mode flux parameters.

Figure 3.14: Flux parameter values before and after the near detector fit. Values are shown as a fraction of the parameter values used to generate the NEUT MC simulation. The pre-fit parameter values and uncertainties are shown as red points and shaded regions, respectively. The post-fit parameter values and uncertainties are shown as blue points and black error bars, respectively. Each bin corresponds to a single parameter, arranged in the same order as in Tables A.1 and A.2. Reproduced from Ref. [137].

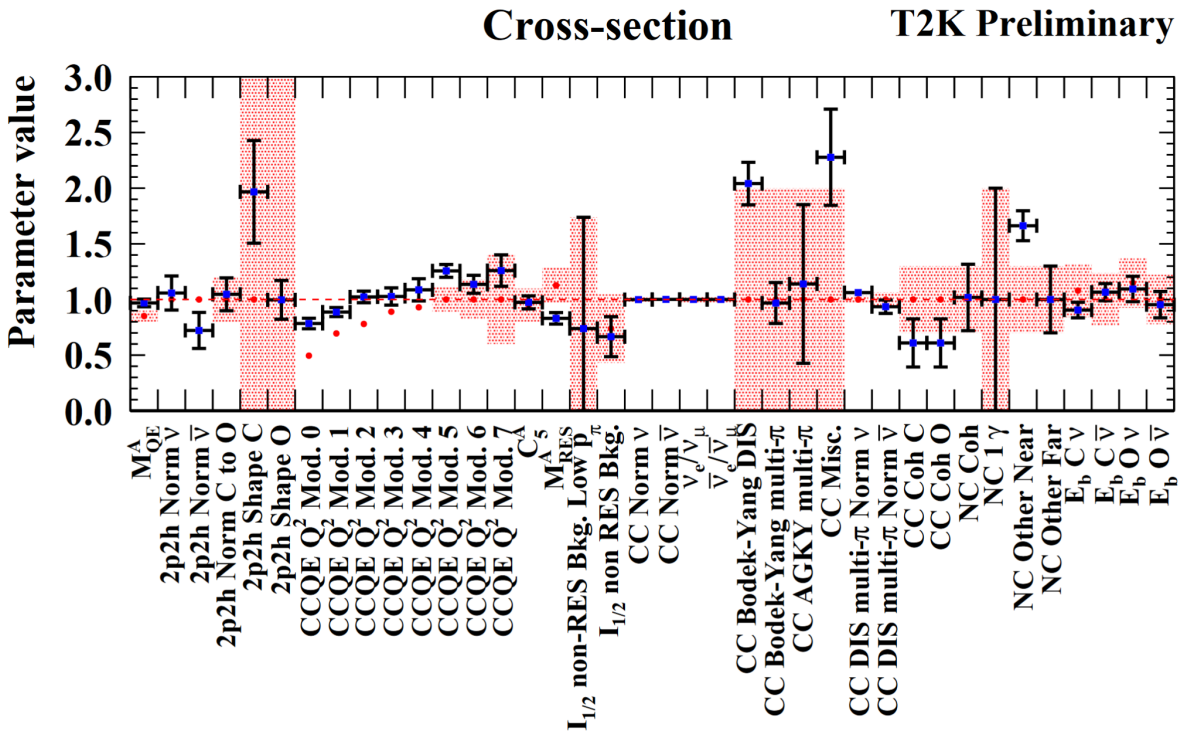

Figure 3.15: Interaction model parameter values before and after the near detector fit. Values are shown as a fraction of the parameter values used to generate the NEUT MC simulation. The pre-fit parameter values and uncertainties are shown as red points and shaded regions, respectively. The post-fit parameter values and uncertainties are shown as blue points and black error bars, respectively. Reproduced from Ref. [137].

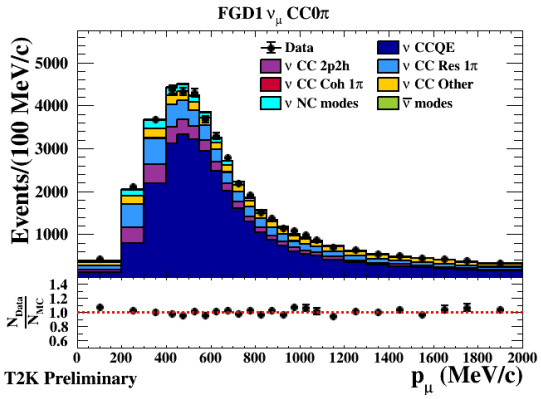

(a) ν-mode ν_μ CC0π selection.

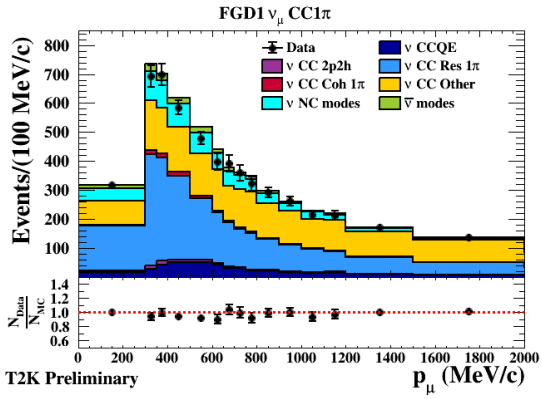

(b) ν-mode ν_μ CC1π selection.

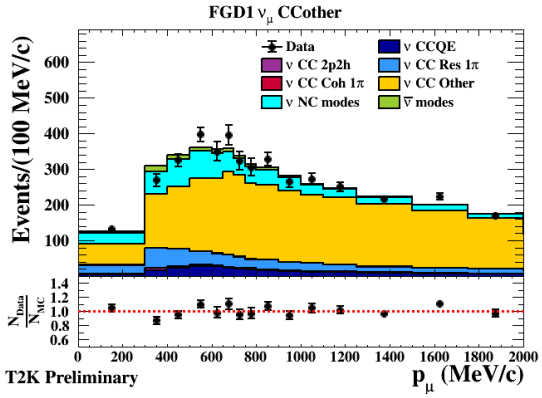

(c) ν-mode ν_μ CCother selection.

Figure 3.16: p_μ projections of observed (dots) and postfit MC distributions (coloured histogram stack) at FGD1 in ND280. Reproduced from Ref. [137].

3.3.4 — SK samples and systematics

A series of datasets containing simulated or observed events in the Super-Kamiokande (Super-K) detector are examined to constrain the parameters of neutrino oscillations. These datasets are specifically designed to capture events originating from a neutrino beam, excluding contributions from solar or atmospheric sources. The focus is on selecting high-purity samples of $\overset{(-)}{\nu}_{\mu}$ and $\overset{(-)}{\nu}_{e}$ events resembling Charged-Current Quasi-Elastic (CCQE) and CC1π interactions. Samples related to $\overset{(-)}{\nu}_{\tau}$ are not considered since their impact is negligible at the energies probed by the T2K experiment due to the high threshold energy for $\overset{(-)}{\tau}$ production (3.5 GeV) as stated in Ref. [141].

Previously, T2K analyses only included one sample resembling CC1π events based on the selection of $\overset{(-)}{\nu}_{e}$. However, this latest analysis, described in Ref. [142], introduces two new samples resembling $\overset{(-)}{\nu}_{\mu}$ CC1π events. These samples differ in terms of the number of secondary leptons, but they are combined into a single sixth sample for convenience in the far detector analysis.

It is important to note that the Super-K detector is not magnetized, which means that it cannot directly differentiate between neutrinos and antineutrinos. The determination of whether a sample is neutrino-like or antineutrino-like is based on the beam mode. Therefore, the analysis presented in the dissertation utilizes the following samples:

- ν-mode samples: ν_μ / $\bar{\nu}_\mu$ CCQE-like, ν_e / $\bar{\nu}_e$ CCQE-like and ν_eCC1π^+-like.
- $\bar{\nu}$-mode samples: ν_μ / $\bar{\nu}_\mu$ CCQE-like and ν_e / $\bar{\nu}_e$ CCQE-like.

The subsequent sections will provide a comprehensive explanation of the criteria applied to construct these datasets. Initially, the common selection cuts shared by all samples will be outlined in Section 3.3.5. Following this, the specific selection criteria for each sample, namely ν_μ / $\bar{\nu}_\mu$ CCQE-like, ν_e / $\bar{\nu}_e$ CCQE-likeand ν_eCC1π^+-likewill be detailed in Sections 3.3.6 to 3.3.8, respectively. The selection criteria for each sample are individually tailored to maximize sensitivity to θ_{23} and δ_{CP}, drawing upon atmospheric neutrino data as a basis, as discussed in Ref. [78] (also covered in Section 3.4.1). The optimization process for the selection criteria is elaborated in Ref. [143] and Ref. [142].

3.3.5 — Common Selection Criteria

Several selection criteria are common to all the analyzed samples, and they are as follows:

- **Good beam spread**: This criterion ensures that events resulting from a specific beam spread are considered in the analysis. Parameters related to the beamline conditions, such as beam direction and horn currents, must meet acceptable criteria. Additionally, a minimum number of PMT hits is required to account for background "dark noise." Two GPS data sets are utilized to ensure precise time synchronization between the Tokai and Kamioka sites. Events that coincide with failures in both GPS systems or exhibit discrepancies in their timing characteristics are rejected [144].

- **Data Quality**: Sub-runs, which correspond to periods of approximately minutes of data collection, are evaluated based on the condition of the Super-K detector. Sub-runs are accepted or rejected depending on factors such as failures in the data acquisition system or external causes like explosions at the Kamioka mine. Furthermore, data is not collected during specific short data blocks, such as when counters receive a reset signal [144].

- **Time**: Events occurring up to 100 μs before the firing of the beam are rejected to avoid electronic contamination from cosmic muon decays. Events that take place 2 μs before the leading edge of the output beam or more than 10 μs after it are also discarded to prevent contamination [144].

- **Containment**: To ensure accurate measurements of event properties, events must be fully contained within the internal detector and its control volume. Fully contained events are selected to minimize external detector activity. The criteria for determining containment differ based on specific variables, optimizing sensitivity to θ_{23} and δ_{CP} while minimizing systematic uncertainties. Generally, the criteria consider the distance between the event vertex and the closest point on the detector wall (referred to as '*wall*') and the distance from the event top to the detector wall along the track direction (referred to as '*towall*'). These criteria ensure sufficient PMT illumination for reliable analysis [78].

- **Energy**: Events with reconstructed neutrino energies greater than 30 GeV are rejected since they cannot be produced by neutrinos resulting from a 30 GeV proton beam.

These common selection criteria are applied uniformly across all samples to ensure consistent analysis and reliable results.

3.3.6 — ν_μ / $\bar{\nu}_\mu$ CCQE-like Selection Criteria

The selection criteria for accepting ν_μ / $\bar{\nu}_\mu$ CCQE-like events, both in ν-mode and $\bar{\nu}$-mode, are provided in the following list [143, 145]. The impact of these criteria is depicted in Fig. 3.17, Fig. 3.18 Fig. 3.19, Fig. 3.20, and the reconstructed neutrino energy distribution for the selected events is shown in Fig. 3.21. The number of modeled and observed candidate events that pass each selection stage, as well as the selection purity, are specified in Table 3.1 and Table 3.2.

1. **Complete containment**: The event must be fully contained within the internal detector of Super-K and reconstructed within the reference volume, satisfying the criteria of *wall* $>$ 50 cm and *wall* $>$ 250 cm.

2. **Unique Cherenkov ring reconstruction**: Events with more than one charged particle on the Cherenkov threshold, such as pions or other charged leptons, are removed. This criterion eliminates events in the beam spread window that do not correspond to neutrino CCQE interactions, as protons in CCQE interactions rarely reach the Cherenkov threshold. Electron-containing events resulting from Michel muon decay are not removed since they typically occur after the beam spread window due to the muon lifetime.

3. **Cherenkov ring identification**: A Cherenkov ring is identified as $\overset{(-)}{\nu}_{\mu}$-like rather than $\overset{(-)}{\nu}_{e}$-like by requiring $\ln(L_e/L_\mu) < 0.2p_e$, where L represents the probability of the respective particle hypotheses and p_e is the momentum of the reconstructed electron in the $\overset{(-)}{\nu}_{e}$-like hypothesis. Despite comparing quantities in different units, this empirical comparison is justified, as demonstrated in Fig. 3.19.

4. **Muon momentum reconstruction**: The muon momentum is reconstructed, and events with $p_\mu > 200$ MeV/c are considered to exclude charged pions and misidentified electrons resulting from unobserved muon and pion decays.

5. **Michel electron reconstruction**: Events with either one or no electrons resulting from decay of muons are reconstructed. The presence of such electron decay indicates the existence of a muon or pion (via $\pi^{\pm} \to \mu^{\pm}$ decay), even if the parent particle was below the Cherenkov threshold.

6. **Cherenkov ring identification**: A Cherenkov ring is identified as $\overset{(-)}{\nu}_{\mu}$-like rather than π^{+}-like by requiring $\ln(L_{\pi^+}/L_\mu) < 0.15p_\mu$.

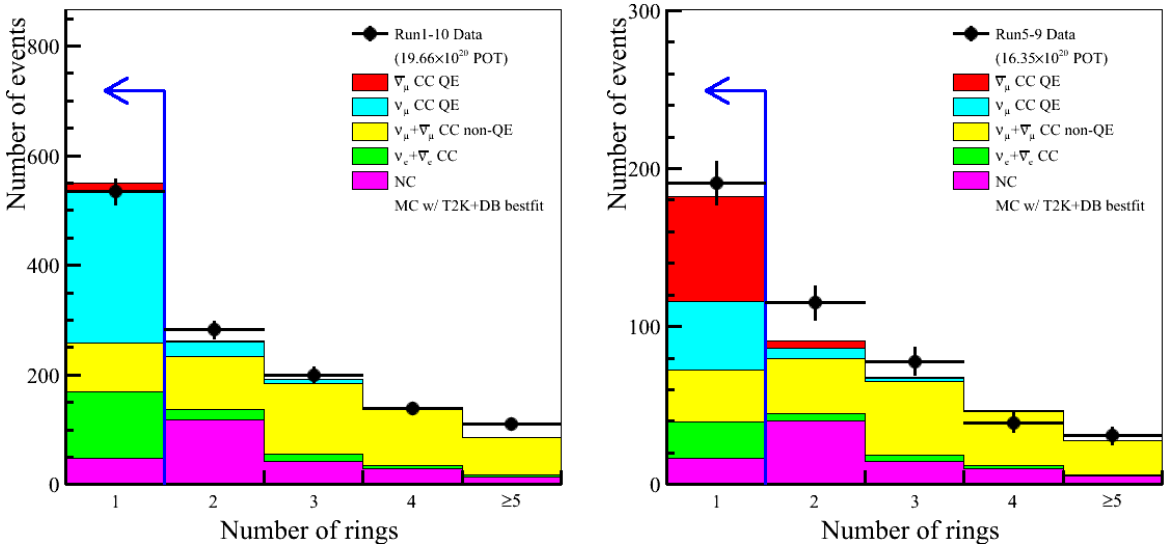

(a) ν-mode.

(b) $\bar{\nu}$-mode.

Figure 3.17: Distribution of the simulated (coloured histograms) and observed (black points) number of reconstructed Cherenkov rings in the ν_μ / $\bar{\nu}_\mu$ CCQE-like sample. The region of accepted events is indicated by the blue arrow. Reproduced from Ref. [145].

Selection Stage	$\nu_e + \bar{\nu}_e$ CC	$\nu + \bar{\nu}$ NC	$\nu_\mu + \bar{\nu}_\mu$ CC non-QE	ν_μ CCQE	$\bar{\nu}_\mu$ CCQE	MC total	Data
Containment	159.2	252.2	487.2	312.5	18.2	1229.4	1266
No. of Cherenkov rings	120.2	48.5	89.2	276.5	16.0	550.4	534
μ vs. e discrimination	0.1	18.3	84.4	270.3	15.9	389.1	367
Momentum threshold	0.1	18.1	84.4	270.0	15.9	388.5	366
No. of Michel electrons	0.1	17.6	58.0	266.4	15.8	357.9	329
μ vs. π^+ discrimination	0.1	8.9	56.7	263.1	15.6	344.4	318
Efficiency (%)	0.1	3.5	11.6	84.2	85.5	28.0	-
Purity (%)	0.0	2.6	16.5	76.4	4.5	-	-

Table 3.1: The expected and observed number of ν-mode ν_μ / $\bar{\nu}_\mu$ CCQE-like candidate events passing each Super-K selection stage. Predictions are generated using the full T2K Runs 1-10 beam exposure, with normal mass ordering and oscillation parameters set close to previous T2K best fit values: $\Delta m^2_{21} = 7.53 \times 10^{-5}$ eV^2/c^4, $\Delta m^2_{32} = 2.54 \times 10^{-3}$ eV^2/c^4, $\sin^2\theta_{12} = 0.304$, $\sin^2\theta_{13} = 0.0219$, $\sin^2\theta_{23} = 0.550$, and $\delta_{CP} = -1.728$. Adapted from Ref. [145].

Selection Stage	$\nu_e + \bar{\nu}_e$ CC	$\nu + \bar{\nu}$ NC	$\nu_\mu + \bar{\nu}_\mu$ CC non-QE	ν_μ CCQE	$\bar{\nu}_\mu$ CCQE	MC total	Data
Containment	35.3	86.6	169.3	52.7	72.7	416.6	454
No. of Cherenkov rings	23.3	16.6	32.7	43.3	66.7	182.6	191
μ vs. e discrimination	0.0	6.3	31.4	42.9	65.8	146.3	154
Momentum threshold	0.0	6.2	31.4	42.9	65.7	146.2	154
No. of Michel electrons	0.0	6.0	24.4	42.2	64.9	137.6	141
μ vs. π^+ discrimination	0.0	2.8	24.0	41.7	64.3	132.8	137
Efficiency (%)	0.0	3.3	14.2	79.1	88.4	31.9	-
Purity (%)	0.0	2.1	18.1	31.4	48.4	-	-

Table 3.2: The expected and observed number of $\bar{\nu}$-mode ν_μ / $\bar{\nu}_\mu$ CCQE-like candidate events passing each Super-K selection stage. Predictions are generated using the full T2K Runs 1-10 beam exposure, with normal mass ordering and oscillation parameters set close to previous T2K best fit values: $\Delta m^2_{21} = 7.53 \times 10^{-5}$ eV^2/c^4, $\Delta m^2_{32} = 2.54 \times 10^{-3}$ eV^2/c^4, $\sin^2\theta_{12} = 0.304$, $\sin^2\theta_{13} = 0.0219$, $\sin^2\theta_{23} = 0.550$, and $\delta_{CP} = -1.728$. Adapted from Ref. [145].

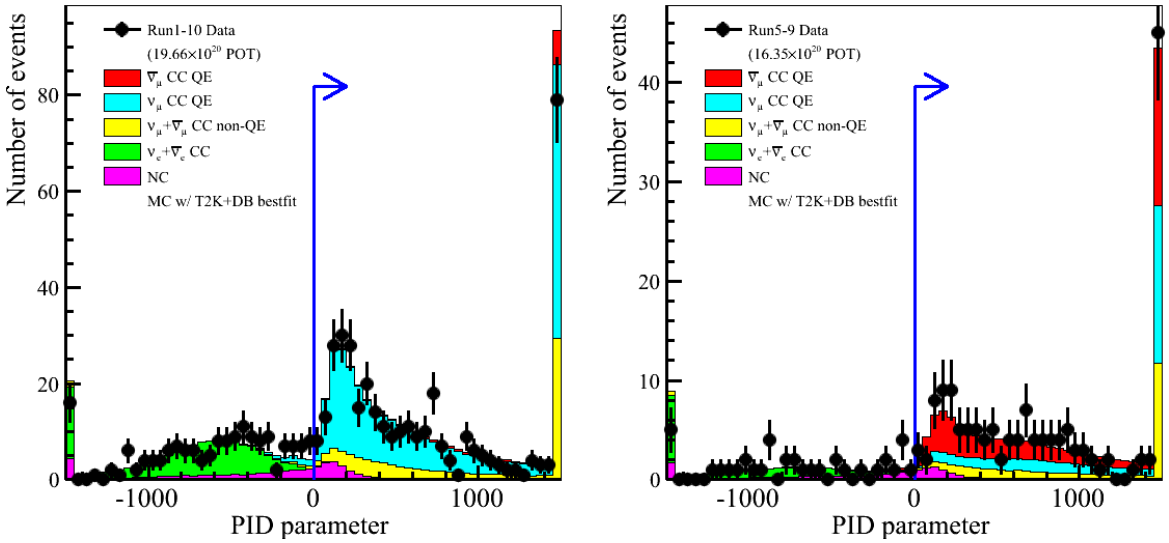

(a) ν-mode. (b) $\bar{\nu}$-mode.

Figure 3.18: ν_μ/ν_e discrimination PID parameter distributions in the ν_μ / $\bar{\nu}_\mu$ CCQE-like sample. Both simulated (coloured histograms) and observed (black points) distributions are shown. This parameter is defined as the distance from the cut described in Item 3 of the above list. The region of accepted events is indicated by the blue arrow. Reproduced from Ref. [145].

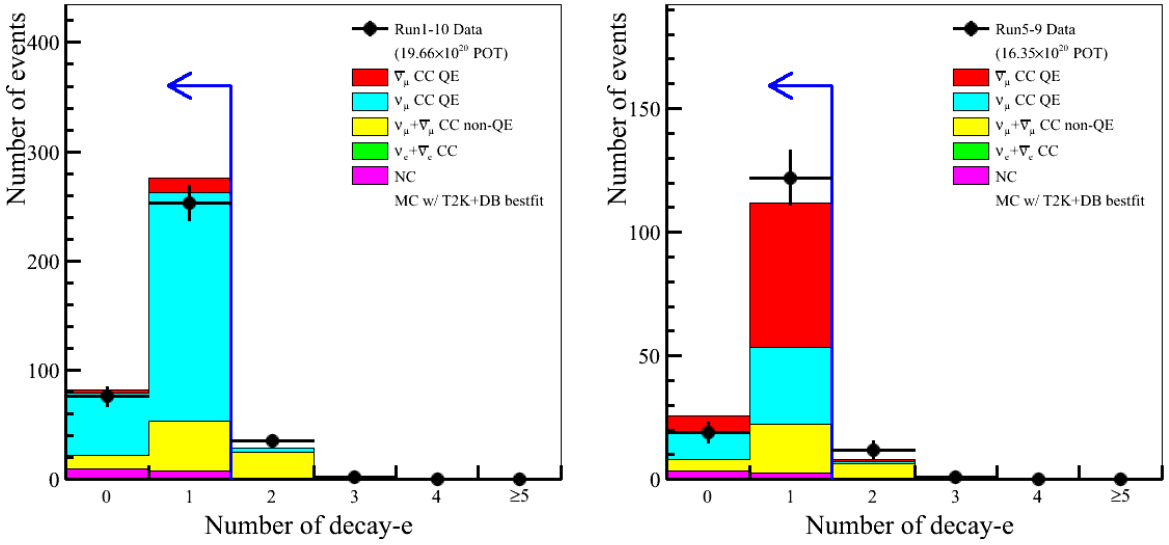

(a) ν-mode. (b) $\bar{\nu}$-mode.

Figure 3.19: Distribution of the simulated (coloured histograms) and observed (black points) number of reconstructed decay electrons in the ν_μ / $\bar{\nu}_\mu$ CCQE-like sample. The region of accepted events is indicated by the blue arrow. Reproduced from Ref. [145].

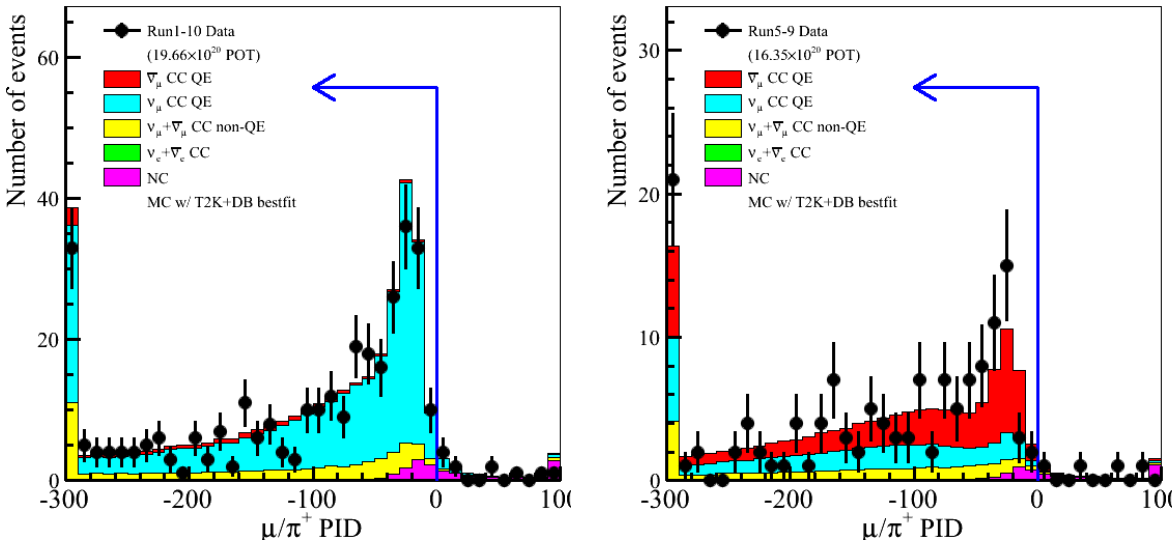

(a) ν-mode. (b) $\bar{\nu}$-mode.

Figure 3.20: ν_μ/π^+ discrimination PID parameter distributions in the ν_μ / $\bar{\nu}_\mu$ CCQE-like sample. Both simulated (coloured histograms) and observed (black points) distributions are shown. This parameter is defined as the distance from the cut described in Item 6 of the above list. The region of accepted events is indicated by the blue arrow. Reproduced from Ref. [145].

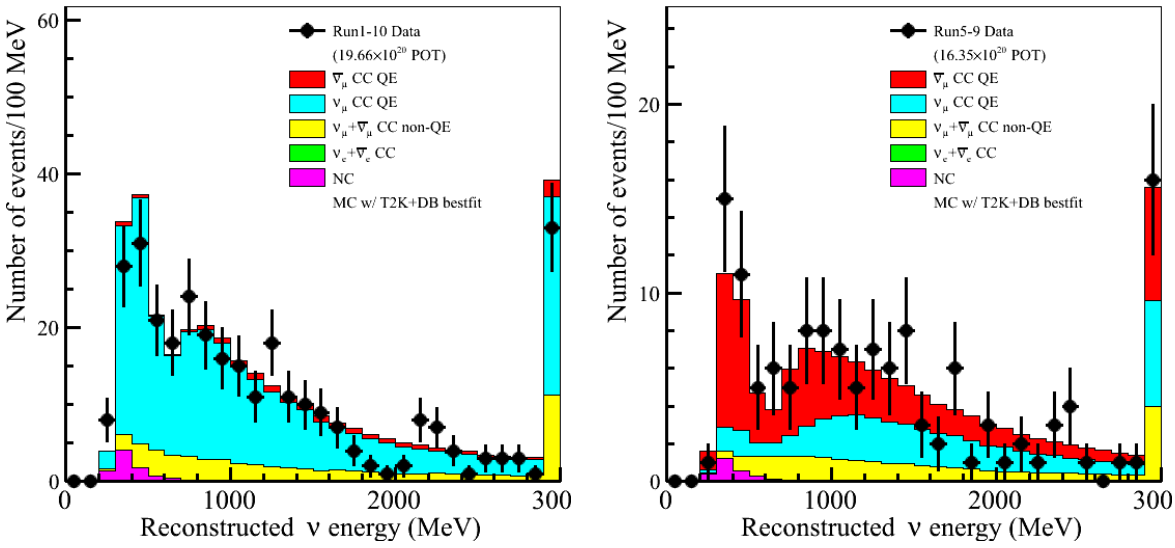

(a) ν-mode. (b) $\bar{\nu}$-mode.

Figure 3.21: Distribution of the simulated (coloured histograms) and observed (black points) reconstructed neutrino energy in the ν_μ / $\bar{\nu}_\mu$ CCQE-like sample, shown after all selection criteria have been applied. Reproduced from Ref. [145].

3.3.7 — ν_e / $\bar{\nu}_e$ CCQE-like Selection Criteria

The criteria for accepting ν_e / $\bar{\nu}_e$ CCQE-like events, both in ν-mode and $\bar{\nu}$-mode, are outlined in the following list [143, 145]. The impact of the known selection criteria can be observed in Fig. 3.22, Fig. 3.23, Fig. 3.24, Fig. 3.25, Fig. 3.26, Fig. 3.27, and the final reconstructed neutrino energy distribution for the selected events is displayed in Fig. 3.28. The number of modeled and observed candidate events that pass each selection step, as well as the efficiency and purity of the selection, are provided in Table 3.3 and Table 3.4.

1. **Complete localization**: The event must be fully contained within the internal Super-K detector and reconstructed within the reference volume, satisfying the criteria of *wall* $>$ 80 cm and *wall* $>$ 170 cm.

2. **Unique Cherenkov ring reconstruction**: Events with more than one charged particle above the Cherenkov threshold, such as pions or other charged leptons, within the beam spread window are removed. This criterion does not eliminate CCQE events as protons produced in neutrino CCQE interactions rarely reach the Cherenkov threshold. Electron-containing events resulting from Michel decay of muons are also not eliminated since they typically occur after the beam-scattering window due to the muon lifetime.

3. **Apparent energy threshold**: Events with apparent energy $>$ 100 MeV are accepted to exclude sub-threshold muon decay impurities [78].

4. **Michel electron decay exclusion**: Events with electrons resulting from the decay of muons are not reconstructed. The presence of such electron decay indicates the existence of a muon or pion (via $\pi^{\pm} \rightarrow \mu^{\pm}$ decay), even if the parent particle was below the Cherenkov threshold.

5. **Reconstructed neutrino energy range**: The reconstructed neutrino energy must be less than 1250 MeV, as the expected number of oscillating $\overset{(-)}{\nu}_e$ events is negligible at high energies. The background contributions from $\overset{(-)}{\nu}_e$ and neutral current (NC) interactions dominate in this energy range, as shown in Fig. 3.26.

6. **Cherenkov ring identification**: A Cherenkov ring is identified as $\overset{(-)}{\nu}_e$-like rather than π^0-like by requiring $\ln(L_{\pi^0}/L_e) < 175 - 0.875 m_{\pi^0}$, where m_{π^0} is the reconstructed mass of π^0 in MeV/c^2 units.

Selection Stage	$\nu_\mu + \bar{\nu}_\mu$ CC	$\nu_e + \bar{\nu}_e$ CC	$\nu + \bar{\nu}$ NC	$\nu_\mu \to \nu_e$ CC	$\bar{\nu}_\mu \to \bar{\nu}_e$ CC	MC total	Data
Containment	886.4	56.7	260.5	109.8	1.0	1314.3	1361
No. of Cherenkov rings	397.2	29.5	49.2	94.0	0.8	570.7	554
e vs. μ discrimination	11.4	29.5	30.9	93.9	0.8	166.4	174
Visible energy threshold	4.3	29.3	21.2	92.7	0.8	148.3	150
No. of Michel electrons	1.2	24.9	18.2	83.9	0.7	128.9	130
E_{rec} threshold	0.8	13.1	14.1	81.2	0.5	109.8	107
e vs. π^0 discrimination	0.4	11.7	6.6	76.2	0.5	95.3	94
Efficiency (%)	0.0	20.6	2.5	69.4	47.0	7.3	-
Purity (%)	0.4	12.2	6.9	79.9	0.5	-	-

Table 3.3: The expected and observed number of ν-mode ν_e / $\bar{\nu}_e$ CCQE-like candidate events passing each Super-K selection stage. Predictions are generated using the full T2K Runs 1-10 beam exposure, with normal mass ordering and oscillation parameters set close to previous T2K best fit values: $\Delta m^2_{21} = 7.53 \times 10^{-5}$ eV^2/c^4, $\Delta m^2_{32} = 2.54 \times 10^{-3}$ eV^2/c^4, $\sin^2\theta_{12} = 0.304$, $\sin^2\theta_{13} = 0.0219$, $\sin^2\theta_{23} = 0.550$, and $\delta_{CP} = -1.728$. Adapted from Ref. [145].

Selection Stage	$\nu_\mu + \bar{\nu}_\mu$ CC	$\nu_e + \bar{\nu}_e$ CC	$\nu + \bar{\nu}$ NC	$\nu_\mu \to \nu_e$ CC	$\bar{\nu}_\mu \to \bar{\nu}_e$ CC	MC total	Data
Containment	321.1	22.7	89.7	6.2	9.7	449.5	498
No. of Cherenkov rings	149.1	11.3	16.9	4.7	8.5	190.4	207
e vs. μ discrimination	2.8	11.3	10.6	4.7	8.5	37.8	41
Visible energy threshold	1.5	11.2	7.4	4.6	8.5	33.6	32
No. of Michel electrons	0.4	9.9	6.3	4.1	8.3	29.0	29
E_{rec} threshold	0.3	4.3	4.7	3.4	7.8	20.5	20
e vs. π^0 discrimination	0.1	3.7	2.1	3.1	7.0	16.1	16
Efficiency (%)	0.0	16.4	2.3	1.4	49.4	72.3	-
Purity (%)	0.9	23.2	12.9	19.2	43.9	-	-

Table 3.4: The expected and observed number of $\bar{\nu}$-mode ν_e / $\bar{\nu}_e$ CCQE-like candidate events passing each Super-K selection stage. Predictions are generated using the full T2K Runs 1-10 beam exposure, with normal mass ordering and oscillation parameters set close to previous T2K best fit values: $\Delta m^2_{21} = 7.53 \times 10^{-5}$ eV^2/c^4, $\Delta m^2_{32} = 2.54 \times 10^{-3}$ eV^2/c^4, $\sin^2\theta_{12} = 0.304$, $\sin^2\theta_{13} = 0.0219$, $\sin^2\theta_{23} = 0.550$, and $\delta_{CP} = -1.728$. Adapted from Ref. [145].

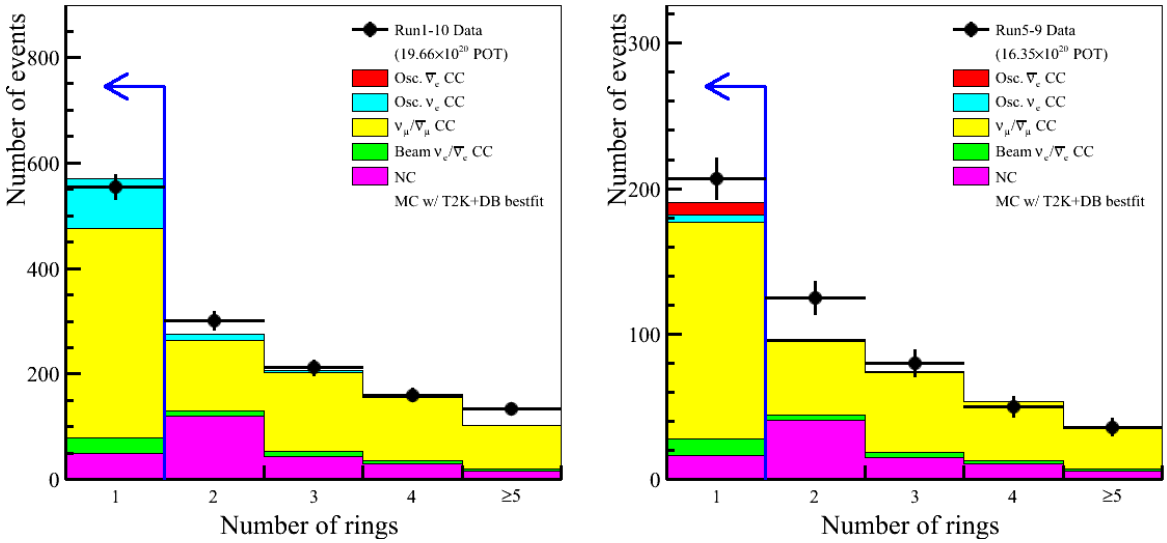

(a) ν-mode.

(b) $\bar{\nu}$-mode.

Figure 3.22: Distribution of the simulated (coloured histograms) and observed (black points) number of reconstructed Cherenkov rings in the ν_e / $\bar{\nu}_e$ CCQE-like sample. The region of accepted events is indicated by the blue arrow. Reproduced from Ref. [145].

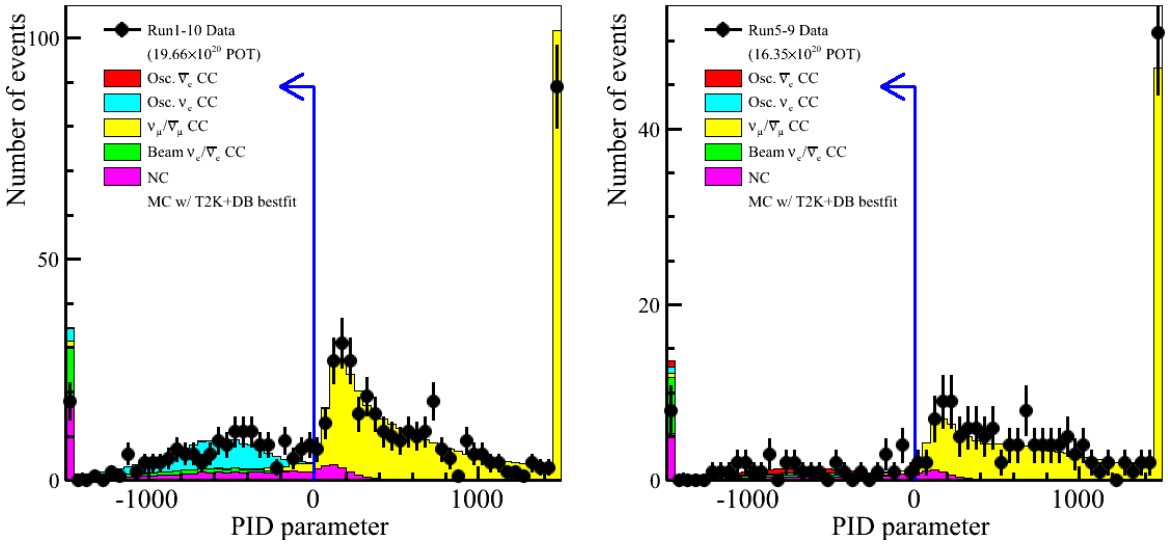

(a) ν-mode.

(b) $\bar{\nu}$-mode.

Figure 3.23: ν_e/ν_μ discrimination PID parameter distributions in the ν_e / $\bar{\nu}_e$ CCQE-like sample. Both simulated (coloured histograms) and observed (black points) distributions are shown. This parameter is defined as the distance from the cut described in Item 6 of the above list. The region of accepted events is indicated by the blue arrow. Reproduced from Ref. [145].

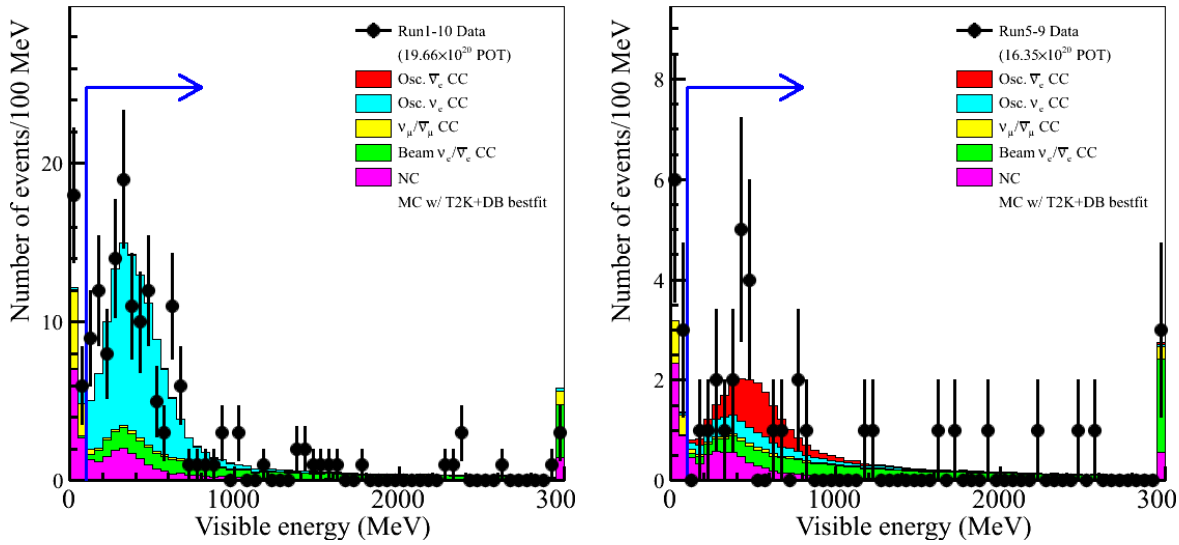

(a) ν-mode.

(b) $\bar{\nu}$-mode.

Figure 3.24: Distribution of the simulated (coloured histograms) and observed (black points) visible energy in the ν_e / $\bar{\nu}_e$ CCQE-like sample. The region of accepted events is indicated by the blue arrow. Reproduced from Ref. [145].

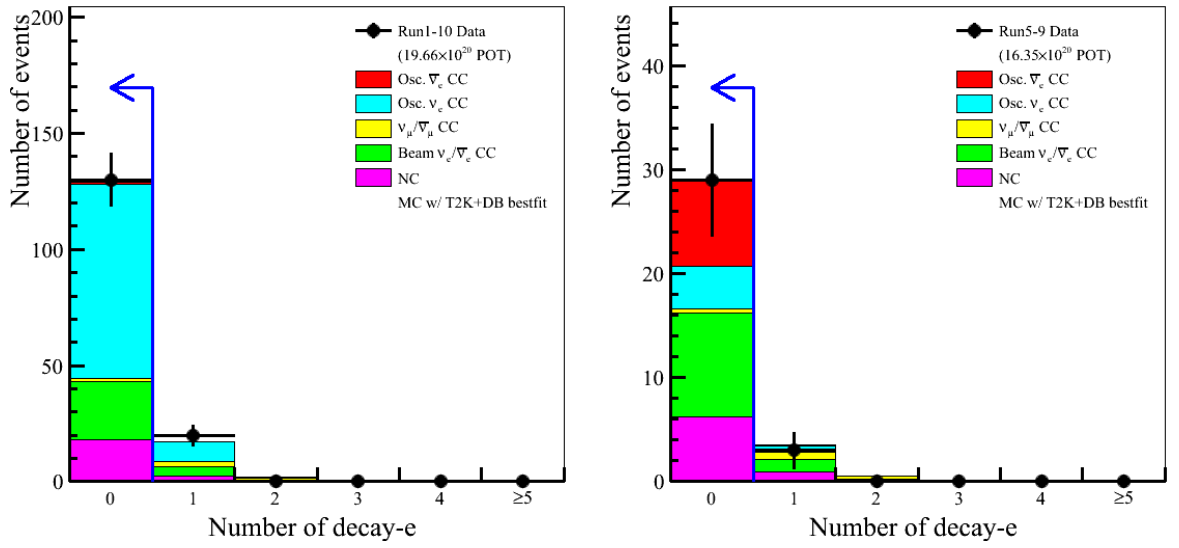

(a) ν-mode.

(b) $\bar{\nu}$-mode.

Figure 3.25: Distribution of the simulated (coloured histograms) and observed (black points) number of reconstructed decay electrons in the ν_e / $\bar{\nu}_e$ CCQE-like sample. The region of accepted events is indicated by the blue arrow. Reproduced from Ref. [145].

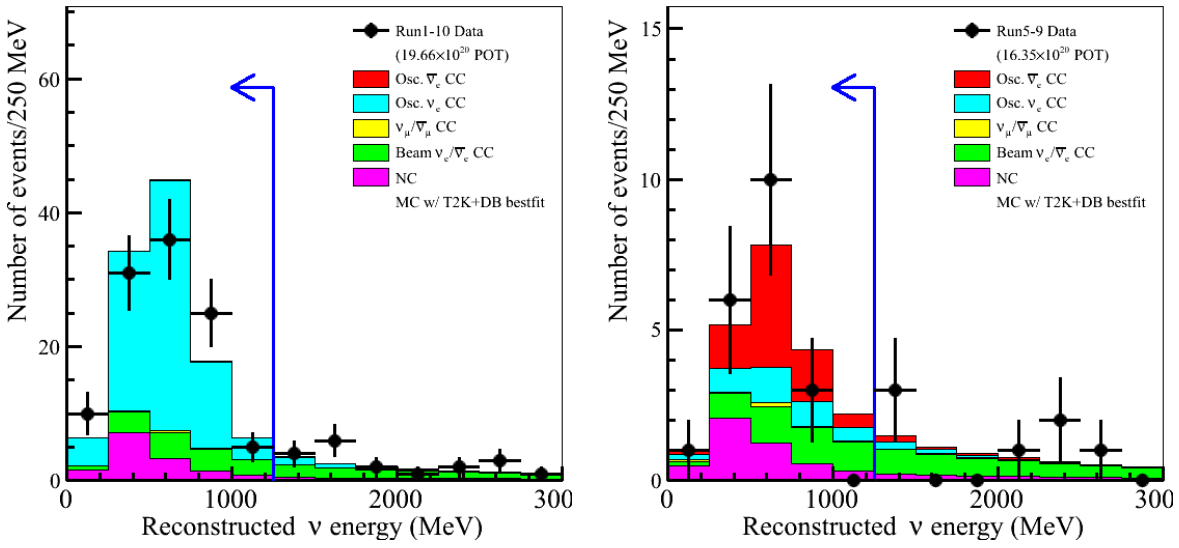

(a) ν-mode. (b) $\bar{\nu}$-mode.

Figure 3.26: Distribution of the simulated (coloured histograms) and observed (black points) reconstructed neutrino energy in the ν_e / $\bar{\nu}_e$ CCQE-like sample. The region of accepted events is indicated by the blue arrow. Reproduced from Ref. [145].

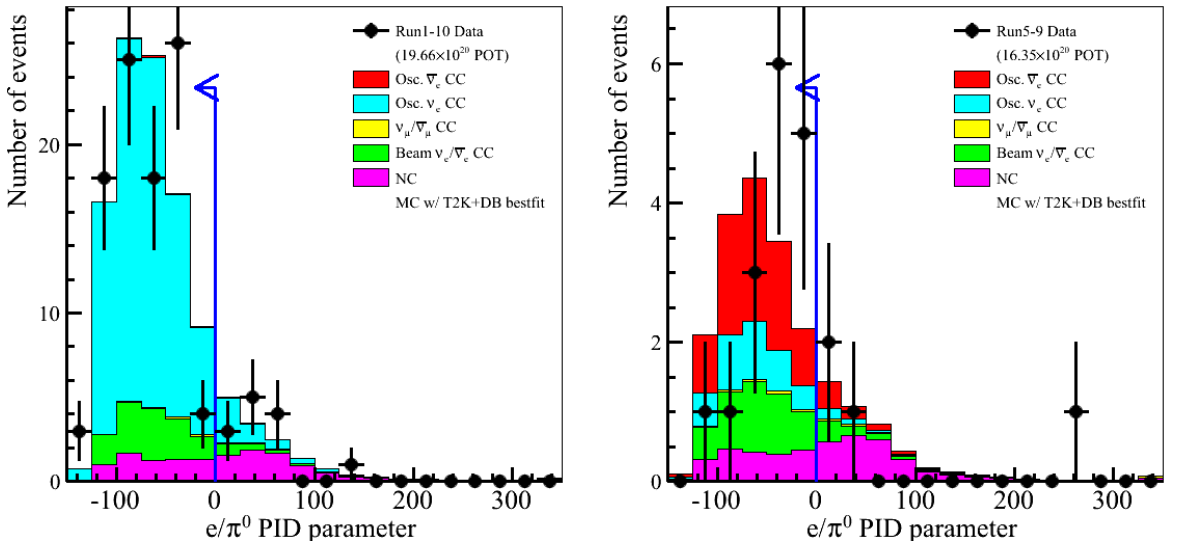

(a) ν-mode. (b) $\bar{\nu}$-mode.

Figure 3.27: ν_e/π^0 discrimination PID parameter distributions in the ν_e / $\bar{\nu}_e$ CCQE-like sample. Both simulated (coloured histograms) and observed (black points) distributions are shown. This parameter is defined as the distance from the cut described in Item 6 of the above list. The region of accepted events is indicated by the blue arrow. Reproduced from Ref. [145].

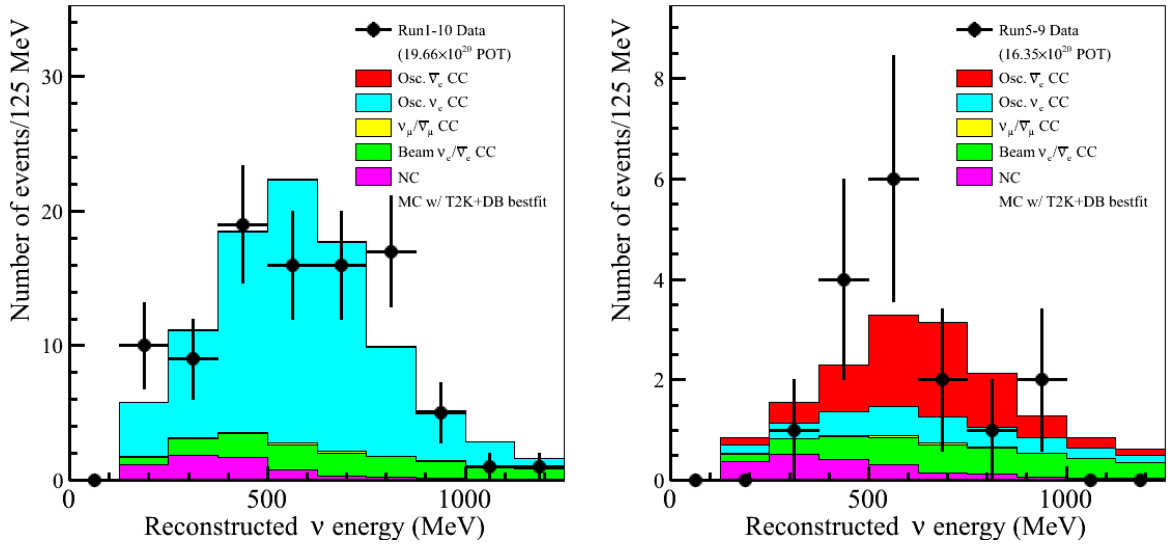

(a) ν-mode.

(b) $\bar{\nu}$-mode.

Figure 3.28: Distribution of the simulated (coloured histograms) and observed (black points) reconstructed neutrino energy in the ν_e / $\bar{\nu}_e$ CCQE-like sample, shown after all selection criteria have been applied. Reproduced from Ref. [145].

3.3.8 — ν_eCC1π^+-like Selection Criteria

The criteria used to accept ν-mode ν_eCC1π^+-like events are the same as for ν_e / $\bar{\nu}_e$ CCQE-like samples described in Section 3.3.7, with the following modifications listed. The effects of the known selection criteria can be seen in Fig. 3.29, Fig. 3.30, Fig. 3.31, and the final reconstructed neutrino energy distribution for the selected events is shown in Fig. 3.32. The number of simulated and observed candidate events that pass each selection stage, as well as the efficiency and purity of the selection, are presented in Table 3.5.

1. **Full localization**: The event must be fully localized within the inner Super-K detector and reconstructed within a confidence volume satisfying the criteria of *wall* $>$ 50 cm and *towall* $>$ 270 cm.

2. **Michel electron decay reconstruction**: The reconstruction includes an electron resulting from the decay of a Michelin muon. The presence of such an electron decay indicates the existence of a muon or pion (through the decay of $\pi^{\pm} \rightarrow \mu^{\pm}$), even if the parent particle was below the Cherenkov threshold.

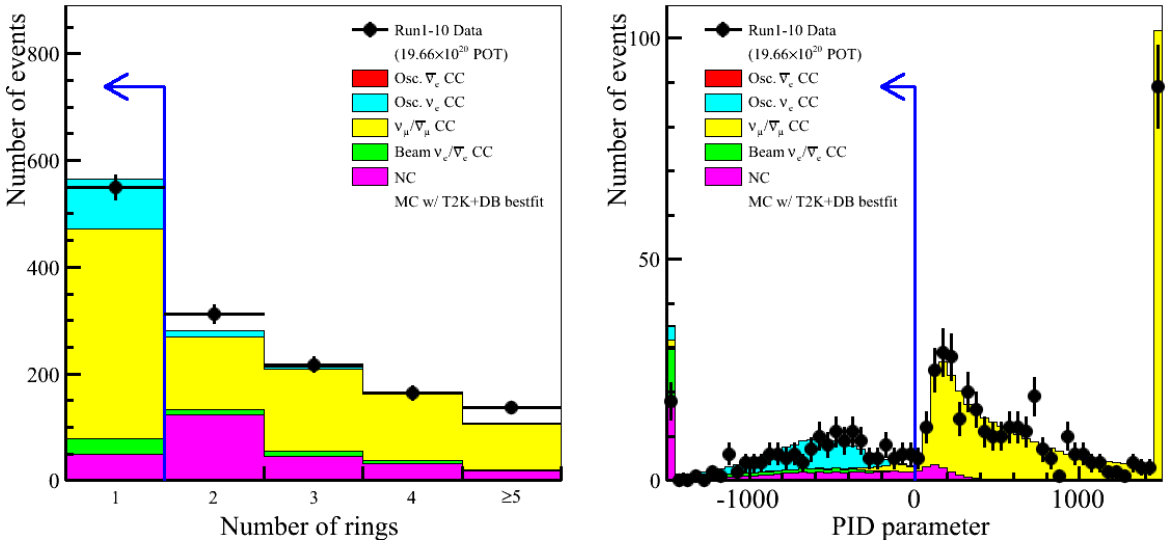

(a) Number of Cherenkov rings.

(b) ν_e/ν_μ PID.

Figure 3.29: Distributions of the simulated (coloured histograms) and observed (black points) number of reconstructed Cherenkov rings and ν_e/ν_μ discrimination PID parameter (defined as the distance from the cut described in Item 6 of Section 3.3.7) in the ν-mode ν_eCC1π^+-like sample. The regions of accepted events are indicated by the blue arrows. Reproduced from Ref. [145].

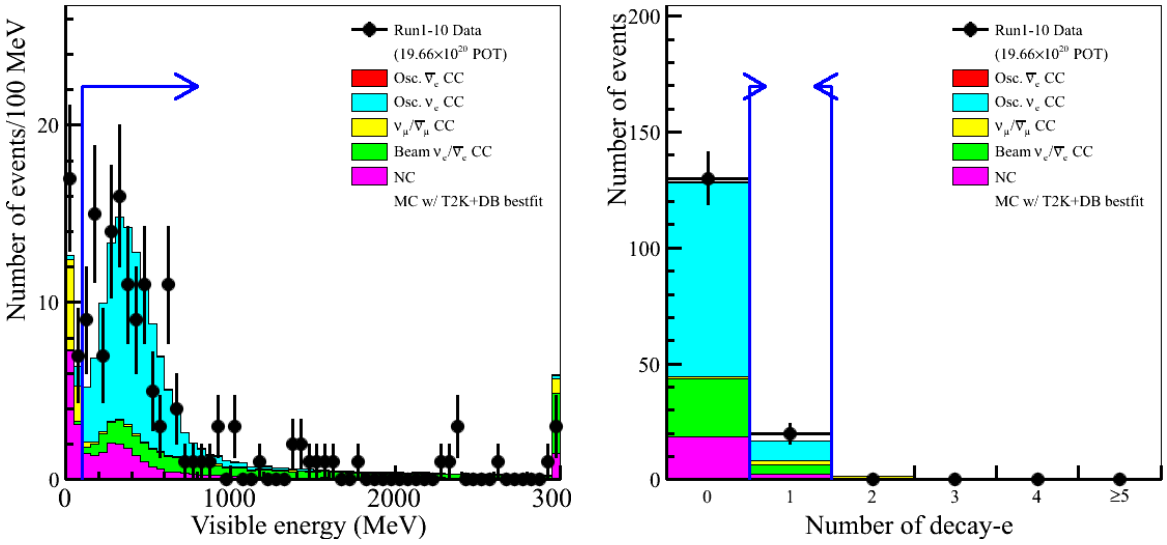

(a) Visible energy.

(b) Number of decay electrons.

Figure 3.30: Distributions of the simulated (coloured histograms) and observed (black points) visible energy and the number of reconstructed decay electrons in the neutrino multiring ν_e -like sample. The regions of accepted events are indicated by the blue arrows. Reproduced from Ref. [145].

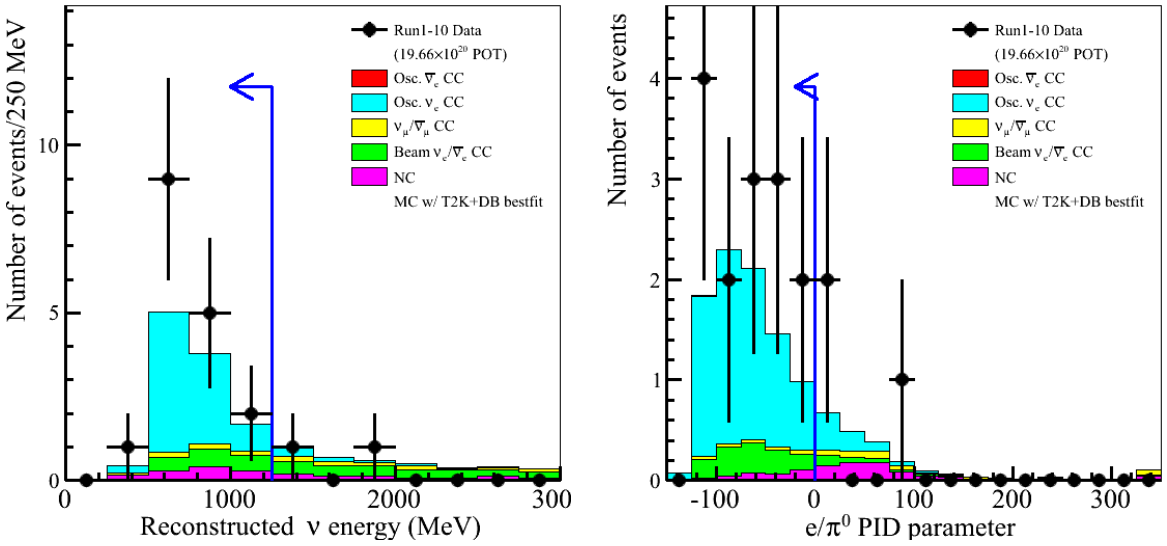

(a) Reconstructed neutrino energy.

(b) ν_e/π^0 PID.

Figure 3.31: Distributions of the simulated (coloured histograms) and observed (black points) reconstructed neutrino energy and ν_e/π^0 discrimination PID parameter (defined as the distance from the cut described in Item 6 of Section 3.3.7) in the ν-mode ν_eCC1π^+-like sample. The regions of accepted events are indicated by the blue arrows. Reproduced from Ref. [145].

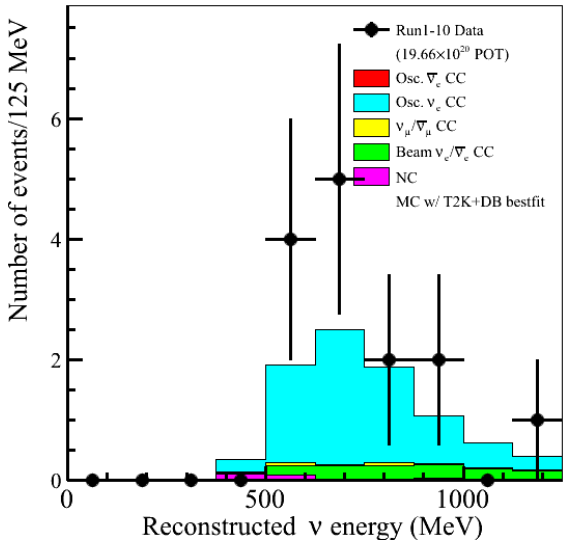

Figure 3.32: Distribution of the simulated (coloured histograms) and observed (black points) reconstructed neutrino energy in the neutrino multiring ν_e -like sample, shown after all selection criteria have been applied. Reproduced from Ref. [145].

Selection Stage	$\nu_\mu + \bar{\nu}_\mu$ CC	$\nu_e + \bar{\nu}_e$ CC	$\nu + \bar{\nu}$ NC	$\nu_\mu \to \nu_e$ CC	$\bar{\nu}_\mu \to \bar{\nu}_e$ CC	MC total	Data
Containment	893.2	57.6	266.5	109.8	1.0	1328.1	1379
No. of Cherenkov rings	392.0	29.6	49.6	93.7	0.8	565.7	550
e vs. μ discrimination	10.7	29.5	32.0	93.6	0.8	166.6	169
Visible energy threshold	3.6	29.4	21.6	92.3	0.8	147.6	145
No. of Michel electrons	1.8	4.1	2.4	8.6	0.0	16.8	20
E_{rec} threshold	0.5	1.4	1.1	7.8	0.0	10.9	17
e vs. π^0 discrimination	0.2	1.2	0.3	7.1	0.0	8.8	14
Efficiency (%)	0.0	2.0	0.1	6.4	0.9	0.7	-
Purity (%)	2.0	13.1	3.8	80.9	0.1	-	-

Table 3.5: The expected and observed number of ν-mode ν_eCC1π^+-like candidate events passing each Super-K selection stage. Predictions are generated using the full T2K Runs 1-10 beam exposure, with normal mass ordering and oscillation parameters set close to previous T2K best fit values: $\Delta m^2_{21} = 7.53 \times 10^{-5}$ eV^2/c^4, $\Delta m^2_{32} = 2.54 \times 10^{-3}$ eV^2/c^4, $\sin^2\theta_{12} = 0.304$, $\sin^2\theta_{13} = 0.0219$, $\sin^2\theta_{23} = 0.550$, and $\delta_{CP} = -1.728$. Adapted from Ref. [145].

3.4 — Super-K Detector and Cross-Section Uncertainties

There are several uncertainties related to vibration analysis that cannot be addressed or constrained by installing a nearby detector. These uncertainties include Super-K detector errors, secondary interaction (SI) effects, and photonuclear effects (PN). While the latter two effects have been explained in detail in Section 3.2.6, the specific effects of the Super-K detector will be discussed in Section 3.4.1.

To account for these uncertainties, covariance matrices are constructed for each group of uncertainties to capture their magnitude and correlations. These matrices are then combined by summing the uncertainties in quadrature, resulting in a single covariance matrix for Super-K. This combined matrix is subsequently used in the oscillation analysis.

To simulate neutrino interactions in Super-K, the NEUT MC generator is employed. Additionally, a dedicated software package called SKDETSIM v13p90 is used to simulate particle propagation within Super-K and to model the effects of the detector.

3.4.1 — Super-K Detector Effects

To generate event samples in Super-K for potential events, a set of selection criteria is applied, which is explained in detail in the 3.3.4 section. However, uncertainties can arise in the variables used for these selection criteria due to the performance of the detector, leading to uncertainties in the event rates for each sample. Due to the complexity of generating Super-K Monte Carlo (MC), it is not feasible to directly incorporate detector errors into the oscillation analysis. Therefore, the combined effect of all detector uncertainties on the predicted event rates in Super-K is considered, and a normalization error is applied to each combination of sample, reaction mode, and kinematics. This approach is further described in [145].

- ν_μ / $\bar{\nu}_\mu$ CCQE-like sample (in both ν and $\bar{\nu}$ modes):
  - True $\overset{(-)}{\nu}_\mu$ CCQE-like events: $E_{\text{rec}} \in [0.0, 0.4], [0.4, 1.1], [1.1, 30]$ GeV bins.
  - True $\overset{(-)}{\nu}_\mu$ CC non-QE-like events for all E_{rec}.
  - True $\overset{(-)}{\nu}_e$ CC events for all E_{rec}.
  - True NC events for all E_{rec}.
- ν_e / $\bar{\nu}_e$ CCQE-like sample (in both ν and $\bar{\nu}$ modes), with the same $E_{\text{rec}} \in [0.0, 0.35], [0.35, 0.8], [0.8, 1.25]$ GeV bins for all reaction modes:
  - True oscillated $\overset{(-)}{\nu}_e$ CCQE-like events.
  - True unoscillated $\overset{(-)}{\nu}_e$ CC events.
  - True $\overset{(-)}{\nu}_\mu$ CC events.
  - True NC events.
- ν-mode ν_eCC1π^+-like sample, with the same $E_{\text{rec}} \in [0.3, 0.8], [0.8, 1.25]$ GeV bins for all reaction modes:

- True oscillated $\overset{(-)}{\nu}_e$ CCQE-like events.
- True unoscillated $\overset{(-)}{\nu}_e$ CC events.
- True $\overset{(-)}{\nu}_\mu$ CC events.
- True NC events.

- ν-mode ν_μCC1π^+-like sample, with the same :
  - True ν_μ CCQE-like events: $E_{\text{rec}} \in [0.0, 0.8], [0.8, 2.0], [2.0, 30]$ GeV bins.
  - True $\overset{(-)}{\nu}_\mu$ CC non-QE-like events: $E_{\text{rec}} \in [0.0, 0.8], [0.8, 2.0], [2.0, 30]$ GeV bins.
  - True $\overset{(-)}{\nu}_\mu$ pion production events: $E_{\text{rec}} \in [0.0, 0.8], [0.8, 2.0], [2.0, 30]$ GeV bins.
  - True $\overset{(-)}{\nu}_e$ CC events for all E_{rec}.
  - True NC events: $E_{\text{rec}} \in [0.0, 1.5], [1.5, 2.5], [2.5, 30]$ GeV bins.

In the aforementioned list, where the ranges of E_{rec} were split, the chosen ranges were designed to cover the region around the peak probability of fluctuations, with a bin on each side of this range (except for the case of ν-mode ν_eCC1π^+-like where no events were observed below the region of maximum probability of fluctuations).

Uncertainties in the detector can be categorized into various contributions, as listed in Table 3.6. The uncertainty associated with each contribution was evaluated using data from the specified controls [78, 145].

Contribution	Uncertainty (%)	Sample used for estimation
Vertex location and track direction	0.3-0.4	Cosmic μ
Michel electron tagging efficiency	1.0	
Fake Michel electron tagging rate	0.2	
Misidentifying μ as e	30	
NCπ^0 rejection efficiency	26	Hybrid π^0
Reconstructed neutrino energy scale	2.13	Cosmic μ and atmospheric π^0
e/μ, e/π^0 & μ/π^+ PID selections and Cherenkov ring counting	(discussed in text)	Atmospheric neutrinos

Table 3.6: Contributions to the Super-K detector uncertainties along with the control samples used to estimate them. Adapted from Refs. [78, 145].

To incorporate the uncertainties arising from the Super-K detector, a covariance matrix is constructed using the methodology outlined in [78]. First, the Monte Carlo (MC) simulation is weighted by the systematic

parameter flow and cross-section values obtained after the Near Detector (ND) tuning, which utilize the total flow and cross-section models described in sections Section 3.1 and Section 3.2, respectively. This differs from the simplified model used for the atmospheric neutrino fit mentioned earlier. The neutrino oscillation probabilities are then applied using the values of $\sin^2\theta_{12}$, Δm^2_{21}, and $\sin^2\theta_{13}$ from the global best fit [124], while the values of $\sin^2\theta_{23}$, $|\Delta m^2_{3j}|$, and δ_{CP} are taken as the most probable values from [146].

Next, the detector errors are randomly sampled one million times, and each of these instances is used to weight the MC predictions and generate event frequency distributions for each kinematic bin discussed earlier in this section. A covariance matrix is constructed from these distributions, where each row/column corresponds to a specific kinematic bin. Finally, the uncertainty associated with the reconstructed energy scale is added to this matrix as an uncorrelated input, as explained earlier.

3.4.2 — Uncertainties in Secondary Interaction and Photonuclear Effects

As discussed in section 3.2.6, secondary pion interactions (SI) and photonuclear effects (PN) can introduce changes in the observed final state topology in Super-K, potentially leading to a bias in the reconstructed neutrino energy. These effects are not solely limited to the next detector but can be better characterized in Super-K due to its higher sensitivity.

The impact of pion SI on the Super-K detector is modeled using a cascade model that incorporates normalization errors associated with the probabilities of each type of pion-nucleus interaction (refer toFig. 3.12). PN interactions are also modeled in the Super-K MC simulation, allowing for the absorption of photons (produced from $\pi^0 \to \gamma\gamma$ decay) without the emission of detectable radiation above the Cherenkov threshold. The cross-section for PN interactions includes a normalization uncertainty of 100% [146].

To account for the uncertainties in the interactions between SI and PN pions, the probabilities of these interactions are randomly varied according to their respective uncertainties. The resulting kinematic distributions are used to construct a covariance matrix, following the same procedure and kinematic binning as described above for the detector uncertainties.

3.4.3 — Combined Uncertainties: Super-K Detector, SI, and PN

The detector covariance matrix and the SI+PN covariance matrix are combined by adding them in quadrature. This results in a single covariance matrix that encompasses all the uncertainties. The combined covariance matrix, as shown in Fig. 3.33, is then used in the jitter analysis, where each row/column of the matrix corresponds to a normalization uncertainty acting on the specified kinematic bins.

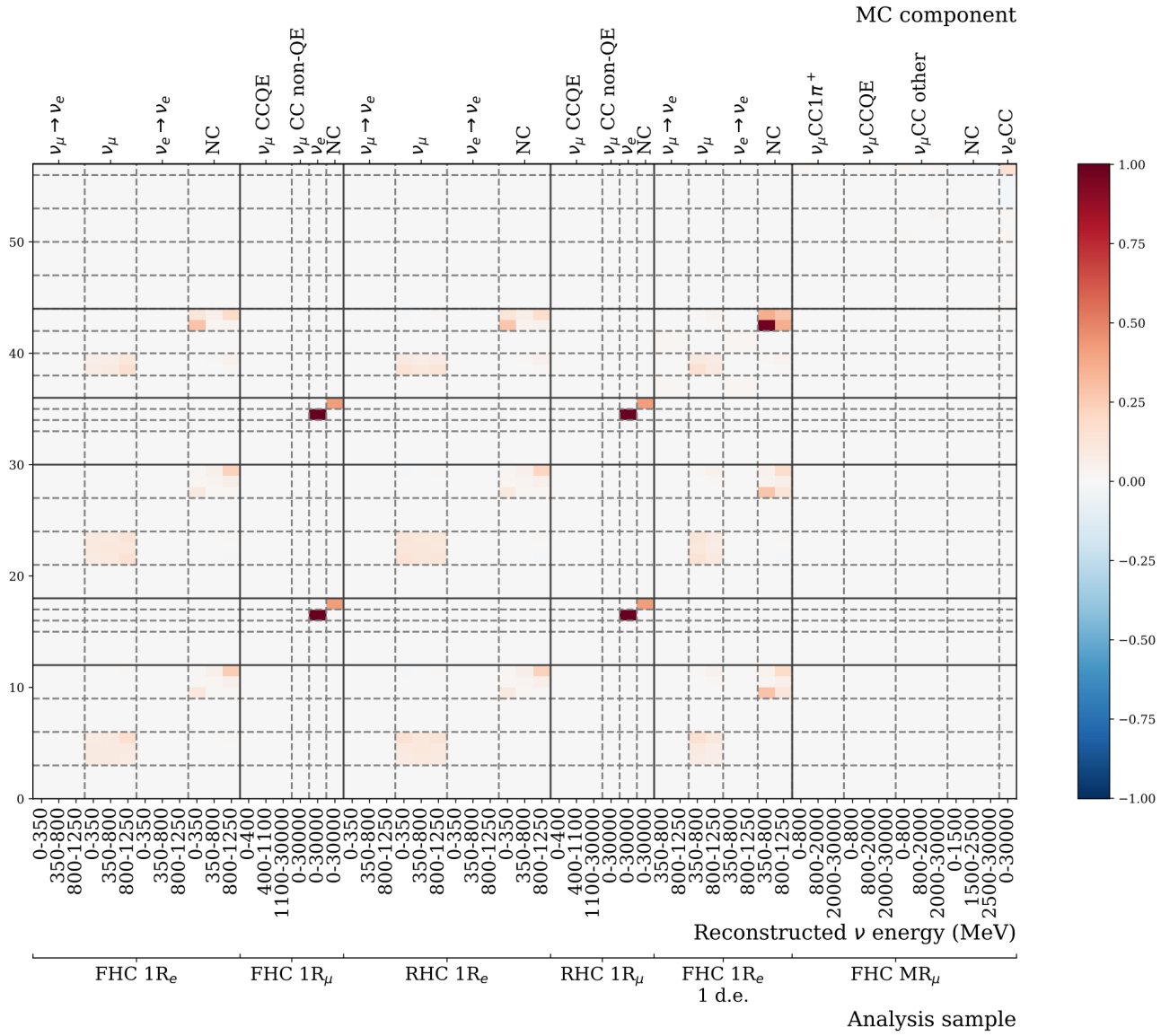

Figure 3.33: The Super-K detector + SI + PN covariance matrix. Reproduced from [17]

4 — Oscillation analysis methodology and implementation

To infer constraints on the oscillation parameters, a frequentist approach is used to generate confidence intervals based on marginal log-likelihood ratios. This is done by simultaneously analyzing the kinematic distributions of the five Super-K event samples, taking into account the rate and shape while also accounting for systematic uncertainties in the flux, interaction, and detector models. Systematic uncertainties are accounted for using systematic parameters, which weight the nominal MC prediction while considering their relative uncertainties and prior constraints. The evaluation of the marginal likelihood of a given physics hypothesis and construction of confidence intervals are explained in this section. Further details on the analysis procedure can be found in [147].

4.1 — Evaluation of a hypothesis Likelihood

To assess the probability of a given set of oscillation parameters, it is necessary to create binned expected kinematic distributions for those parameters and compare them to the observed distributions. This subsection begins by discussing the process for creating the expected distributions before demonstrating how the likelihood and marginal likelihoods are computed.

4.1.1 — Generating Expected Kinematic Distributions

The kinematic distributions predicted and observed for each sample are binned into reconstructed neutrino energy, E_{rec}, for the μ-like samples, and both E_{rec} and reconstructed lepton angle, θ, for the e-like samples. The specific bin edges used are further described in section Moreover, each sample is separated into several true reaction modes (a combination of neutrino-nucleus interaction mode and initial and final neutrino flavor), listed in section

The predicted number of events in the r^{th} reconstructed bin, which is a two-dimensional (E_{rec}, θ) bin, for the s^{th} Super-K sample is generated according to 4.1, where each contributing term is explained as follows:

$$N^{\text{exp}}\left(\vec{o}, \vec{f}, s, r\right) = \sum_{m} \sum_{t} \sum_{r\prime} P\left(\vec{o}, m, t\right) \cdot T\left(f^{SK}_{E;r}, r, r\prime\right) \cdot S\left(\vec{f}, m, t, r\prime\right) \cdot N^{MC}\left(s, m, r\prime, t\right) \tag{4.1}$$

- $N^{MC}\left(s, m, r\prime, t\right)$ is the binned input nominal predicted number of Super-K events in the MC sample, with true reaction mode m in the true neutrino energy bin t and the reconstructed bin $r\prime$. This is referred to as the 'MC template' and is produced without oscillation probabilities applied, with systematic parameters applied at their nominal 'generated' values, and is normalised to the collected exposure in each event sample.

- $S\left(\vec{f}, m, t, r\prime\right)$ is an overall, multiplicative, systematic error factor depending on a vector of systematic parameters, $\vec{f}$, each of which may be a function of the reaction mode m, the true energy bin t and the reconstructed bin $r\prime$. The choice of systematic parameters is dependant on the uncertainties present in the flux, interaction, and detector models used to produce the nominal MC.

- $T\left(f^{SK}_{E;r}, r, r\prime\right)$ is a transfer function describing the migration of events between the reconstructed bins r and $r\prime$ due to uncertainty in the Super-K reconstructed energy scale, expressed here in terms of the systematic parameter $f^{SK}_{E;r}$.

- $P\left(\vec{o}, m, t\right)$ is the three-flavour oscillation probability with matter effects evaluated with expected oscillation parameters, $\vec{o}$, and at the centre of the true energy bin t containing Super-K MC events corresponding to mode m. This is not applied to events corresponding to NC interactions, as these interactions do not depend on the relative proportions of each neutrino flavour. The oscillation probability is computed within VALOR using a bespoke calculator following the numerical method described in Section 3.1 of Ref [148].

The product of these quantities are summed over all bins corresponding to MC truth information to obtain $N^{\text{exp}}\left(\vec{o}, \vec{f}, s, r\right) = \sum_{m,t,r\prime} N^{MC}\left(s, m, r\prime, t\right) \cdot S\left(\vec{f}, m, t, r\prime\right) \cdot T\left(f^{SK}_{E;r}, r, r\prime\right) \cdot P\left(\vec{o}, m, t\right)$, and thus the expected kinematic distributions, which are explicitly a function of reconstructed quantities only, and are therefore directly comparable to the observed kinematic distributions.

4.1.2 — Construction of the Likelihood

The Poisson log-likelihood ratio is computed for the expected kinematic distribution based on the observed kinematic distribution in each sample. The data is denoted by D.

$$-2\ln\lambda_s\left(\mathrm{D} \mid \vec{o}, \vec{f}\right) = 2\sum_r \left[N_r^{\text{obs}} \cdot \ln\left(\frac{N_r^{\text{obs}}}{N_r^{\text{exp}}}\right) + N_r^{\text{exp}} - N_r^{\text{obs}}\right] \tag{4.2}$$

where λ_s is the likelihood ratio in a given sample, $N_r^{\text{exp}} \equiv N^{\text{exp}}(\vec{o}, \vec{f}, s, r)$ of Eq. (4.1) is the expected number of events in a kinematic bin, and $N_r^{\text{obs}} \equiv N^{\text{obs}}(s, r)$ is the observed number of data events in the same kinematic bin. Here, 'data' can refer to either real data collected by the T2K experiment, or pseudo-data containing an integer number of events generated from an assumed set of true oscillation and systematic parameter values.

The total log-likelihood is calculated as follows:

$$\lambda\left(\mathrm{D} \mid \vec{o}, \vec{f}\right) = \prod_s \lambda_s\left(\mathrm{D} \mid \vec{o}, \vec{f}\right) \tag{4.3}$$

The total likelihood of Eq. (4.3) is dependant on both the systematic and oscillation parameters, but it is desirable for the resulting confidence regions to be a function of the oscillation parameters only. Additionally, producing a confidence region as a function of *all* oscillation parameters would be computationally intractable, so instead multiple confidence regions are produced, each corresponding to at most two oscillation parameters, plus the mass ordering. These are denoted as the 'parameters of interest', $\vec{o}_I$, while all other $N_f = \mathcal{O}(100)$ oscillation and systematic parameters are treated as 'nuisance parameters', $\vec{f}'$, and are eliminated by converting the total likelihood into the marginal likelihood, λ_{marg}. This is calculated as in Eq. (4.4) by integrating the product of the total likelihood and the (analysis-specific) nuisance parameter prior PDFs, π, over the corresponding parameter space, F'.

$$\lambda_{\text{marg}}\left(\mathrm{D} \mid \vec{o}_I\right) = \int_{F'} \lambda\left(\mathrm{D} \mid \vec{o}, \vec{f}\right) \cdot \pi\left(\vec{f}'\right) d^{N_f}\vec{f}' = \frac{1}{n}\sum_{i=1}^{n} \lambda\left(\mathrm{D} \mid \vec{o}_I, \vec{f}_i'\right) \tag{4.4}$$

In practice, this integration is performed numerically by randomly drawing n sets of nuisance parameters, as in the right-hand side of Eq. (4.4), with correlations between systematic parameters accounted for using Cholesky decomposition [149] of their respective covariance matrices .Many (typically $\geq 10^4$) randomly drawn sets of $\vec{f}'$ are required to adequately sample F', with n being chosen for each analysis based on the number of nuisance parameters and how tightly constraining each prior PDF is. The space F' is regarded as being adequately sampled if the resulting confidence regions do not significantly change when different sets of n independent random samples are instead used. Additionally, any $\vec{f}'$ which either results in a negative number of events or sets any parameters outside of their physical ranges is re-thrown.

4.2 — Construction of Confidence Regions

The previous subsection described the construction of the marginal likelihood for a fixed set of values for the parameter(s) of interest, $\vec{o}_I$; however, the objective is to construct confidence regions on the allowed values of these parameters. So, the marginal likelihood of Eq. (4.4) is evaluated at a number of evenly spaced 'grid points' in the space of $\vec{o}_I$, chosen to balance the resolution of the resulting best fit points and confidence intervals against computational feasibility. Then, the ratio to the maximum marginal likelihood across all grid points, $\lambda_{\text{marg}}^{\text{max}}$, is taken, and the coordinates of this grid point are taken to be the best fit point, $\vec{o}_{I,\text{bf}}$. The n randomly drawn sets of nuisance parameters used in calculating the marginal likelihood are the same across all grid points, so that only the parameters of interest change between grid points.

As described by Wilks' theorem [150], in the large sample limit, the negative log-likelihood ratio asymptotically tends towards a χ^2 distribution, and for brevity will hereafter be denoted $\Delta\chi^2$, defined in Eq. (4.5). This quantity is the test statistic used to construct confidence regions by finding all grid points for which Eq. (4.6) is satisfied, where $\Delta\chi^2_{\text{crit}}$ denotes the critical value at the $X\%$ confidence level.

$$\Delta\chi^2 \equiv \Delta\chi^2\left(\mathrm{D} \mid \vec{o}_I\right) = -2\ln\left[\frac{\lambda_{\mathrm{marg}}\left(\mathrm{D} \mid \vec{o}_I\right)}{\lambda_{\mathrm{marg}}^{\mathrm{max}}\left(\mathrm{D} \mid \vec{o}_{I,\mathrm{bf}}\right)}\right] \tag{4.5}$$

$$\Delta\chi^2 < \Delta\chi^2_{\mathrm{crit}}\left(\vec{o}_I, X\right) \tag{4.6}$$

Two different methods are used to evaluate the critical values. Typically, the critical values do not depend on the parameter(s) of interest and are pre-computed as the critical values of the χ^2 distribution [149]. This is known as the constant $\Delta\chi^2$ method, and in this analysis, will be used to produce confidence regions for all oscillation parameters except for 1D δ_{CP}. The constant $\Delta\chi^2$ method is applicable only when Wilks' theorem holds, and otherwise may give incorrect coverage. This is the case for δ_{CP}, where its cyclic nature and the presence of physical boundaries (in the event rates) at $\delta_{CP} = \pm\frac{\pi}{2}$ results in incorrect coverage, as has been observed in previous T2K analyses [78,151]. This is also the case, albeit to a lesser extent, for $\sin^2\theta_{23}$, where the boundary corresponding to maximal ν_μ disappearance has been shown to adversely affect the coverage [152]. To account for this, a second method is used where the critical values at each grid point are determined numerically, and is referred to as the 'Feldman-Cousins' (FC) method, as described in Ref [153]. This method is computationally intensive to a nearly prohibitive extent, so is used only for the main result of this analysis, the 1D δ_{CP} confidence regions, and with a coarser grid of points than that used for the calculation of the marginal likelihood.

The procedure for calculating Feldman-Cousins critical values as a function of δ_{CP} and mass ordering is as follows. A number of grid points are defined in the range $\delta_{CP} = [-\pi, +\pi]$ and in each mass ordering. At all points, critical values are calculated as follows and collated to form $\Delta\chi^2_{\mathrm{crit}}\left(\vec{o}_I, X\right)$:

1. In order to provide the correct coverage, many (typically $> 10^4$) ensembles of expected kinematic distributions are generated at each grid point, each produced assuming the δ_{CP} and mass ordering of the grid point and accounting for both statistical and nuisance parameter uncertainties, as follows. The resulting expected kinematic distributions have integer event rates and are referred to as 'pseudo-experiments'.

   (a) To account for uncertainties in the nuisance parameters during the generation of each pseudo-experiment, these parameters are randomly sampled according to the same prior PDFs as used in the marginalisation method. The exception to this is for the 'atmospheric' parameters $\sin^2\theta_{23}$ and Δm^2_{3j}, where the T2K constraint on these parameters is incorporated into the constraint on δ_{CP} as prior knowledge by randomly drawing the atmospheric parameters from the marginal likelihood distribution resulting from a simultaneous fit to a simulated data set with the following true values (see): $\sin^2\theta_{12}$ and Δm^2_{12} taken from global fits, and $\sin^2\theta_{23}$, Δm^2_{3j}, $\sin^2\theta_{13}$ and δ_{CP} equal to the best fit points from the fit to T2K data. This treatment of the atmospheric parameters is used instead of taking the marginal likelihood distribution directly from the T2K data fit, as such a method would cause the critical values close to the best fit value of δ_{CP} to become smaller due to the generated pseudo-experiments artificially corresponding more closely to the observed data, shrinking the confidence region.

(b) The randomly selected nuisance parameter values are taken together with the parameter of interest values and are used to generate kinematic distributions according to Section 4.1.1.

(c) To account for statistical uncertainties during the generation of each pseudo-experiment, the event rates in each kinematic bin are randomly fluctuated according to a Poisson distribution with mean equal to the un-fluctuated event rate.

2. For each pseudo-experiment, a test statistic value is calculated as follows:

(a) The pseudo-experiment is marginalised with respect to all parameter of interest grid points used for the data fit (see Table 4.7) and $\lambda_{\text{marg}}\left(\text{E} \mid \vec{o}_I\right)$ is calculated, where E denotes a pseudo-experiment.

(b) The marginal likelihood at the $\vec{o}_I$ corresponding to the true grid point, $\lambda_{\text{marg}}\left(\text{E} \mid \vec{o}_{I,\text{true}}\right)$, is extracted.

(c) The marginal likelihood maximised across all $\vec{o}_I$ (i.e. across both δ_{CP} and mass orderings), $\lambda^{\text{max}}_{\text{marg}}\left(\text{E} \mid \vec{o}_{I,\text{bf}}\right)$, is extracted.

(d) The test statistic, $\Delta\chi^2_{\text{FC}}$ is calculated according to Eq. (4.7). This is analogous to the test statistic used for the constant $\Delta\chi^2$ method (see Eq. (4.5)), but here a pseudo-experiment takes the place of the observed data, and due to $\vec{o}_{I,\text{true}}$ being known for pseudo-experiments, $\Delta\chi^2_{\text{FC}}$ is a fixed value rather than having explicit $\vec{o}_I$ dependence.

$$\Delta\chi^2_{\text{FC}} = -2\ln\left[\frac{\lambda_{\text{marg}}\left(\text{E} \mid \vec{o}_{I,\text{true}}\right)}{\lambda^{\text{max}}_{\text{marg}}\left(\text{E} \mid \vec{o}_{I,\text{bf}}\right)}\right] \tag{4.7}$$

3. A probability density distribution of $\Delta\chi^2_{\text{FC}}$, $f\left(\Delta\chi^2_{\text{FC}}\right)$, is formed from all pseudo-experiments at this grid point.

4. Critical values at the $X\%$ confidence level, $\Delta\chi^2_{\text{crit}} \equiv \Delta\chi^2_{\text{crit,FC}}\left(\vec{o}_{I,\text{true}}, X\right)$, are then defined as

$$\Delta\chi^2_{\text{crit,FC}} : \int_0^{\Delta\chi^2_{\text{crit,FC}}} f\left(\Delta\chi^2_{\text{FC}}\right) d\left(\Delta\chi^2_{\text{FC}}\right) = X\% \tag{4.8}$$

4.3 — Summary of Analysis Inputs and Implementation Choices

4.3.1 — Beam Exposure

This analysis is performed using Super-K data from the full T2K Run 1-10 data collection period (see Section 2.1), corresponding to beam exposures of 1.97×10^{21} POT and 1.63×10^{21} POT in ν and $\bar{\nu}$ modes, respectively. Systematic parameters are constrained using the fit to near detector data described in Section Section 3.3, using T2K Run 2-9 data, corresponding to exposures of 1.50×10^{21} POT and 0.83×10^{21} POT in ν and $\bar{\nu}$ modes, respectively. These data sets are used at the near detectors because the barrel ECAL had not yet been installed during T2K Run 1 and the Run 10 data has not yet been analysed at the near detectors.

4.3.2 — Reaction Modes

The neutrino-nucleus interaction model is as described in Section 3.2. In brief, interactions are simulated by a NEUT MC simulation using the following base models: the nuclear ground state model for CCQE interactions uses the Benhar Spectral Function model [79]; 2p2h interactions are modelled according to Nieves et al. [154]; pion production is modelled according to the Rein-Sehgal [102] model, with a NEUT Cascade model describing pion SI and FSI; DIS interactions are modelled using the GRV98 [119] parton distribution functions, with modifications to the low-Q^2 region according to Bodek and Yang [120]. All of which have been tuned to external data [75, 76].

68 true reaction modes (neutrino-nucleus interaction type + initial and final neutrino flavours) are used in the analysis to categorise Super-K MC events. The majority of the energy range spanned by the T2K flux is below the threshold for τ or $\bar{\tau}$ production, so charged current (CC) reaction modes involving ν_τ or $\bar{\nu}_\tau$ are neglected. Additionally, for the neutral current (NC) reaction modes, $\overset{(-)}{\nu}_\alpha$ is taken as being a mixture of $\overset{(-)}{\nu}_\mu + \overset{(-)}{\nu}_e + \overset{(-)}{\nu}_\tau$ as a result of oscillations, so to avoid double-counting, no corresponding oscillated reaction modes are used. Also, no NCQE or NC2p2h reaction modes are considered, as these are effectively elastic neutrino-nucleus scatters and would not be visible in Super-K. The reaction modes considered in this analysis are as follows:

- 6 CC quasi-elastic interactions (CCQE);
  $\nu_\mu , \bar{\nu}_\mu , \nu_e , \bar{\nu}_e , \nu_\mu \rightarrow \nu_e , \bar{\nu}_\mu \rightarrow \bar{\nu}_e$
- 6 CC two particle two hole interactions (CC2p2h);
  $\nu_\mu , \bar{\nu}_\mu , \nu_e , \bar{\nu}_e , \nu_\mu \rightarrow \nu_e , \bar{\nu}_\mu \rightarrow \bar{\nu}_e$
- 6 CC single neutral pion resonant production (CC1π^0);
  $\nu_\mu , \bar{\nu}_\mu , \nu_e , \bar{\nu}_e , \nu_\mu \rightarrow \nu_e , \bar{\nu}_\mu \rightarrow \bar{\nu}_e$
- 6 CC single charged pion resonant production (CC1$\pi^\pm$);
  $\nu_\mu , \bar{\nu}_\mu , \nu_e , \bar{\nu}_e , \nu_\mu \rightarrow \nu_e , \bar{\nu}_\mu \rightarrow \bar{\nu}_e$
- 6 CC coherent pion production (CCcoh);
  $\nu_\mu , \bar{\nu}_\mu , \nu_e , \bar{\nu}_e , \nu_\mu \rightarrow \nu_e , \bar{\nu}_\mu \rightarrow \bar{\nu}_e$
- 6 CC multiple pion production (CCmulti-π);
  $\nu_\mu , \bar{\nu}_\mu , \nu_e , \bar{\nu}_e , \nu_\mu \rightarrow \nu_e , \bar{\nu}_\mu \rightarrow \bar{\nu}_e$
- 6 CC deep inelastic scattering (CCDIS);
  $\nu_\mu , \bar{\nu}_\mu , \nu_e , \bar{\nu}_e , \nu_\mu \rightarrow \nu_e , \bar{\nu}_\mu \rightarrow \bar{\nu}_e$
- 6 Groups of miscellaneous CC processes (CCmisc);
  $\nu_\mu , \bar{\nu}_\mu , \nu_e , \bar{\nu}_e , \nu_\mu \rightarrow \nu_e , \bar{\nu}_\mu \rightarrow \bar{\nu}_e$
- 4 NC single neutral pion production (NC1π^0); $\nu_\mu , \bar{\nu}_\mu , \nu_e , \bar{\nu}_e$

- 4 NC single charged pion production (NC1$\pi^{\pm}$); ν_μ , $\bar{\nu}_\mu$, ν_e , $\bar{\nu}_e$
- 4 NC coherent interactions (NCcoh); ν_μ , $\bar{\nu}_\mu$, ν_e , $\bar{\nu}_e$
- 4 NC single gamma production (NC1γ); ν_μ , $\bar{\nu}_\mu$, ν_e , $\bar{\nu}_e$
- 4 Groups of miscellaneous NC processes (NCmisc); ν_μ , $\bar{\nu}_\mu$, ν_e , $\bar{\nu}_e$

In the above list of reaction modes, the following CC processes form the 'miscellaneous' category: CC1K, CC1η, CC diffractive pion production, and CC1γ. The NC miscellaneous category is formed of the equivalent NC processes, in addition to NC multiple pion production and NC DIS, and without NC1γ, which is tracked separately. Processes that are neither listed here nor in the above list are not tracked in the NEUT MC simulation.

4.3.3 — Kinematic Binning

The expected and observed kinematic distributions share the same binning schemes. They are binned in E_{rec}, for the μ-like samples, and (E_{rec}, θ) for the e-like samples, as specified in Tables 4.1 to 4.3. As mentioned in Section 4.1.1, the Super-K MC events are placed into MC templates binned in $(E_{\text{true}}, E_{\text{rec}}, \theta)$ before being summed over E_{true} bins. This E_{true} binning is the same for all samples and is specified in Table 4.4.

The μ-like samples are binned in E_{rec} up to 30 GeV, after which the neutrino flux is negligible. The e-like samples are only binned up to 1.25 GeV, as beyond this energy, the flux is primarily composed of NC and the intrinsic unoscillated ν_e and $\bar{\nu}_e$ components of the beam [145].

The binning schemes have been optimised (as described in Appendix I of Ref. [141]) to balance sensitivity to the oscillation parameters against computational requirements while ensuring a non-negligible number of events in each bin of the kinematic distributions.

The e-like samples include multiple θ bins for the following reasons. Measurements of both neutrinos and antineutrinos are required to effectively measure δ_{CP}, so it is important to separate $\nu_\mu \rightarrow \nu_e$ and $\bar{\nu}_\mu \rightarrow \bar{\nu}_e$ flavour components. As shown in Figs. 4.1 and 4.3, while the ν-mode and $\bar{\nu}$-mode ν_e / $\bar{\nu}_e$ CCQE-like samples appear similar in E_{rec} their shape is clearly different in θ.

4.3.4 — Treatment of Systematic and Oscillation Parameters

A total of 137 systematic parameters are incorporated into the analysis to account for the effects of systematic uncertainties in the flux, detector and interaction models. These are detailed in Chapter A. All systematic parameters are randomised (accounting for correlations) when computing the marginal likelihood of Eq. (4.4), using a multivariate Gaussian prior PDF as defined by two covariance matrices, with the only exceptions being the 2p2h energy dependence parameters $\left(f^{\text{ND}}_{Shape_{2p2hLowE\nu}}, f^{\text{ND}}_{Shape_{2p2hHghE\nu}}, f^{\text{ND}}_{Shape_{2p2hLowE\bar{\nu}}}, f^{\text{ND}}_{Shape_{2p2hHighE\bar{\nu}}}\right)$, which use uniform prior PDFs due to a lack of constraint from both the near d etectors and external data (see Section 3.2.3). These covariance matrices are the near detector matrix (see Section Section 3.3), characterising flux and cross-section systematic parameters, and the Super-K matrix (see Section 3.4), charactering detector effects in Super-K as well as secondary interactions (SI) and the photonuclear effect (PN).

Range	Single Bin Width	Number of Bins
$0 - 3$ GeV	0.05 GeV	60
$3 - 4$ GeV	0.25 GeV	4
$4 - 6$ GeV	0.5 GeV	4
$6 - 10$ GeV	1 GeV	4
$10 - 30$ GeV	20 GeV	1
$0 - 180°$	$180°$	1

Table 4.1: (E_{rec}, θ) binning scheme used for both expected and observed kinematic distributions in the ν-mode and $\bar{\nu}$-mode ν_μ / $\bar{\nu}_\mu$ CCQE-like samples. There are a total of 73 E_{rec} and 1 θ bins.

Range	Single Bin Width	Number of Bins
$0 - 1.25$ GeV	0.05 GeV	25
$0 - 140°$	$10°$	14
$140 - 180°$	$40°$	1

Table 4.2: (E_{rec}, θ) binning scheme used for both expected and observed kinematic distributions in the ν-mode and $\bar{\nu}$-mode ν_e / $\bar{\nu}_e$ CCQE-like samples. There are a total of 25 E_{rec} and 15 θ bins.

Range	Single Bin Width	Number of Bins
$0 - 0.4$ GeV	0.4 GeV	1
$0.4 - 0.55$ GeV	0.15 GeV	1
$0.55 - 1.25$ GeV	0.1 GeV	7
$0 - 180°$	$60°$	3

Table 4.3: (E_{rec}, θ) binning scheme used for both expected and observed kinematic distributions in the ν-mode ν_eCC1π^+-like sample. There are a total of 9 E_{rec} and 3 θ bins.

Range (GeV)	Single Bin Width (GeV)	Number of Bins
$0.0 - 0.3$	0.05	6
$0.3 - 1$	0.025	28
$1 - 3$	0.05	40
$3 - 3.5$	0.1	5
$3.5 - 4$	0.5	1
$4 - 5$	1	1
$5 - 7$	2	1
$7 - 10$	3	1
$10 - 30$	20	1

Table 4.4: E_{true} binning scheme used in all samples to bin Super-K MC events. There are a total of 84 E_{true} bins.

Oscillation parameters are randomised according to the prior PDFs defined in Table 4.5. T2K has little sensitivity to θ_{12} and Δm^2_{21}, so these parameters are constrained with Gaussian prior PDFs from the PDG2019 global fit average ($\sin^2 2\theta_{12} = 0.851 \pm 0.020$ and $\Delta m^2_{21} = [7.53 \pm 0.18] \times 10^{-5}$ eV^2/c^4) [124]. As T2K is sensitive to $\sin^2\theta_{23}$, $|\Delta m^2_{3j}|$, and δ_{CP}, uniform prior PDFs spanning the entire range of these parameters would be applicable, although in practice their parameter space is sampled in reduced ranges (as listed in Table 4.5). This is done in order to maintain efficiency (adequately sampling the full ranges requires a computationally-intractable number of samples), while ensuring that reducing these ranges does not alter the results.

T2K is sensitive to and produces constraints on θ_{13}; however, the world's most accurate measurements of this parameter are from reactor antineutrino experiments (see Section 1.3). So, to better constrain this parameter and obtain increased sensitivity to other parameters, the PDG2019 global fit [124] reactor average of 0.0853 ± 0.0027 is used as a prior PDF on $\sin^2 2\theta_{13}$ for most measurements presented in the Chapter 5. This prior PDF will subsequently be referred to as the 'gaussian reactor constraint' and constraints produced with it will be denoted 'T2K with gaussian reactor constraint'.

As discussed in Section 4.1.2, the interference parameter space is chosen randomly to calculate the marginal probability and that the number of samples depends on the dimension this space and how severely it is limited by previous PDFs. Therefore the number Random samples vary depending on the number of parameters of interest and whether the reactor limit is applied or not applied as shown in Table 4.6. The marginal probability is estimated at various grid points in the parameter space of interest. as specified in Table 4.7.

Parameter(s)	Prior PDF	Range
$\sin^2\theta_{23}$	Uniform	$[0.3, 0.7]$
$\sin^2\theta_{13}$ T2K-only	Uniform	$[0, 0.4]$
$\sin^2 2\theta_{13}$ reactors	Gaussian	0.0853 ± 0.0027
$\sin^2 2\theta_{12}$	Gaussian	0.851 ± 0.020
$\lvert\Delta m^2_{3j}\rvert$	Uniform	$[2.3, 2.7] \times 10^{-3}$ eV^2/c^4
Δm^2_{21}	Gaussian	$(7.53 \pm 0.18) \times 10^{-5}$ eV^2/c^4
δ_{CP}	Uniform	$[-\pi, +\pi]$
Mass Ordering	Fixed	NO or IO

Table 4.5: Oscillation parameters prior PDFs used in the T2K Run 1-10 oscillation analysis. All Gaussian priors are from [124].

Number of Parameters of Interest	With Reactor Constraint	Without Reactor Constraint
1	4×10^4	8×10^4
2	1×10^4	2×10^4

Table 4.6: The number of randomly drawn samples of the nuisance parameter space used to compute the marginal likelihood, varying with the number of parameters of interest and whether the constraint on $\sin^2 2\theta_{13}$ from reactor experiments is used.

Parameter(s) of interest	Number of Points	Range
$\sin^2\theta_{23}$	101	$[0.3, 0.7]$
$\sin^2\theta_{13}$ T2K-only	101	$[0.007, 0.053]$
$\lvert\Delta m^2_{3j}\rvert$	101	$[2.2, 2.8] \times 10^{-3}$ eV^2/c^4
δ_{CP}	101	$[-\pi, \pi]$
$\sin^2\theta_{23}$, $\lvert\Delta m^2_{3j}\rvert$	81×51	$[0.3, 0.7]$, $[2.2, 2.8] \times 10^{-3}$ eV^2/c^4
$\sin^2\theta_{13}$, δ_{CP} T2K-only	81×51	$[0.007, 0.053]$, $[-\pi, \pi]$
$\sin^2\theta_{13}$, δ_{CP} T2K+reactor	81×51	$[0.015, 0.036]$, $[-\pi, \pi]$

Table 4.7: The grid points used to evaluate the marginal likelihood as a function of the parameter(s) of interest. The grid points are evenly spaced within the specified ranges.

To determine the expected frequency of events, kinematic distributions and sensitivities, various sets of simulated pseudodata are used, each is called an "Asimov" data set. They are generated using an assumed set of fixed oscillations and systematic values of the parameters and without statistical fluctuations. Asimov data sets are used as representative data in to determine the average sensitivity to oscillation parameters without the need to generate large numbers pseudodata sets. Asimov data sets are called "Asimov A". and the values of the oscillation parameters are selected as follows and summarized in Table 4.8. Systematic parameters are set at their nominal values.

Asimov A - Central values of the global fit PDG2019 averages are used for $\sin^2 2\theta_{12}$, Δm^2_{21}, and $\sin^2 2\theta_{13}$, while for other oscillation parameters the most probable values are from T2K Run 1-4 ν-mode Bayesian analysis [146] is used (which remains close to the best recent T2K). appropriate values [92]). In particular, the Asimov A data set corresponds to almost the maximum Violation of CP and the value $\sin^2\theta_{23}$ in the upper octant. the purpose of this the data set is designed to evaluate expected results close to the most likely parameter values (as indicated by the above T2K results), before revealing the observed data.

Parameter(s)	Asimov A	Asimov B	Asimov BF NO	Asimov BF IO
$\sin^2\theta_{23}$	0.528	0.45	0.552	0.556
$\sin^2\theta_{13}$ reactors	0.0218	0.0218	0.0218	0.0221
$\sin^2\theta_{12}$	0.307	0.307	0.307	0.307
$\lvert\Delta m^2_{3j}\rvert$ $\left(10^{-3}\ \mathrm{eV}^2/\mathrm{c}^4\right)$	2.51	2.51	2.49	2.46
Δm^2_{21} $\left(10^{-5}\ \mathrm{eV}^2/\mathrm{c}^4\right)$	7.53	7.53	7.53	7.53
δ_{CP}	-1.60	0	-2.01	-1.38
Mass Ordering	Normal	Normal	Normal	Inverted

Table 4.8: Four sets of Asimov oscillation parameters values used to compute expected event rates and kinematic distributions. The Asimov A and B parameter sets are used to evaluate the sensitivity of T2K to the oscillation parameters before un-blinding the data. The Asimov BF NO/IO sets use the best-fit points from fits to the T2K Run 1-10 data for all oscillation parameters except for $\sin^2\theta_{12}$ and Δm^2_{12}, for which the PDG2019 [124] global best-fit vales are used. The Asimov BF NO/IO sets are used to calculate Feldman-Cousins critical values (see Section 4.1.2).

4.4 — Predicted Kinematic Distributions and Event Rates

This section presents the expected kinematic distributions and event rates. Unless otherwise stated, all forecasts are generated using the Asimov A parameters shown. in Table 4.8 (because Asimov A values are closer to previous T2K best fit values than Asimov B values) and with full exposure to the T2K Run 1-10 beam. In addition, the impact of systematic uncertainties in such forecasts be discussed

Figures 4.2 and 4.3 displays non-oscillating kinematic distribution and predicted by Azimov A, respectively. Comparison of these distributions clearly shows the "failure" of fluctuations near the flux peak in samples similar to μ corresponding to the disappearance of $\overset{(-)}{\nu}_{\mu}$, and samples similar to e show a corresponding increase in events from the appearance of $\overset{(-)}{\nu}_{e}$. Furthermore, in the samples of ν_e / $\bar{\nu}_e$ CCQE-like in dimension θ, there is a clear separation of $\nu/\bar{\nu}$, as shown Fig. 4.1. While samples like μ extend up to E_{rec} = 30 GeV, these graphs only show up to 3 GeV to highlight the regions of highest probability of oscillations, but the full range used in probability calculations.

Integrating the kinematic distributions over E_{rec} and θ gives overall event rate for each sample. They are shown for the four predicted swings. pseudo datasets and observed data from T2K Run 1-10 in Table 4.9. In addition, this is shown broken down by the contributions of the individual reaction modes. for Asimov's prediction on Tables B.1 to B.5. As Table 4.9 shows, T2K can clearly distinguish between no hesitation and Asimov A set of pseudodata and, as shown in Section 1.3, it is convincingly shown that neutrinos oscillate,

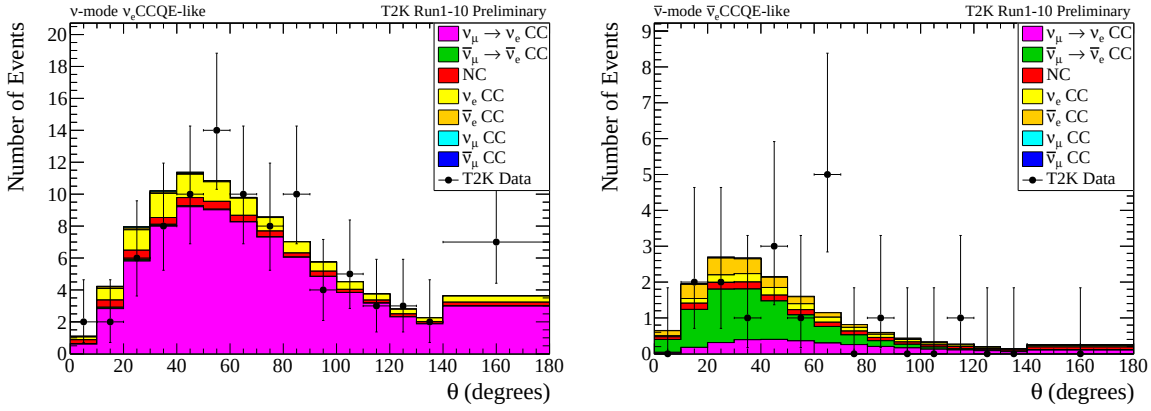

(a) ν-mode ν_e / $\bar{\nu}_e$ CCQE-like sample.

(b) $\bar{\nu}$-mode ν_e / $\bar{\nu}_e$ CCQE-like sample.

Figure 4.1: θ projections of the Asimov A predicted kinematic distributions (coloured histograms) shown in Figs. 4.3c and 4.3d, compared to observed kinematic distributions (black or white/blue points). Predictions are generated with the Asimov A oscillation parameter values in Table 4.8, nominal values of the systematic parameters, and are normalised to the T2K Run 1-10 beam exposure. The uncertainty shown around the data points on the 1D plots accounts for statistical uncertainty only. The uncertainty range is chosen to include all points for which the measured number of data events is inside the 68% confidence interval of a Poisson distribution centred at that point.

therefore, the case of the absence of oscillations will not be considered further in the dissertation.

Sample		Predicted Asimov Hypothesis				Observed
		No osc.	A	B	BF NO	
ν-mode	ν_μ / $\bar{\nu}_\mu$ CCQE-like	1571.4	345.5	361.8	354.0	318
	ν_e / $\bar{\nu}_e$ CCQE-like	19.6	93.8	69.8	95.2	94
	ν_eCC1π^+-like	2.9	8.8	6.8	8.9	14
$\bar{\nu}$-mode	ν_μ / $\bar{\nu}_\mu$ CCQE-like	444.5	135.1	138.8	137.9	137
	ν_e / $\bar{\nu}_e$ CCQE-like	6.3	15.9	16.4	16.9	16
Best-fit $-2\ln\lambda$		-	8.4	8.6	8.2	476.2

Table 4.9: Predicted and observed event rates in each sample, using the full T2K Run 1-10 beam exposure and data. Four different hypotheses have been used to generate the predictions: no neutrino oscillations, the Asimov A and B oscillation parameter sets defined in Table 4.8, and an Asimov parameter set with true values equal to the T2K Run 1-10 best fit values (Asimov BF NO) from Table 5.3. Also shown are the best-fit $-2\ln\lambda$ values for the predicted and observed data, with a detailed discussion of the agreement between data and prediction following in **??**.

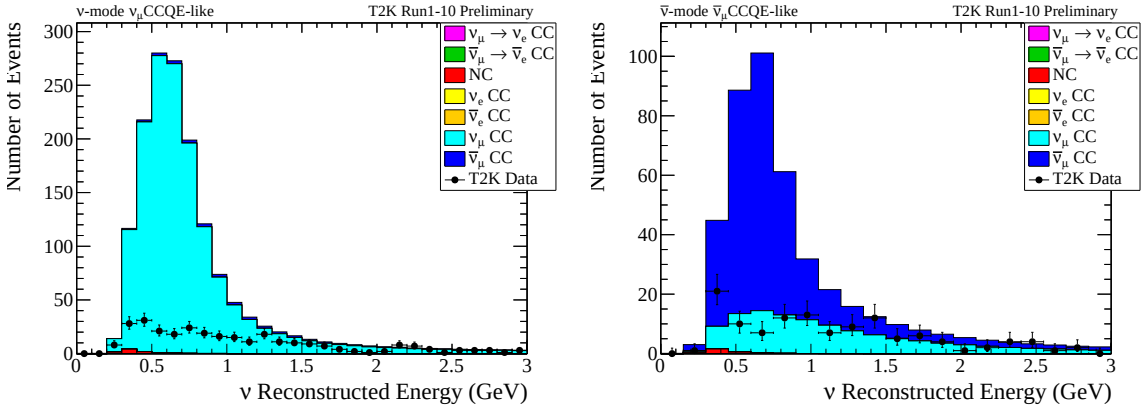

(a) ν-mode ν_μ / $\bar{\nu}_\mu$ CCQE-like sample.

(b) $\bar{\nu}$-mode ν_μ / $\bar{\nu}_\mu$ CCQE-like sample.

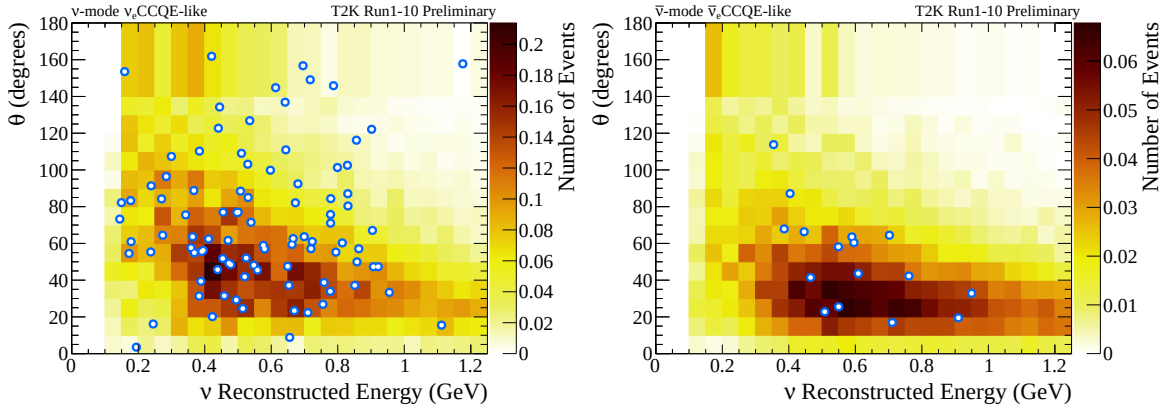

(c) ν-mode ν_e / $\bar{\nu}_e$ CCQE-like sample.

(d) $\bar{\nu}$-mode ν_e / $\bar{\nu}_e$ CCQE-like sample.

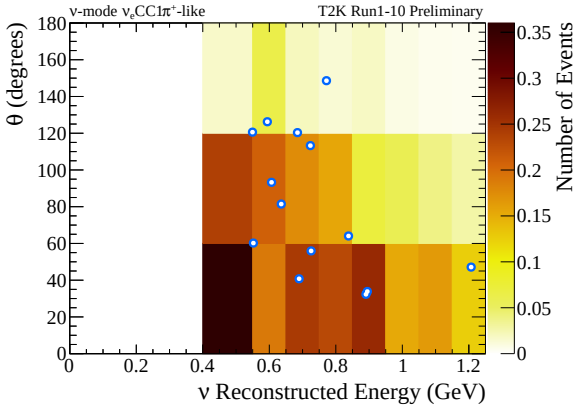

(e) ν-mode ν_eCC1π^+-like sample.

Figure 4.2: Unoscillated predicted kinematic distributions (coloured histograms) compared to the T2K Run 1-10 observed kinematic distributions (black or white/blue points). Predictions are generated under the assumption of no neutrino oscillations, with nominal values of the systematic parameters, and are normalised to the T2K Run 1-10 beam exposure. The uncertainty shown around the data points on the 1D plots accounts for statistical uncertainty only. The uncertainty range is chosen to include all points for which the measured number of data events is inside the 68% confidence interval of a Poisson distribution centred at that point.

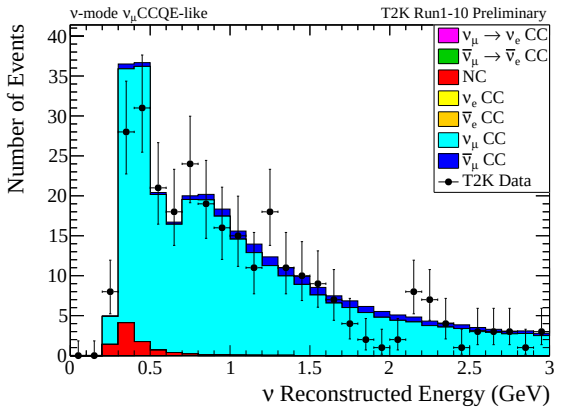

(a) ν-mode ν_μ / $\bar{\nu}_\mu$ CCQE-like sample.

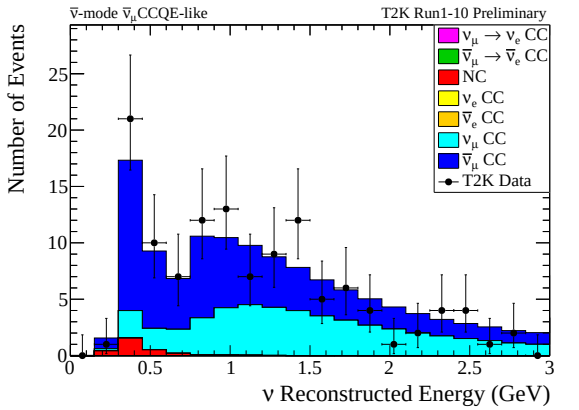

(b) $\bar{\nu}$-mode ν_μ / $\bar{\nu}_\mu$ CCQE-like sample.

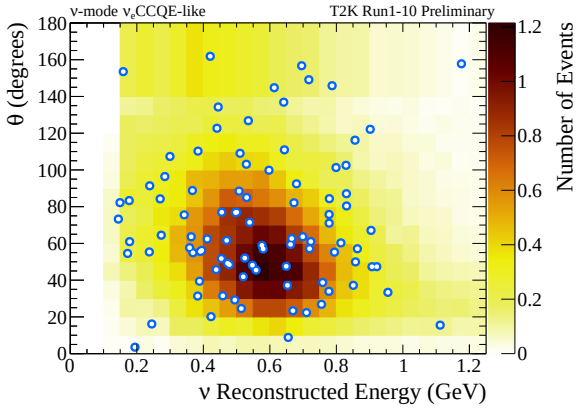

(c) ν-mode ν_e / $\bar{\nu}_e$ CCQE-like sample.

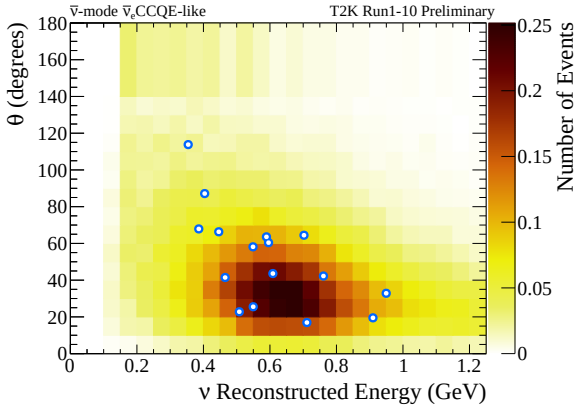

(d) $\bar{\nu}$-mode ν_e / $\bar{\nu}_e$ CCQE-like sample.

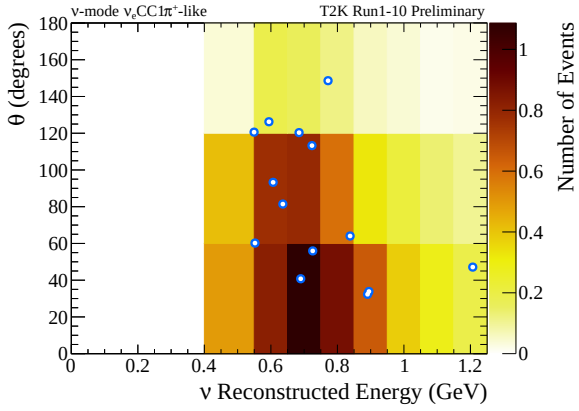

(e) ν-mode ν_eCC1π^+-like sample.

Figure 4.3: Asimov A predicted kinematic distributions (coloured histograms) compared to observed kinematic distributions (black or white/blue points). Predictions are generated with the Asimov A oscillation parameter values in Table 4.8, nominal values of the systematic parameters, and are normalised to the T2K Run 1-10 beam exposure. The uncertainty shown around the data points on the 1D plots accounts for statistical uncertainty only. The uncertainty range is chosen to include all points for which the measured number of data events is inside the 68% confidence interval of a Poisson distribution centred at that point.

4.4.1 — Effect of Systematic Uncertainties on the Predicted Kinematic Distributions

This analysis includes 137 systematic parameters to account for the effects of flow, cross section, and a Super-K + SI + PN uncertainty detector. Of these parameters, almost all flow and cross section parameters are limited to near detector fitting (see Chapter A). It is important understand the effect of systematic uncertainties on the predicted kinematic distributions, especially on the ratio of the frequency of ν and $\bar{\nu}$ events for the following reasons:

- In general, underestimating the size of systematic uncertainties leads to underestimation of the uncertainty of predicted kinematic distributions, which leads to a parameter space that is consistent with observations and therefore artificially fitted restrictions on the observed oscillation parameters. Conversely, overestimating the size of systematic practices uncertainties leads to an artificial weakening of the observed restrictions on the oscillation parameters.

- If there are correlations between systematic parameters, but they are not taken into account (or taken into account incorrectly), the limits of the oscillation parameters could be shifted. This is proved for δ_{CP} as follows: the effect of δ_{CP} is to introduce the difference between $P\left(\nu_\mu \to \nu_e\right)$ and $P\left(\bar{\nu}_\mu \to \bar{\nu}_e\right)$, as a result of which the frequency of events of type ν-mode ($\bar{\nu}$-mode) e reaches a minimum (maximum) at $+\frac{\pi}{2}$ and maximum (minimum) at $-\frac{\pi}{2}$. On this basis, measurements of the frequency of e-like events in both ν-modeand $\bar{\nu}$-mode are critical to the determination of δ_{CP}. Thus, if there is an anti-correlation between the event rates ν and $\bar{\nu}$ due to systematic effects, the expected frequency of events like ν-mode and $\bar{\nu}$-mode e for each value of δ_{CP} may change to mimic an event the rates that would be obtained for different values of δ_{CP} in the absence of such anti-correlation, which leads to a distorted (i.e., shifted) constraint on δ_{CP}.

  Of particular importance in this regard are the correlated parameters, which represent the uncertainties in section ratios ν_e/ν_μ and $\bar{\nu}_e/\bar{\nu}_\mu$ CC, σ_{ν_e} and $\sigma_{\bar{\nu}_e}$, which apply respectively to the ν_μ and ν_e events. Fractional error of your near detector fit $\sim 2.8\%$ and they are partially anticorrelated, with off-diagonal entries in the covariance matrix -0.0004 [155]. As shown in Table 4.10, these parameters make the main contribution to the systematic errors in the frequency of events like e and give the largest contribution to uncertainty is made by the ratio of ν to $\bar{\nu}$ e-rates of similar events.

For the reasons listed above, it is important to correctly model systematic uncertainties. and their proportions. As detailed in Chapter 3, the list of uncertainties are generalized and (due to matching to the near detector, atmospheric Super-K data, and external data) leads to predictions that are generally in excellent agreement with the data. On the near detector and Super-K atmospheric landings, correlations between systematic parameters are automatically taken into account and limited. For some interaction processes, the most especially 2p2h (see Section 3.2.3), there are a number of competing valid interaction models, potentially having different systematic uncertainties.

Effect of each category of systematic parameter on the expected frequency of events shown in Table 4.10

with unlimited effects cross section parameters are also displayed individually. This shows that ν-mode ν_eCC1π^+-like the sample has the highest systematic uncertainty of all samples, mainly due to Super-K detector, SI and PN errors.Fig. 4.4 shows comparison between landing before ND and landing after ND E_{rec} projections of nominal kinematic distributions of Asimov A and related 1σ systematic uncertainties. Distributions after fitting show a significant reduction in systematic uncertainties. compared to preset distributions, clearly demonstrating the clipping value near the detector.

Error source	ν_μ / $\bar{\nu}_\mu$ CCQE-like		ν_eCC1π^+-like	ν_e / $\bar{\nu}_e$ CCQE-like		
	ν-mode	$\bar{\nu}$-mode	ν-mode	ν-mode	$\bar{\nu}$-mode	$\nu/\bar{\nu}$
SK detector + SI + PN	2.2	1.9	13.2	3.0	4.0	1.3
Flux+xsec (constr.)	2.0	2.3	4.0	2.0	2.3	1.7
2p2h energy dependence	0.4	0.4	0.0	0.2	0.2	0.2
Isospin $\frac{1}{2}$ non-res. (low p_π)	0.5	2.6	0.1	0.2	2.3	2.1
σ_{ν_e} , $\sigma_{\bar{\nu}_e}$	0.4	0.4	2.7	2.6	1.5	3.0
NC 1γ	0.4	0.4	0.0	1.4	2.4	1.0
NC misc.	0.5	0.5	0.8	0.3	0.4	0.3
Flux+xsec (un-constr.)	0.6	2.6	2.7	2.9	3.6	3.8
All syst.	3.1	4.1	14.1	4.8	6.0	4.4

Table 4.10: Fractional uncertainties (%) on the event rates by error source and sample, calculated with expected events rates generated according to the Asimov A oscillation parameter values from Table 4.8 and by randomly drawing 10^4 sets of the indicated systematic parameters. The final column is the fractional uncertainty (%) on the ratio of ν-mode to $\bar{\nu}$-mode events in the ν_e / $\bar{\nu}_e$ CCQE-like sample. The central block of rows show the contributions to the uncertainties from the cross-section (xsec) parameters that are un-constrained in the near detector fit. The final row, 'All syst.', does not include the effects of any oscillation parameters. For all uncertainties except for those in the final row, not all correlations are taken into account, so the sum in quadrature of the individual uncertainties is not expected to equal the total error.

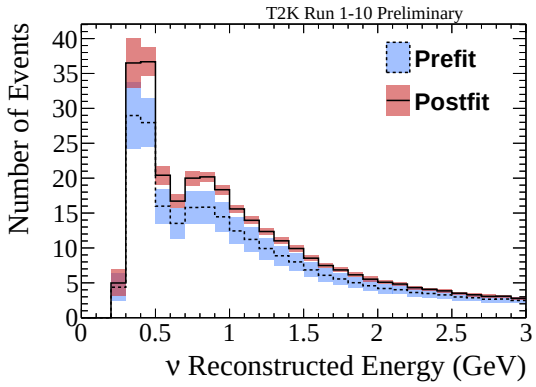

(a) ν-mode ν_μ / $\bar{\nu}_\mu$ CCQE-like sample.

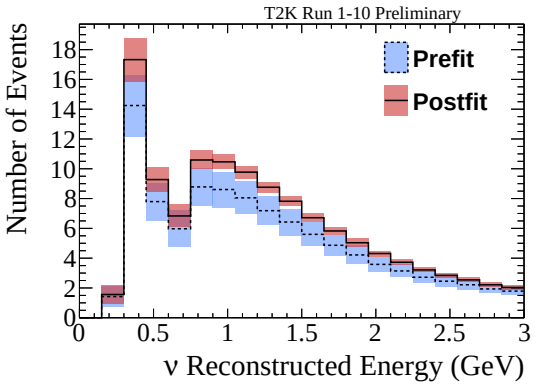

(b) $\bar{\nu}$-mode ν_μ / $\bar{\nu}_\mu$ CCQE-like sample.

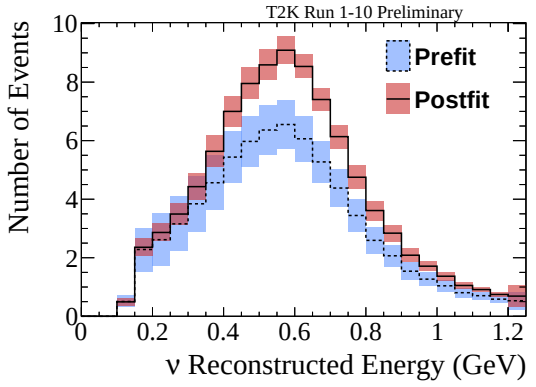

(c) ν-mode ν_e / $\bar{\nu}_e$ CCQE-like sample.

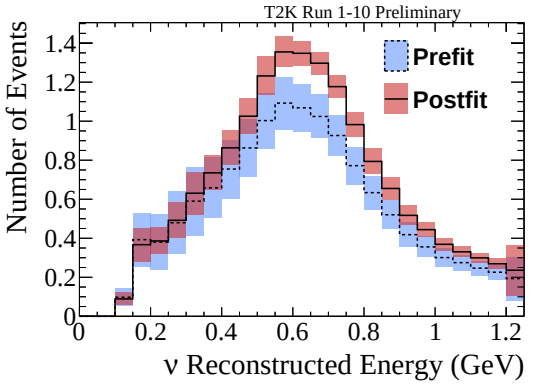

(d) $\bar{\nu}$-mode ν_e / $\bar{\nu}_e$ CCQE-like sample.

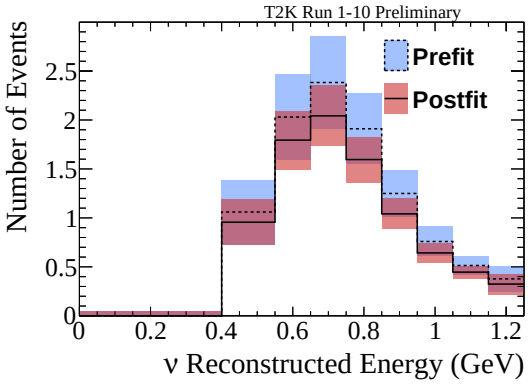

(e) ν-mode ν_eCC1π^+-like sample.

Figure 4.4: Predicted nominal E_{rec} distributions (black lines) with $\pm 1\sigma$ systematic errors (shaded regions), both pre and post near detector fit. Generated with the Asimov A oscillation parameter values in Table 4.8 and by randomly sampling 10000 sets of systematic parameters.

5 — Oscillation analysis results

As it has been said earlier in Chapter 3, although the T2K experiment is sensitive to and provides constraints on the mixing angle θ_{13}, the world's most accurate measurements of this parameter are obtained from reactor antineutrino experiments. In order to better constrain this parameter and increase sensitivity to other parameters, the PDG2019 global fit [124] uses the reactor average of 0.0853 ± 0.0027 as a prior probability density function (PDF) on $\sin^2 2\theta_{13}$. In order to simplify the implementation, the constraint it is considered to follow the Gaussian distribution with the mean and sigma corresponding to forehand mentioned from the PDG2019 global best fit value and its error respectively. Such approach has advantages and drawbacks. Clearly, an implementation withing T2K analysis software, in particularly in VALOR analysis software, is straight forward and does not slow down calculations. However, it is just an assumption as oscillation analysis chain, described in Chapter 3, is quite complex. Therefore, the main motivation of the present study is exploring alternative ways of taking into account reactor data, potentially improving a currently used one.

Looking at the reactor experiments results, most of these has an asymmetric error band, i.e. would not be possible to describe by a Gaussian distribution. This discrepancy may have an impact on the fit result. Also, in a current analysis, when the constraint is applied, it is applied only on $\sin^2 \theta_{13}$, therefor a prior correlation between θ_{13} and mass spiting term is never taken into account. And the last but not least, reactor experiments, usually can measure Δm^2 with a precision, comparable to T2K results. A constraint applied on Δm^2 as well as on $\sin^2 \theta_{13}$, should reduce an error on Δm^2_{32} (Δm^2_{13}) measurements.

This chapter is dedicated to a discussion of a way to take into account all mentioned points and results of a chosen implementation.

5.1 — Reactor constraint

The global fit is based on results of DoubleChooz, RENO and Daya Bay reactor experiments, however, it is strongly dominated by Daya Bay. The Daya Bay experiment is a particle physics experiment conducted in southern China to study neutrino oscillation. It features a complex experimental setup designed to detect and study neutrinos emitted by nuclear reactors. The experiment is located near the Daya Bay and Ling Ao nuclear power plants in Guangdong province, China. These power plants serve as the neutrino sources for the experiment. Reactors in these plants emit electron antineutrinos as a byproduct of the nuclear fission process.

The Daya Bay experiment comprises eight identical antineutrino detectors (ADs) arranged in three exper-

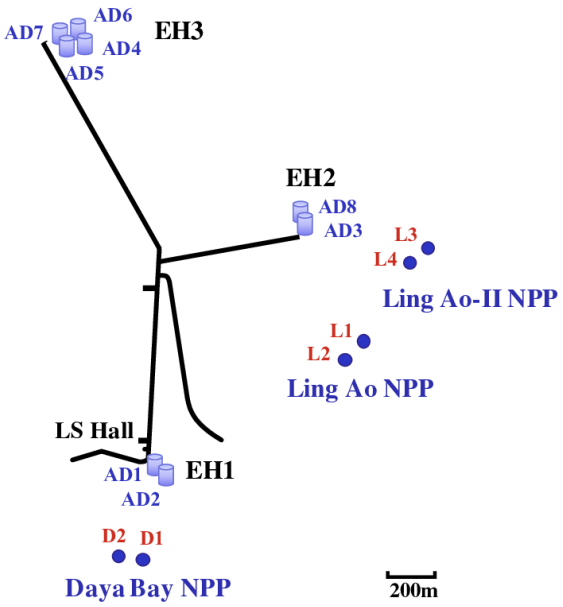

Figure 5.1: Layout of the full configuration of the Daya Bay experiment with eight antineutrino detectors (ADs) installed in three underground experimental halls (EHs). The dots represent reactor cores, labeled as D1, D2, L1, L2, L3 and L4. Reproduced from [18].

imental halls (see Fig. 5.1). Two ADs are located in each near experimental hall (EH1 and EH2), while four ADs are situated in the far hall (EH3). The experiment utilizes six reactor cores, with two cores positioned approximately 365 meters away from EH1 and four cores situated around 505 meters from EH2. The average geometric baseline to EH3, encompassing all six cores, measures 1663 meters.

Each AD consists of three concentric cylindrical vessels. The innermost vessel, made of acrylic, contains 20 tons of gadolinium-doped liquid scintillator (Gd LS), serving as the primary target for electron antineutrinos ($\bar{\nu}_e$). Surrounding the target vessel is another acrylic vessel filled with undoped liquid scintillator (LS), which enhances the detection efficiency for gamma rays produced within the target. The outermost vessel, made of stainless steel, houses a total of 192 8-inch photomultiplier tubes (PMTs) evenly distributed along its surface. The PMTs are immersed in mineral oil [19].

The multiple detectors at different distances from the reactors enable scientists to measure the change in the neutrino flux as the neutrinos travel through the Earth. The varying distances between the detectors provide valuable data for studying neutrino oscillation and accurately measuring the oscillation parameters, such as the mixing angle θ_{13} .

Fig. 5.2, shows Daya Bay likelihood surface for Δm_{ee} and $\sin^2\theta_{13}$, with projections for single parameters. The error band for Δm^2 is comparable to T2K one. This likelihood surface if a part of Daya Baya public data release of 2018 analysis corresponding to 1958 days of detector operation [19]. The world leading results on $\sin^2\theta_{13}$ and mentioned comparability for Δm^2 with T2K, makes Daya Bay an ideal source for this study. Using its likelihood surface directly as a constraint, instead of a Gaussian approximation, will allow to indeed check the effect of the asymmetry of the surface, correctly treat the correlation counted as negligible

in current analysis and, furthermore, take an advantage of the the reactor experiments being sensitive to the mass splitting parameter Δm^2 .

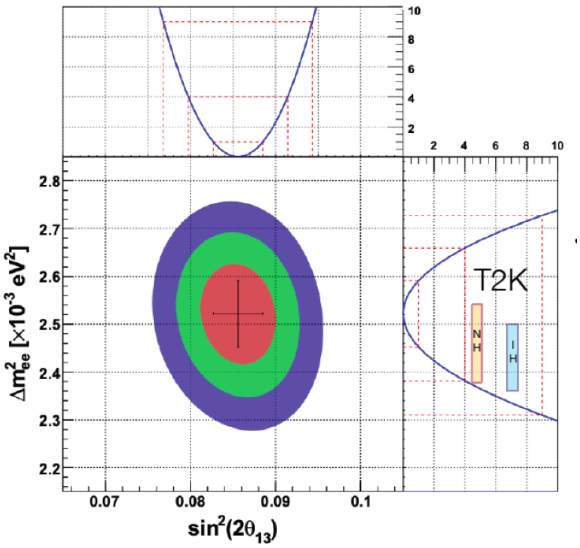

Figure 5.2: Daya Bay likelihood surface for theta13 and Δm_{ee} with 1D projections [19]. T2K preferred regions for Δm_{ee} : orange bar for NH (Δm^2_{13}) and blue for IH (Δm^2_{32})

5.2 — Sensitivities with reactor constraint

Sensitivity studies were conducted to assess T2K ability to measure various oscillation parameters of interest under an oscillation hypotheses, using the Asimov A oscillation parameter values listed in Table 4.8. The sensitivity was evaluated using both mass orderings and with different constraints: with Gaussian constraint on $\sin^2 2\theta_{13}$ from reactor experiments and with Day Bay likelihood surface as a constraint on both Δm^2 and $\sin^2 \theta_{13}$, according to the method described in Chapter 4.

The resulting $\Delta\chi^2$ functions and corresponding confidence regions are presented in Figures 5.3a-5.3c for δ_{CP}, $\sin^2 \theta_{23}$, and $|\Delta m^2_{3j}|$, respectively. There is no figure for $\sin^2 \theta_{13}$, as T2K sensitivity is dominated by any type of reactor constraint and therefore it is out of interest in a scope of this study. In addition, 2D confidence regions are shown in Figures 5.4a-5.4d to explore an effect of correlations between oscillation parameters.

Due to computational constraints, the constant $\Delta\chi^2$ method was used to construct confidence regions, rather than the more accurate Feldman-Cousins method described in Section 4.2. As a result, the expected coverage of confidence regions may not be perfectly accurate.

The use of graphical reactor constrain if advantageous for measurements of Δm^2_{32} (see Fig. 5.3b,). It improves T2K sensitivity to this parameter, reducing 1σ region in $\sim$ 1.4 times i.e. in $\sim \sqrt{2}$, as expected. The difference in best fit values on the Fig. 5.3b appears due to application of a constraint on Δm^2_{32} together with $\sin^2 \theta_{13}$, while a gaussian penalty applies a constraint on Δm^2_{32} only. However, there is no significant impact on other oscillation parameters (see Figs. 5.3a and 5.3c), nor on their correlations (see Figs. 5.4a, 5.4c and 5.4d). This proves a robustness of current T2K analysis approach to reactor constraint: use of 1D constraint.

Although it does not allow to benefit from all information reactor experiments provide, an agreement between obtained results proves 1D gaussian approximation being good enough. Best-fit points and confidence interval resulting from the 1D fits are displayed Table 5.1.

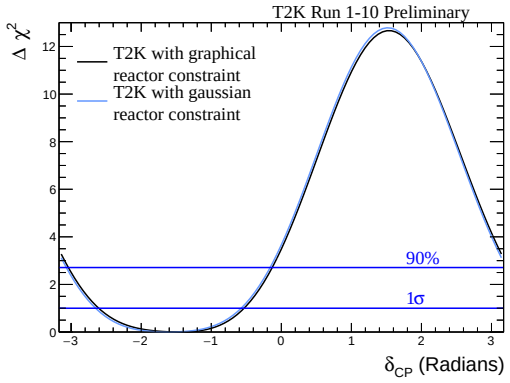

(a) A comparison of T2K sensitivity with a standard reactor constraint and a use of likelihood surface for CP violating phase δ_{CP}

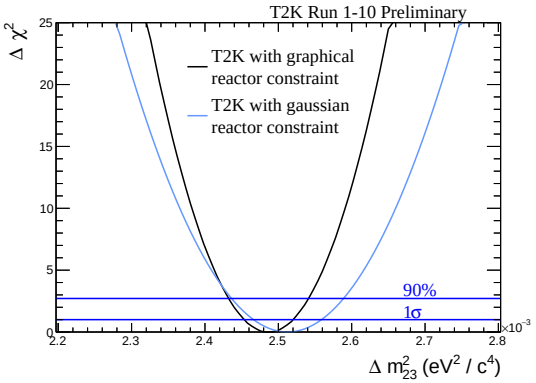

(b) A comparison of T2K sensitivity with a standard reactor constraint and a use of likelihood surface for Δm^2_{32}

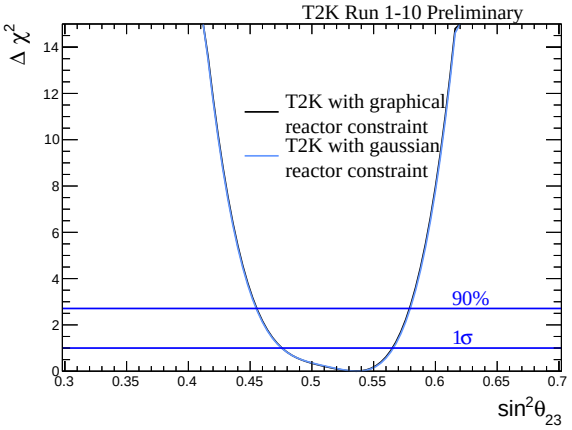

(c) A comparison of T2K sensitivity with a standard reactor constraint and a use of likelihood surface for $\sin^2\theta_{23}$

Figure 5.3: Comparisons of 1D sensitivity contours with gaussian and graphical reactor constraints applied.

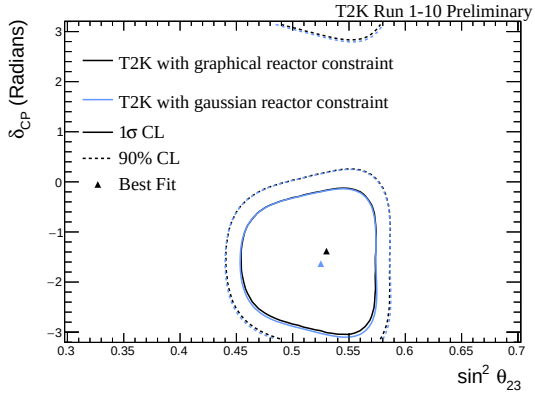

(a) A comparison of T2K sensitivity with a standard reactor constraint and a use of likelihood surface for $\sin^2\theta_{23}$ vs. δ_{CP}

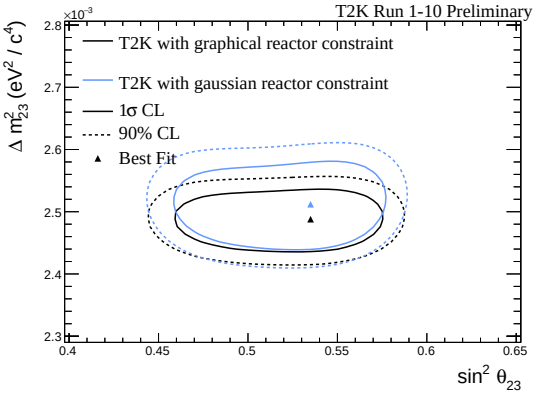

(b) A comparison of T2K sensitivity with a standard reactor constraint and a use of likelihood surface for Δm^2_{32} vs. $\sin^2\theta_{23}$

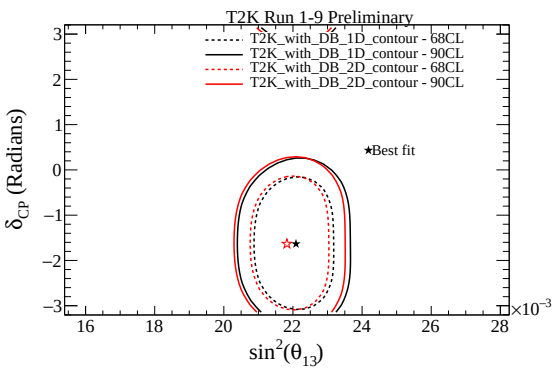

(c) A comparison of T2K sensitivity with a standard reactor constraint and a use of likelihood surface for δ_{CP} vs. $\sin^2\theta_{13}$

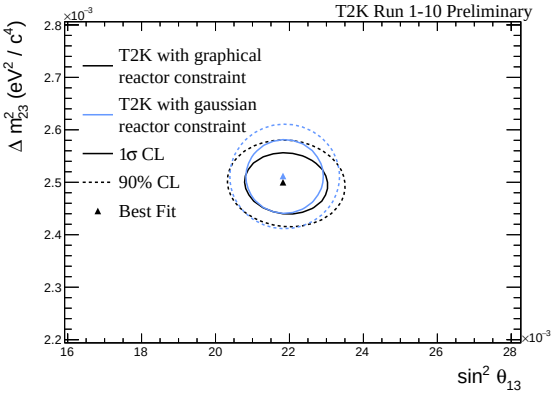

(d) A comparison of T2K sensitivity with a standard reactor constraint and a use of likelihood surface for Δm^2_{32} vs. $\sin^2\theta_{13}$

Figure 5.4: Comparisons of 2D sensitivity contours with gaussian and graphical reactor constraints applied.

Parameter	Reactor Constraint	Best-Fit	1σ Interval	90% Interval
$\sin^2\theta_{23}$	Gaussian	0.536	$[0.476, 0.566]$	$[0.455, 0.580]$
	Graphical	0.536	$[0.476, 0.565]$	$[0.455, 0.579]$
Δm^2_{32}	Gaussian	2.512	$[2.466, 2.559]$	$[2.436, 2.589]$
$(10^{-3}\text{eV}^2/\text{c}^4)$	Graphical	2.488	$[2.454, 2.520]$	$[2.432, 2.541]$
δ_{CP}	Gaussian	-1.634	$[-2.650, -0.573]$	$[-3.068, -0.160]$
	Graphical	-1.445	$[-2.606, -0.533]$	$[-3.04, -0.130]$

Table 5.1: Predicted oscillation parameter best-fit, 1σ, and 90% confidence intervals, shown both with and without the constraint on $\sin^2 2\theta_{13}$ from reactor experiments. All intervals are obtained from 1D fits to the parameter of interest. The intervals are calculated using the constant $\Delta\chi^2$ method described in Section 4.2.

5.2.1 — Mass ordering study

The ratio E/L of the T2K experiment does not allow one to clearly discriminate between mass ordering. A conclusion about the preference towards normal (NO) or inverted (IO) mass ordering in T2K oscillation analysis is usually driven by posterior probabilities in pure Bayesian analysis. However, as it has been shown previously, adding the Daya Bay result on Δm^2 to T2K improves the sensitivity to the mass splitting term and can potentially affect the sensitivity to the mass ordering too. Here the study is performed within a combined Bayesian-Frequentest VALOR analysis framework.

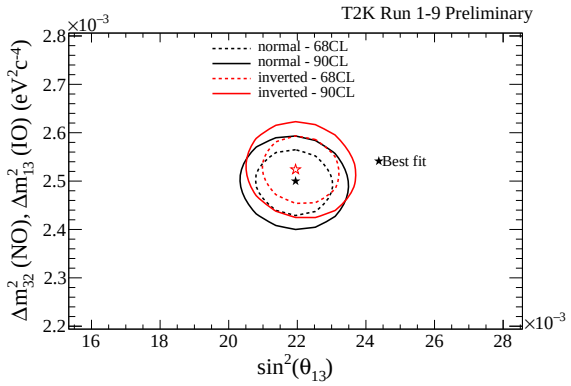

Figure 5.5: A comparison of T2K sensitivity for mass splitting term and $\sin^2\theta_{13}$ in case of normal and inverted mass ordering (in both cases normal mass ordering is assumed to be true). In both cases a graphical reactor constraint is applied.

A $\Delta\chi^2_{IO-NO}$ was calculated using the results from fits of Δm^2 vs $\sin^2\theta_{13}$ for normal and inverted mass hierarchy. For the case of T2K, T2K with a gaussian reactor constraint and T2K with Daya Bay likelihood surface constraint (Fig. 5.5), study shows (Table 5.2) that latter option gives an increase in mass ordering separation: ~ 1.97 times in comparison with T2K only result and ~ 1.15 times in comparison with gaussian reactor constraint. Table 5.2 also shows that normal mass ordering is preferred over inverted, which is consistent with T2K official result [78].

χ^2	NO	IO	$\Delta\chi^2_{IO-NO}$
T2K only	9.460	10.838	1.378
T2K with gaussian constraint	9.977	12.340	2.363
T2K with Daya Bay likelihood surface constraint	10.029	12.740	2.711

Table 5.2: χ^2 values for T2K predicted best fit value for normal and inverted mass ordering. In both cases normal mass ordering is assumed to be true.

5.3 — Data results

The aim of this section is to use the T2K Run 1-10 data set to establish a effect of using different constraint, described earlier, on limitations on the oscillation parameters of the three-flavour PMNS model.

The observed $\Delta\chi^2$ functions and the corresponding 1D confidence regions are shown in Fig. 5.6a-Fig. 5.6c for δ_{CP}, and $|\Delta m^2_{3j}|$ and $\sin^2\theta_{23}$, respectively. Also, to show an effect on correlations between the oscillation parameters, 2D confidence regions are presented in Fig. 5.7a-Fig. 5.7d. Best-fit points and confidence interval resulting from the 1D fits are displayed Table 5.3. All such confidence regions are constructed using the constant $\Delta\chi^2$ method (see Section 4.2). Data fit results are consistent with sensitivity studies. There is a slight difference between a central value for δ_{CP} parameter (see Fig. 5.6a), however it does not lead to a significant change in confidence region. The use of graphical reactor constraint on Δm^2_{32} , as for sensitivity studies, narrows a 1σ region by ~ 1.4 times in comparison to the result with standard gaussian constraint applied (see Fig. 5.6b).

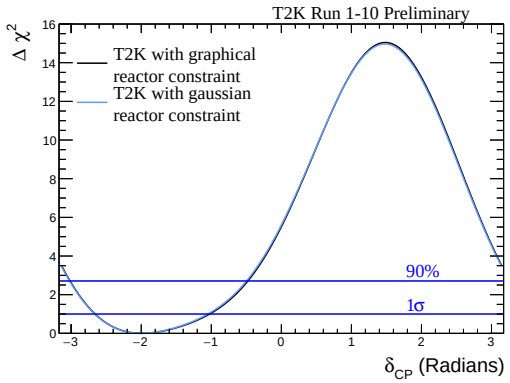

(a) A comparison of T2K data result with a standard reactor constraint and a use of likelihood surface for CP violating phase δ_{CP}

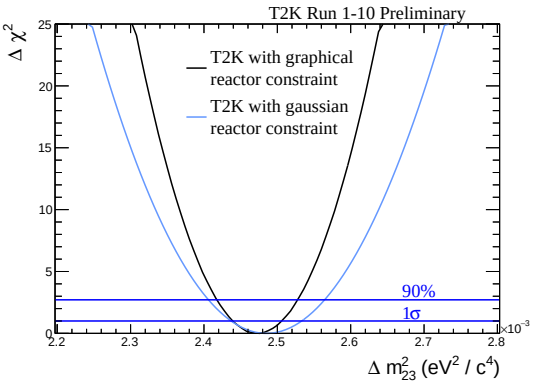

(b) A comparison of T2K data result with a standard reactor constraint and a use of likelihood surface for Δm^2_{32}

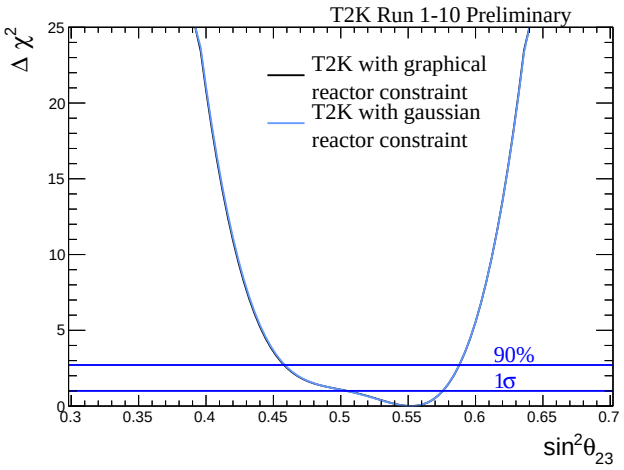

(c) A comparison of T2K data result with a standard reactor constraint and a use of likelihood surface for $\sin^2\theta_{23}$

Figure 5.6: Comparisons of 1D data fit contours with gaussian and graphical reactor constraints applied.

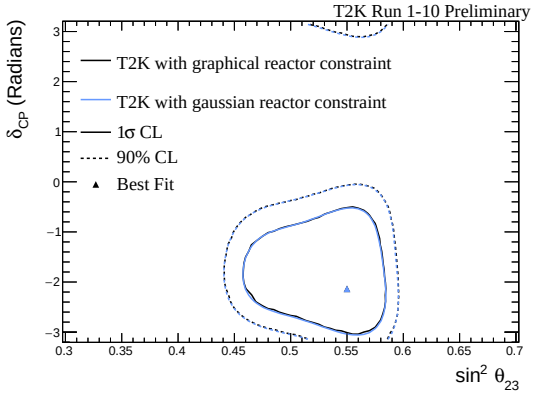

(a) A comparison of T2K result with a standard reactor constraint and a use of likelihood surface for $\sin^2\theta_{23}$ vs. δ_{CP}

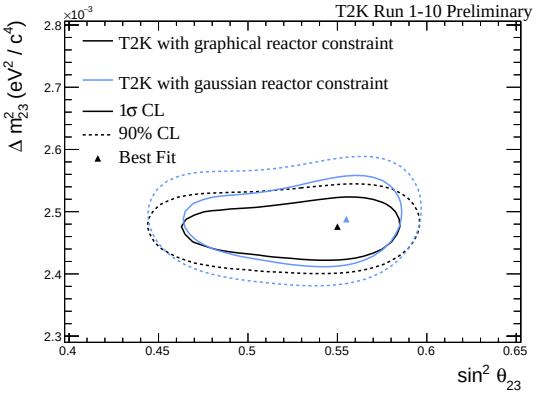

(b) A comparison of T2K result with a standard reactor constraint and a use of likelihood surface for Δm^2_{32} vs. $\sin^2\theta_{23}$

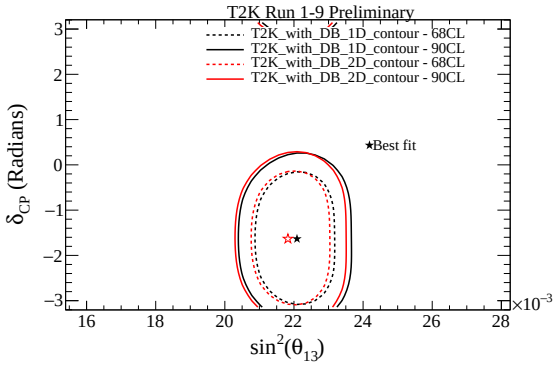

(c) A comparison of T2K data result with a standard reactor constraint and a use of likelihood surface for δ_{CP} vs. $\sin^2\theta_{13}$

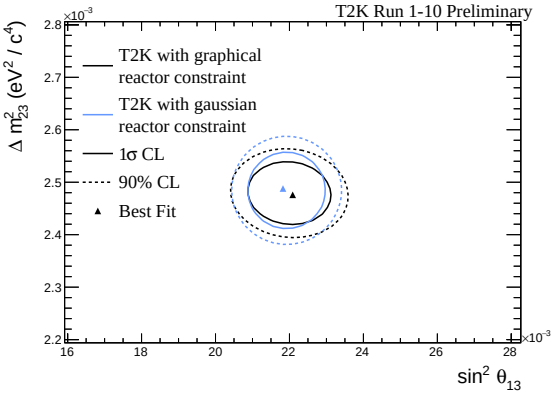

(d) A comparison of T2K data result with a standard reactor constraint and a use of likelihood surface for Δm^2_{32} vs. $\sin^2\theta_{13}$

Figure 5.7: Comparisons of 2D data fit contours with gaussian and graphical reactor constraints applied.

As for mass ordering study, data fit result stays in agreement with sensitivity studies (see Table 5.4) showing an improvement in separation between NO and IO of ~ 1.9 times in comparison to T2K only data fit and ~ 1.16 time in comparison to T2K with a gaussian constraint applied data fit.

Parameter	Reactor Constraint	Best-Fit	1σ Interval	90% Interval
$\sin^2\theta_{23}$	Gaussian	0.552	$[0.504, 0.576]$	$[0.459, 0.588]$
	Graphical	0.552	$[0.504, 0.576]$	$[0.458, 0.588]$
Δm^2_{32}	Gaussian	2.482	$[2.437, 2.533]$	$[2.406, 2.533]$
$(10^{-3}\text{eV}^2/\text{c}^4)$	Graphical	2.476	$[2.439, 2.506]$	$[2.418, 2.528]$
δ_{CP}	Gaussian	-2.010	$[-2.664, -1.050]$	$[-3.024, -0.497]$
	Graphical	-2.010	$[-2.658, -1.024]$	$[-3.017, -0.477]$

Table 5.3: The measured oscillation parameter best-fit, 1σ, and 90% confidence intervals, shown both with and without the constraint on $\sin^2 2\theta_{13}$ from reactor experiments. All intervals are obtained from 1D fits to the parameter of interest. The intervals are calculated using the constant $\Delta\chi^2$ method described in Section 4.2.

χ^2	NO	IO	$\Delta\chi^2_{IO-NO}$
T2K only	475.392	476.166	0.774
T2K with gaussian constraint	478.907	480.174	1.267
T2K with Daya Bay likelihood surface constraint	475.821	477.296	1.475

Table 5.4: χ^2 values for T2K data best fit value for normal and inverted mass ordering. In both cases normal mass ordering is assumed to be true.

6 — Scintillator ageing studies

During the modern era of high precision neutrino physics measurements it has become increasingly important to deepen our understanding of detector performance. It is common for neutrino detector systems to be fully or partially composed of polystyrene-based scintillator bars, and most experiments now gather data for over a decade. Therefore it is crucial to investigate how the performance of such sensitive materials change with time. As it has been described in the Chapter 2,T2K's two near detectors are primarily composed of plastic scintillators of different shapes and origin. The data, collected since the experiment began to operate in 2010, provide an opportunity to perform comprehensive studies of scintillator ageing.

The issue of plastic scintillator ageing is long known [156], and there are many studies aimed at measuring, characterizing and developing stabilization methods for these widely used materials (see for example [157–163]). These studies often consider the impact of potentially controllable environmental factors such as temperature and humidity on the long-term performance of the materials, as well as ways to chemically stabilize them.

The exact mechanism for scintillator ageing occurring within the T2K near detectors is unknown, but there are a number of potentially contributing factors:

- Mechanical stressing of the scintillator causing the development of crazes or shears within the material [164]. These inhibit the uniform scattering of light within the scintillator, preventing transmission through total internal reflection.

- Fogging of the scintillators due to water penetrating into the material and condensing [165]. This increases the opacity of the scintillator and is a significant problem where the materials are exposed to very high humidity conditions with large temperature variations.

- Oxidation of the scintillator through photochemical processes that lead to the production of peroxides causing the yellowing of the material [166]. This reduces the light yield from the scintillator and has been observed in the accelerated ageing test performed on the scintillator bars used by the MINOS experiment [69], which are materially identical to the FGD, ECaL and PØD subsystems of T2K as described in Chapter 2.

The study, presented in this chapter, does not differentiate between forehand listed ageing factors.

The selected data samples and the analysis methodology are described in the Section 6.1, the rate of degradation of the T2K scintillator is presented in section Section 6.3, along with predictions for the future response

of the detectors in section Section 6.5 and an attempt to disentangle whether the ageing is dominated by the degradation of the scintillator or wavelength shifting (WLS) fibres in section Section 6.4.

6.1 — LY measurement

The degradation in scintillator response can be quantified by measuring the change over time of the average light yield observed from the passage of minimum ionizing particles (MIP), through ND280 subsystems. The recorded and calibrated response of an MPPC due to the passage of a MIP through a scintillator bar constitutes a "hit" within a subsystem. Due to the varying geometry and acceptance of the subsystems, several different MIP samples were used for the analysis: beam neutrino interactions, cosmic ray muons recorded concurrently with each T2K Run, or sand muon data. Sand muons are produced by interactions of the beam neutrinos with the ground and walls which surround the detector complex. When such an interaction occurs close enough to the detector, high energy muons may propagate to and be detected by the near detectors.

In all cases the MIP light yield corrected to account for the length of the MIP's path through the scintillator bar based on the track angle, and attenuation in the WLS fibre based on the reconstructed position along the scintillator bar.

Regular (∼weekly) adjustments were made to the MPPC overvoltage to account for temperature variations in order to maintain a stable gain, and therefore detector response, over time. This was achieved by stepping through a range of bias voltages and measuring the difference (gain) between the pedestal and single photo-electron response for each MPPC. The correlation between measured gain as function of voltage was used to extract the appropriate overvoltage to be applied to each MPPC. For ND280 this is supplemented by more frequent calibrations (∼3 hourly) that are derived from the recorded detector temperature (FGD) or directly from the pedestal and single photoelectron response of the MPPCs (ECal, SMRD, PØD) and applied during offline reconstruction. An additional empirically derived corrections were also applied to account for the changes in photodetection efficiency, cross talk and after-pulsing as function of overvoltage [167, 168].

T2K first became operational in March 2010 and neutrino beam data had been recorded during 11 separate T2K Run periods by the end of 2021, as shown in figure 2.6 and table 2.1. Data taken during T2K Runs 2–9 were used by ND280 subsystems, respectively, in the analyses described by this chapter.

For all subsystems within ND280, the MPPC response (hits) for MIP-like tracks measured during each T2K Run were combined to create histograms of accumulated charge per unit length. These histograms were then fitted with the convolution of a Gaussian distribution and a Landau distribution [169], see figure 6.1. This distribution models the typical energy loss of high-energy particles in matter, along with a Gaussian term to account for detector smearing effects.

The MIP light yield is taken to be the most probable value (MPV) of the Landau-Gaussian fit function. Calibrations designed to maintain the light yield over time, and therefore account for any ageing of the scintillator, are disabled.

Different MIP track selection criteria were developed for each subsystem, dependent upon the detector geometry and chosen data sample.

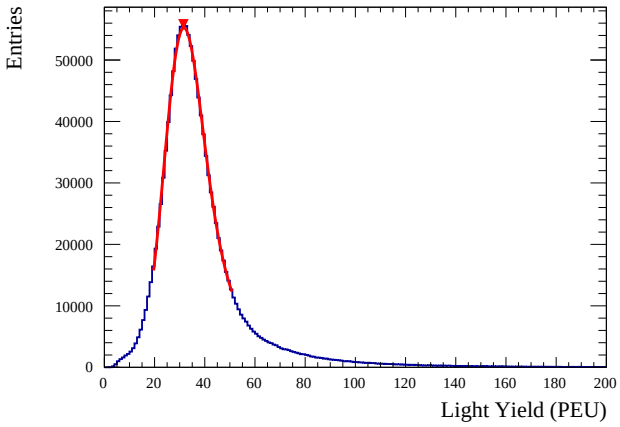

Figure 6.1: Example MIP light yield distribution in ECal Barrel X after calibrations and corrections are applied. The MIP most probable value (MPV) in Pixel Equivalent Units (PEU) is extracted from a Landau-Gaussian fit to the distribution. A PEU corresponds to the signal of a single MPPC pixel.

6.1.1 — PØD

The PØD detector uses a sand muon data sample to monitor the scintillator response. This control sample is selected in the following way:

1. There is only one 3D track reconstructed within the PØD during the beam trigger readout window,
2. This track passes through the first and the last PØDule,
3. Track angle with respect to the beam direction, θ, fulfils the following condition: $\cos\theta \geq 0.8$ (forward going, as measured at the upstream face of the PØD).

These criteria select a sample of MIPs traveling through the detector, leaving hits with well measured 3D positions. The light yield per unit path length for each individual hit is aggregated for each T2K Run separately for each of the four Super-PØDules.

6.1.2 — FGD

The FGD (as the PØD) uses a sand muon data sample to monitor the scintillator response. This control sample only includes events where there is just one 3D track reconstructed within each FGD during the beam trigger readout window. The light yield per unit path length for each individual hit is aggregated together for both FGDs for each T2K Run.

6.1.3 — ECal

During normal detector operation, high statistic samples of cosmic ray muons traversing the ND280 ECals are routinely recorded. These provide an ideal sample by which to monitor and calibrate the response of the detector modules.

The cosmic ray trigger requires the coincidence of hits to occur within two outer regions on opposite sides of the ND280 detector, outside of the time window used for neutrino beam triggers. These hits can occur within the SMRD, Downstream ECal and most upstream Super-PØDule and indicate that a cosmic ray has traversed ND280. The MIP tracks are then individually reconstructed in 3D using a linear fitting algorithm, with the hits required to have recorded a valid charge and have adjacent hits in each 2D view. The calibrated light yield on each bar is then obtained and can be normalized to account for the angle of incidence of the MIP with respect to the scintillator bar, and optionally the attenuation of the scintillation light as it propagates through the WLS fibre to the MPPC. The attenuation correction normalizes the response of interactions at any position along the bar to the response observed at 1 m from the MPPC.

The measured light yield of individual MIP interactions are aggregated for each month or T2K Run separately for the different bar lengths. The analysis presented here uses a random sampling of 5% of all ND280 subruns (the data recorded during ∼20 minutes of nominal ND280 operation) from each T2K Run to give excellent statistical coverage over all periods of interest.

6.1.4 — SMRD

For the SMRD both beam and cosmic data samples can be used. However, in most ND280 cosmic trigger configurations the SMRD is not uniformly sampled, leaving some regions statistically limited, unlike in the case of the beam mode triggers. Moreover, only a fraction of the recorded cosmic data sample gets processed. Hence the current study was performed using the beam data sample. The track selection requires:

1. The highest momentum track reconstructed within the beam trigger readout window has an interaction vertex within the SMRD fiducial volume,
2. The track crosses at least one TPC,
3. The track particle identification hypothesis is consistent with being muon-like.

The light yield per unit path length for each individual SMRD hit is aggregated together for each T2K Run.

6.2 — Light Yield Stability Uncertainty

During each data aggregation period (time bin) the measured light yield will vary with time due to changes in the stability of the MPPC response, for example due to overvoltage fluctuations caused by changes in ambient temperature. Such fluctuations affect not only the gain but also the photon detection efficiency. Every effort is made to measure and calibrate out these variations, however this is an imperfect process. Therefore, each subsystem attempts to measure the inherent variation in light yield response within each time bin, and then includes that variation as a systematic uncertainty on the ND280 subsystem MIP MPV.

For all ND280 subsystems, to assess the light yield stability within each time bin, the contributing data samples were split into shorter (reduced) time periods. Within each reduced time period, the MIP response was fitted with the Landau-Gaussian convolution, and the MIP MPV extracted. For each time bin, the standard

deviation of the MIP MPVs for the contributing reduced time periods was calculated and taken as the light yield stability uncertainty.

Due to the variation in event rates for the samples used in the MIP MPV estimation for the different ND280 subsystems, the length of the reduced time periods varies between the subsystems to ensure a good balance between temporal granularity and obtaining sufficient statistics to perform an accurate Landau-Gaussian fit. For the ECal, the high statistics of the cosmic ray sample allows data to be aggregated into periods of ∼20 minute duration (the period of one ND280 subrun), however for the FGD and PØD, the slower accrual rate of sand muon data means the data was aggregated into periods of one-month and two-weeks, respectively. For the SMRD, the T2K Runs with the highest statistics were studied and the data aggregated into one week periods. The largest standard deviation, among the T2K Runs, was then taken as the error to be conservatively applied to all SMRD data points. The range of uncertainties, and modal uncertainty, across all data periods are shown in table 6.1. Most uncertainty values lie close to modal value, with a few exceptions which push out the maximum range to higher values.

Table 6.1: Absolute range and modal light yield stability uncertainties in PEU for each subsystem. Also shown is the range and modal uncertainties as a percentage of the recorded MPV the absolute uncertainties account for in their associated time bins.

Subsystem	Uncertainty Range		Modal Uncertainty	
	Absolute Value (PEU)	% of MPV	Absolute Value (PEU)	% of MPV
PØD	0.02–0.57	0.11–2.57	∼0.20	∼0.90
ECal (Single-ended)	0.07–2.19	0.28–8.24	∼0.15	∼0.80
ECal (Double-ended)	0.05–1.22	0.33–7.35	∼0.10	∼0.90
FGD	0.10–0.29	0.51–1.33	∼0.15	∼0.70
SMRD	0.79–1.33	1.4–2.3	1.33	2.3

6.3 — Annual light yield reduction

The distribution of the ND280 MIP MPV was extracted for each subsystem during each T2K Run and then fitted with a linear function in order to calculate the overall drop in light yield and annual decrements, see figure 6.2.

The data is aggregated by T2K Run for the PØD, FGD and SMRD, with the time error being the standard deviation in time stamp of all MIP hits during each T2K Run. For the ECal, the higher statistic allows for the data to be instead aggregated on a per month basis, or per J-PARC Main Ring Run (usually around 1 month), respectively. The fit is only applied to the data from January 2012 onwards for the ND280 subsystems as the current calibration procedures and cosmic ray triggering prescale were not finalized until that time.

As described in the previous section, for the PØD and ECal subsystems (see sections 6.1.1 and 6.1.3 respectively) the study has been performed for all sub-modules or bar types separately, see figures 6.2a and 6.2b.

Without knowledge of the ageing mechanism(s) degrading ND280 subsystems it is difficult to know what

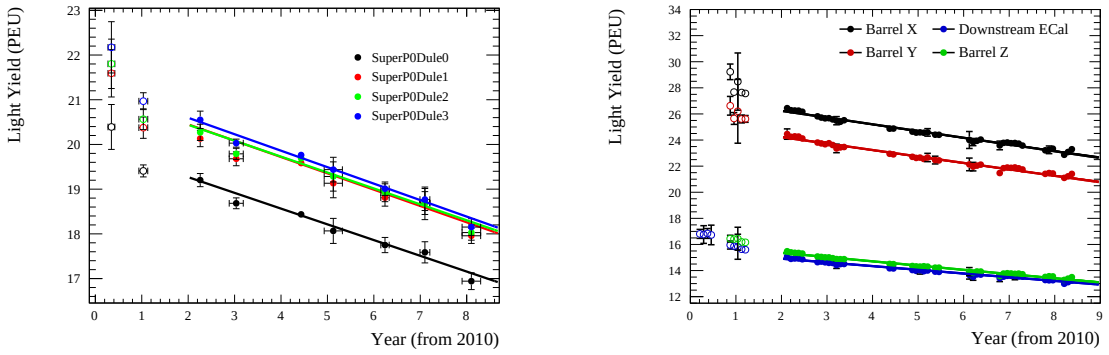

(a) PØD.

(b) ECal.

(c) FGD.

(d) SMRD.

Figure 6.2: Light yield change in each subsystem for T2K Runs 3–9. The x-error bars (time) show the standard deviation in the hit times for each data aggregation period, and the y-error bars (light yield) show the quadratic sum of the light yield stability uncertainty and the uncertainty on the Landau-Gaussian MIP MPV. Hollow data points are excluded from the data fits.

Table 6.2: Linear fit parameters to PØD, FGD, SMRD and ECal data from figure 6.2 and the annual percentage reduction, relative to the 2012 fit values. Single-ended readout bars are mirrored on one end.

Subsystem	Readout Type	A (PEU)	B (PEU/yr)	χ^2/NDF	Annual Reduction (%)
Super-PØDule 0	Single-ended	19.97 ± 0.15	0.35 ± 0.03	$4.35/5 = 0.87$	1.82 ± 0.16
Super-PØDule 1	Single-ended	21.17 ± 0.16	0.36 ± 0.04	$10.39/5 = 2.08$	1.76 ± 0.20
Super-PØDule 2	Single-ended	21.15 ± 0.17	0.36 ± 0.03	$9.14/5 = 1.83$	1.76 ± 0.15
Super-PØDule 3	Single-ended	21.33 ± 0.16	0.37 ± 0.03	$5.46/5 = 1.09$	1.80 ± 0.15
FGD	Single-ended	22.68 ± 0.19	0.27 ± 0.04	$0.74/5 = 0.15$	1.22 ± 0.18
SMRD	Double-ended	60.86 ± 1.48	0.54 ± 0.26	$2.62/5 = 0.52$	0.90 ± 0.44
Barrel X	Single-ended	27.27 ± 0.06	0.52 ± 0.01	$33.09/37 = 0.89$	1.98 ± 0.04
Barrel Y	Single-ended	25.21 ± 0.08	0.49 ± 0.01	$31.88/37 = 0.86$	2.02 ± 0.04
Barrel Z	Double-ended	16.01 ± 0.04	0.33 ± 0.01	$36.60/37 = 0.99$	2.15 ± 0.07
Downstream	Double-ended	15.48 ± 0.06	0.28 ± 0.01	$11.57/37 = 0.31$	1.87 ± 0.07

form the time dependence on the ageing rate should be expected to take. A priori it might be expected that an exponential function would be suitable, and fits of this form are used for projecting the future response of the most important subsystems in section 6.5. However, given the observed data distributions and timescale studied a simple linear fit is found to be appropriate, and are applied in the form:

$$f(t) = A - Bt\,, \tag{6.1}$$

where A is the fitted light yield in PEU at year 0 (2010), B is the gradient of the fit in PEU per year, and t is the year since 2010. The fit parameters are shown in table 6.2.

The degradation of the scintillator appears to be reasonably consistent across all subsystems. All show a reduction in light yield within the range ∼0.3–0.5 PEU per year, equivalent to an annual light yield reduction of 0.9–2.2% relative to their 2012 fit values.

The 1% difference separating the highest and lowest degradation rates between the materially identical FGD (1.2%) and ECal (Barrel Z 2.2%), is not surprising given the differences in production dates for the scintillator bars, and the varying environmental conditions they had experienced during their production, transportation, and positioning within ND280. All of the aforementioned factors will have contributed to differences in the temperature, humidity and UV exposure of the bars across their lifetimes, and so impacted upon their respective ageing profiles.

The higher statistics of the ECal allows for a finer assessment of its ageing rate. An initial rapid ageing is observed within the first two years of operation, followed by a near linear reduction beyond 2012, however it is unclear if this is a real effect or just an artefact of the changes in calibration procedure and cosmic ray triggering prescale. The higher ECal light yield obtained by the Barrel X and Y bars is due to the combination of direct and reflected light signals for these single-ended (mirrored) readout channels, compared to direct transmission only for the double-ended readout of the Barrel Z and Downstream bars.

Results from the MINOS experiment, which uses materially identical bars to the FGD, ECal and PØD, showed ageing rates of ∼2% per year [69] over 3 and 4.5 year periods measured with their near and far detectors respectively, in good agreement with the higher rates we obtain from the ECal and PØ.

The MINERνA experiment found a substantially higher rate of ageing for their scintillator bars, equivalent to a $\sim$7.5% annual reduction in light yield over a 2 year study period [170]. It is unclear why MINERνA measured such a high rate of degradation as their scintillator composition is again identical to that used by MINOS and most T2K subsystems. It might be possible that MINERνA has sampled an initial rapid ageing of their scintillator, as perhaps indicated in the earliest ECal data points as discussed above, and also anecdotally observed by MINOS [69]; and that further study of later data would show a reduced ageing rate in line with those measured by T2K and MINOS. For completeness, if a linear fit is applied only to the currently excluded Downstream ECal data recorded during the 2010–2011 period, an annual light loss rate of 1.33 ± 0.29 PEU per year on an initial light yield of 17.2 ± 0.3 is obtained. This is equivalent to annual reduction in light yield of $7.7 \pm 1.7\%$ which is in excellent agreement with the MINERνA result.

6.4 — Separation of ECal Scintillator and Fibre Degradation

The results shown in section 6.3 combines the ageing of the scintillator bars with that of the WLS fibres[1], therefore a second approach was applied to separate the two effects within the ECal data. Without applying the attenuation correction, the MIP MPV response is extracted at different distances from the sensor for each bar type during each T2K Run, see figure 6.3.

The best fit to the data was achieved by applying a double-exponential fit, which accounts for the short and long components of the fibre attenuation, of the form:

$$f(x) = S \exp\left(\frac{-x}{\lambda_S}\right) + L \exp\left(\frac{-x}{\lambda_L}\right), \tag{6.2}$$

where S and L are the fitted light yield in PEU at 0 cm from the MPPC for the short and long components of the exponential function, respectively; λ_S and λ_L are the associated short and long attenuation lengths; and x is the distance from the MPPC in cm.

6.4.1 — Scintillator Degradation

The parameters of the double-exponential fits can be used to calculate the predicted total MIP light yield at a distance of 0 cm from the MPPC, $S + L$. This should remove the dependence on the propagation of the light down the WLS fibre and the decrease in evaluated light yield will only be dependent on the ageing of the scintillator. The results for this evaluation are shown in figure 6.4 with both a linear and exponential fit applied to the data from 2012.

The linear fit is of the form:

$$f(t) = A - Bt, \tag{6.3}$$

where A is the fitted total MIP light yield ($S + L$) in PEU at year 0 (2010), B is the gradient of the fit in PEU per year, and t is the time in years since 2010. The fit parameters are shown in table 6.3.

[1] Any degradation of the coupling between the fibre and the MPPC, either through loss of transparency of the epoxy or gradual displacement of the fibre also contributes to the results.

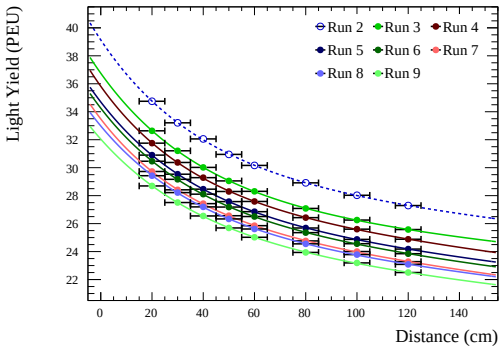

(a) ECal Barrel X.

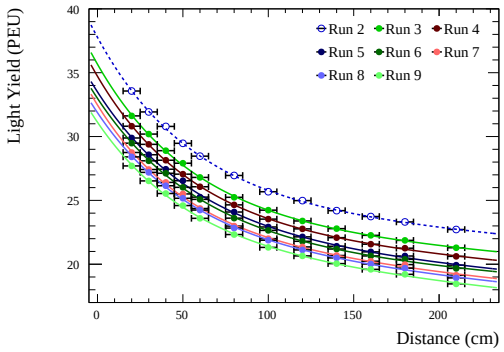

(b) ECal Barrel Y.

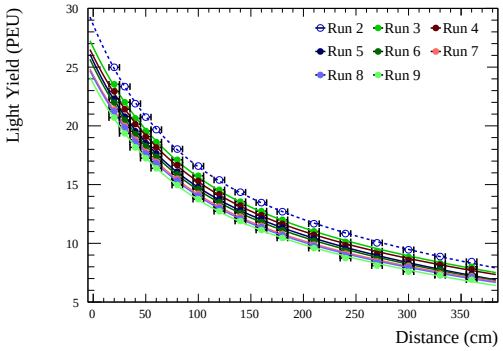

(c) ECal Barrel Z.

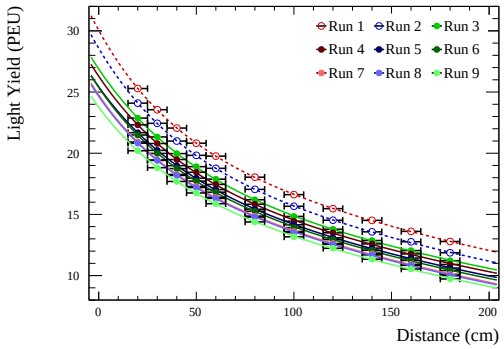

(d) Downstream ECal.

Figure 6.3: ECal light yield as a function of distance to the MPPC for each T2K Run. The errors on the data points are only the uncertainty on the Landau-Gaussian fit MPV at each distance point, no light yield stability uncertainty is applied. Results of the fits to the hollow data points are excluded from the subsequent data fits.

For the single-ended (mirrored) readout bars the reduction in light yield from the scintillator ageing is $\sim$0.75 PEU per year, and for the double-ended readout bars it is $\sim$0.50 PEU per year. This is a reduction of $\sim$2.1% for the single-ended (mirrored) bars, and $\sim$1.9% per year for the double-ended bars.

The exponential fit is of the form:

$$f\left(t\right) = A\exp\left(\frac{-t}{\tau}\right), \tag{6.4}$$

where A is the fitted total MIP light yield $(S+L)$ in PEU at year 0 (2010), τ is the time constant of the exponent in years, and t is the year since 2010. The fit parameters are shown in table 6.4.

For the linear fits the annual reduction in light yield is consistent within $\sim 1\sigma$ of the reference degradation shown in table 6.2, and similarly the time constant for the exponential fits is consistent within $\sim 1\sigma$ of the reference values shown in table 6.6. This suggests the ageing is dominated by the degradation of the scintillator rather than the WLS fibres.

The exception to this is the Barrel Z results which lie $\sim 2\sigma$ from the reference values and imply a slower rate of degradation than those shown in the earlier results of section 6.3 and 6.5. This is likely due to some loss in MIP hit efficiency at the furthest distances from the MPPCs as the scintillator degrades. This would truncate the rising edge of the MIP light yield distribution, see for example at a distance of 360 cm in figure

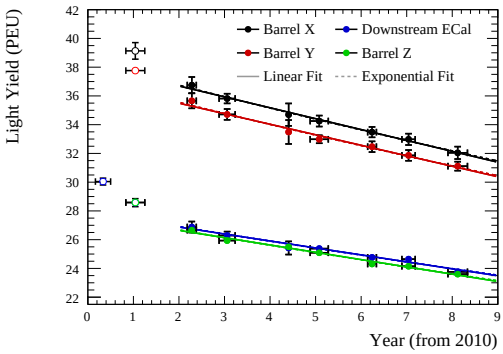

Figure 6.4: Light yield as evaluated at 0 cm from the MPPC for each ECal bar type. Hollow data points are excluded from the data fits.

Table 6.3: Linear fit parameters to ECal light yield at 0 cm from the MPPC from figure 6.4, and annual percentage reduction in light yield, relative to 2012 fit value. Reference results, in parentheses, from the linear fit in table 6.2 are included for comparison

ECal Bar Type	Readout Type	A (PEU)	B (PEU/yr)	χ^2/NDF	Annual Reduction (Ref.) (%)
Barrel X	Single-ended	38.21 ± 0.50	0.76 ± 0.09	$0.45/5 = 0.09$	2.07 ± 0.25 (1.98 ± 0.04)
Barrel Y	Single-ended	36.94 ± 0.47	0.73 ± 0.08	$1.40/5 = 0.28$	2.06 ± 0.23 (2.02 ± 0.05)
Barrel Z	Double-ended	27.65 ± 0.18	0.50 ± 0.03	$3.66/5 = 0.73$	1.88 ± 0.11 (2.15 ± 0.07)
Downstream	Double-ended	27.87 ± 0.32	0.49 ± 0.05	$2.69/5 = 0.54$	1.82 ± 0.18 (1.87 ± 0.07)

6.5, shifting the extracted MIP MPV to a slightly higher value than might be otherwise expected. The result would be an underestimate in the degradation rate extracted with this technique for the Barrel Z bars, leading to the discrepancy when making comparisons with the reference values.

Fortunately any loss in hit efficiency at the furthest distances from the MPPCs will have negligible impact on the overall hit reconstruction efficiency as the MPPC on the opposing end of the bars will continue to efficiently reconstruct these hits, as only one MPPC is required to reconstruct a hit on the double-ended readout bars.

This is confirmed by separate studies monitoring hit efficiency in the ECal modules which observed a negligible reduction ($\sim$0.1%) in the single-hit efficiency (requiring a hit in the single-ended readout bars, or at least one hit on either end of the double-ended readout bars) across all bar types during the current lifetime of the ECal. For the double-end readout bars the double-hit efficiency (requiring a hit on both ends of a scintillator bar) has reduced by $\sim$2% over the current lifetime.

In the future there may be some concern regarding the reconstruction of hits at the centre of the Barrel Z bars, where hits are equidistant from both sensors, and so where any impact on reconstruction efficiency will first become apparent. However, this is not a concern for the current data as shown by the MIP light yield distribution at a distance of 200 cm in figure 6.5, but will need to be monitored.

Table 6.4: Exponential fit parameters to ECal light yield at 0 cm from the MPPC from figure 6.4. Reference time constants, in parentheses, from the exponential fit in table 6.6 are included for comparison.

ECal Bar Type	Readout Type	A (PEU)	τ (Ref.) (yr)		χ^2/NDF
Barrel X	Single-ended	38.4 ± 0.5	45.2 ± 5.1	(47.7 ± 1.1)	$0.37/5 = 0.07$
Barrel Y	Single-ended	37.2 ± 0.5	45.2 ± 4.8	(45.7 ± 1.3)	$1.11/5 = 0.22$
Barrel Z	Double-ended	27.8 ± 0.02	49.5 ± 3.0	(44.1 ± 0.9)	$3.22/5 = 0.64$
Downstream	Double-ended	28.0 ± 0.3	51.6 ± 5.3	(49.2 ± 2.6)	$2.82/5 = 0.56$

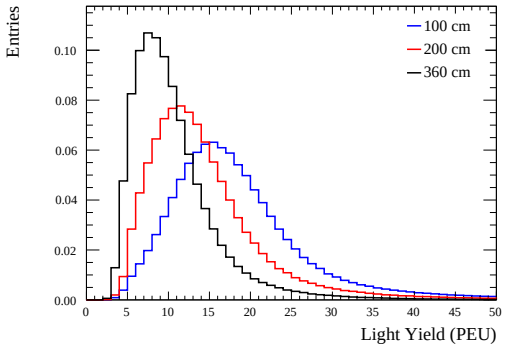

Figure 6.5: MIP light yield distribution in the ECal Barrel Z bars during T2K Run 9, for cosmic rays passing at distances of 100, 200 and 360 cm from the MPPCs.

6.4.2 — Fibre Degradation

Along with extracting the light yield from the fits in figure 6.3, it is also possible to study the change in the short and long attenuation length components of the double-exponential fit, λ_S and λ_L, respectively, for the WLS fibres. These are shown in figure 6.6 with linear fits applied to the data from 2012 of the form:

$$\lambda_i(t) = \lambda_i(0) - k_i t\,, \tag{6.5}$$

where $\lambda_i = \{\lambda_S, \lambda_L\}$ is the short or long attenuation length in cm at year 0 (2010), $k_i = \{k_S, k_L\}$ is the gradient of the fit in cm per year, and t is the year since 2010. The fit parameters are shown in table 6.5.

The short attenuation length varies between 36 and 72 cm, increasing as the bar length increases, and it appears to be consistent with minimally $(< 1\%)$ or not degrading with time. The exception to this is the Downstream ECal which shows a higher degradation rate of $3.51 \pm 0.69\%$, although if the earlier Run 1 and 2 data were to be included this would substantially reduce.

For the long attenuation length, the single-ended (mirrored) bars have much longer attenuation lengths compared to the double-ended readout bars, ~1120 and ~2220 cm for the Barrel X and Y bars, respectively, compared to ~520 and ~355 cm for the Barrel Z and Downstream bars, respectively. This discrepancy is due to the mirrored bars having two signals, direct transmission down the WLS fibres to the MPPCs, and reflected transmission, the combination of which is not accounted for in the fits, and so these are not true measurements of the long attenuation length.

For comparison, early fibre scanning work during construction on the ND280 ECals measured short and

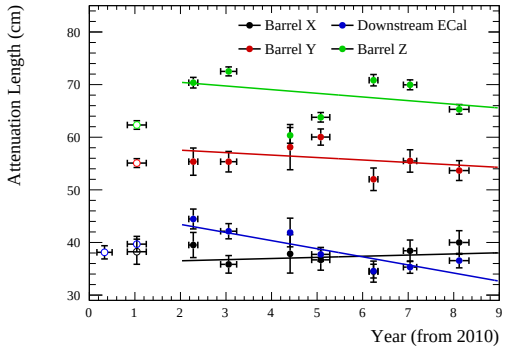

(a) Short attenuation length.

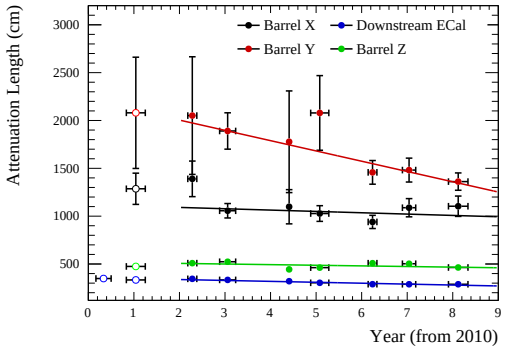

(b) Long attenuation length.

Figure 6.6: Short and long attenuation lengths, λ_S and λ_L respectively, from equation 6.2. Hollow data points are excluded from the data fits. Note the suppressed 0 for the ordinate of figure 6.6a.

Table 6.5: Linear fit parameters to ECal short and long attenuation length components of double-exponential fits from figure 6.6, and the annual percentage reduction, relative to 2012 fit values.

		Short Attenuation Length Component			
ECal Bar Type	Readout Type	λ_S (0) (cm)	k_S (cm/yr)	χ^2/NDF	Annual Reduction (%)
Barrel X	Single-ended	36.1 ± 2.3	-0.22 ± 0.41	$5.21/5 = 1.04$	-0.60 ± 1.12
Barrel Y	Single-ended	58.5 ± 2.4	0.47 ± 0.42	$11.10/5 = 2.22$	0.82 ± 0.73
Barrel Z	Double-ended	71.8 ± 1.1	0.70 ± 0.19	$87.16/5 = 17.43$	0.99 ± 0.27
Downstream	Double-ended	46.4 ± 1.8	1.52 ± 0.29	$8.48/5 = 1.70$	3.51 ± 0.69
		Long Attenuation Length Component			
ECal Bar Type	Readout Type	λ_L (0) (cm)	k_L (cm/yr)	χ^2/NDF	Annual Reduction (%)
Barrel X	Single-ended	1119 ± 117	13.9 ± 19.8	$5.98/5 = 1.20$	1.27 ± 1.82
Barrel Y	Single-ended	2218 ± 262	107.2 ± 35.6	$1.68/5 = 0.34$	5.35 ± 1.92
Barrel Z	Double-ended	520 ± 6	6.6 ± 1.1	$146.47/5 = 29.29$	1.30 ± 0.22
Downstream	Double-ended	354 ± 7	9.1 ± 1.1	$13.29/5 = 2.67$	2.71 ± 0.33

long attenuation lengths for the WLS fibres in the range 21–31 cm and 390–410 cm, respectively [168].

Kuraray have also measured the attenuation length of their fibres from light yield measurements over a distance range of 100–300 cm, fitting the distribution with a single exponential function and extracting an attenuation length of >350 cm [171], in agreement with our long attenuation length results.

The Mu2e collaboration which also uses Kuraray Y-11 WLS fibres has measured the attenuation length of the fibres, but over substantially longer fibre lengths of 25 m. In a 2015 study they applied a double-exponential fit to their data of the same form shown in equation 6.2 and extracted short and long attenuation lengths of 4.76 and 9.02 m, respectively [172]. A later study in 2018 separated the data into two independent exponential fits over the ranges 0.5–3.0 m and 3.0–25.0 m, and again extracting short and long attenuation lengths, this time of 5.1 ± 0.2 and 8.2 ± 0.1 m, respectively [173]. In both cases their short attenuation length measurement is consistent with the (double-ended readout bars) long attenuation lengths we have obtained. Perhaps of greater interest though are their measurements of attenuation length as a function of wavelength which show

very short attenuation lengths of less than 50 cm at 490 nm, approaching the peak quantum efficiency for our MPPCs which occurs at 440 nm [174] (unfortunately the Mu2e measurements do not extend to wavelengths below 490 nm) and longer attenuation lengths of ∼400 cm at 510 nm.

Kuraray Y-11 WLS fibres absorb light over wavelengths of ∼360–490 nm, and emit between ∼460–570 nm [171]. Our two attenuation length measurements can then be readily explained. A short attenuation length attributed to the overlapping absorption and emission regions of the Y-11 WLS fibres around ∼475 nm (near the maximum quantum efficiency of the MPPCs), and a longer attenuation length coinciding with the emission only region of the Y-11 WLS fibres at >490 nm (mean emission value of ∼510 nm [168]), as corroborated by the single wavelength Mu2e attenuation length measurements.

Irrespective of the mirroring or not, the long attenuation lengths do appear to be degrading by between 1.27% and 5.35% per year, although the single-ended (mirrored) bars have significant uncertainties on those rates.

As to why the long attenuation length would show degradation whilst the short attenuation length does not is unknown. Potentially a wavelength dependent change in the opacity of the fibres has occurred, allowing shorter wavelengths (<490 nm) to propagate in a consistent manner over the current lifetime of the WLS fibres, whilst increasing the opacity to longer wavelengths (>490 nm). However this is purely conjecture and we cannot ascribe a mechanism for such behaviour.

6.5 — Projected Future Response

The PØD subsystem of the ND280 is being decommissioned in 2022 to allow for the upgrade of the ND280 detector [175]. The remaining ECal, FGD, SMRD and INGRID subsystems will be retained in their current form, and so an understanding of their future response will become increasingly important as the T2K near detectors continue operating into the T2K-II [176] and the Hyper-Kamiokande [177] eras.

As such the future response of the ECal, FGD and INGRID subsystems has been projected through until 2040. The SMRD is excluded from this study as its initial light yield is substantially higher than for the other subsystems and its rate of degradation is lower. As such the likelihood of the light yield from this subsystem dropping below any reconstruction threshold is not considered to be an issue for the time period considered.

Although a linear fit to the data in section 6.3 results in a reasonable agreement, an exponential fit is better physically motivated. Figure 6.7 shows the projected future response from the earlier linear fits, and from the application of an exponential fit to the ECal and FGD data from 2012, and the INGRID data from 2010, onwards. The exponential fit is of the form:

$$f\left(t\right) = A \exp\left(\frac{-t}{\tau}\right), \tag{6.6}$$

where A is the fitted light yield in PEU at year 0 (2010), τ is the time constant of the exponent in years, and t is the year since 2010. The fit parameters are shown in table 6.6.

The time constant τ is consistent, ∼44–49 years, for all ECal bar types, along with the light yield constant A for the pairs of single-ended (mirrored), ∼26 PEU, and double-ended, ∼16 PEU, readout bars. The resultant

Table 6.6: Exponential fit parameters to ECal, FGD and INGRID data from figure 6.7.

ECal Bar Type	Readout Type	A (PEU)	τ (yr)	χ^2/NDF
Barrel X	Single-ended (mirrored)	27.39 ± 0.07	47.7 ± 1.1	$27.82/37 = 0.75$
Barrel Y	Single-ended (mirrored)	25.34 ± 0.08	45.7 ± 1.3	$28.27/37 = 0.76$
Barrel Z	Double-ended	16.10 ± 0.04	44.1 ± 0.9	$29.64/37 = 0.80$
Downstream	Double-ended	15.55 ± 0.07	49.2 ± 2.6	$10.28/37 = 0.28$
FGD	Single-ended (mirrored)	22.72 ± 0.20	80.3 ± 11.1	$0.68/5 = 0.14$
INGRID	Single-ended (mirrored)	24.61 ± 0.11	52.9 ± 2.4	$82.27/33 = 2.49$

χ^2/NDF for the exponential fits are marginally reduced by ∼0.1–0.2 compared to the corresponding linear fits shown in table 6.2.

The INGRID time constant of 52.9 ± 2.4 years is marginally longer that those recorded by the ECal, and the resultant χ^2/NDF for the exponential fit has slightly reduced by 0.22. The FGD records a significantly longer time constant of 80.3 ± 11.1 years and a negligible increase of 0.01 in its χ^2/NDF for the exponential fit compared to the linear fit. As with the linear ageing results (see table 6.2), some variation in the degradation rates between the different subsystems is expected due to the varying age and environmental exposure profiles of the scintillator bars, although why the FGD should be such an outlier is unclear.

The anticipated ECal response drops by ∼50% or ∼60% over thirty years for all bar types from extrapolations of the exponential and linear fits, respectively. This remains above the minimum charge threshold of 5.5 PEU required for use in the current ECal offline reconstruction algorithms. The value of this threshold has been chosen to avoid discrepancies between data and the current MC simulation at low charges. It should be possible to lower the current charge threshold through more detailed simulation of the detector response, for example including bar non-uniformity and improved MPPC dark-noise rate, and through enhancing the reconstruction algorithms. Without improvement there is a risk that information will be lost for particle interactions which deposit energy at values below the MIP MPV, potentially limiting the physics reach of analyses which utilise the ECals.

The FGD and INGRID subsystems expect their MIP MPV or MOM response to reduce by ∼30% and ∼40%, respectively, over thirty years under the hypothesis of an exponential decline. For both detectors this increases by a further ∼5-10% for a linear decline. For both scenarios this remains far above the hit thresholds of 5.0 and 2.5 PEU, respectively, currently used by the offline reconstruction algorithms for these detectors. If the true rate of ageing were to be higher, such as the ∼50–60% light yield reduction currently projected by the ECal, this would still not be a concern for these subsystems.

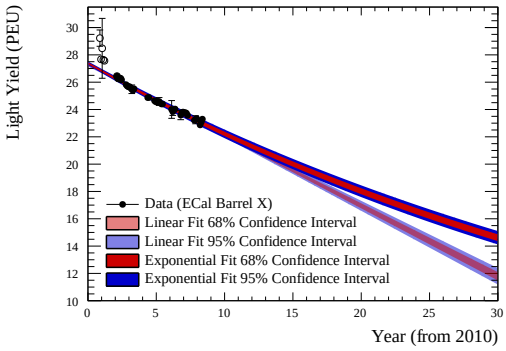

(a) ECal Barrel X.

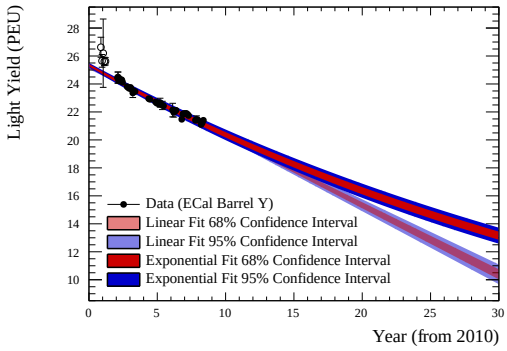

(b) ECal Barrel Y.

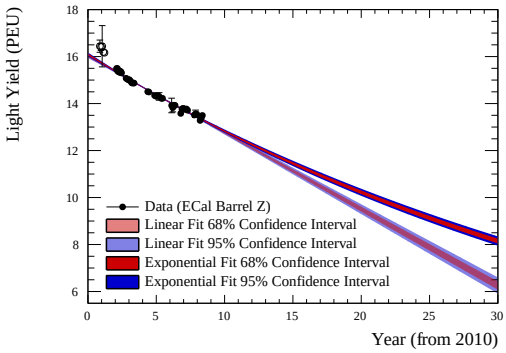

(c) ECal Barrel Z.

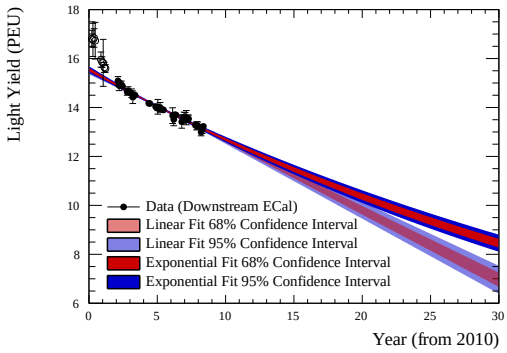

(d) Downstream ECal.

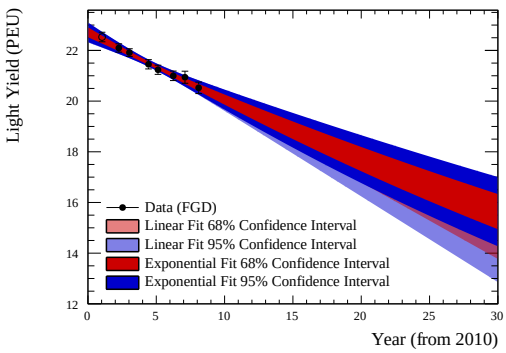

(e) FGD.

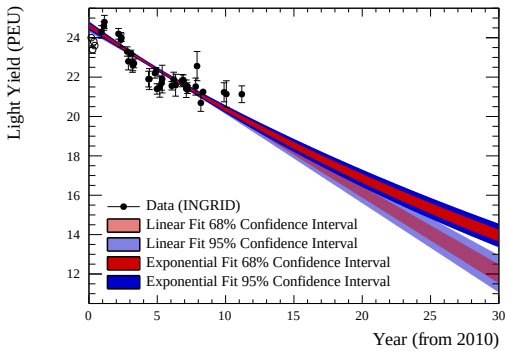

(f) INGRID.

Figure 6.7: Projected light yield for each ECal bar type, FGD and INGRID, showing the 68% and 95% confidence intervals extracted from both the linear and exponential fits to the data. Hollow data points are excluded from the data fits.

7 — Conclusion

n this thesis, both analyses were conducted using the beam data obtained from the T2K experiment. The analysis with a graphical constraint from Daya Baya experiment as well as plastic scintillator ageing study used data with an exposure of 1.9664×10^{21} POT in neutrino-mode running and 1.6346×10^{21} POT in antineutrino-mode running.

Using the Daya Bay data-fit probability surface for $\sin^2\theta_{13}$ and Δm^2 does not show any significant change in T2K's sensitivity to oscillation parameters, apart from a $\sqrt{2}$ improvement in Δm^2 1σ error band, due to error ranges comparable between T2K and Daya Bay. However, this method may be a way to more accurately handle correlations between oscillation parameters by setting constraints from reactor experiments. Since it does not slow down the computation time, it has the potential to be used within the VALOR experimental framework for future analysis. The mass ordering study carried out within this analysis shows an increase in the separation between the preferences of the normal and inverted mass orderings of ~ 1.9 times in comparison to T2K only and ~ 1.15 time in comparison to T2K with a gaussian constraint applied. Sensitivity studies were found to be in agreement with data fits, confirming all beforehand mentioned improvements in Δm^2 error size and separation between normal and inverted mass orderings.

And the last, for the scintillator ageing study, the decline in the performance of the scintillator material seems to be uniform across all T2K's near subdetectors. The results indicate that all subsystems exhibit a decrease in light yield ranging from approximately 0.3 to 0.5 photoelectrons per unit (PEU) per year. This translates to an annual reduction in light yield of 0.9% to 2.2% when compared to the 2012 fit values. These results are consistent with studies performed by a MINOS [69] experiment, which was using scintillator bars identical to some of the T2K's detectors. The results obtained from this study are important for modeling the performance of the ND280 detector in the future T2K-II phase. Additionally, some of the scintillator bars used in the update of the near detector complex are the same as those currently in use or new, but produced from similar materials by same manufacturers, making the obtained results even more relevant. At the moment, ageing constants are applied as a part of standard detector data calibration corrections.

Resumen

7.1 — Introdución

El estudio de los neutrinos ha sido un área fascinante de investigación en la física de partículas durante más de 80 años. Los neutrinos son partículas subatómicas notoriamente difíciles de detectar, pero juegan un papel crucial en nuestra comprensión del universo. Las oscilaciones de neutrinos, en las que los neutrinos cambian de un tipo a otro mientras viajan por el espacio, se propusieron por primera vez en la década de 1950 y luego se confirmaron mediante una serie de experimentos innovadores en las décadas de 1990 y 2000.

El descubrimiento del neutrino se remonta a la década de 1930 cuando los físicos Enrico Fermi y Wolfgang Pauli propusieron su existencia para explicar la aparente de conservación de energía en ciertos tipos de decaimiento nuclear. La primera evidencia experimental de la existencia del neutrino surgió en la década de 1950 a partir de estudios sobre el decaimiento beta nuclear, en el que un neutrón en un núcleo se desintegra en un protón, un electrón y un antineutrino. La existencia del antineutrino fue predicha por la misma teoría que predijo el neutrino y fue detectado por primera vez en 1956 por científicos en el reactor nuclear de Savannah River en Carolina del Sur.

Durante las décadas siguientes, los científicos continuaron estudiando neutrinos, pero todavía eran difíciles de detectar y medir. En la década de 1960 y 1970, los físicos Ray Davis y John Bahcall comenzaron una serie de experimentos para medir el flujo de neutrinos solares, que se producen en las reacciones de fusión que tienen lugar en el interior del sol. Sin embargo, descubrieron que solo estaban detectando una fracción del número esperado de neutrinos. Esto se denominó problema de los neutrinos solares y permaneció sin resolver durante varias décadas.

En la década de 1980 y 1990, se diseñó una nueva generación de experimentos para estudiar neutrinos de fuentes cósmicas y de reactores nucleares. Estos experimentos utilizaron detectores grandes, como el detector Kamiokande en Japón y el Observatorio de Neutrinos de Sudbury en Canadá, para detectar neutrinos midiendo los pequeños destellos de luz producidos cuando un neutrino interactúa con la materia.

Estos experimentos proporcionaron la primera evidencia de oscilaciones de neutrinos, en las que los neutrinos cambian de un tipo a otro mientras viajan por el espacio. La teoría de las oscilaciones de neutrinos se propuso por primera vez en la década de 1950, pero no se confirmó hasta las décadas de 1990 y 2000. El detector Super-Kamiokande en Japón proporcionó la primera evidencia definitiva de oscilaciones de neutrinos en 1998, cuando mostró que el número de neutrinos muónicos detectados era menor de lo esperado, lo que sugiere que

algunos de los neutrinos muónicos habían oscilado a neutrinos tauónicos.

El experimento T2K, que comenzó en 2010, es uno de los experimentos líderes en este campo, diseñado para estudiar las oscilaciones de neutrinos midiendo la aparición y desaparición de neutrinos a medida que viajan a través de la atmósfera terrestre. Utiliza un haz de neutrinos producido por un acelerador de protones ubicado en la costa este de Japón y dirigido hacia un detector ubicado a 295 km de distancia en el laboratorio subterráneo Super-Kamiokande. Al estudiar las propiedades de los neutrinos que llegan al detector, el experimento T2K puede determinar la probabilidad de oscilaciones de neutrinos y medir los parámetros de oscilación.

El estudio de las oscilaciones de neutrinos es una de las áreas más emocionantes de la física de partículas hoy en día. Los neutrinos son las partículas más abundantes en el universo, pero son notoriamente difíciles de detectar. Esto se debe a que interactúan débilmente con la materia y pueden pasar por enormes cantidades de material sin ser absorbidos ni dispersados.

El experimento T2K ya ha realizado importantes contribuciones a nuestra comprensión de las oscilaciones de neutrinos. En 2011, el experimento proporcionó la primera evidencia de la aparición de neutrinos electrónicos en un haz de neutrinos muónicos, lo que fue un gran avance en el campo. Desde entonces, el experimento T2K ha continuado recolectando datos y mejorando sus técnicas de medición, lo que ha llevado a mediciones aún más precisas de los parámetros de oscilación de neutrinos.

Los oscillaciones de neutrinos sigue siendo un área de investigación activa, con muchas preguntas sin respuesta que solo se pueden responder a través de estudios adicionales. Por ejemplo, el experimento aún no ha determinado el ordenamiento de las masas de los neutrinos, que es una pieza crucial de información para comprender la naturaleza de los neutrinos. Además, todavía hay mucho por aprender sobre las propiedades de los neutrinos y antineutrinos, como su fase de violación de CP, que podría tener importantes implicaciones para nuestra comprensión del universo temprano.

Todas estas preguntas abiertas requieren una refinación significativa de las tecnologías y enfoques que estamos utilizando ahora, tanto para el análisis de datos experimentales como para el estudio más cercano del rendimiento de los detectores que se están utilizando.

7.2 — Análisis de oscilaciones

La cadena de simulación utilizada para producir modelos necesarios para el análisis de oscilaciones se describe y resume de la siguiente manera.

Inicialmente, se pronostican los espectros de flujo para los detectores cercano y lejano utilizando simulaciones FLUKA y JNUBEAM. Se definen una variedad de incertidumbres relacionadas con la normalización del flujo de Super-K, donde la contribución más significativa a estas incertidumbres proviene de las interacciones hadrónicas. Estas incertidumbres se minimizan posteriormente a través de un ajuste a las multiplicidades de hadrones observadas en el experimento NA61/SHINE [74, 178, 179].

Resumimos los modelos de interacción implementados en la simulación MC NEUT para interacciones neutrino-núcleo en ambos detectores cercano y lejano. Se utiliza la función espectral Benhar [79] para modelar el estado nuclear inicial para las interacciones CCQE, mientras que se emplea el modelo más sencillo de gas

de Fermi relativista para todas las demás interacciones [76]. Se usa el modelo de Nieves et al. [154] para las interacciones 2p2h, y se utiliza el modelo de Rein-Sehgal [102] para la producción de piones, con un modelo de cascada NEUT que describe la SI y FSI de los piones. Se utilizan las funciones de distribución de partículas GRV98 [119] para modelar las interacciones DIS, con modificaciones en la región de baja Q^2 según Bodek y Yang [120]. Todos estos modelos se han ajustado a datos externos [75, 76]. Cada uno de estos modelos está asociado con varias incertidumbres, resultantes de parámetros de modelo no acotados, discrepancias entre los datos observados y las predicciones del modelo, o predicciones diferentes entre varios modelos de interacción válidos y entre sí.

En el lado del detector cercano, hay tres muestras de eventos de detector cercano utilizados: CC 0π, CC1π, y CC otros. Las predicciones simuladas de ND280 se ajustan a los datos observados del detector cercano, teniendo en cuenta todas las muestras, la influencia de las estadísticas limitadas del MC, así como todas las incertidumbres del flujo, la interacción y el detector ND280. El ajuste proporciona restricciones sobre los parámetros sistemáticos de los modelos de flujo e interacción, que luego se pasan a los análisis de oscilación como un vector de valores de parámetros de mejor ajuste y como una matriz de covarianza que contiene las incertidumbres y correlaciones de los parámetros [137].

En cuanto al detector lejano, hay cinco muestras de eventos estándar en el detector Super-K: la muestra de ν_μ / $\bar{\nu}_\mu$ CCQE-like, la muestra de ν_e / $\bar{\nu}_e$ CCQE-like y la muestra de ν_eCC1π^+-like. Para estas muestras corresponden diversas fuentes de incertidumbres tales como interacciones secundarias, efectos foto-nucleares, localización del vértice, dirección de la trayectoria, identificación de partículas, conteo de anillos de Cherenkov y reconstrucción de energía neutrónica. Estas incertidumbres se combinan en incertidumbres globales de normalización que abarcan energía neutrónica y tipos de interacción reconstruidos. Las incertidumbres resultantes se presentan como un vector de valores de mejor ajuste de parámetros y una matriz de covarianza que incluye las incertidumbres y correlaciones de los parámetros. Estos valores se utilizan posteriormente en los análisis de oscilación como indica [145].

Las restricciones en los parámetros de oscilación de interés se infieren produciendo intervalos de confianza frecuentistas a partir de relaciones de verosimilitud logarítmica marginal producidas mediante el análisis simultáneo de la tasa y la forma de las distribuciones cinemáticas de las cinco muestras de eventos de Super-K, teniendo en cuenta las incertidumbres sistemáticas en los modelos de flujo, interacción y detección. Las incertidumbres sistemáticas se caracterizan mediante parámetros sistemáticos, que actúan para ponderar la predicción nominal de MC teniendo en cuenta sus incertidumbres relativas y restricciones previas. El procedimiento general de análisis se describe con más detalle en [147]. Se pueden encontrar más detalles sobre las entradas del análisis de oscilaciones, la metodología y las opciones de implementación en los Chapter 3 y Chapter 4.

T2K es sensible y produce restricciones en θ_{13}; sin embargo, las mediciones más precisas del mundo de este parámetro son de experimentos con antineutrinos en reactores. Para restringir mejor este parámetro y obtener una mayor sensibilidad a otros parámetros, el ajuste global de PDG2019 [124] promedio de reactores de $0{,}0853 \pm 0{,}0027$ se usa como referencia previa PDF en $\sin^2 2\theta_{13}$ para la mayoría de las medidas presentadas en el Chapter 5. Este PDF anterior se denominará posteriormente „restricción del reactor “y las restricciones

producidas con él se denotará „T2K con restricción de reactor gaussiano“.

Para simplificar la implementación, la restricción se considera que sigue la distribución gaussiana con la media y sigma correspondiente al golpe de derecha mencionado en el valor de mejor ajuste global del PDG2019. Este enfoque tiene sus ventajas e inconvenientes. Claramente, una implementación dentro del software de análisis T2K, en particular en el software de análisis VALOR, es sencilla y no ralentiza los cálculos. Sin embargo, es solo una suposición, que se ha hecho exactamente para simplificar el análisis de oscilación. La eschema, descrita en Chapter 3,ya está bastante compleja. Por lo tanto, la principal motivación del presente estudio es explorar formas alternativas de tener en cuenta los datos del reactor, mejorando potencialmenteel uno que se utiliza actualmente.

En cuanto a los resultados de los experimentos del reactor, la mayoría de estos ha una banda de error asimétrica, es decir, no sería posible describirla mediante una distribución gaussiana. Esta discrepancia puede tener un impacto en el ajuste resultante. Además, en un análisis actual, cuando se aplica la restricción, se aplica solo en $\sin^2\theta_{13}$, por lo tanto una correlación previa entre θ_{13} y la diferencia de masa. Por último, pero no menos importante, los experimentos de los neutrinos de reactores, gracias a sus especificaciones pueden medir Δm^2 con una precisión comparable a los resultados de T2K. Una restricción aplicada en Δm^2 así como en $\sin^2\theta_{13}$ debería reducir un error en las medidas de Δm^2_{32} (Δm^2_{13}).

Sin embargo, el ajuste global se basa en los resultados de muchos experimentos de reactores, fuertemente dominados por Daya Bay. El experimento de Daya Bay [19] es un innovador experimento de oscilación de neutrinos ubicado en Guangdong, China. Fue diseñado para medir con precisión el ángulo de mezcla θ_{13}, uno de los parámetros clave que gobiernan las oscilaciones de neutrinos. El experimento involucra múltiples detectores de antineutrinos ubicados a diferentes distancias de una planta de energía nuclear, eso permite a medir precismente los parametros de oscillaciones de los antineutrinos entre diferentes sabores a medida que viajan por el espacio. Los resultados líderes en el mundo en la medicón de $\sin^2\theta_{13}$ y la compatibilidad mencionada para Δm^2 con T2K hacen de Daya Bay una fuente ideal para este estudio. Usar su superficie de probabilidad directamente como una restricción, en lugar de una aproximación gaussiana, permitirá verificar el efecto de la asimetría de la superficie, tratar correctamente la correlación contada como insignificante en el análisis actual y, además, aprovechar que los experimentos reactorales son sensibles al parámetro de división de masas Δm^2 .

Se realizaron estudios de sensibilidad para evaluar la capacidad de T2K para medir varios parámetros de oscilación de interés bajo una hipótesis de oscilación, utilizando los valores de parámetros de oscilación de Asimov A enumerados en la tabla 4.8. La sensibilidad se evaluó utilizando ordenaciones de masas y con diferentes restricciones: con restricción gaussiana en $\sin^2 2\theta_{13}$ de los experimentos del reactor y con la superficie de probabilidad de Daya Bay como una restricción en ambos Δm^2 y $\sin^2\theta_{13}$, según el método descrito en Chapter 4.

Debido a restricciones computacionales, se utilizó el método constante $\Delta\chi^2$ para construir regiones de confianza, en lugar del método más preciso de Feldman-Cousins descrito en la Sección 4.2. Como resultado, la cobertura esperada de las regiones de confianza puede no ser perfectamente precisa.

El uso de la restricción del reactor gráfico es ventajoso para las mediciones de Δm^2_{32} (ver Fig. 7.1,). Mejora

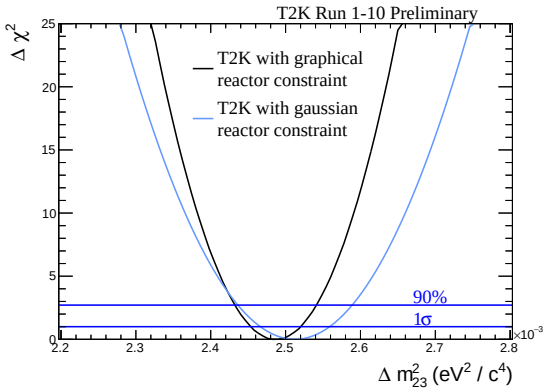

Figura 7.1: Una comparación de la sensibilidad T2K con una restricción de reactor estándar y un uso de la superficie de probabilidad para Δm^2_{32}

χ^2	NO	I)	$\Delta\chi^2_{IO-NO}$
Solo T2K	9.459	10.838	1.378
T2K con restricción gaussiana	9.977	12.340	2.362
T2K con restricción de superficie de probabilidad de Daya Bay	10.028	12.739	2.711

Cuadro 7.1: χ^2 valores para T2K valor de mejor ajuste predicho para pedidos de masa normal e invertida. En ambos casos se supone que el orden de masas normal es verdadero.

la sensibilidad de T2K a este parámetro, reduciendo la región 1σ en $\sim 1{,}4$ veces, es decir, en $\sim \sqrt{2}$, como se esperaba. La diferencia en los valores de mejor ajuste en Fig. 7.3 aparecen debido a la aplicación de una restricción en Δm^2_{32} junto con $\sin^2\theta_{13}$, mientras que una penalización gaussiana aplica una restricción solo en Δm^2_{32} . Sin embargo, no hay un impacto significativo en otros parámetros de oscilación (ver Figs. 5.3a and 5.3c), ni sobre sus correlaciones (ver Figs. 5.4a, 5.4c and 5.4d). Esto demuestra la solidez del enfoque de análisis T2K actual para la restricción del reactor: uso de la restricción 1D. Aunque no permite beneficiarse de toda la información que proporcionan los experimentos de reactor, un acuerdo entre los resultados obtenidos demuestra que la aproximación gaussiana 1D es lo suficientemente buena. Puntos de mejor ajuste e intervalo de confianza resultantes de los ajustes 1D se muestran en Table 5.1.

El estudio de sensibilidad ha demostrado que el uso del restricion gráfico de reactores es ventajoso para las mediciones de Δm^2_{32} (ver Fig. 5.3b, Fig. 5.4b), Fig. 5.4d) permite excluir una región más grande que con el uso de una restricción gaussiana ($\approx \sqrt{2}$). La relación E/L del experimento T2K no permite discriminar claramente entre hiercarcia de masa de los neutrinos. Una conclusión sobre la preferencia hacia el orden de masa normal (NO) o invertido (IO) en el análisis de oscilación T2K generalmente está impulsado por probabilidades posteriores en análisis puro bayesiano . Sin embargo, como se mostró anteriormente, al sumar el resultado de Daya Bay en Δm^2 a T2K mejora la sensibilidad al término de diferencia de masa y puede potencialmente afectar la sensibilidad a la ordenación en masa también.

Se calculó $\Delta\chi^2_{IO-NO}$ usando los resultados de los ajustes de Δm^2 vs $\sin^2\theta_{13}$ para la jerarquía de masa normal e invertida. Para el caso de T2K, T2K con una restricción de reactor gaussiano y T2K con restricción

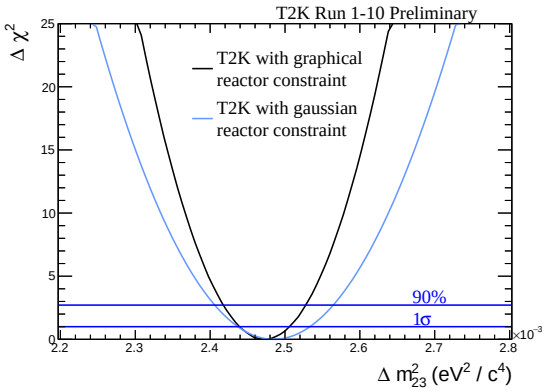

Figura 7.2: Comparación del resultado de los datos T2K con una restricción de reactor estándar y un uso de la superficie de probabilidad para Δm^2_{32} .

χ^2	NO	IO	$\Delta\chi^2_{IO-NO}$
Solo T2K	475.392	476.166	0.774
T2K con restricción gaussiana	478.907	480.174	1.267
T2K con restricción de superficie de probabilidad de Daya Bay	475.821	477.296	1.475

Cuadro 7.2: χ^2 valores para datos T2K valor de mejor ajuste para pedidos de masa normal e invertida. En ambos casos se supone que el orden de masas normal es verdadero.

de superficie de probabilidad de Daya Bay, estudio muestra (Table 7.4) que la última opción da un aumento en separación entre el ordenamiento de la masa de los neutrinos: $\sim 1{,}97$ veces en comparación con el resultado T2K solamente y $\sim 1{,}15$ veces en comparación con la restricción del reactor Gaussiana.

Los resultados del ajuste de datos son consistentes con los estudios de sensibilidad. Hay una ligera diferencia entre un valor central para δ_{CP} (ver Fig. 5.6a), sin embargo, no conduce a un cambio significativo en la región de confianza. Tanto el uso de la restricción del reactor gráfico en Δm^2_{32} , como para los estudios de sensibilidad, estrechan una región de 1σ en $\sim 1{,}4$ veces en comparación con la resultado con el restricción gaussiana estándar aplicada (ver Fig. 7.4).

En cuanto al estudio de ordenamiento de masa de los neutrinos, el resultado del ajuste de datos se mantiene de acuerdo con los estudios de sensibilidad (ver Table 7.2) que muestran una mejora en la separación entre NO e IO de $\sim 1{,}9$ veces en comparación con el ajuste de datos solo de T2K e incluso una mejor separación de $\sim 1{,}16$ veces en comparación con T2K con un ajuste de datos aplicado con restricción gaussiana.

7.3 — Envejecimiento de los detectores de centelleo de plástico

Otro factor que afecta a T2K es la comprensión del rendimiento del detector. El complejo de detectores cercanos proporciona la mayoría de las restricciones cruciales sobre los parámetros de interacción de neutrinos, utilizados en el análisis de oscilación. Sin embargo, ha estado en uso durante más de una década, una

edad significativa para un centelleador plástico que opera en un campo magnético. Por lo tanto, una parte del trabajo actual se centra en el estudio del envejecimiento de las barras de centello del detector cercano.

El problema del envejecimiento del centelleador plástico es bien conocido [156], y existen numerosos estudios destinados a medir, caracterizar y desarrollar métodos de estabilización para estos materiales ampliamente utilizados (consulte, por ejemplo, [157–163]). Estos estudios a menudo consideran el impacto de factores ambientales potencialmente controlables, como la temperatura y la humedad, en el rendimiento a largo plazo de los materiales, así como formas de estabilizarlos químicamente.

El mecanismo exacto del envejecimiento del centelleador en los detectores cercanos de T2K es desconocido, pero hay varios factores potencialmente contribuyentes:

- El estrés mecánico del centelleador que causa el desarrollo de grietas o cortes dentro del material [164]. Estos inhiben la dispersión uniforme de la luz dentro del centelleador, impidiendo la transmisión a través de la reflexión total interna.

- El empañamiento de los centelleadores debido a la penetración de agua en el material y la condensación [165]. Esto aumenta la opacidad del centelleador y es un problema significativo donde los materiales están expuestos a condiciones de humedad muy alta con grandes variaciones de temperatura.

- La oxidación del centelleador a través de procesos fotoquímicos que conducen a la producción de peróxidos que causan el amarillamiento del material [166]. Esto reduce el rendimiento de luz del centelleador y se ha observado en la prueba de envejecimiento acelerado realizada en las barras de centelleador utilizadas por el experimento MINOS [69], que son materialmente idénticas a los subsistemas FGD, ECaL y PØD de T2K como se describe en Capítulo 2.

El estudio presentado en este capítulo no diferencia entre los factores de envejecimiento mencionados anteriormente.

Para comenzar, es importante observar de cerca la composición del complejo de detectores cercanos de T2K.

Los primeros neutrinos encuentran un complejo de detectores cercanos, ubicado a 280 metros de la estación de destino. Aquí se supone que el flujo contiene principalmente neutrinos aún no oscilados. El detector INGRID se encuentra en línea recta con el eje del haz, mientras que el complejo ND280 está desplazado 2.5°. Ambos detectores están compuestos principalmente de contadores de centelleo plástico de diversas formas y orígenes.

INGRID está situado exactamente en el eje del haz de T2K y es crucial para el monitoreo directo de la tasa y estabilidad del haz junto con la medición de las secciones transversales de interacción de neutrinos en objetivos de hierro y del centelleador. El detector en sí consta de 14 módulos tipo sándwich de placas de hierro y centelleador rodeados por paneles de veto. Los módulos de INGRID forman una cruz, centrada en el eje del haz con una precisión de 0,4 mrad. Los módulos laterales se utilizan para medir la asimetría del haz.

Las barras de centelleo extruidas de INGRID fueron fabricadas en 2007-2008 en Fermilab utilizando poliestireno DowStyron 663 W dopado con un $1\,\%$ de PPO y un $0{,}03\,\%$ de POPOP. Cada barra está recubierta con una capa de TiO_2 para reflejar difusamente la luz del centelleador. Una fibra de desplazamiento de longitud

de onda (WLS) Kuraray Y11 pasa por el centro de la barra y recoge la luz para llevarla hacia una lectura de MPPC de Hammamtsu en el extremo no espejado de la barra.

El detector cercano fuera del eje está situado a 280 metros del blanco y a 2.5° grados con respecto al eje del haz. ND280 mide el flujo y espectro para las diferentes especies de neutrinos en el haz antes de la oscilación, así como varias secciones eficaces de interacción de neutrinos con los materiales del detector, por ejemplo, agua y carbono. Un conocimiento preciso del haz de neutrinos inicial es crucial para predecir el flujo y espectro de neutrinos en el detector lejano, y por lo tanto, para determinar los parámetros de oscilación de neutrinos. Además, la medición de la sección eficaz de ν_μ proporciona una gran restricción a los fondos para la búsqueda de aparición de ν_e.

Un detector de piones neutros (PØD), tres cámaras de proyección temporal (TPC) y dos detectores de granulometría fina (FGD) componen el núcleo, conocido como la parte "tracker"de ND280. El tracker está rodeado por calorímetros electromagnéticos (ECaL) y luego por un imán, reutilizado después de los experimentos UA1 [68] y NOMAD. Los espacios de aire del imán están equipados con el detector de alcance muónico lateral (SMRD). El imán proporciona un campo magnético de 0.2T que es crucial para distinguir partículas cargadas positiva y negativamente.

Excepto por las cámaras de proyección temporal, todos los subsistemas del complejo de detectores ND280 utilizan barras centelladoras como material activo de detección. Cuando una partícula pasa a través de estos detectores, excita electrones de valencia en el material de la barra, que luego emiten fotones con una longitud de onda de alrededor de 420 nm. Para la lectura de las señales, se utilizan contadores de fotones de píxeles múltiples (MPPC) en lugar de PMT debido al campo magnético. Se utilizan fibras de cambio de longitud de onda (WLS) para transportar fotones a los MPPC, cambiando su longitud de onda de azul a verde. Las barras centelladoras utilizadas en los detectores ND280 fueron producidas entre 2006 y 2009 y provienen de varios fabricantes.

Para medir la degradación en la respuesta del centellador, se registró el rendimiento de luz de las partículas ionizantes mínimas (MIP) que pasaban a través de los subsistemas ND280 y se calibraron como hits. Se utilizaron interacciones de neutrinos del haz, muones cósmicos o datos de muones de arena (los muones producidos en reaciones de los neutrinos en material que rodea el detector) como muestras de MIP. El rendimiento de luz de la MIP se corrigió en función de la longitud del camino de la MIP y la atenuación en la fibra WLS. Se realizaron ajustes regulares a la sobretensión de los MPPC para mantener una ganancia estable. T2K ha estado en funcionamiento desde 2010 y se utilizaron datos de las ejecuciones 2 a 9 en los análisis. Para todos los subsistemas, se crearon histogramas de carga acumulada por unidad de longitud mediante la combinación de respuestas de MPPC para pistas similares a MIP y se ajustaron con una distribución Gaussiana-Landau.

La distribución de la MPV de MIP de ND280 se extrajo para cada subsistema durante cada ejecución de T2K y luego se ajustó con una función lineal para calcular la caída general en el rendimiento de luz y los decrementos anuales.

Los datos se agregan por T2K Run para el PØD, FGD y SMRD, con el error de tiempo siendo la desviación estándar en la marca de tiempo de todos los hits de MIP durante cada T2K Run. Para el ECal, la mayor estadística permite que los datos se agreguen por mes o por cada T2K Run del J-PARC Main Ring (generalmente

Cuadro 7.3: Parámetros de ajuste lineal para los datos del PØD, FGD, SMRD y ECal de la figura 6.2 y la reducción porcentual anual, en relación a los valores de ajuste de 2012. Las barras de lectura de un solo extremo están espejadas en un extremo.

Subsystem	Readout Type	A (PEU)	B (PEU/yr)	χ^2/NDF	Annual Reduction (%)
Super-PØDule 0	Single-ended	$19{,}97 \pm 0{,}15$	$0{,}35 \pm 0{,}03$	$4{,}35/5 = 0{,}87$	$1{,}82 \pm 0{,}16$
Super-PØDule 1	Single-ended	$21{,}17 \pm 0{,}16$	$0{,}36 \pm 0{,}04$	$10{,}39/5 = 2{,}08$	$1{,}76 \pm 0{,}20$
Super-PØDule 2	Single-ended	$21{,}15 \pm 0{,}17$	$0{,}36 \pm 0{,}03$	$9{,}14/5 = 1{,}83$	$1{,}76 \pm 0{,}15$
Super-PØDule 3	Single-ended	$21{,}33 \pm 0{,}16$	$0{,}37 \pm 0{,}03$	$5{,}46/5 = 1{,}09$	$1{,}80 \pm 0{,}15$
FGD	Single-ended	$22{,}68 \pm 0{,}19$	$0{,}27 \pm 0{,}04$	$0{,}74/5 = 0{,}15$	$1{,}22 \pm 0{,}18$
SMRD	Double-ended	$60{,}86 \pm 1{,}48$	$0{,}54 \pm 0{,}26$	$2{,}62/5 = 0{,}52$	$0{,}90 \pm 0{,}44$
Barrel X	Single-ended	$27{,}27 \pm 0{,}06$	$0{,}52 \pm 0{,}01$	$33{,}09/37 = 0{,}89$	$1{,}98 \pm 0{,}04$
Barrel Y	Single-ended	$25{,}21 \pm 0{,}08$	$0{,}49 \pm 0{,}01$	$31{,}88/37 = 0{,}86$	$2{,}02 \pm 0{,}04$
Barrel Z	Double-ended	$16{,}01 \pm 0{,}04$	$0{,}33 \pm 0{,}01$	$36{,}60/37 = 0{,}99$	$2{,}15 \pm 0{,}07$
Downstream	Double-ended	$15{,}48 \pm 0{,}06$	$0{,}28 \pm 0{,}01$	$11{,}57/37 = 0{,}31$	$1{,}87 \pm 0{,}07$

alrededor de 1 mes), respectivamente. El ajuste solo se aplica a los datos a partir de enero de 2012 para los subsistemas de ND280 ya que los procedimientos de calibración actuales y la preescala de desencadenamiento de rayos cósmicos no se finalizaron hasta ese momento. Para los subsistemas PØD y ECal, el estudio se ha realizado para todos los submódulos o tipos de barras por separado.

Sin conocimiento de los mecanismos de envejecimiento que degradan los subsistemas ND280, es difícil saber qué forma se espera que tome la dependencia temporal de la tasa de envejecimiento. A priori, podría esperarse que una función exponencial fuera adecuada. Sin embargo, dada la distribución de datos observados y la escala de tiempo estudiada, se encuentra que un ajuste lineal simple es apropiado y se aplica en la forma:

$$f(t) = A - Bt\,, \tag{7.1}$$

donde A es la producción de luz ajustada en PEU en el año 0 (2010), B es la pendiente del ajuste en PEU por año, y t es el año desde 2010. Los parámetros de ajuste se muestran en la tabla 7.3.

La degradación del centelleador parece ser bastante consistente en todos los subsistemas. Todos muestran una reducción en el rendimiento de la luz en el rango de aproximadamente 0.3-0.5 PEU por año, lo que equivale a una reducción anual del rendimiento de la luz del 0.9-2.2 % en relación con sus valores de ajuste de 2012.

7.4 — Conclusiones

En esta tesis, ambos análisis se realizaron utilizando los datos de haz obtenidos del experimento T2K. Tanto el análisis con una restricción gráfica del experimento de Daya Baya, así como el estudio de envejecimiento del centelleador plástico, utilizaron datos con una exposición de $1,9664 \times 10^{21}$ POT en funcionamiento en modo neutrino y $1,6346 \times 10^{21}$ POT en funcionamiento en modo antineutrino.

El uso de la superficie de probabilidad de ajuste de datos de Daya Bay para $\sin^2\theta_{13}$ y Δm^2 no muestra ningún cambio significativo en la sensibilidad de T2K a los parámetros de oscilación, además de una mejora de $\sqrt{2}$ en la banda de error Δm^2 1σ, debido a los rangos de error comparable entre T2K y Daya Bay. Sin

embargo, este método puede ser una forma de manejar con mayor precisión las correlaciones entre parámetros de oscilación mediante el establecimiento de restricciones de los experimentos del reactor. Como no ralentiza el tiempo de cálculo, tiene el potencial de usarse dentro del marco experimental VALOR para análisis futuros. El estudio de ordenamientos en masa llevado a cabo dentro de este análisis muestra un aumento en la separación entre las preferencias de los ordenamientos de masa normal e invertida de $\sim 1,9$ veces en comparación con T2K solamente y $\sim 1,15$ veces en comparación con T2K con una restricción gaussiana aplicada. Se encontró que los estudios de sensibilidad están de acuerdo con los ajustes de datos, lo que confirma todas las mejoras mencionadas anteriormente en el tamaño del error Δm^2 y la separación entre la masa normal y la invertida. pedidos

Y por último, para el estudio de envejecimiento del centelleador, la disminución en el rendimiento del material del centelleador parece ser uniforme en todos los subdetectores cercanos de T2K. Los resultados indican que todos los subsistemas exhiben una disminución en el rendimiento de luz que oscila entre aproximadamente 0,3 y 0,5 fotoelectrones por unidad (PEU) por año. Esto se traduce en una reducción anual del rendimiento de luz del 0,9 % al 2,2 % en comparación a los valores de ajuste de 2012. Table 7.3 muestra los parámetros de ajuste lineal para los datos PØD, FGD, SMRD y ECal y la reducción porcentual anual, con respecto a los valores fijados para 2012. Las barras de lectura de un solo extremo se reflejan en un extremo. Estos resultados son consistentes con los estudios realizados por el experimento MINOS [69], que usaba barras de centelleo idénticas a algunos de los detectores del T2K. Los resultados obtenidos de este estudio son importantes para modelar el rendimiento del detector ND280 en la futura fase T2K-II. Además, algunas de las barras de centelleo utilizadas en la actualización del complejo de detectores cercanos son las mismas que las que se utilizan actualmente. Antiguos o nuevos, pero producidos con materiales similares por los mismos fabricantes, lo que hace que los resultados obtenidos sean aún más relevantes. Por el momento, las constantes de envejecimiento se aplican como parte de las correcciones de calibración de datos del detector estándar.

Summary

7.5 — Introducion

The study of neutrinos has been a fascinating area of research in particle physics for more than 80 years. Neutrinos are subatomic particles that are notoriously difficult to detect, but play a crucial role in our understanding of the universe. Neutrino oscillations, in which neutrinos change from one type to another as they travel through the space, were first proposed in the 1950s and later confirmed by a series of groundbreaking experiments in the decades of the 1990s and 2000s.

The discovery of the neutrino dates back to the 1930s when physicists Enrico Fermi and Wolfgang Pauli proposed their existence to explain the apparent conservation of energy in certain types of nuclear decay. The first experimental evidence of the neutrino arose in the 1950s from studies on nuclear beta decay, in which a neutron in a nucleus decays into a proton, an electron and an antineutrino. The existence of the antineutrino was predicted by the same theory that predicted the neutrino, and it was detected. for the first time in 1956 by scientists at the Savannah River nuclear reactor in South Carolina.

Over the next few decades, scientists continued to study neutrinos, but they were still difficult to detect and measure. In the 1960s and 1970s, physicists Ray Davis and John Bahcall began a series of experiments to measure the flux of solar neutrinos, that occur in the fusion reactions that power the sun. However, they found that they were only detecting a fraction of the number expected from neutrinos. This became known as the solar neutrino problem and remained unsolved for several decades.

In the 1980s and 1990s, a new generation of experiments was designed to study neutrinos from cosmic sources and from nuclear reactors. These experiments used large detectors, such as the Kamiokande detector in Japan and the Sudbury Neutrino Observatory in Canada, to detect neutrinos by measuring the tiny flashes of light produced when a neutrino interacts with matter.

These experiments provided the first evidence for neutrino oscillations, in which neutrinos change from one type to another. while traveling through space. The theory of neutrino oscillations was first proposed in the 1950s, but not confirmed. until the 1990s and 2000s. The Super-Kamiokande detector in Japan provided the first definitive evidence of neutrino oscillations in 1998, when he showed that the number of detected muon neutrinos was lower than expected, suggesting that some of the muon neutrinos had oscillated to tau neutrinos.

The T2K experiment, which began in 2010, is one of the leading experiments in this field, designed to study

neutrino oscillations by measuring the appearance and disappearance of neutrinos as they travel through the terrestrial atmosphere. It uses a neutrino beam produced by a proton accelerator located on the east coast of Japan. and directed towards a detector located 295 km away in the underground Super-Kamiokande laboratory. By studying the properties of neutrinos arriving at the detector, the T2K experiment can determine the probability of neutrino oscillations and measure the oscillation parameters

The study of neutrino oscillations is one of the most exciting areas of particle physics today. Neutrinos are the most abundant particles in the universe, but they are notoriously difficult to detect. This is because they interact weakly with matter and can pass through huge amounts of material without being absorbed or dispersed.

The T2K experiment has already made important contributions to our understanding of neutrino oscillations. In 2011, the experiment provided the first evidence for the appearance of electron neutrinos in a muon neutrino beam, which was a breakthrough in the field. Since then, the T2K experiment has continued to collect data and improve its measurement techniques, which has led to even more precise measurements of neutrino oscillation parameters.

Neutrino oscillations remain an area of active research, with many unanswered questions that can only be resolved through additional studies. For example, the ordering of neutrino masses hasn't been determined yet, which is a crucial piece of information for understanding the nature of neutrinos. Besides, there's still a lot to learn. on the properties of neutrinos and antineutrinos, such as their CP violation phase, which could have important implications for our understanding of the early universe.

All of these open questions require significant refinement of the technologies and approaches we are now using, both for the analysis of experimental data and for the closer study of the performance of the detectors that are being used.

7.6 — Oscillation analysis

The simulation chain used to produce models needed for oscillation analysis It is described and summarized as follows.

Initially, the flux spectra for the near and far detectors are predicted using FLUKA and JNUBEAM simulations. A variety of uncertainties related to the normalization of the Super-K flux are defined, where the largest contribution significant to these uncertainties comes from hadronic interactions. These uncertainties are subsequently minimized through a fit to the hadron multiplicities observed in the NA61/SHINE [74, 178, 179] experiment.

Shortly summarizing the interaction models implemented in the MC NEUT simulation for neutrino-nucleus interactions in both near and far detectors. The spectral function Benhar [79] is used to model the initial nuclear state for CCQE interactions, while using the simpler Fermi gas model relativistic for all other interactions [76]. The Nieves et al. model is used. [154] for 2p2h interactions, and the Rein-Sehgal [102] model is used for pion production, with a model NEUT cascade that describes the SI and FSI of the pions. The particle distribution functions GRV98 [119] are used to model DIS interactions, with modifications in the region of low Q^2

according to Bodek and Yang [120]. All these models have been fitted to external data [75,76]. Each of these models is associated with various uncertainties, resulting from unbounded model parameters, discrepancies between data observed and the model's predictions, or different predictions between several competing and valid interaction models.

On the near detector side, there are three samples of near detector events used: CC 0π, CC1π, and CC other. The simulated predictions of ND280 fit the observed data from the near detector, taking all samples into account, the influence of the limited statistics of the MC, as well as all the uncertainties of the flow, the interaction and the ND280 detector. The fit provides constraints on the systematic parameters of the flow and interaction models, which are then passed to oscillation analyzes as a vector of best-fit parameter values and as a covariance matrix containing the uncertainties and correlations of the parameters [137].

As for the far detector, there are five standard event samples in the Super-K detector: the ν_μ / $\bar{\nu}_\mu$ CCQE-likesample, the ν_e / $\bar{\nu}_e$ CCQE-likesample, and the ν_eCC$1\pi^+$-likesample. Various sources of uncertainties correspond to these samples, such as secondary interactions, photonuclear effects, vertex location, trajectory direction, particle identification, Cherenkov ring count and neutron energy reconstruction. These uncertainties are combined into global normalization uncertainties. covering neutron energy and reconstructed types of interaction. The resulting uncertainties are presented as a vector of best-fit parameter values and a covariance matrix that includes the uncertainties and parameter correlations. These values are later used in oscillation analysis as [145].

Constraints on the oscillation parameters of interest are inferred by producing frequentist confidence intervals a from marginal log-likelihood ratios produced by simultaneous analysis of rate and shape of the kinematic distributions of the five Super-K event samples, taking into account systematic uncertainties in flow, interaction and detection models. Systematic uncertainties are characterized by systematic parameters, which act to weight the nominal MC prediction taking into account their relative uncertainties and prior constraints. The general analysis procedure is described in more detail in T2K-TN306. More details on the oscillation analysis inputs, methodology and implementation options can be found in Chapter 3 and Chapter 4.

T2K is sensitive and produces constraints on θ_{13}; however, the most accurate measurements in the world of this parameter are from experiments with antineutrinos in reactors. So, to better constrain this parameter and get higher sensitivity to other parameters, PDG2019 [124] global fit of reactors average of 0.0853 ± 0.0027 is used as a previous reference PDF in $\sin^2 2\theta_{13}$ for most of the measurements presented in the Chapter 5. This above PDF will be referred to later as „reactor constraint“ and the constraints produced with it will be denoted „T2K with Gaussian reactor constraint“.

To simplify implementation, the restriction is considered to follow the Gaussian distribution with the mean and sigma corresponding to the forehand mentioned in the PDG2019 global best fit value and es. This approach has its advantages and drawbacks. Clearly, an implementation within the T2K analysis software, in particular the VALOR analysis software, is simple and does not slow down the calculations. However, it is just an assumption, which has been made, exactly, to simplify the process, such as oscillation analysis. A scheme, described in Chapter 3, is already quite complex. Therefore, the main motivation of the present study is to explore alternatives ways to factor in reactor data, potentially improving one currently in use.

As for the results of the reactor experiments, most of these have an asymmetric error band, that is, it would not be possible to describe it by means of a Gaussian distribution. This discrepancy may have an impact on the fit result. Also, in a current analysis, when the constraint is applied, it is applied only on $\sin^2\theta_{13}$, thus a prior correlation between θ_{13} and mass spitting And last but not least, experiments with reactors can usually measure Δm^2 with an accuracy comparable to T2K results. A constraint applied on Δm^2 as well as $\sin^2\theta_{13}$ should reduce an error in Δm^2_{32} (Δm^2_{13}) measurements.

However, the global constraint is based on the results of many reactor experiments, strongly dominated by Daya Bay. The Daya Bay [19] experiment is an innovative neutrino oscillation experiment located in Guangdong, China. It was designed to accurately measure the mixing angle θ_{13}, one of the key parameters of neutrino oscillations. The experiment involves multiple antineutrino detectors located at different distances from a nuclear power plant, allowing for precise measurements of the rate at which antineutrinos oscillate between different flavors as they travel through space.

The world leading results in $\sin^2\theta_{13}$ and the mentioned compatibility for Δm^2 with T2K make Daya Bay an ideal source for this study. Using your probability surface directly as a constraint, instead of a Gaussian approximation, will allow you to check the effect of the surface asymmetry, correctly treat counted correlation as negligible in the current analysis and, in addition, take advantage of the reactor the experiments are sensitive to the mass division parameter Δm^2 .

Sensitivity studies were conducted to assess T2K ability to measure various oscillation parameters of interest under an oscillation hypotheses, using the Asimov A oscillation parameter values listed in Table 4.8. The sensitivity was evaluated using both mass orderings and with different constraints: with Gaussian constraint on $\sin^2 2\theta_{13}$ from reactor experiments and with Day Bay likelihood surface as a constraint on both Δm^2 and $\sin^2\theta_{13}$, according to the method described in Chapter 4.

Due to computational constraints, the constant $\Delta\chi^2$ method was used to construct confidence regions, rather than the more accurate Feldman-Cousins method described in Section 4.2. As a result, the expected coverage of confidence regions may not be perfectly accurate.

The use of graphical reactor constrain if advantageous for measurements of Δm^2_{32} (see Fig. 7.3,). It improves T2K sensitivity to this parameter, reducing 1σ region in ~ 1.4 times i.e. in $\sim \sqrt{2}$, as expected. The difference in best fit values on the Fig. 7.3 appears due to application of a constraint on Δm^2_{32} together with $\sin^2\theta_{13}$, while a gaussian penalty applies a constraint on Δm^2_{32} only. However, there is no significant impact on other oscillation parameters (see Figs. 5.3a and 5.3c), nor on their correlations (see Figs. 5.4a, 5.4c and 5.4d). This proves a robustness of current T2K analysis approach to reactor constraint: use of 1D constraint. Although it does not allow to benefit from all information reactor experiments provide, an agreement between obtained results proves 1D gaussian approximation being good enough. Best-fit points and confidence interval resulting from the 1D fits are displayed Table 5.1.

The ratio E/L of the T2K experiment does not allow one to clearly discriminate between mass ordering. A conclusion about the preference towards normal (NO) or inverted (IO) mass ordering in T2K oscillation analysis is usually driven by posterior probabilities in pure Bayesian analysis. However, as it has been shown previously, adding the Daya Bay result on Δm^2 to T2K improves the sensitivity to the mass splitting term and

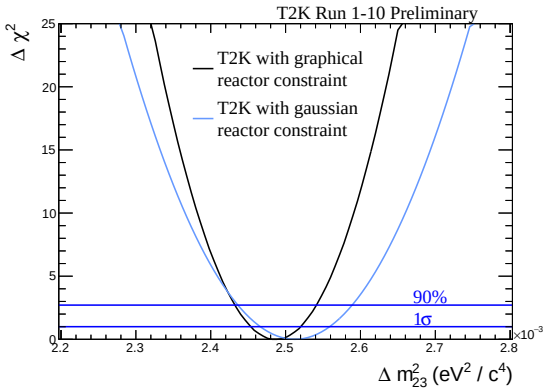

Figure 7.3: A comparison of T2K sensitivity with a standard reactor constraint and a use of likelihood surface for Δm^2_{32}

χ^2	NO	IO	$\Delta\chi^2_{IO-NO}$
T2K only	9.460	10.838	1.378
T2K with gaussian constraint	9.977	12.340	2.363
T2K with Daya Bay likelihood surface constraint	10.029	12.740	2.711

Table 7.4: χ^2 values for T2K predicted best fit value for normal and inverted mass ordering. In both cases normal mass ordering is assumed to be true.

can potentially affect the sensitivity to the mass ordering too.

A $\Delta\chi^2_{IO-NO}$ was calculated using the results from fits of Δm^2 vs $\sin^2\theta_{13}$ for normal and inverted mass hierarchy. For the case of T2K, T2K with a gaussian reactor constraint and T2K with Daya Bay likelihood surface constraint, study shows (Table 7.4) that latter option gives an increase in mass ordering separation: $\sim$ 1.97 times in comparison with T2K only result and $\sim$ 1.15 times in comparison with gaussian reactor constraint.

Data fit results are consistent with sensitivity studies. There is a slight difference between a central value for δ_{CP} parameter (see Fig. 5.6a), however it does not lead to a significant change in confidence region. The use of graphical reactor constraint on Δm^2_{32} , as for sensitivity studies, narrows a 1σ region by $\sim$ 1.4 times in comparison to the result with standard gaussian constraint applied (see Fig. 7.4).

As for mass ordering study, data fit result stays in agreement with sensitivity studies (see Table 7.5) showing an improvement in separation between NO and IO of $\sim$ 1.9 times in comparison to T2K only data fit and even better separation of $\sim$ 1.16 times in comparison to T2K with a gaussian constraint applied data fit.

7.7 — Ageing of scintillator detectors

Another factor that affects T2K is the understanding of detector performance. The near detector complex provides most of the crucial constraints on the neutrino interaction parameters, used in the oscillation analysis. However, it has been in use for over a decade, a significant age for a plastic scintillator that operates in a

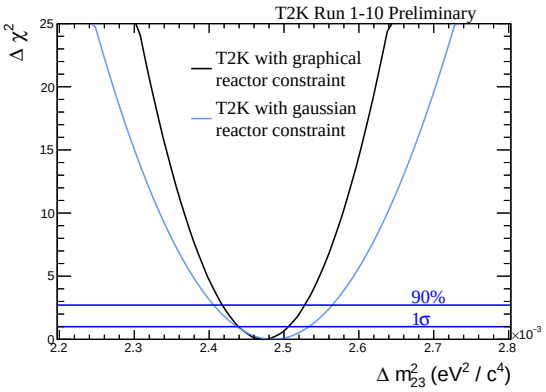

Figure 7.4: A comparison of T2K data result with a standard reactor constraint and a use of likelihood surface for Δm^2_{32} .

χ^2	NO	IO	$\Delta\chi^2_{IO-NO}$
T2K only	475.392	476.166	0.774
T2K with gaussian constraint	478.907	480.174	1.267
T2K with Daya Bay likelihood surface constraint	475.821	477.296	1.475

Table 7.5: χ^2 values for T2K data best fit value for normal and inverted mass ordering. In both cases normal mass ordering is assumed to be true.

magnetic field. Therefore, a part of the current work is focused on the study of the scintillation bars aging of the near detector.

The problem of plastic scintillator aging is well known [156], and there are numerous studies aimed at measuring, characterizing and developing stabilization methods for these widely used materials. (see, for example, [157–163]). These studies often consider the impact of potentially controllable environmental factors, such as temperature and humidity, on the long-term performance of the materials, as well as ways to chemically stabilize them.

The exact mechanism of scintillator aging in T2K near detectors is unknown, but there are several factors. Potential Contributors:

- The mechanical stress of the scintillator that causes the development of cracks or cuts within the [164] material. These inhibit the uniform dispersion of light within the scintillator, preventing transmission through total internal reflection.

- The fogging of the scintillators due to the penetration of water into the material and condensation [165]. This increases the opacity of the scintillator and is a significant problem where materials are exposed to conditions of very high humidity with large temperature variations.

- The oxidation of the scintillator through photochemical processes that lead to the production of peroxides that cause yellowing of the material [166]. This reduces the light output of the scintillator and has been observed in the accelerated aging test performed on the scintillator bars used by the MINOS exper-

iment [69], which are materially identical to the subsystems FGD, ECaL and PØD of T2K as described in Chapter 2.

The study presented in this chapter does not differentiate between the aging factors mentioned above.

To begin, it is important to take a close look at the composition of T2K's near detector complex.

The first neutrinos find a nearby detector complex, located 280 meters from the target station. here is assumes that the flow contains mainly neutrinos not yet oscillated. The INGRID detector is in a straight line with the axis of the beam, while the ND280 complex is displaced 2.5°.

Both detectors are composed primarily of plastic scintillator counters of various shapes and origins.

INGRID is located exactly on the T2K beam axis and is crucial for direct monitoring of beam rate and stability together with the measurement of neutrino interaction cross sections in iron and scintillator targets. The detector itself consists of 14 iron plate and scintillator sandwich modules surrounded by veto panels. The INGRID modules form a cross, centered on the axis of the beam with a precision of 0.4 mrad. The side modules are used to measure the asymmetry of the beam.

INGRID extruded scintillation bars were manufactured in 2007-2008 in Fermilab using DowStyron 663 W polystyrene doped with 1% of PPO and 0.03% of POPOP. Each bar is coated with a layer of TiO_2 to diffusely reflect the light from the scintillator. A Kuraray Y11 Wavelength Shift Fiber (WLS) passes through the center of the bar and collects the light to lead her towards a Hammamtsu MPPC readout at the non-mirrored end of the bar.

The off-axis near detector is located 280 meters from the target and 2.5° degrees from the axis of the beam. ND280 measures the flux and spectrum for the different species of neutrinos in the beam before the oscillation, as well as several interaction cross sections of neutrinos with the detector materials, for example, water and carbon. A precise knowledge of the neutrino beam initial is crucial to predict the flux and spectrum of neutrinos in the far detector, and therefore, to determine the neutrino oscillation parameters. In addition, the measurement of the effective section of ν_μ provides a large constraint on the funds for the spawn quest of ν_e.

One neutral pion detector (PØD), three Time Projection Chambers (TPC) and two fine granulometry detectors (FGD) make up the core, known as the "tracker" part of ND280. The tracker is surrounded by electromagnetic calorimeters (ECaL) and then by a magnet, reused after the UA1 [68] and NOMAD experiments. The air spaces of the magnet are equipped with the Lateral Muon Range Detector (SMRD). The magnet provides a 0.2T magnetic field which is crucial for distinguish positively and negatively charged particles.

Except for the time projection cameras, all subsystems of the ND280 detector complex scintillator bars are used as active detection material. When a particle passes through these detectors, it excites valence electrons in the rod material, which then emit photons with a wavelength of around 420 nm. For the reading of the signals, Multi-Pixel Photon Counters (MPPC) are used instead of PMT due to the magnetic field. Wavelength Shift Fibers (WLS) are used to transport photons to the MPPCs, changing their wavelength from blue to green. The scintillator bars used in the ND280 detectors were produced between 2006 and 2009 and come from various manufacturers.

To measure degradation in scintillator response, the minimum ionizing particle (MIP) average light yield

Table 7.6: Linear fit parameters for the PØD, FGD, SMRD and ECal data and the annual percentage reduction, in relation to the 2012 fit values. single end are mirrored at one end.

Subsystem	Readout Type	A (PEU)	B (PEU/yr)	χ^2/NDF	Annual Reduction (%)
Super-PØDule 0	Single-ended	19.97 ± 0.15	0.35 ± 0.03	$4.35/5 = 0.87$	1.82 ± 0.16
Super-PØDule 1	Single-ended	21.17 ± 0.16	0.36 ± 0.04	$10.39/5 = 2.08$	1.76 ± 0.20
Super-PØDule 2	Single-ended	21.15 ± 0.17	0.36 ± 0.03	$9.14/5 = 1.83$	1.76 ± 0.15
Super-PØDule 3	Single-ended	21.33 ± 0.16	0.37 ± 0.03	$5.46/5 = 1.09$	1.80 ± 0.15
FGD	Single-ended	22.68 ± 0.19	0.27 ± 0.04	$0.74/5 = 0.15$	1.22 ± 0.18
SMRD	Double-ended	60.86 ± 1.48	0.54 ± 0.26	$2.62/5 = 0.52$	0.90 ± 0.44
Barrel X	Single-ended	27.27 ± 0.06	0.52 ± 0.01	$33.09/37 = 0.89$	1.98 ± 0.04
Barrel Y	Single-ended	25.21 ± 0.08	0.49 ± 0.01	$31.88/37 = 0.86$	2.02 ± 0.04
Barrel Z	Double-ended	16.01 ± 0.04	0.33 ± 0.01	$36.60/37 = 0.99$	2.15 ± 0.07
Downstream	Double-ended	15.48 ± 0.06	0.28 ± 0.01	$11.57/37 = 0.31$	1.87 ± 0.07

was recorded. that passed through the ND280 subsystems and were calibrated as hits. We used interactions from beam neutrinos, cosmic muons, or data from sand cores as IPM samples. The light performance of the MIP was corrected as a function of the MIP path length and attenuation in the WLS fiber. Regular adjustments to the surge voltage of the MPPCs were made to maintain a stable gain. T2K has been in operation since 2010 and data from runs 2 through 9 in the analyses. For all subsystems, histograms of cumulative charge per unit length were created by combining MPPC responses for tracks similar to MIP and fitted with a Gaussian-Landau distribution.

The ND280 MIP MPV distribution was extracted for each subsystem during each T2K run and then it was fitted with a linear function to calculate the overall drop in light yield and annual decreases.

Data is aggregated by T2K Run for the PØD, FGD and SMRD, with the time error being the standard deviation in the timestamp of all MIP hits during each T2K Run. For the ECal, the highest statistic allows data to be aggregated per month or per each T2K Run of the J-PARC Main Ring (usually around 1 month), respectively. The adjustment only applies to data as of January 2012 for ND280 subsystems as current calibration procedures and the cosmic ray trigger prescale were not finalized until that time. For the PØD and ECal subsystems, the study has been carried out for all submodules or bar types separately.

Without knowledge of the aging mechanisms that degrade ND280 subsystems, it is difficult to know which shape is expected to take the time dependence of the rate of aging. A priori, an exponential function might be expected to be suitable. However, given the observed data distribution and the time scale studied, a simple linear fit is found to be appropriate and is applied in the form:

$$f(t) = A - Bt\,, \tag{7.2}$$

where A is the adjusted light production in PEUs in year 0 (2010), B is the slope of the adjustment in PEUs per year, and t is the year from 2010. The fit parameters are shown in the table 7.3. Scintillator degradation seems to be fairly consistent across all subsystems. All show a reduction in light yield in the range of about 0.3-0.5 PEU per year, which equates to an annual light yield reduction of 0.9-2.2% relative to their 2012 fit values.

7.8 — Conclusion

In this thesis, both analyses were conducted using the beam data obtained from the T2K experiment. The analysis with a graphical constraint from Daya Baya experiment as well as plastic scintillator ageing study used data with an exposure of 1.9664×10^{21} POT in neutrino-mode running and 1.6346×10^{21} POT in antineutrino-mode running.

Using the Daya Bay data-fit probability surface for $\sin^2 \theta_{13}$ and Δm^2 does not show any significant change in T2K's sensitivity to oscillation parameters, apart from a $\sqrt{2}$ improvement in Δm^2 1σ error band, due to error ranges comparable between T2K and Daya Bay. However, this method may be a way to more accurately handle correlations between oscillation parameters by setting constraints from reactor experiments. Since it does not slow down the computation time, it has the potential to be used within the VALOR experimental framework for future analysis. The mass ordering study carried out within this analysis shows an increase in the separation between the preferences of the normal and inverted mass orderings of ~ 1.9 times in comparison to T2K only and ~ 1.15 time in comparison to T2K with a gaussian constraint applied. Sensitivity studies were found to be in agreement with data fits, confirming all beforehand mentioned improvements in Δm^2 error size and separation between normal and inverted mass orderings.

And the last, for the scintillator ageing study, the decline in the performance of the scintillator material seems to be uniform across all T2K's near subdetectors. The results indicate that all subsystems exhibit a decrease in light yield ranging from approximately 0.3 to 0.5 photoelectrons per unit (PEU) per year. This translates to an annual reduction in light yield of 0.9% to 2.2% when compared to the 2012 fit values. Table 7.3 shows the linear fit parameters for the PØD, FGD, SMRD and ECal data and the annual percentage reduction, relative to the 2012 set values. Single-ended reading bars are mirrored at one end. These results are consistent with studies performed by a MINOS [69] experiment, which was using scintillator bars identical to some of the T2K's detectors. The results obtained from this study are important for modeling the performance of the ND280 detector in the future T2K-II phase. Additionally, some of the scintillator bars used in the update of the near detector complex are the same as those currently in use or new, but produced from similar materials by same manufacturers, making the obtained results even more relevant. At the moment, ageing constants are applied as a part of standard detector data calibration corrections.

Appendices

A — Flux, Interaction Model, and Detector Systematic Parameters used in the T2K Run 1-10 Analysis

A total of 50 flux, 42 interaction/cross-section, and 45 Super-K detector + SI + PN systematic parameters have been used in the T2K Run 1-10 analysis in order to account for the effects of systematic uncertainties. These parameters are summarised, along with their nominal and pre/post-fit uncertainties, in Tables A.1 to A.6 [137]. A number of the cross-section parameters are intentionally not constrained during the near detector fit due to a lack of sensitivity to these parameters at the near detectors; however, they are included in the analyses presented in this thesis as Super-K is sensitive to them. These are $f^{\text{ND}}_{Shape_{BgRESlowPpi}}$, $f^{\text{ND}}_{Norm_{NC1\gamma}}$, $f^{\text{ND}}_{Shape_{2p2hlowEnu}}$, $f^{\text{ND}}_{Shape_{2p2hhighEnu}}$, $f^{\text{ND}}_{Shape_{2p2hlowEnubar}}$, $f^{\text{ND}}_{Shape_{2p2hhighEnubar}}$, $f^{\text{ND}}_{Norm_{\bar{\nu}_e\rightarrow\bar{\nu}_\mu}}$, $f^{\text{ND}}_{Norm_{\nu_e\rightarrow\nu_\mu}}$, and $f^{\text{ND}}_{Norm_{NCOthfar}}$, and in the following tables such parameters have equal prefit and postfit fractional errors. The systematic parameters 1σ fractional errors and correlations between them are shown in Figs. A.1, A.2 and 3.33.

Two types of systematic parameters are listed in the tables below: normalisation and shape parameters. Normalisation parameters (any parameter not labelled as 'Shape') simply act to scale the event rates in all applicable $(E_{\text{true}}, E_{\text{rec}}, \theta)$ kinematic bins and for all relevant interaction modes, as indicated, and the scaling factor is equal to the parameter value. Shape parameters also act to scale the event rates in all applicable kinematic bins and interaction modes, but the scaling factor can be different for each bin and interaction mode and are determined by response functions of arbitrary shape. These response functions are pre-calculated by the XsecResponse [180] software package.

All parameter values and their uncertainties are listed as a fraction of the corresponding parameter value (if non-zero) used to generate the NEUT v5.4.0 MC and SKDETSIM simulations, so do not necessarily directly correspond to the value of a physical quantity. For all parameters related to Super-K flux, detector, SI, and PN uncertainties, these generated values are 1. For the interaction model parameters, the generated values are listed in Ref. [75]. For example, the generated M_A^{QE} value in NEUT v5.4.0 is 1.03 GeV [75], while the post ND fit nominal value of the corresponding systematic parameter in VALOR, $f^{\text{ND}}_{Shape_{M_A^{QE}}}$, is 0.969, corresponding to a postfit M_A^{QE} value of 0.998 GeV.

Index	Parameter	Description	Best fit	1σ pre/postfit fractional error
0	$f^{\mathrm{ND}}_{0;t,r}$	ν-mode ν_μ flux norm., E_{true} = 0.0 - 0.4 GeV	1.110	0.067 / 0.048
1	$f^{\mathrm{ND}}_{1;t,r}$	ν-mode ν_μ flux norm., E_{true} = 0.4 - 0.5 GeV	1.095	0.057 / 0.039
2	$f^{\mathrm{ND}}_{2;t,r}$	ν-mode ν_μ flux norm., E_{true} = 0.5 - 0.6 GeV	1.082	0.053 / 0.034
3	$f^{\mathrm{ND}}_{3;t,r}$	ν-mode ν_μ flux norm., E_{true} = 0.6 - 0.7 GeV	1.075	0.047 / 0.032
4	$f^{\mathrm{ND}}_{4;t,r}$	ν-mode ν_μ flux norm., E_{true} = 0.7 - 1.0 GeV	1.063	0.074 / 0.039
5	$f^{\mathrm{ND}}_{5;t,r}$	ν-mode ν_μ flux norm., E_{true} = 1.0 - 1.5 GeV	1.031	0.070 / 0.037
6	$f^{\mathrm{ND}}_{6;t,r}$	ν-mode ν_μ flux norm., E_{true} = 1.5 - 2.5 GeV	1.032	0.062 / 0.035
7	$f^{\mathrm{ND}}_{7;t,r}$	ν-mode ν_μ flux norm., E_{true} = 2.5 - 3.5 GeV	1.008	0.074 / 0.041
8	$f^{\mathrm{ND}}_{8;t,r}$	ν-mode ν_μ flux norm., E_{true} = 3.5 - 5.0 GeV	0.975	0.089 / 0.036
9	$f^{\mathrm{ND}}_{9;t,r}$	ν-mode ν_μ flux norm., E_{true} = 5.0 - 7.0 GeV	0.924	0.102 / 0.037
10	$f^{\mathrm{ND}}_{10;t,r}$	ν-mode ν_μ flux norm., E_{true} = 7.0 - 30.0 GeV	0.907	0.117 / 0.045
11	$f^{\mathrm{ND}}_{11;t,r}$	ν-mode $\bar{\nu}_\mu$ flux norm., E_{true} = 0.0 - 0.7 GeV	1.056	0.093 / 0.084
12	$f^{\mathrm{ND}}_{12;t,r}$	ν-mode $\bar{\nu}_\mu$ flux norm., E_{true} = 0.7 - 1.0 GeV	1.045	0.062 / 0.052
13	$f^{\mathrm{ND}}_{13;t,r}$	ν-mode $\bar{\nu}_\mu$ flux norm., E_{true} = 1.0 - 1.5 GeV	1.039	0.074 / 0.061
14	$f^{\mathrm{ND}}_{14;t,r}$	ν-mode $\bar{\nu}_\mu$ flux norm., E_{true} = 1.5 - 2.5 GeV	1.049	0.080 / 0.069
15	$f^{\mathrm{ND}}_{15;t,r}$	ν-mode $\bar{\nu}_\mu$ flux norm., E_{true} = 2.5 - 30.0 GeV	1.037	0.079 / 0.063
16	$f^{\mathrm{ND}}_{16;t,r}$	ν-mode ν_e flux norm., E_{true} = 0.0 - 0.5 GeV	1.087	0.057 / 0.040
17	$f^{\mathrm{ND}}_{17;t,r}$	ν-mode ν_e flux norm., E_{true} = 0.5 - 0.7 GeV	1.075	0.054 / 0.036
18	$f^{\mathrm{ND}}_{18;t,r}$	ν-mode ν_e flux norm., E_{true} = 0.7 - 0.8 GeV	1.063	0.052 / 0.035
19	$f^{\mathrm{ND}}_{19;t,r}$	ν-mode ν_e flux norm., E_{true} = 0.8 - 1.5 GeV	1.042	0.059 / 0.038
20	$f^{\mathrm{ND}}_{20;t,r}$	ν-mode ν_e flux norm., E_{true} = 1.5 - 2.5 GeV	0.998	0.082 / 0.041
21	$f^{\mathrm{ND}}_{21;t,r}$	ν-mode ν_e flux norm., E_{true} = 2.5 - 4.0 GeV	0.981	0.086 / 0.039
22	$f^{\mathrm{ND}}_{22;t,r}$	ν-mode ν_e flux norm., E_{true} = 4.0 - 30.0 GeV	0.983	0.095 / 0.055
23	$f^{\mathrm{ND}}_{23;t,r}$	ν-mode $\bar{\nu}_e$ flux norm., E_{true} = 0.0 - 2.5 GeV	1.023	0.098 / 0.086
24	$f^{\mathrm{ND}}_{24;t,r}$	ν-mode $\bar{\nu}_e$ flux norm., E_{true} = 2.5 - 30.0 GeV	1.095	0.132 / 0.114

Table A.1: Summary of ν-mode flux systematic normalisation parameters.

Index	Parameter	Description	Best fit	1σ pre/postfit fractional error
25	$f^{\mathrm{ND}}_{0;t,r}$ $\bar{\nu}$-mode	$\bar{\nu}$-mode ν_μ flux norm., E_{true} = 0.0 - 0.7 GeV	1.107	0.086 / 0.061
26	$f^{\mathrm{ND}}_{1;t,r}$ $\bar{\nu}$-mode	$\bar{\nu}$-mode ν_μ flux norm., E_{true} = 0.7 - 1.0 GeV	1.067	0.065 / 0.046
27	$f^{\mathrm{ND}}_{2;t,r}$ $\bar{\nu}$-mode	$\bar{\nu}$-mode ν_μ flux norm., E_{true} = 1.0 - 1.5 GeV	1.072	0.061 / 0.038
28	$f^{\mathrm{ND}}_{3;t,r}$ $\bar{\nu}$-mode	$\bar{\nu}$-mode ν_μ flux norm., E_{true} = 1.5 - 2.5 GeV	1.072	0.068 / 0.041
29	$f^{\mathrm{ND}}_{4;t,r}$ $\bar{\nu}$-mode	$\bar{\nu}$-mode ν_μ flux norm., E_{true} = 2.5 - 30.0 GeV	1.024	0.069 / 0.041
30	$f^{\mathrm{ND}}_{5;t,r}$ $\bar{\nu}$-mode	$\bar{\nu}$-mode $\bar{\nu}_\mu$ flux norm., E_{true} = 0.0 - 0.4 GeV	1.093	0.068 / 0.052
31	$f^{\mathrm{ND}}_{6;t,r}$ $\bar{\nu}$-mode	$\bar{\nu}$-mode $\bar{\nu}_\mu$ flux norm., E_{true} = 0.4 - 0.5 GeV	1.087	0.059 / 0.041
32	$f^{\mathrm{ND}}_{7;t,r}$ $\bar{\nu}$-mode	$\bar{\nu}$-mode $\bar{\nu}_\mu$ flux norm., E_{true} = 0.5 - 0.6 GeV	1.067	0.057 / 0.038
33	$f^{\mathrm{ND}}_{8;t,r}$ $\bar{\nu}$-mode	$\bar{\nu}$-mode $\bar{\nu}_\mu$ flux norm., E_{true} = 0.6 - 0.7 GeV	1.063	0.047 / 0.032
34	$f^{\mathrm{ND}}_{9;t,r}$ $\bar{\nu}$-mode	$\bar{\nu}$-mode $\bar{\nu}_\mu$ flux norm., E_{true} = 0.7 - 1.0 GeV	1.092	0.079 / 0.042
35	$f^{\mathrm{ND}}_{10;t,r}$ $\bar{\nu}$-mode	$\bar{\nu}$-mode $\bar{\nu}_\mu$ flux norm., E_{true} = 1.0 - 1.5 GeV	1.055	0.079 / 0.041
36	$f^{\mathrm{ND}}_{11;t,r}$ $\bar{\nu}$-mode	$\bar{\nu}$-mode $\bar{\nu}_\mu$ flux norm., E_{true} = 1.5 - 2.5 GeV	1.010	0.063 / 0.042
37	$f^{\mathrm{ND}}_{12;t,r}$ $\bar{\nu}$-mode	$\bar{\nu}$-mode $\bar{\nu}_\mu$ flux norm., E_{true} = 2.5 - 3.5 GeV	1.007	0.066 / 0.048
38	$f^{\mathrm{ND}}_{13;t,r}$ $\bar{\nu}$-mode	$\bar{\nu}$-mode $\bar{\nu}_\mu$ flux norm., E_{true} = 3.5 - 5.0 GeV	0.955	0.090 / 0.061
39	$f^{\mathrm{ND}}_{14;t,r}$ $\bar{\nu}$-mode	$\bar{\nu}$-mode $\bar{\nu}_\mu$ flux norm., E_{true} = 5.0 - 7.0 GeV	0.959	0.086 / 0.057
40	$f^{\mathrm{ND}}_{15;t,r}$ $\bar{\nu}$-mode	$\bar{\nu}$-mode $\bar{\nu}_\mu$ flux norm., E_{true} = 7.0 - 30.0 GeV	0.930	0.119 / 0.093
41	$f^{\mathrm{ND}}_{16;t,r}$ $\bar{\nu}$-mode	$\bar{\nu}$-mode ν_e flux norm., E_{true} = 0.0 - 2.5 GeV	1.031	0.091 / 0.071
42	$f^{\mathrm{ND}}_{17;t,r}$ $\bar{\nu}$-mode	$\bar{\nu}$-mode ν_e flux norm., E_{true} = 2.5 - 30.0 GeV	1.029	0.085 / 0.066
43	$f^{\mathrm{ND}}_{18;t,r}$ $\bar{\nu}$-mode	$\bar{\nu}$-mode $\bar{\nu}_e$ flux norm., E_{true} = 0.0 - 0.5 GeV	1.082	0.058 / 0.042
44	$f^{\mathrm{ND}}_{19;t,r}$ $\bar{\nu}$-mode	$\bar{\nu}$-mode $\bar{\nu}_e$ flux norm., E_{true} = 0.5 - 0.7 GeV	1.071	0.054 / 0.037
45	$f^{\mathrm{ND}}_{20;t,r}$ $\bar{\nu}$-mode	$\bar{\nu}$-mode $\bar{\nu}_e$ flux norm., E_{true} = 0.7 - 0.8 GeV	1.058	0.056 / 0.042
46	$f^{\mathrm{ND}}_{21;t,r}$ $\bar{\nu}$-mode	$\bar{\nu}$-mode $\bar{\nu}_e$ flux norm., E_{true} = 0.8 - 1.5 GeV	1.037	0.057 / 0.041
47	$f^{\mathrm{ND}}_{22;t,r}$ $\bar{\nu}$-mode	$\bar{\nu}$-mode $\bar{\nu}_e$ flux norm., E_{true} = 1.5 - 2.5 GeV	1.007	0.080 / 0.061
48	$f^{\mathrm{ND}}_{23;t,r}$ $\bar{\nu}$-mode	$\bar{\nu}$-mode $\bar{\nu}_e$ flux norm., E_{true} = 2.5 - 4.0 GeV	1.008	0.090 / 0.069
49	$f^{\mathrm{ND}}_{24;t,r}$ $\bar{\nu}$-mode	$\bar{\nu}$-mode $\bar{\nu}_e$ flux norm., E_{true} = 4.0 - 30.0 GeV	1.089	0.152 / 0.127

Table A.2: Summary of $\bar{\nu}$-mode flux systematic normalisation parameters.

Index	Parameter	Description	Best fit	1σ pre/postfit fractional error
50	$f^{\text{ND}}_{Norm_{2p2h\nu}}$	2p2h norm. for ^{16}O	1.058	1.000 / 0.153
51	$f^{\text{ND}}_{Shape_{C_5^A}}$	C_5^A nucleon to Δ transition axial form factor	0.974	0.149 / 0.058
52	$f^{\text{ND}}_{Shape_{Bg_{RES}}}$	Scale of isospin $\frac{1}{2}$ nonres. background	0.665	0.308 / 0.180
53	$f^{\text{ND}}_{Shape_{BgRESlowPpi}}$	Scale of isospin $\frac{1}{2}$ nonres. background ($\bar{\nu}$, $p_\pi < 0.2$ GeV)	0.738	1.000 / 1.000
54	$f^{\text{ND}}_{Shape_{M_A^{QE}}}$	CCQE axial-mass scaling factor	0.969	0.050 / 0.034
55	$f^{\text{ND}}_{Shape_{M_A^{RES}}}$	Resonance-production axial-mass scaling factor	0.831	0.158 / 0.052
56	$f^{\text{ND}}_{Norm_{NCcoh}}$	NC coherent norm.	1.018	0.300 / 0.299
57	$f^{\text{ND}}_{Norm_{\nu_e\to\nu_\mu}}$	CC ν_e norm.	1.000	0.028 / 0.028
58	$f^{\text{ND}}_{Norm_{NC1\gamma}}$	NC 1γ norm.	1.000	1.000 / 1.000
59	$f^{\text{ND}}_{Norm_{\bar{\nu}_e\to\bar{\nu}_\mu}}$	CC $\bar{\nu}_e$ norm.	1.000	0.028 / 0.028
60	$f^{\text{ND}}_{Norm_{2p2h\bar{\nu}}}$	$\bar{\nu}$ 2p2h norm. for ^{16}O	0.722	1.000 / 0.162
61	$f^{\text{ND}}_{Shape_{2p2h\nu}}$	ν 2p2h ^{16}O shape	-0.003	3.000 / 0.174
62	$f^{\text{ND}}_{Norm_{2p2hCtoO}}$	2p2h ^{12}C to ^{16}O norm.	1.046	0.200 / 0.147
63	$f^{\text{ND}}_{Shape_{2p2hLowE\nu}}$	2p2h energy dependence ($\nu < 0.6$ GeV)	1.000	1.000 / 1.000
64	$f^{\text{ND}}_{Shape_{2p2hHghE\nu}}$	2p2h energy dependence ($\nu > 0.6$ GeV)	1.000	1.000 / 1.000
65	$f^{\text{ND}}_{Shape_{2p2hLowE\bar{\nu}}}$	2p2h energy dependence ($\bar{\nu} < 0.6$ GeV)	1.000	1.000 / 1.000
66	$f^{\text{ND}}_{Shape_{2p2hHighE\bar{\nu}}}$	2p2h energy dependence ($\bar{\nu} > 0.6$ GeV)	1.000	1.000 / 1.000
67	$f^{\text{ND}}_{Shape_{Q^2{}_0}}$	CCQE Q^2 norm. ($0.00 - 0.05$ GeV^2)	-0.216	0.165 / 0.047
68	$f^{\text{ND}}_{Shape_{Q^2{}_1}}$	CCQE Q^2 norm. ($0.05 - 0.10$ GeV^2)	-0.113	0.145 / 0.040
69	$f^{\text{ND}}_{Shape_{Q^2{}_2}}$	CCQE Q^2 norm. ($0.10 - 0.15$ GeV^2)	0.023	0.130 / 0.052
70	$f^{\text{ND}}_{Shape_{Q^2{}_3}}$	CCQE Q^2 norm. ($0.15 - 0.20$ GeV^2)	0.027	0.150 / 0.077

Table A.3: Summary of cross section systematic parameters.

Index	Parameter	Description	Best fit	1σ pre/postfit fractional error
71	$f^{\text{ND}}_{Shape_{{Q^2}_4}}$	CCQE Q^2 norm. ($0.20 - 0.25$ GeV^2)	0.087	0.160 / 0.099
72	$f^{\text{ND}}_{Shape_{{Q^2}_5}}$	CCQE Q^2 norm. ($0.25 - 0.50$ GeV^2)	0.257	0.110 / 0.058
73	$f^{\text{ND}}_{Shape_{{Q^2}_6}}$	CCQE Q^2 norm. ($0.50 - 1.005$ GeV^2)	0.136	0.180 / 0.081
74	$f^{\text{ND}}_{Shape_{{Q^2}_7}}$	CCQE Q^2 norm. (> 1.00 GeV^2)	0.259	0.400 / 0.141
75	$f^{\text{ND}}_{Shape_{\Delta EbO\nu}}$	^{16}O nucleon removal energy shift for ν (MeV)	2.546	6.000 / 3.076
76	$f^{\text{ND}}_{Shape_{\Delta EbO\bar{\nu}}}$	^{16}O nucleon removal energy shift for $\bar{\nu}$ (MeV)	-1.262	6.000 / 3.189
77	$f^{\text{ND}}_{Norm_{CC\nu}}$	Coulomb shift scale factor for ν	0.999	0.020 / 0.020
78	$f^{\text{ND}}_{Norm_{CC\bar{\nu}}}$	Coulomb shift scale factor for $\bar{\nu}$	1.001	0.010 / 0.010
79	$f^{\text{ND}}_{Shape_{CCBYDIS}}$	Bodek-Yang corrections for CC DIS	1.042	1.000 / 0.191
80	$f^{\text{ND}}_{Shape_{CCBYMPi}}$	Bodek-Yang corrections for CC multi-π	-0.032	1.000 / 0.184
81	$f^{\text{ND}}_{Shape_{CCAGKYMPi}}$	Reweight of multi-π multiplicity model	0.139	1.000 / 0.713
82	$f^{\text{ND}}_{Norm_{CCMisc}}$	CC1γ, CC1K and CC1η norm.	2.278	1.000 / 0.432
83	$f^{\text{ND}}_{Norm_{CCDISMPi\nu}}$	ν CC DIS and multi-π norm.	1.062	0.035 / 0.030
84	$f^{\text{ND}}_{Norm_{CCDISMPi\bar{\nu}}}$	$\bar{\nu}$ CC DIS and multi-π norm.	0.935	0.065 / 0.060
85	$f^{\text{ND}}_{Norm_{CCCohO}}$	^{16}O CC coherent norm.	0.609	0.300 / 0.216
86	$f^{\text{ND}}_{Norm_{NCOthfar}}$	NC miscellaneous norm.	1.000	0.300 / 0.300
87	$f^{\text{ND}}_{Shape_{FSIQElowP}}$	π FSI (QE scattering $p_\pi < 0.5$ GeV)	0.826	0.293 / 0.095
88	$f^{\text{ND}}_{Shape_{FSIQEhighP}}$	π FSI (QE scattering $p_\pi > 0.4$ GeV)	0.748	0.471 / 0.157
89	$f^{\text{ND}}_{Shape_{FSIInelastic}}$	π FSI (hadron production $p_\pi > 0.4$ GeV)	1.715	1.099 / 0.308
90	$f^{\text{ND}}_{Shape_{FSIAbsorption}}$	π FSI (absorption $p_\pi < 0.5$ GeV)	1.190	0.308 / 0.124
91	$f^{\text{ND}}_{Shape_{FSIchargeexchange}}$	π FSI (charge exchange $p_\pi > 0.4$ GeV)	0.777	0.438 / 0.345

Table A.4: Summary of cross section systematic parameters (continued).

Index	Parameter	Description	1σ fractional error
92	$f^{SK}_{0;t,r}$	E_{rec} = 0.00 - 0.40 GeV; $\nu_\mu/\bar{\nu}_\mu$ CCQE; ν-mode ν_μ / $\bar{\nu}_\mu$ CCQE-like	0.008
93	$f^{SK}_{1;t,r}$	E_{rec} = 0.40 - 1.10 GeV; $\nu_\mu/\bar{\nu}_\mu$ CCQE; ν-mode ν_μ / $\bar{\nu}_\mu$ CCQE-like	0.010
94	$f^{SK}_{2;t,r}$	E_{rec} = 1.10 - 30.00 GeV; $\nu_\mu/\bar{\nu}_\mu$ CCQE; ν-mode ν_μ / $\bar{\nu}_\mu$ CCQE-like	0.012
95	$f^{SK}_{3;t,r}$	E_{rec} = 0.00 - 30.00 GeV; $\nu_\mu/\bar{\nu}_\mu$ CCnQE; ν-mode ν_μ / $\bar{\nu}_\mu$ CCQE-like	0.048
96	$f^{SK}_{4;t,r}$	E_{rec} = 0.00 - 30.00 GeV; $\nu_e/\bar{\nu}_e$/sigν_e CC; ν-mode ν_μ / $\bar{\nu}_\mu$ CCQE-like	1.007
97	$f^{SK}_{5;t,r}$	E_{rec} = 0.00 - 30.00 GeV; all NC; ν-mode ν_μ / $\bar{\nu}_\mu$ CCQE-like	0.649
98	$f^{SK}_{6;t,r}$	E_{rec} = 0.00 - 0.35 GeV; Osc. ν_e CC; ν-mode ν_e / $\bar{\nu}_e$ CCQE-like	0.029
99	$f^{SK}_{7;t,r}$	E_{rec} = 0.35 - 0.80 GeV; Osc. ν_e CC; ν-mode ν_e / $\bar{\nu}_e$ CCQE-like	0.028
100	$f^{SK}_{8;t,r}$	E_{rec} = 0.80 - 1.25 GeV; Osc. ν_e CC; ν-mode ν_e / $\bar{\nu}_e$ CCQE-like	0.042
101	$f^{SK}_{9;t,r}$	E_{rec} = 0.00 - 0.35 GeV; $\nu_\mu/\bar{\nu}_\mu$ CC; ν-mode ν_e / $\bar{\nu}_e$ CCQE-like	0.296
102	$f^{SK}_{10;t,r}$	E_{rec} = 0.35 - 0.80 GeV; $\nu_\mu/\bar{\nu}_\mu$ CC; ν-mode ν_e / $\bar{\nu}_e$ CCQE-like	0.304
103	$f^{SK}_{11;t,r}$	E_{rec} = 0.80 - 1.25 GeV; $\nu_\mu/\bar{\nu}_\mu$ CC; ν-mode ν_e / $\bar{\nu}_e$ CCQE-like	0.444
104	$f^{SK}_{12;t,r}$	E_{rec} = 0.00 - 0.35 GeV; $\nu_e/\bar{\nu}_e$ CC; ν-mode ν_e / $\bar{\nu}_e$ CCQE-like	0.025
105	$f^{SK}_{13;t,r}$	E_{rec} = 0.35 - 0.80 GeV; $\nu_e/\bar{\nu}_e$ CC; ν-mode ν_e / $\bar{\nu}_e$ CCQE-like	0.030
106	$f^{SK}_{14;t,r}$	E_{rec} = 0.80 - 1.25 GeV; $\nu_e/\bar{\nu}_e$ CC; ν-mode ν_e / $\bar{\nu}_e$ CCQE-like	0.055
107	$f^{SK}_{15;t,r}$	E_{rec} = 0.00 - 0.35 GeV; all NC; ν-mode ν_e / $\bar{\nu}_e$ CCQE-like	0.410
108	$f^{SK}_{16;t,r}$	E_{rec} = 0.35 - 0.80 GeV; all NC; ν-mode ν_e / $\bar{\nu}_e$ CCQE-like	0.192
109	$f^{SK}_{17;t,r}$	E_{rec} = 0.80 - 1.25 GeV; all NC; ν-mode ν_e / $\bar{\nu}_e$ CCQE-like	0.496

Table A.5: Summary of SK detector + SI + PN systematic normalisation parameters.

Index	Parameter	Description	1σ fractional error
110	$f^{SK}_{0;t,r}$ $\bar{\nu}$-mode	E_{rec} = 0.00 - 0.40 GeV; $\nu_\mu/\bar{\nu}_\mu$ CCQE; $\bar{\nu}$-mode ν_μ / $\bar{\nu}_\mu$ CCQE-like	0.008
111	$f^{SK}_{1;t,r}$ $\bar{\nu}$-mode	E_{rec} = 0.40 - 1.10 GeV; $\nu_\mu/\bar{\nu}_\mu$ CCQE; $\bar{\nu}$-mode ν_μ / $\bar{\nu}_\mu$ CCQE-like	0.008
112	$f^{SK}_{2;t,r}$ $\bar{\nu}$-mode	E_{rec} = 1.10 - 30.00 GeV; $\nu_\mu/\bar{\nu}_\mu$ CCQE; $\bar{\nu}$-mode ν_μ / $\bar{\nu}_\mu$ CCQE-like	0.009
113	$f^{SK}_{3;t,r}$ $\bar{\nu}$-mode	E_{rec} = 0.00 - 30.00 GeV; $\nu_\mu/\bar{\nu}_\mu$ CCnQE; $\bar{\nu}$-mode ν_μ / $\bar{\nu}_\mu$ CCQE-like	0.048
114	$f^{SK}_{4;t,r}$ $\bar{\nu}$-mode	E_{rec} = 0.00 - 30.00 GeV; $\nu_e/\bar{\nu}_e$/sigν_e CC; $\bar{\nu}$-mode ν_μ / $\bar{\nu}_\mu$ CCQE-like	1.007
115	$f^{SK}_{5;t,r}$ $\bar{\nu}$-mode	E_{rec} = 0.00 - 30.00 GeV; all NC; $\bar{\nu}$-mode ν_μ / $\bar{\nu}_\mu$ CCQE-like	0.651
116	$f^{SK}_{6;t,r}$ $\bar{\nu}$-mode	E_{rec} = 0.00 - 0.35 GeV; Osc. ν_e CC; $\bar{\nu}$-mode ν_e / $\bar{\nu}_e$ CCQE-like	0.036
117	$f^{SK}_{7;t,r}$ $\bar{\nu}$-mode	E_{rec} = 0.35 - 0.80 GeV; Osc. ν_e CC; $\bar{\nu}$-mode ν_e / $\bar{\nu}_e$ CCQE-like	0.030
118	$f^{SK}_{8;t,r}$ $\bar{\nu}$-mode	E_{rec} = 0.80 - 1.25 GeV; Osc. ν_e CC; $\bar{\nu}$-mode ν_e / $\bar{\nu}_e$ CCQE-like	0.054
119	$f^{SK}_{9;t,r}$ $\bar{\nu}$-mode	E_{rec} = 0.00 - 0.35 GeV; $\nu_\mu/\bar{\nu}_\mu$ CC; $\bar{\nu}$-mode ν_e / $\bar{\nu}_e$ CCQE-like	0.374
120	$f^{SK}_{10;t,r}$ $\bar{\nu}$-mode	E_{rec} = 0.35 - 0.80 GeV; $\nu_\mu/\bar{\nu}_\mu$ CC; $\bar{\nu}$-mode ν_e / $\bar{\nu}_e$ CCQE-like	0.339
121	$f^{SK}_{11;t,r}$ $\bar{\nu}$-mode	E_{rec} = 0.80 - 1.25 GeV; $\nu_\mu/\bar{\nu}_\mu$ CC; $\bar{\nu}$-mode ν_e / $\bar{\nu}_e$ CCQE-like	0.336
122	$f^{SK}_{12;t,r}$ $\bar{\nu}$-mode	E_{rec} = 0.00 - 0.35 GeV; $\nu_e/\bar{\nu}_e$ CC; $\bar{\nu}$-mode ν_e / $\bar{\nu}_e$ CCQE-like	0.026
123	$f^{SK}_{13;t,r}$ $\bar{\nu}$-mode	E_{rec} = 0.35 - 0.80 GeV; $\nu_e/\bar{\nu}_e$ CC; $\bar{\nu}$-mode ν_e / $\bar{\nu}_e$ CCQE-like	0.032
124	$f^{SK}_{14;t,r}$ $\bar{\nu}$-mode	E_{rec} = 0.80 - 1.25 GeV; $\nu_e/\bar{\nu}_e$ CC; $\bar{\nu}$-mode ν_e / $\bar{\nu}_e$ CCQE-like	0.060
125	$f^{SK}_{15;t,r}$ $\bar{\nu}$-mode	E_{rec} = 0.00 - 0.35 GeV; all NC; $\bar{\nu}$-mode ν_e / $\bar{\nu}_e$ CCQE-like	0.410
126	$f^{SK}_{16;t,r}$ $\bar{\nu}$-mode	E_{rec} = 0.35 - 0.80 GeV; all NC; $\bar{\nu}$-mode ν_e / $\bar{\nu}_e$ CCQE-like	0.197
127	$f^{SK}_{17;t,r}$ $\bar{\nu}$-mode	E_{rec} = 0.80 - 1.25 GeV; all NC; $\bar{\nu}$-mode ν_e / $\bar{\nu}_e$ CCQE-like	0.468
128	$f^{SK}_{0;t,r}$ ν_eCC1π^+-like	E_{rec} = 0.30 - 0.80 GeV; Osc. ν_e CC; ν-mode ν_eCC1π^+-like	0.146
129	$f^{SK}_{1;t,r}$ ν_eCC1π^+-like	E_{rec} = 0.80 - 1.25 GeV; Osc. ν_e CC; ν-mode ν_eCC1π^+-like	0.120
130	$f^{SK}_{2;t,r}$ ν_eCC1π^+-like	E_{rec} = 0.30 - 0.80 GeV; $\nu_\mu/\bar{\nu}_\mu$ CC; ν-mode ν_eCC1π^+-like	0.418
131	$f^{SK}_{3;t,r}$ ν_eCC1π^+-like	E_{rec} = 0.80 - 1.25 GeV; $\nu_\mu/\bar{\nu}_\mu$ CC; ν-mode ν_eCC1π^+-like	0.302
132	$f^{SK}_{4;t,r}$ ν_eCC1π^+-like	E_{rec} = 0.30 - 0.80 GeV; $\nu_e/\bar{\nu}_e$ CC; ν-mode ν_eCC1π^+-like	0.144
133	$f^{SK}_{5;t,r}$ ν_eCC1π^+-like	E_{rec} = 0.80 - 1.25 GeV; $\nu_e/\bar{\nu}_e$ CC; ν-mode ν_eCC1π^+-like	0.146
134	$f^{SK}_{6;t,r}$ ν_eCC1π^+-like	E_{rec} = 0.30 - 0.80 GeV; all NC; ν-mode ν_eCC1π^+-like	0.998
135	$f^{SK}_{7;t,r}$ ν_eCC1π^+-like	E_{rec} = 0.80 - 1.25 GeV; all NC; ν-mode ν_eCC1π^+-like	0.546
136	$f^{SK}_{E;r}$	Super-K E_{rec} scale	0.021

Table A.6: Summary of SK detector + SI + PN systematic normalisation parameters (continued).

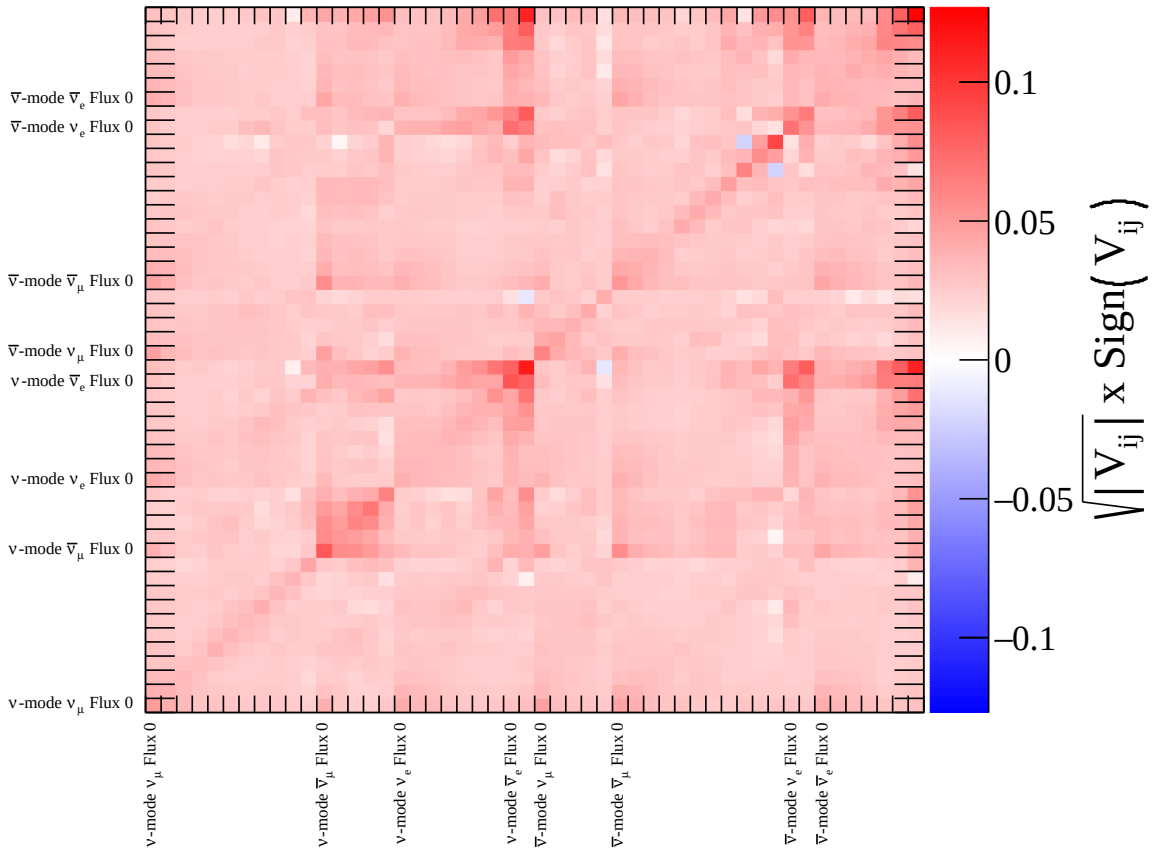

Figure A.1: The flux covariance matrix resulting from the near detector fit. The parameters are presented in the same order as in Tables A.1 and A.2.

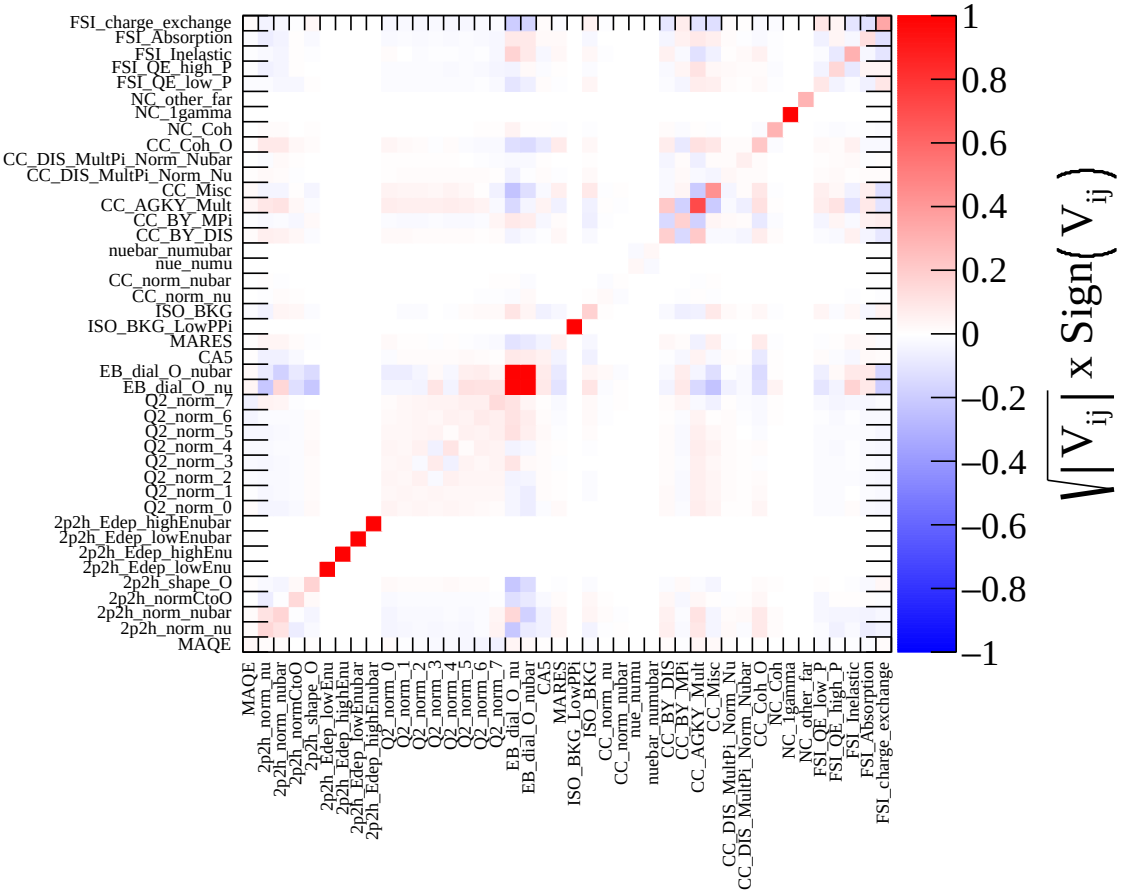

Figure A.2: The cross-section covariance matrix resulting from the near detector fit.

B — Predicted Event Rates for the T2K Run 1-10 Analysis

Tables B.1 to B.5 show the predicted event rates generated with the full T2K Run 1-10 beam exposure (see Section 2.1) and with the Asimov A oscillation parameters listed in Table 4.8. Shown are both the total predicted event rates and the contributions from all true reaction modes.

	$\nu_\mu \to \nu_\mu$	$\bar{\nu}_\mu \to \bar{\nu}_\mu$	$\nu_e \to \nu_e$	$\nu_\mu \to \nu_e$	$\bar{\nu}_e \to \bar{\nu}_e$	$\bar{\nu}_\mu \to \bar{\nu}_e$	Total
CCQE	224.6762	13.9450	0.0053	0.0428	0.0004	0.0002	238.6700
CC1$\pi^\pm$	35.9936	3.2272	0.0035	0.0391	0.0001	0.0000	39.2635
CC1π^0	6.5506	0.4460	0.0000	0.0066	0.0000	0.0000	7.0033
CCcoh	0.3084	0.0707	0.0000	0.0000	0.0000	0.0000	0.3791
CC2p2h	39.0220	2.0948	0.0018	0.0130	0.0000	0.0000	41.1317
CCDIS	0.8147	0.0442	0.0000	0.0000	0.0000	0.0000	0.8589
CCmulti-π	7.6338	0.4421	0.0010	0.0022	0.0000	0.0000	8.0791
CCmisc	1.2084	0.0741	0.0000	0.0000	0.0000	0.0000	1.2825
NC1$\pi^\pm$	5.3290	0.1973	0.1155	N/A	0.0110	N/A	5.6528
NC1π^0	0.5151	0.0191	0.0160	N/A	0.0015	N/A	0.5517
NCcoh	0.0000	0.0000	0.0005	N/A	0.0000	N/A	0.0005
NCmisc	2.4032	0.1343	0.0993	N/A	0.0101	N/A	2.6469
NC1γ	0.0092	0.0000	0.0000	N/A	0.0000	N/A	0.0092
Total	324.4644	20.6947	0.2429	0.1037	0.0233	0.0003	345.5293

Table B.1: Event rates for the ν-mode ν_μ / $\bar{\nu}_\mu$ CCQE-like sample, generated with the Asimov A oscillation parameter values in Table 4.8 and nominal values of the systematic parameters.

	$\nu_\mu \to \nu_\mu$	$\bar{\nu}_\mu \to \bar{\nu}_\mu$	$\nu_e \to \nu_e$	$\nu_\mu \to \nu_e$	$\bar{\nu}_e \to \bar{\nu}_e$	$\bar{\nu}_\mu \to \bar{\nu}_e$	Total
CCQE	34.0427	59.3696	0.0015	0.0006	0.0019	0.0030	93.4194
CC1$\pi^\pm$	8.4598	8.7887	0.0004	0.0007	0.0003	0.0002	17.2500
CC1π^0	1.5285	1.2326	0.0001	0.0001	0.0000	0.0000	2.7613
CCcoh	0.0629	0.2156	0.0000	0.0000	0.0000	0.0002	0.2787
CC2p2h	7.7405	7.0818	0.0004	0.0007	0.0003	0.0003	14.8239
CCDIS	0.1382	0.1123	0.0000	0.0000	0.0000	0.0000	0.2505
CCmulti-π	1.9899	1.0450	0.0001	0.0001	0.0001	0.0002	3.0353
CCmisc	0.3567	0.1718	0.0000	0.0000	0.0001	0.0000	0.5286
NC1$\pi^\pm$	0.6827	0.9456	0.0263	N/A	0.0222	N/A	1.6767
NC1π^0	0.0773	0.0756	0.0034	N/A	0.0015	N/A	0.1578
NCcoh	0.0006	0.0000	0.0000	N/A	0.0000	N/A	0.0006
NCmisc	0.6242	0.3481	0.0255	N/A	0.0139	N/A	1.0117
NC1γ	0.0000	0.0000	0.0000	N/A	0.0000	N/A	0.0000
Total	55.7039	79.3867	0.0577	0.0022	0.0403	0.0039	135.1946

Table B.2: Event rates for the $\bar{\nu}$-mode ν_μ / $\bar{\nu}_\mu$ CCQE-like sample, generated with the Asimov A oscillation parameter values in Table 4.8 and nominal values of the systematic parameters.

	$\nu_\mu \to \nu_\mu$	$\bar{\nu}_\mu \to \bar{\nu}_\mu$	$\nu_e \to \nu_e$	$\nu_\mu \to \nu_e$	$\bar{\nu}_e \to \bar{\nu}_e$	$\bar{\nu}_\mu \to \bar{\nu}_e$	Total
CCQE	0.2691	0.0103	8.0402	59.5872	0.2998	0.3473	68.5539
CC1$\pi^\pm$	0.0393	0.0032	1.2321	6.0308	0.0778	0.0624	7.4457
CC1π^0	0.0126	0.0007	0.2662	1.2368	0.0100	0.0077	1.5339
CCcoh	0.0000	0.0001	0.0097	0.0418	0.0028	0.0028	0.0572
CC2p2h	0.0532	0.0019	1.5280	9.0715	0.0542	0.0510	10.7597
CCDIS	0.0000	0.0000	0.0106	0.0009	0.0019	0.0000	0.0135
CCmulti-π	0.0195	0.0003	0.1833	0.1261	0.0084	0.0031	0.3406
CCmisc	0.0006	0.0002	0.0279	0.0288	0.0016	0.0005	0.0596
NC1$\pi^\pm$	0.2956	0.0129	0.0090	N/A	0.0008	N/A	0.3183
NC1π^0	1.9777	0.0795	0.0392	N/A	0.0047	N/A	2.1011
NCcoh	0.3158	0.0314	0.0062	N/A	0.0019	N/A	0.3553
NCmisc	0.5671	0.0238	0.0187	N/A	0.0025	N/A	0.6121
NC1γ	1.4978	0.0653	0.0337	N/A	0.0031	N/A	1.5999
Total	5.0481	0.2298	11.4048	76.1239	0.4696	0.4747	93.7509

Table B.3: Event rates for the ν-mode ν_e / $\bar{\nu}_e$ CCQE-like sample, generated with the Asimov A oscillation parameter values in Table 4.8 and nominal values of the systematic parameters.

	$\nu_\mu \to \nu_\mu$	$\bar{\nu}_\mu \to \bar{\nu}_\mu$	$\nu_e \to \nu_e$	$\nu_\mu \to \nu_e$	$\bar{\nu}_e \to \bar{\nu}_e$	$\bar{\nu}_\mu \to \bar{\nu}_e$	Total
CCQE	0.0348	0.0529	1.0389	2.2586	1.6464	5.7498	10.7815
CC1$\pi^{\pm}$	0.0097	0.0143	0.2060	0.3188	0.2753	0.6692	1.4933
CC1π^{0}	0.0026	0.0032	0.0428	0.0690	0.0344	0.0759	0.2279
CCcoh	0.0000	0.0005	0.0012	0.0018	0.0132	0.0422	0.0589
CC2p2h	0.0104	0.0077	0.2473	0.4147	0.2386	0.7025	1.6211
CCDIS	0.0000	0.0000	0.0005	0.0003	0.0010	0.0000	0.0019
CCmulti-π	0.0030	0.0023	0.0432	0.0227	0.0185	0.0129	0.1025
CCmisc	0.0010	0.0000	0.0082	0.0037	0.0044	0.0013	0.0187
NC1$\pi^{\pm}$	0.0520	0.0427	0.0019	N/A	0.0011	N/A	0.0977
NC1π^{0}	0.2484	0.3414	0.0103	N/A	0.0084	N/A	0.6084
NCcoh	0.0449	0.1509	0.0016	N/A	0.0029	N/A	0.2003
NCmisc	0.1348	0.0632	0.0069	N/A	0.0029	N/A	0.2078
NC1γ	0.1746	0.2868	0.0069	N/A	0.0053	N/A	0.4736
Total	0.7163	0.9657	1.6155	3.0896	2.2525	7.2538	15.8936

Table B.4: Event rates for the $\bar{\nu}$-mode ν_e / $\bar{\nu}_e$ CCQE-like sample, generated with the Asimov A oscillation parameter values in Table 4.8 and nominal values of the systematic parameters.

	$\nu_\mu \to \nu_\mu$	$\bar{\nu}_\mu \to \bar{\nu}_\mu$	$\nu_e \to \nu_e$	$\nu_\mu \to \nu_e$	$\bar{\nu}_e \to \bar{\nu}_e$	$\bar{\nu}_\mu \to \bar{\nu}_e$	Total
CCQE	0.0514	0.0011	0.0413	0.4154	0.0024	0.0035	0.5152
CC1$\pi^\pm$	0.0396	0.0017	0.8920	6.1824	0.0026	0.0022	7.1206
CC1π^0	0.0254	0.0007	0.0296	0.1560	0.0007	0.0009	0.2133
CCcoh	0.0004	0.0000	0.0164	0.0931	0.0002	0.0001	0.1100
CC2p2h	0.0113	0.0004	0.0283	0.1408	0.0012	0.0012	0.1832
CCDIS	0.0000	0.0002	0.0034	0.0003	0.0000	0.0000	0.0039
CCmulti-π	0.0401	0.0005	0.1427	0.1467	0.0027	0.0012	0.3339
CCmisc	0.0113	0.0001	0.0097	0.0045	0.0002	0.0001	0.0260
NC1$\pi^\pm$	0.0701	0.0029	0.0034	N/A	0.0005	N/A	0.0768
NC1π^0	0.0279	0.0010	0.0008	N/A	0.0000	N/A	0.0297
NCcoh	0.0000	0.0000	0.0000	N/A	0.0000	N/A	0.0000
NCmisc	0.1967	0.0202	0.0107	N/A	0.0020	N/A	0.2297
NC1γ	0.0000	0.0003	0.0000	N/A	0.0002	N/A	0.0005
Total	0.4742	0.0291	1.1783	7.1393	0.0126	0.0092	8.8428

Table B.5: Event rates for the ν-mode ν_eCC1π^+-like sample, generated with the Asimov A oscillation parameter values in Table 4.8 and nominal values of the systematic parameters.

C — Landau-Gaussian Fit

All ND280 sub-detectors apply a Landau-Gaussian convolution fit to extract the MIP MPV response at each point in time. The details of the fit and the results for each sub-detector is described below.

C.1 — ECal

The application of the Landau-Gaussian convolution fit follows the following steps for the ECal.
First a pair of data quality criteria are applied.

1. The MIP light yield distribution must have a minimum of 100 hits, if not the data is disregarded.
2. The `ROOT::TSpectrum` class is used to apply a peak search. The peak search must locate at least one peak or the data is disregarded.

A Gaussian fit is then applied around the peak in the distribution to extract approximate mean and sigma values to use as priors for the Landau-Gaussian convolution.

3. The RMS (σ_{RMS}) of the light yield distribution is extracted and used to define a fit range around the peak (P_{LY}), $P_{\text{LY}} \pm \sigma_{\text{RMS}}$.
4. A Gaussian fit is then applied over the range $P_{\text{LY}} \pm \sigma_{\text{RMS}}$ and the Gaussian mean (μ_{Gaus}) and sigma (σ_{Gaus}) extracted.

The fit range, initial parameter values and limits for the Landau-Gaussian convolution are then calculated.

There are four parameters that define the Landau-Gaussian convolution, the width (scale parameter) of the Landau density (σ_{LD}), the most probable value (location parameter) of the Landau density (μ_{LD}), the total area of the distribution (normalisation parameter, integral $-\infty \rightarrow \infty$) of the convolved distribution (N_{LD}), and the width (sigma) of the Gaussian distribution ($\sigma_{\text{LD-Gaus}}$).

5. The lower bound on the fit range for the Landau-Gaussian convolution is restricted to the higher value of either 0 or $\mu_{\text{Gaus}} - 1.5\sigma_{\text{Gaus}}$; the upper bound is $\mu_{\text{Gaus}} + 2.0\sigma_{\text{Gaus}}$.
6. An initial value for σ_{LD} of 0.1 times the mean value of the full light yield distribution is applied ($0.1\mu_{\text{LY}}$). Lower and upper limits of 0.5 and $100\mu_{\text{LY}}$, respectively, are set.

7. An initial value for μ_{LD} of μ_{Gaus} is applied. Lower and upper limits for the parameter are equal to the lower and upper bounds on the fit range; either 0 or $\mu_{\text{Gaus}} - 1.5\sigma_{\text{Gaus}}$ for the lower limit and $\mu_{\text{Gaus}} + 2.0\sigma_{\text{Gaus}}$ for the upper limit.

8. An initial value for N_{LD} of 1.2 times the integral of the light yield distribution $(1.2N_{\text{LY}})$ is applied. Lower and upper limits of $0.01N_{\text{LY}}$ and $100N_{\text{LY}}$, respectively, are set.

9. An initial value for $\sigma_{\text{LD-Gaus}}$ of σ_{Gaus} is applied. Lower and upper limits of 0.01 and $100\sigma_{\text{Gaus}}$, respectively, are set.

The Landau-Gaussian convolution fit is then applied to the light yield distribution. The Landau-Gaussian convolution is calculated via an integration by sum method as encoded in the ROOT `langaus.C` tutorial example [169]. It has the form:

$f(x) = \frac{N_{\text{LY}}}{\sigma_{\text{LD-Gaus}}\sigma_{\text{LD}}\sqrt{2\pi}} \int_{x-5\sigma_{\text{LD-Gaus}}}^{x+5\sigma_{\text{LD-Gaus}}} \text{Landau}\left(s, \mu_{\text{LD}}, \sigma_{\text{LD}}\right) \times \text{Gaus}\left(x, s, \sigma_{\text{LD-Gaus}}\right) ds$

Where the Landau and Gaus functions are the `ROOT::TMath::Landau()` and `ROOT::TMath::Gaus()` implementations.

10. The Landau-Gaussian convolution fit minimisation is performed by `MINUIT` using the `MIGRAD` algorithm. Once performed the fit is required to have successfully converged and have a returned a $\chi^2/\text{NDF} < 25.0$, otherwise the data is disregarded.

The results of the Landau-Gaussian convolution fits for the MIP MPV data presented in Figure 6.2b are shown in Figures C.1, C.2, C.3 and C.4 for the Barrel X, Barrel Y, Barrel Z and Downstream, respectively, and the associated fit parameters are shown in Table C.1.

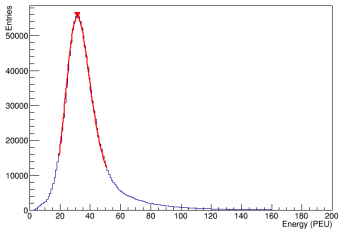

(a) 2010 11

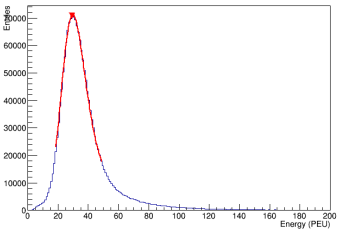

(b) 2010 12

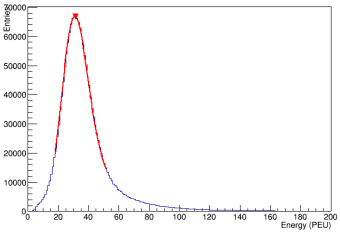

(c) 2011 01

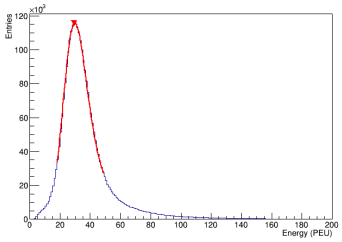

(d) 2011 02

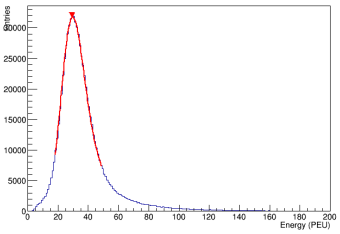

(e) 2011 03

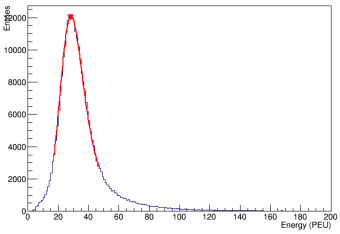

(f) 2012 02

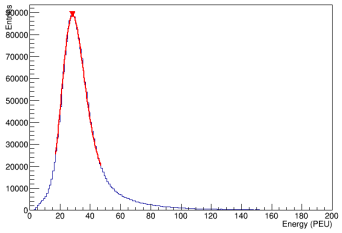

(g) 2012 03

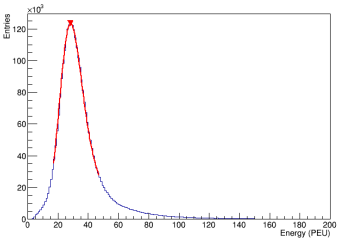

(h) 2012 04

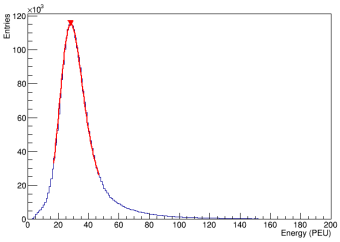

(i) 2012 05

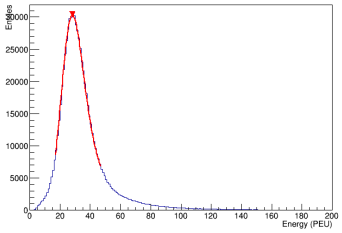

(j) 2012 06

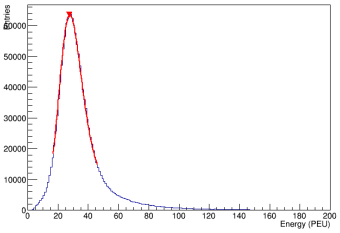

(k) 2012 10

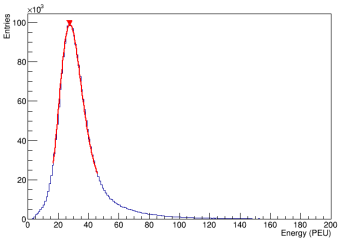

(l) 2012 11

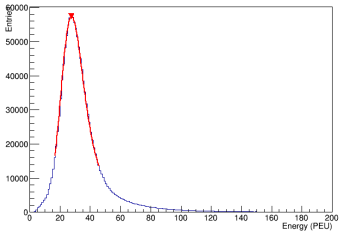

(m) 2012 12

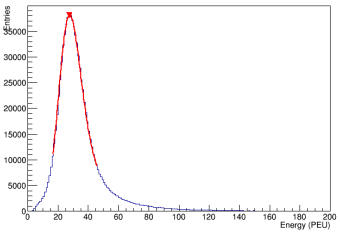

(n) 2013 01

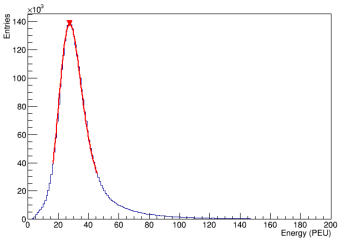

(o) 2013 02

Figure C.1: ECal Barrel X Landau-Gaussian convolution fits.

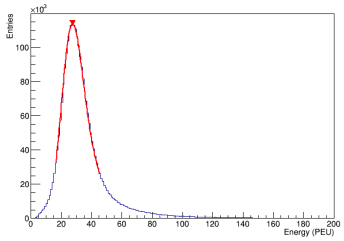

(p) 2013 03

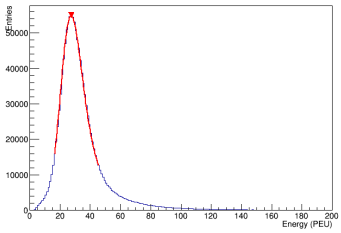

(q) 2013 04

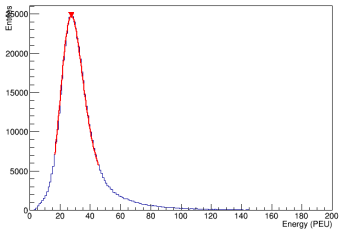

(r) 2013 05

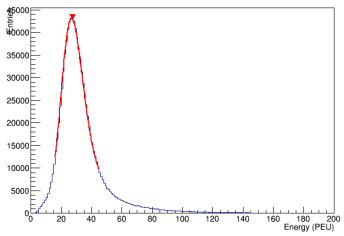

(s) 2014 05

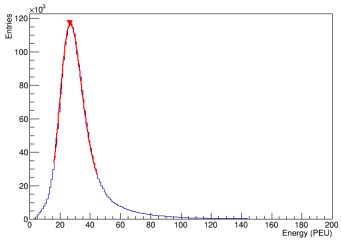

(t) 2014 06

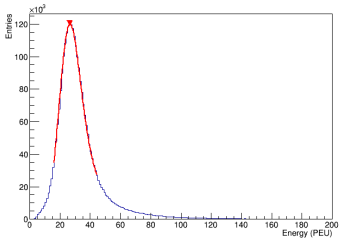

(u) 2014 11

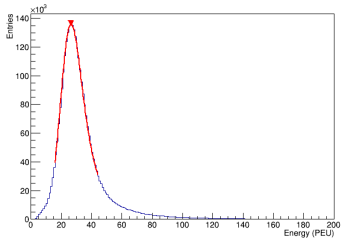

(v) 2014 12

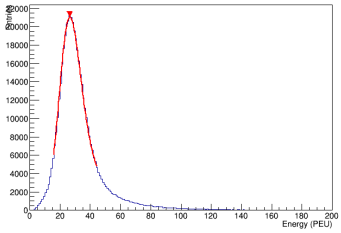

(w) 2015 01

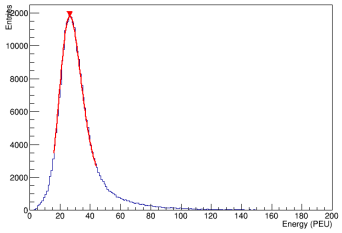

(x) 2015 02

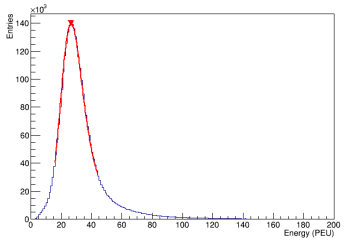

(y) 2015 03

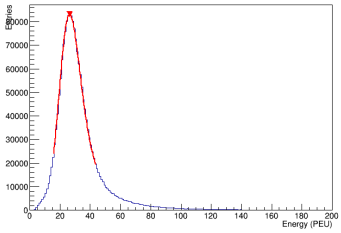

(z) 2015 05

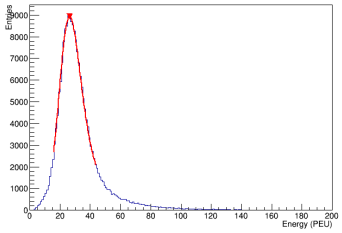

(aa) 2015 06

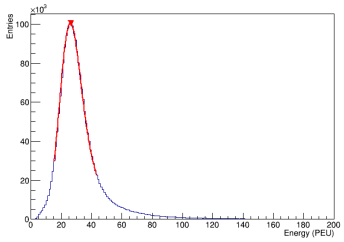

(ab) 2016 02

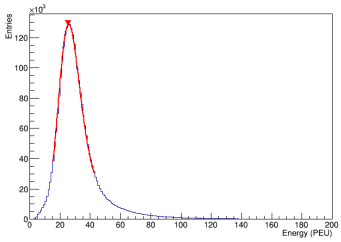

(ac) 2016 03

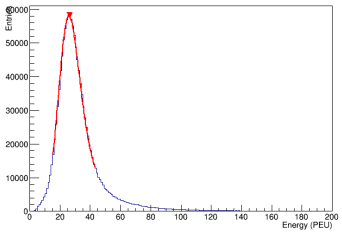

(ad) 2016 04

Figure C.1: ECal Barrel X Landau-Gaussian convolution fits.

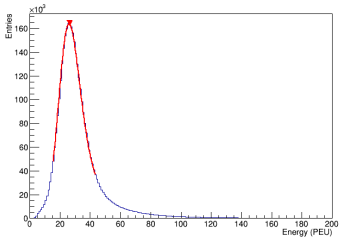

(ae) 2016 05

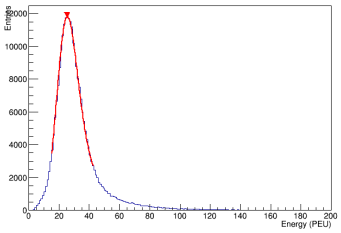

(af) 2016 10

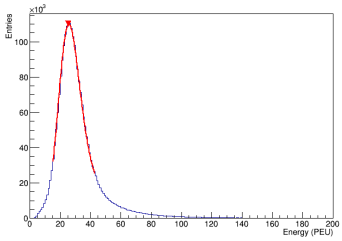

(ag) 2016 11

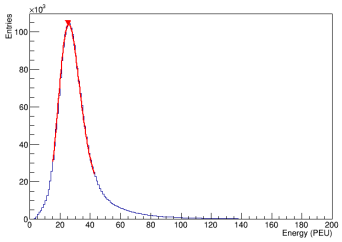

(ah) 2016 12

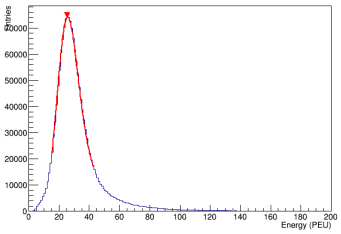

(ai) 2017 01

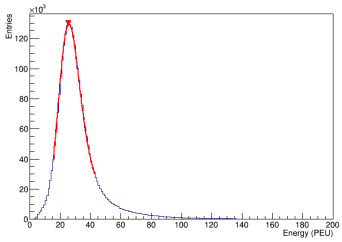

(aj) 2017 02

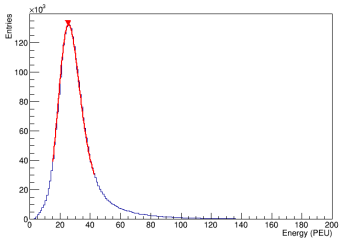

(ak) 2017 03

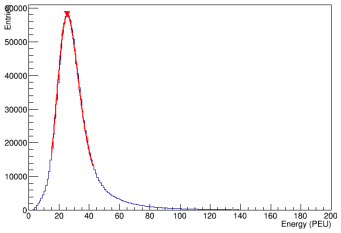

(al) 2017 04

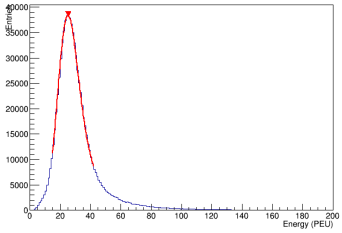

(am) 2017 10

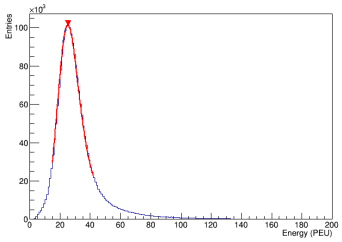

(an) 2017 11

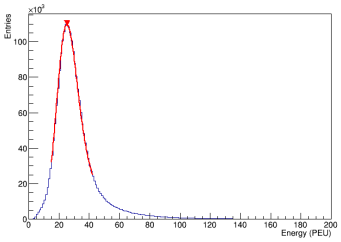

(ao) 2017 12

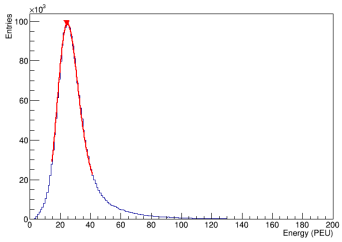

(ap) 2018 03

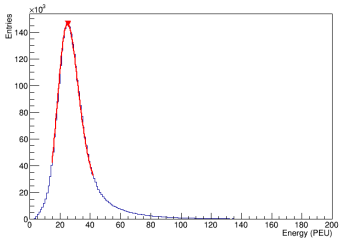

(aq) 2018 04

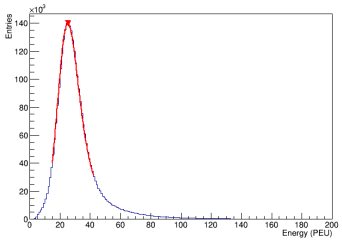

(ar) 2018 05

Figure C.1: ECal Barrel X Landau-Gaussian convolution fits.

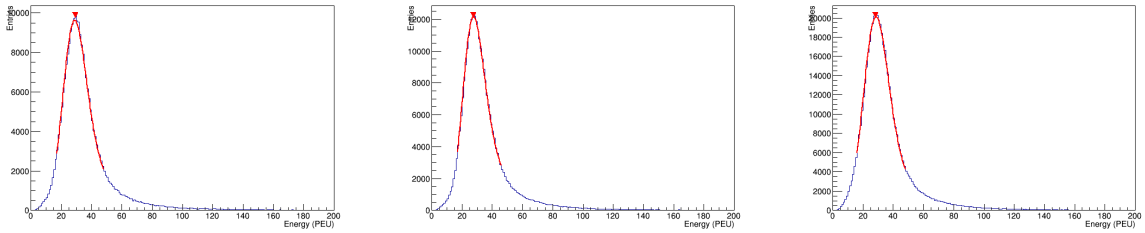

(a) 2010 11

(b) 2010 12

(c) 2011 01

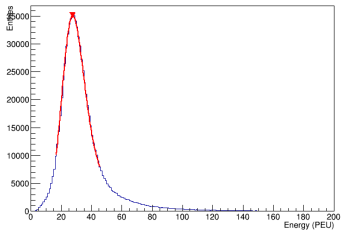

(d) 2011 02

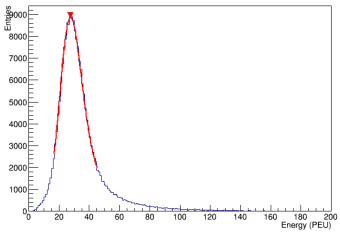

(e) 2011 03

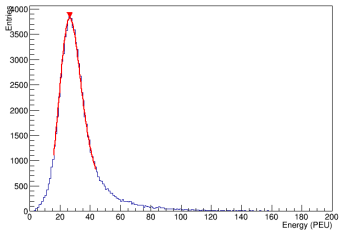

(f) 2012 02

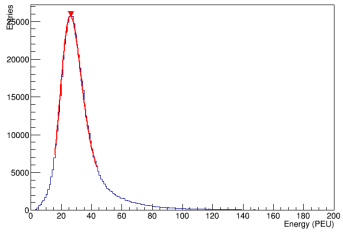

(g) 2012 03

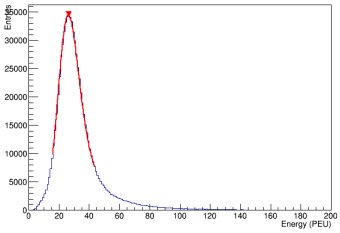

(h) 2012 04

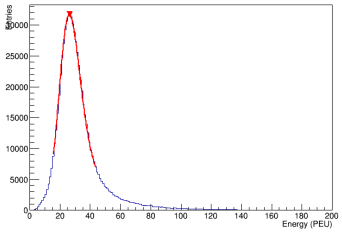

(i) 2012 05

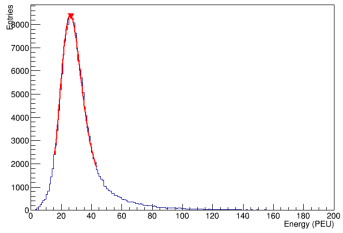

(j) 2012 06

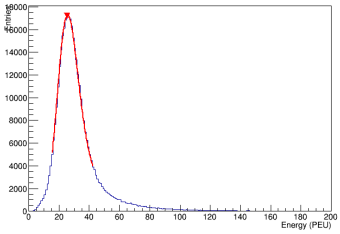

(k) 2012 10

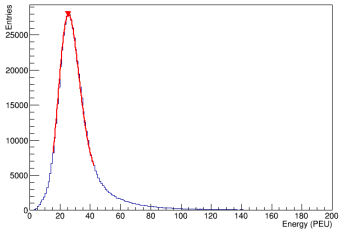

(l) 2012 11

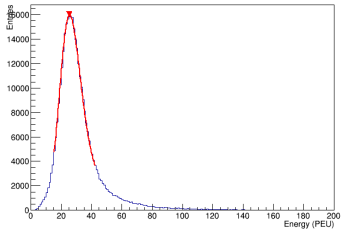

(m) 2012 12

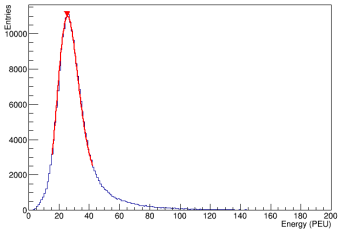

(n) 2013 01

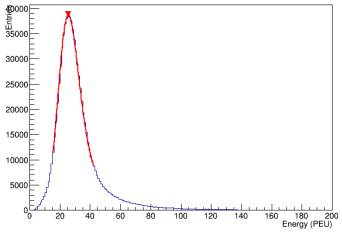

(o) 2013 02

Figure C.2: ECal Barrel Y Landau-Gaussian convolution fits.

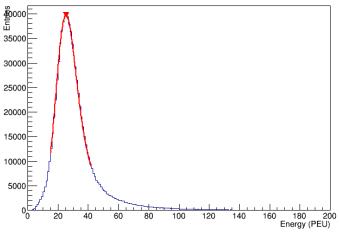

(p) 2013 03

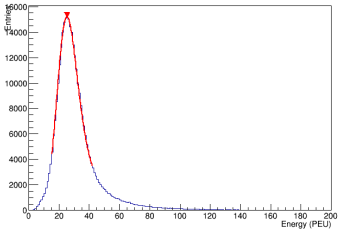

(q) 2013 04

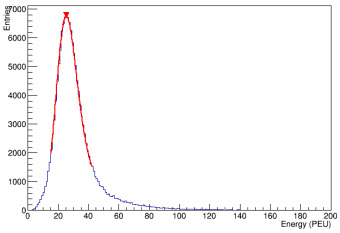

(r) 2013 05

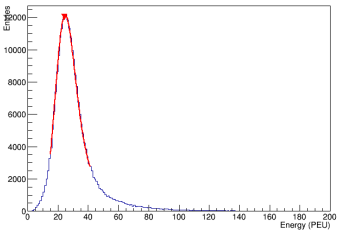

(s) 2014 05

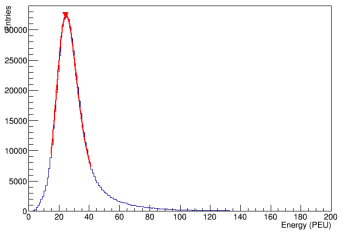

(t) 2014 06

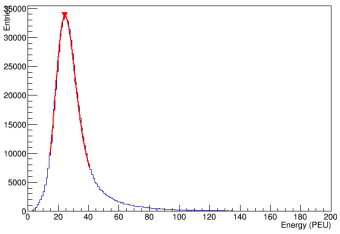

(u) 2014 11

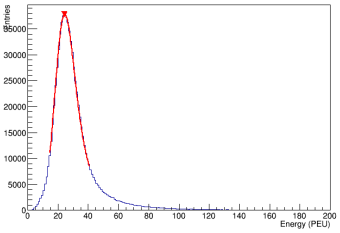

(v) 2014 12

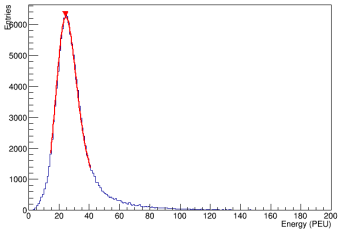

(w) 2015 01

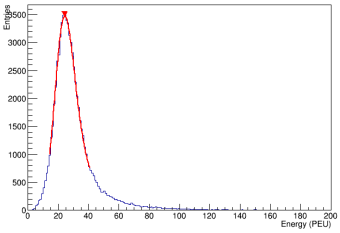

(x) 2015 02

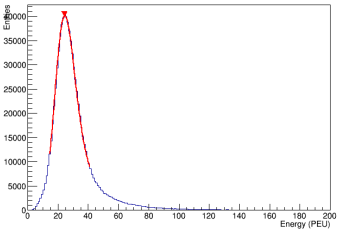

(y) 2015 03

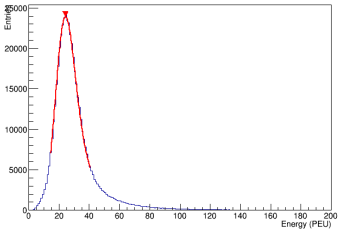

(z) 2015 05

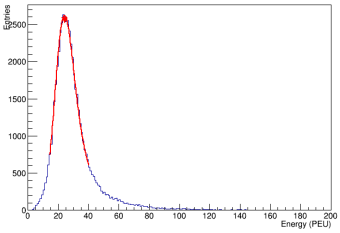

(aa) 2015 06

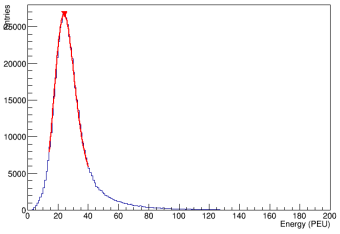

(ab) 2016 02

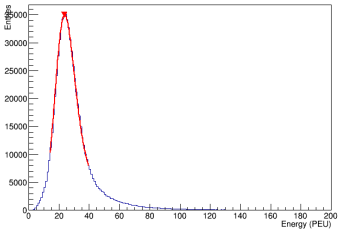

(ac) 2016 03

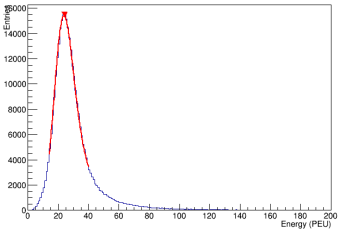

(ad) 2016 04

Figure C.2: ECal Barrel Y Landau-Gaussian convolution fits.

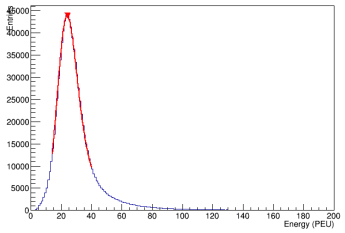

(ae) 2016 05

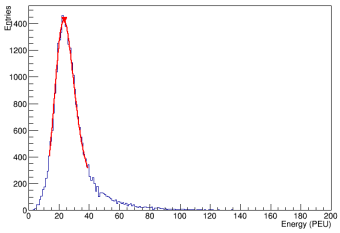

(af) 2016 10

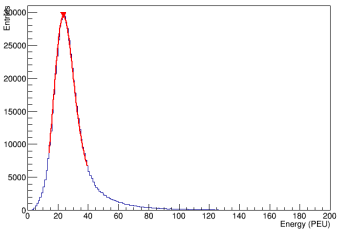

(ag) 2016 11

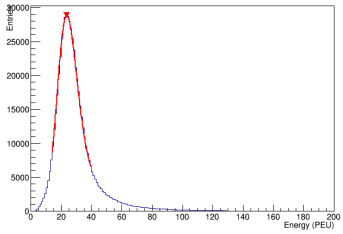

(ah) 2016 12

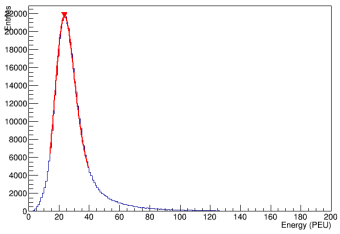

(ai) 2017 01

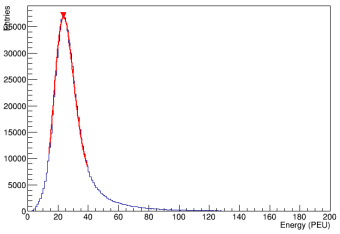

(aj) 2017 02

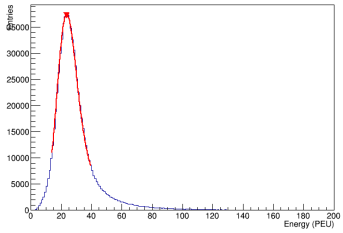

(ak) 2017 03

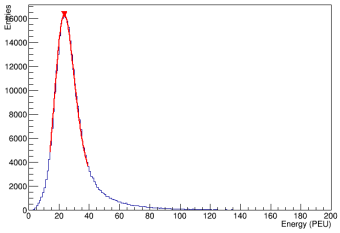

(al) 2017 04

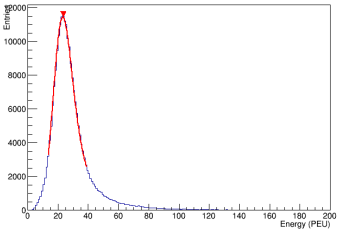

(am) 2017 10

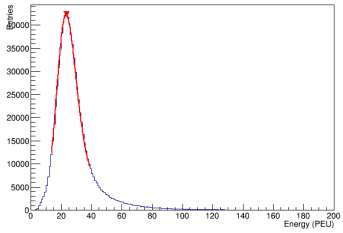

(an) 2017 11

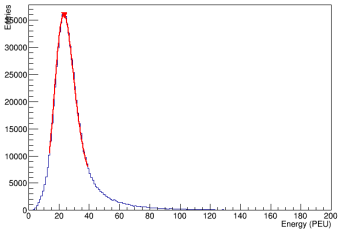

(ao) 2017 12

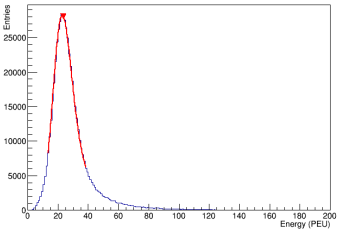

(ap) 2018 03

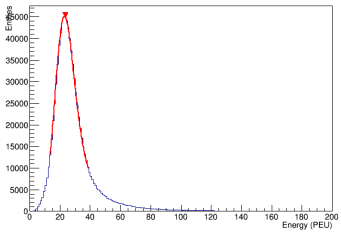

(aq) 2018 04

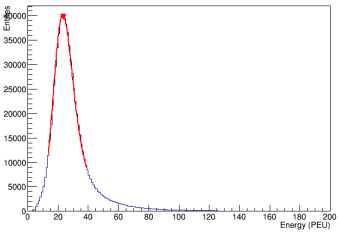

(ar) 2018 05

Figure C.2: ECal Barrel Y Landau-Gaussian convolution fits.

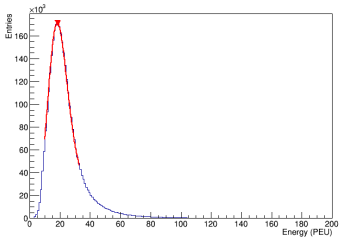

(a) 2010 11

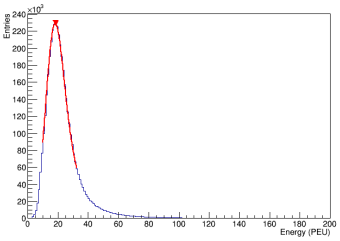

(b) 2010 12

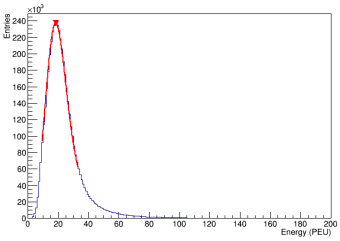

(c) 2011 01

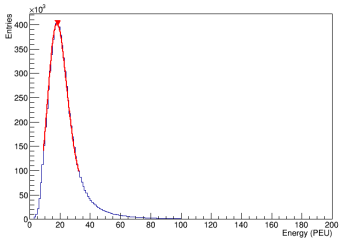

(d) 2011 02

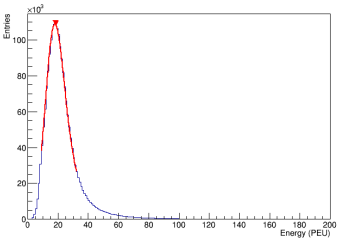

(e) 2011 03

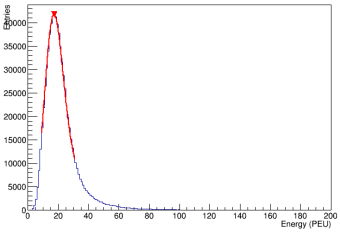

(f) 2012 02

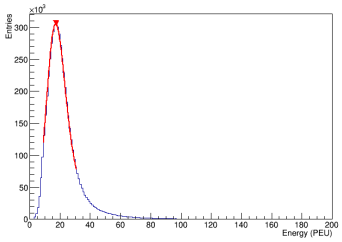

(g) 2012 03

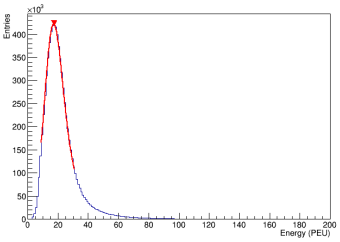

(h) 2012 04

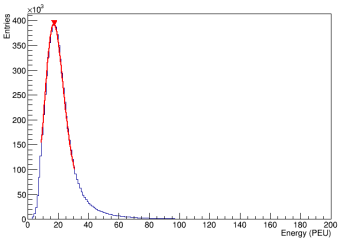

(i) 2012 05

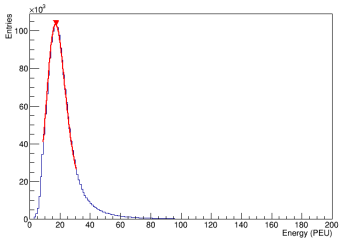

(j) 2012 06

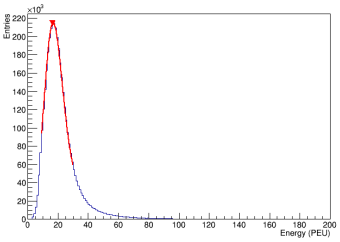

(k) 2012 10

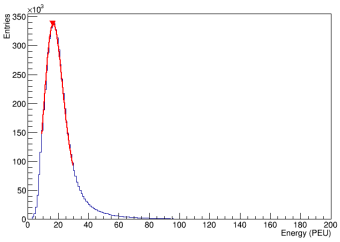

(l) 2012 11

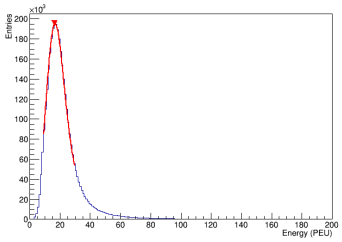

(m) 2012 12

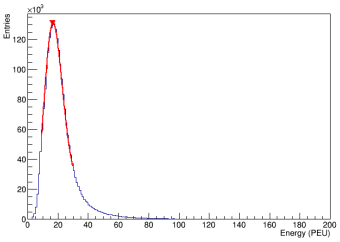

(n) 2013 01

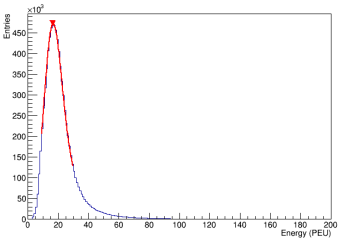

(o) 2013 02

Figure C.3: ECal Barrel Z Landau-Gaussian convolution fits.

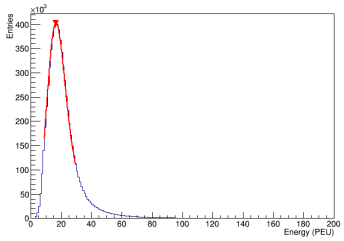

(p) 2013 03

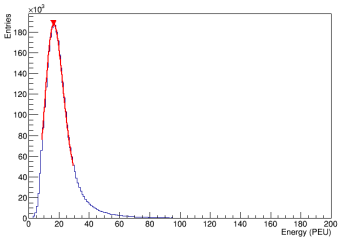

(q) 2013 04

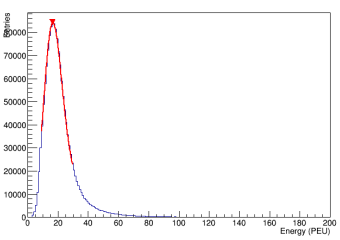

(r) 2013 05

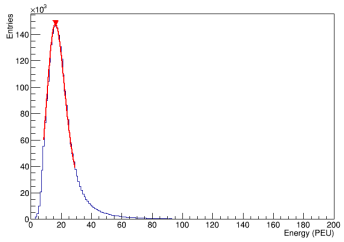

(s) 2014 05

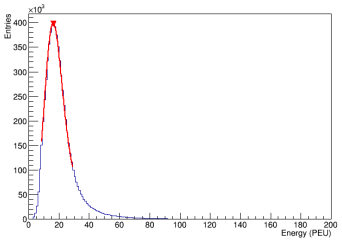

(t) 2014 06

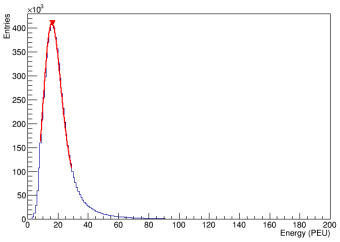

(u) 2014 11

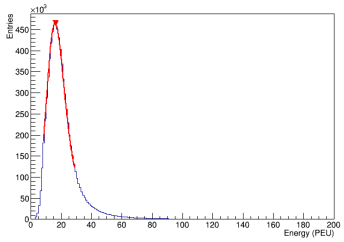

(v) 2014 12

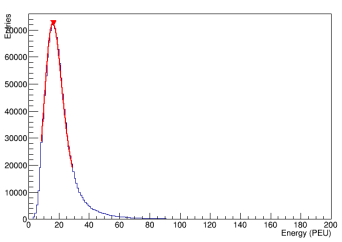

(w) 2015 01

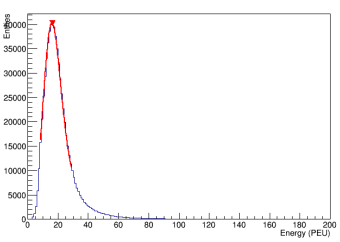

(x) 2015 02

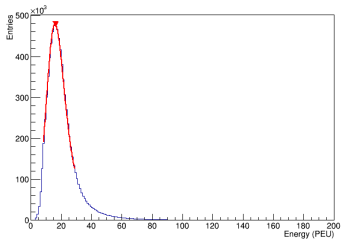

(y) 2015 03

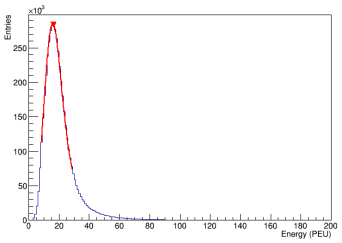

(z) 2015 05

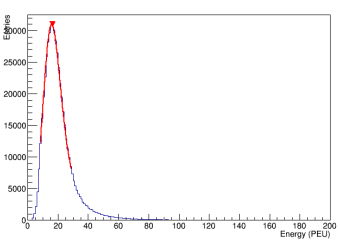

(aa) 2015 06

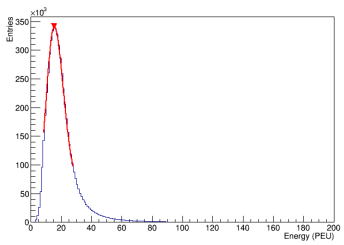

(ab) 2016 02

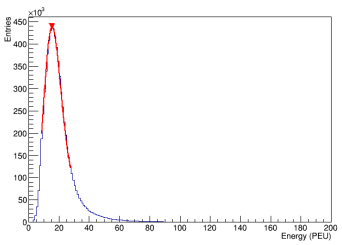

(ac) 2016 03

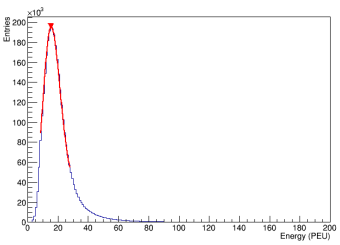

(ad) 2016 04

Figure C.3: ECal Barrel Z Landau-Gaussian convolution fits.

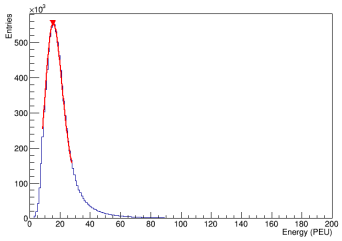

(ae) 2016 05

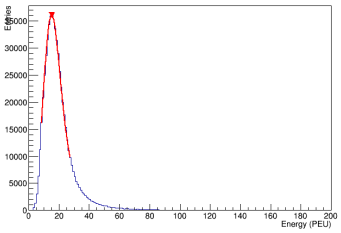

(af) 2016 10

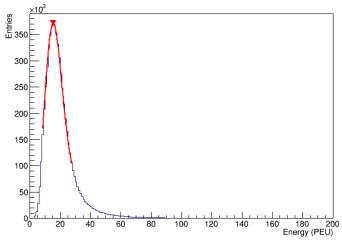

(ag) 2016 11

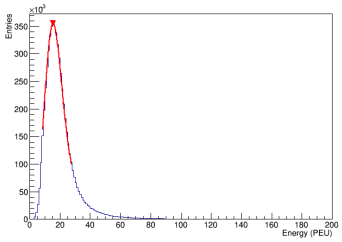

(ah) 2016 12

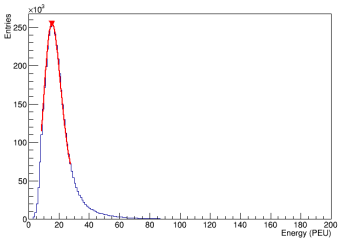

(ai) 2017 01

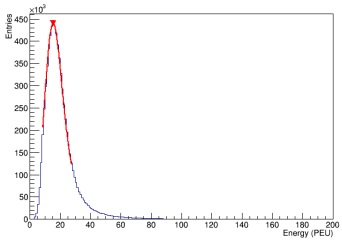

(aj) 2017 02

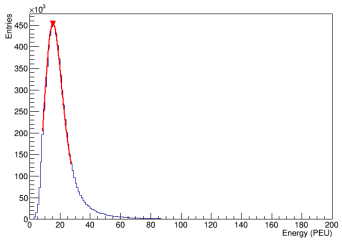

(ak) 2017 03

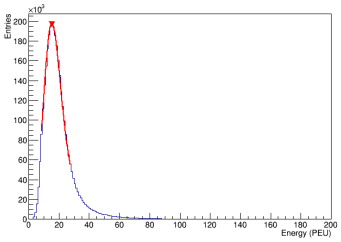

(al) 2017 04

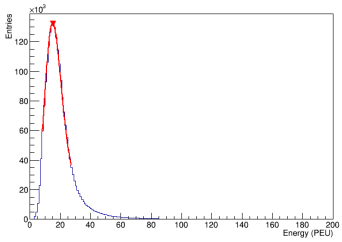

(am) 2017 10

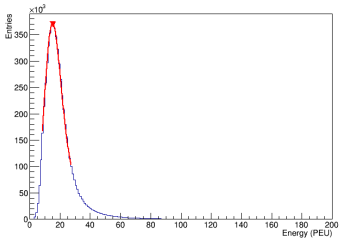

(an) 2017 11

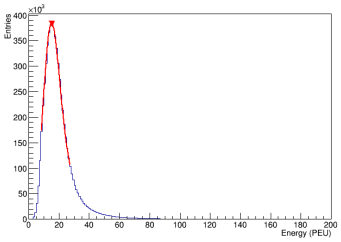

(ao) 2017 12

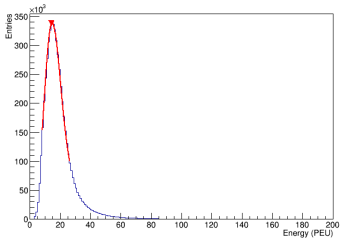

(ap) 2018 03

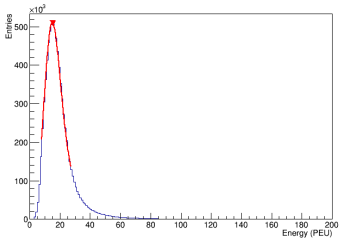

(aq) 2018 04

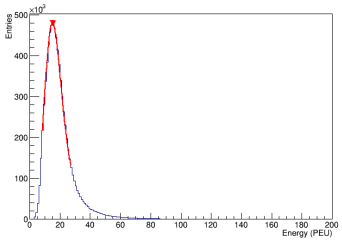

(ar) 2018 05

Figure C.3: ECal Barrel Z Landau-Gaussian convolution fits.

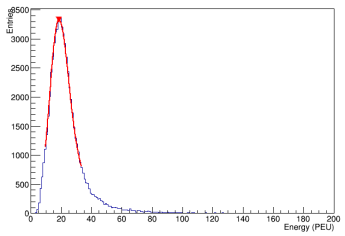

(a) 2010 03

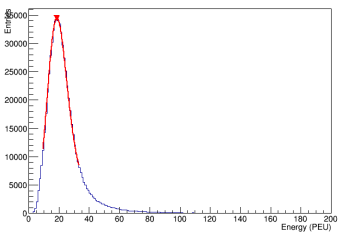

(b) 2010 04

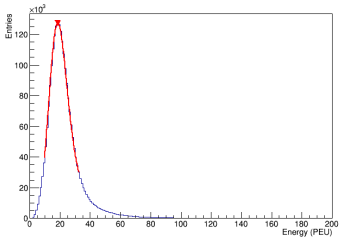

(c) 2010 05

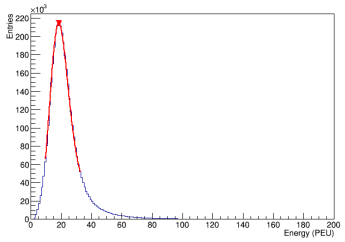

(d) 2010 06

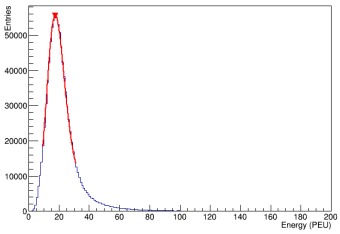

(e) 2010 11

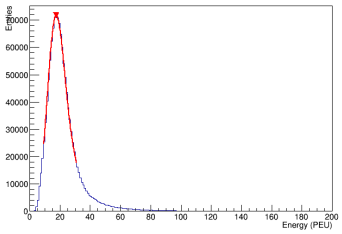

(f) 2010 12

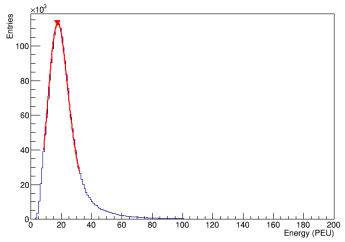

(g) 2011 01

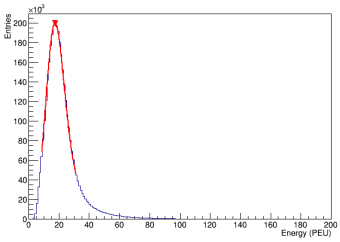

(h) 2011 02

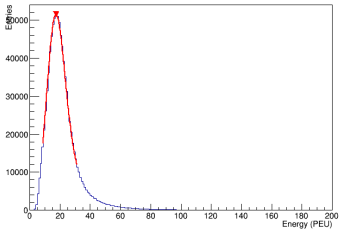

(i) 2011 03

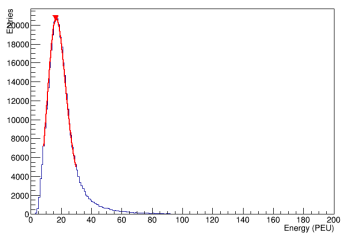

(j) 2012 02

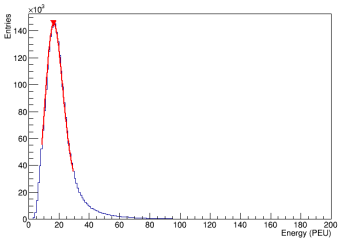

(k) 2012 03

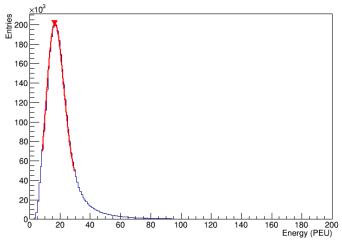

(l) 2012 04

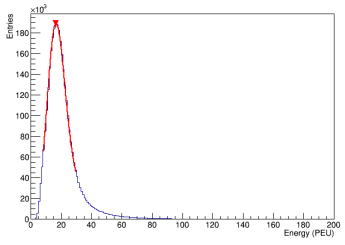

(m) 2012 05

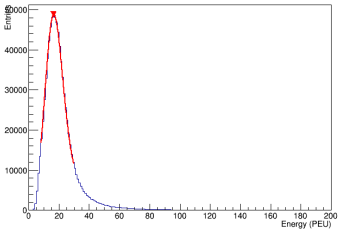

(n) 2012 06

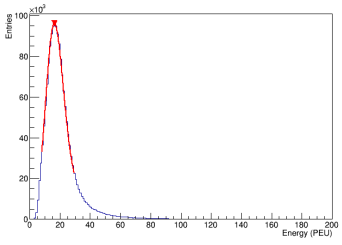

(o) 2012 10

Figure C.4: Downstream ECal Landau-Gaussian convolution fits.

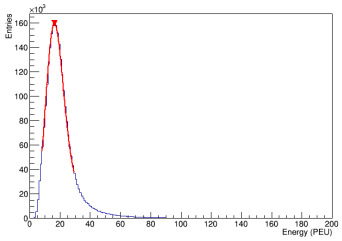

(p) 2012 11

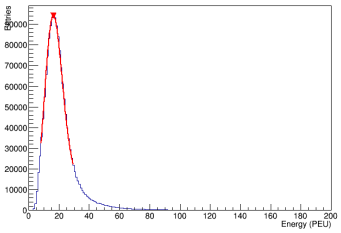

(q) 2012 12

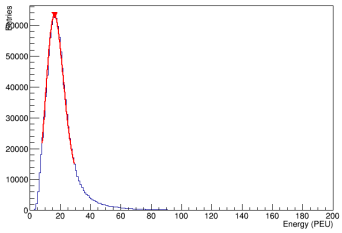

(r) 2013 01

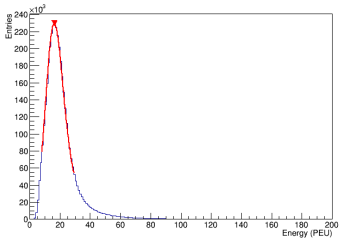

(s) 2013 02

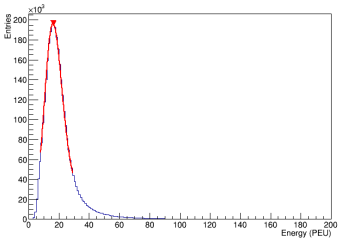

(t) 2013 03

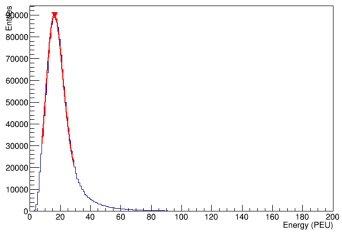

(u) 2013 04

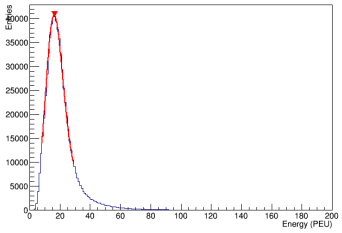

(v) 2013 05

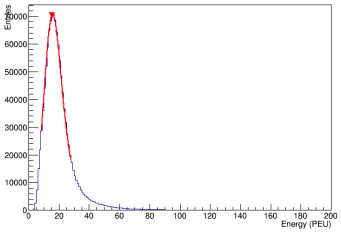

(w) 2014 05

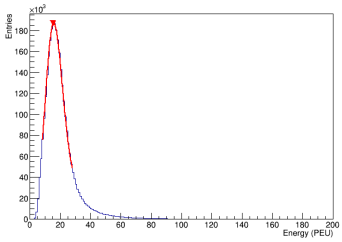

(x) 2014 06

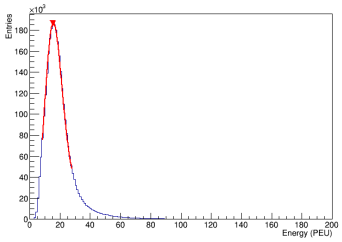

(y) 2014 11

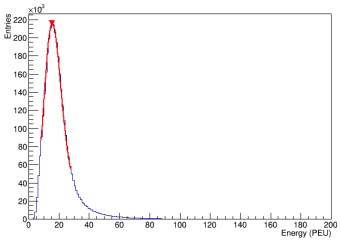

(z) 2014 12

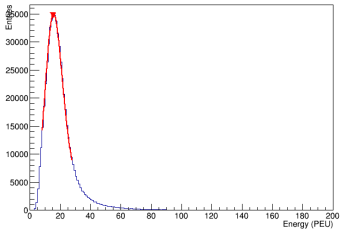

(aa) 2015 01

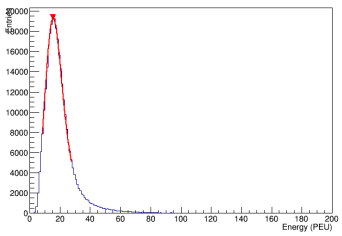

(ab) 2015 02

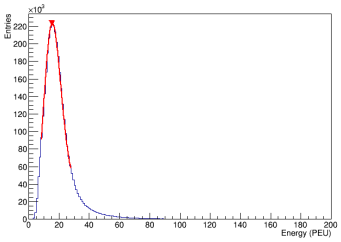

(ac) 2015 03

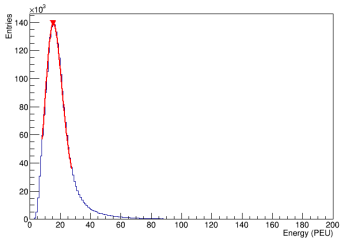

(ad) 2015 05

Figure C.4: Downstream ECal Landau-Gaussian convolution fits.

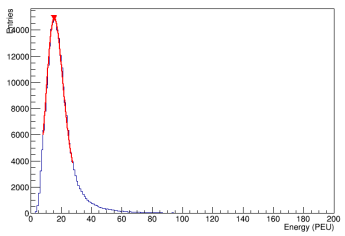

(ae) 2015 06

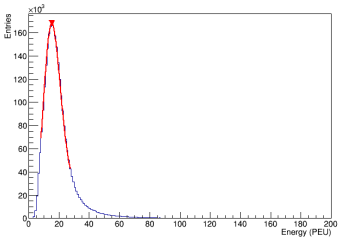

(af) 2016 02

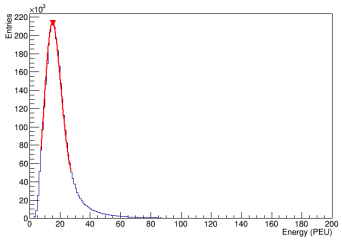

(ag) 2016 03

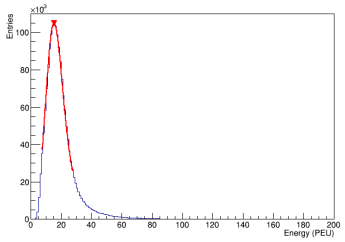

(ah) 2016 04

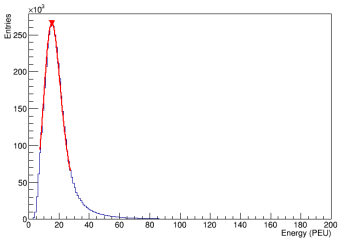

(ai) 2016 05

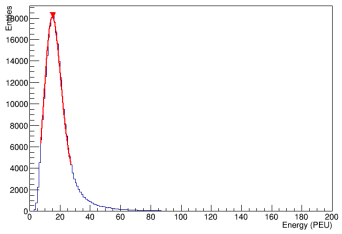

(aj) 2016 10

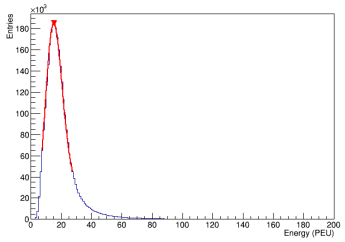

(ak) 2016 11

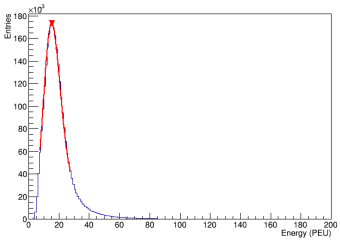

(al) 2016 12

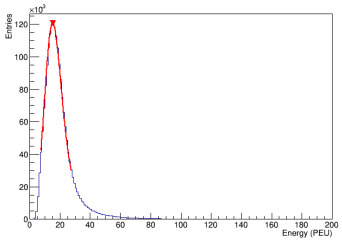

(am) 2017 01

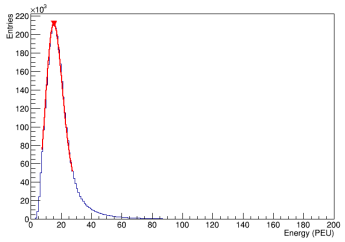

(an) 2017 02

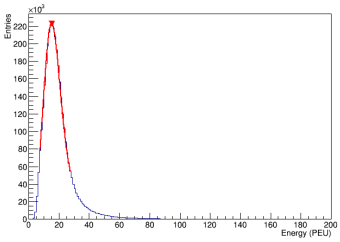

(ao) 2017 03

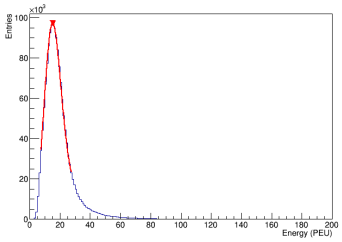

(ap) 2017 04

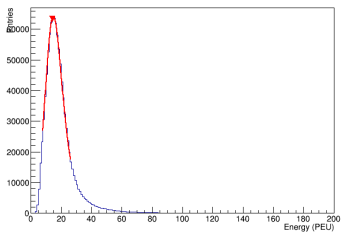

(aq) 2017 10

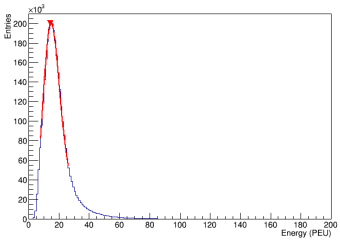

(ar) 2017 11

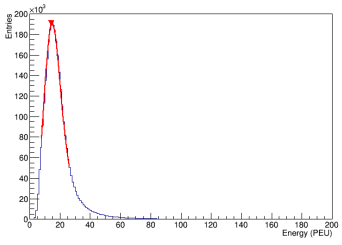

(as) 2017 12

Figure C.4: Downstream ECal Landau-Gaussian convolution fits.

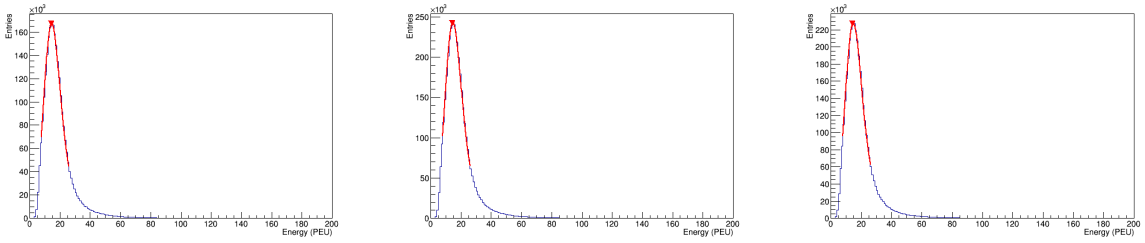

(at) 2018 03 (au) 2018 04 (av) 2018 05

Figure C.4: Downstream ECal Landau-Gaussian convolution fits.

Table C.1: ECal Landau-Gaussian convolution fit parameters.

Year Month	σ_{LD}	μ_{LD}	N_{LD}	$\sigma_{\text{LD-Gaus}}$	χ^2/NDF
Barrel X, single-ended (mirrored) readout					
2010 11	2.72 ± 0.02	29.23 ± 0.01	1401E3 $\pm$ 2E3	6.21 ± 0.03	$229.84/28 = 8.21$
2010 12	3.17 ± 0.03	27.67 ± 0.01	1863E3 $\pm$ 3E3	5.76 ± 0.04	$157.68/26 = 6.06$
2011 01	2.73 ± 0.02	28.48 ± 0.01	1820E3 $\pm$ 3E3	6.98 ± 0.03	$46.18/30 = 1.54$
2011 02	2.93 ± 0.02	27.64 ± 0.01	2945E3 $\pm$ 3E3	5.87 ± 0.03	$149.25/27 = 5.53$
2011 03	2.93 ± 0.03	27.57 ± 0.02	806E3 $\pm$ 2E3	5.86 ± 0.05	$82.14/27 = 3.04$
2012 02	2.78 ± 0.05	26.44 ± 0.03	294E3 $\pm$ 1E3	5.68 ± 0.08	$55.76/26 = 2.14$
2012 03	2.89 ± 0.02	26.28 ± 0.01	2182E3 $\pm$ 3E3	5.56 ± 0.03	$133.19/26 = 5.12$
2012 04	2.83 ± 0.02	26.26 ± 0.01	3015E3 $\pm$ 3E3	5.62 ± 0.02	$135.95/26 = 5.23$
2012 05	2.81 ± 0.02	26.25 ± 0.01	2823E3 $\pm$ 3E3	5.68 ± 0.02	$149.24/26 = 5.74$
2012 06	2.83 ± 0.03	26.17 ± 0.02	739E3 $\pm$ 2E3	5.59 ± 0.05	$31.67/26 = 1.22$
2012 10	2.81 ± 0.02	25.82 ± 0.01	1534E3 $\pm$ 2E3	5.55 ± 0.03	$97.36/25 = 3.89$
2012 11	2.86 ± 0.02	25.72 ± 0.01	2391E3 $\pm$ 3E3	5.45 ± 0.03	$122.12/25 = 4.88$
2012 12	2.85 ± 0.02	25.66 ± 0.01	1384E3 $\pm$ 2E3	5.44 ± 0.04	$58.24/25 = 2.33$
2013 01	2.70 ± 0.03	25.67 ± 0.01	915E3 $\pm$ 2E3	5.64 ± 0.04	$51.43/25 = 2.06$
2013 02	2.81 ± 0.02	25.58 ± 0.01	3333E3 $\pm$ 3E3	5.49 ± 0.02	$124.51/25 = 4.98$
2013 03	2.72 ± 0.02	25.48 ± 0.01	2717E3 $\pm$ 3E3	5.57 ± 0.03	$93.63/25 = 3.75$
2013 04	2.80 ± 0.02	25.40 ± 0.01	1313E3 $\pm$ 2E3	5.45 ± 0.04	$72.35/25 = 2.89$
2013 05	2.77 ± 0.04	25.52 ± 0.02	592E3 $\pm$ 1E3	5.48 ± 0.05	$39.15/25 = 1.57$
2014 05	2.70 ± 0.03	24.87 ± 0.01	1013E3 $\pm$ 2E3	5.44 ± 0.04	$58.23/25 = 2.33$
2014 06	2.67 ± 0.02	24.88 ± 0.01	2732E3 $\pm$ 3E3	5.46 ± 0.02	$169.79/25 = 6.79$
2014 11	2.67 ± 0.02	24.64 ± 0.01	2794E3 $\pm$ 3E3	5.41 ± 0.02	$112.28/25 = 4.49$
2014 12	2.72 ± 0.02	24.57 ± 0.01	3171E3 $\pm$ 3E3	5.33 ± 0.02	$128.56/24 = 5.36$
2015 01	2.66 ± 0.04	24.59 ± 0.02	490E3 $\pm$ 1E3	5.41 ± 0.06	$47.16/25 = 1.89$
2015 02	2.58 ± 0.05	24.56 ± 0.03	272E3 $\pm$ 1E3	5.46 ± 0.08	$43.98/24 = 1.83$
2015 03	2.68 ± 0.02	24.59 ± 0.01	3251E3 $\pm$ 3E3	5.39 ± 0.02	$95.34/24 = 3.97$
2015 05	2.68 ± 0.02	24.41 ± 0.01	1916E3 $\pm$ 3E3	5.29 ± 0.03	$62.18/24 = 2.59$
2015 06	2.66 ± 0.06	24.40 ± 0.03	208E3 $\pm$ 1E3	5.40 ± 0.09	$44.14/24 = 1.84$
2016 02	2.55 ± 0.02	24.00 ± 0.01	2317E3 $\pm$ 3E3	5.52 ± 0.02	$72.40/25 = 2.90$
2016 03	2.59 ± 0.02	23.84 ± 0.01	2934E3 $\pm$ 3E3	5.32 ± 0.02	$118.14/24 = 4.92$
2016 04	2.57 ± 0.02	23.94 ± 0.01	1320E3 $\pm$ 2E3	5.35 ± 0.03	$56.56/24 = 2.36$
2016 05	2.57 ± 0.01	24.03 ± 0.01	3744E3 $\pm$ 3E3	5.40 ± 0.02	$206.36/25 = 8.25$

Continued on next page

Table C.1 – continued from previous page

Year Month	σ_{LD}	μ_{LD}	N_{LD}	$\sigma_{\text{LD-Gaus}}$	χ^2/NDF
2016 10	2.55 ± 0.05	23.59 ± 0.02	266E3 ± 1E3	5.30 ± 0.07	$35.13/24 = 1.46$
2016 11	2.57 ± 0.02	23.78 ± 0.01	2499E3 ± 3E3	5.33 ± 0.02	$111.64/24 = 4.65$
2016 12	2.55 ± 0.02	23.81 ± 0.01	2366E3 ± 3E3	5.38 ± 0.02	$115.11/24 = 4.80$
2017 01	2.52 ± 0.02	23.76 ± 0.01	1679E3 ± 2E3	5.38 ± 0.03	$73.29/24 = 3.05$
2017 02	2.54 ± 0.02	23.77 ± 0.01	2941E3 ± 3E3	5.37 ± 0.02	$129.14/24 = 5.38$
2017 03	2.53 ± 0.02	23.73 ± 0.01	3001E3 ± 3E3	5.38 ± 0.02	$135.55/24 = 5.65$
2017 04	2.54 ± 0.02	23.57 ± 0.01	1308E3 ± 2E3	5.33 ± 0.03	$71.04/24 = 2.96$
2017 10	2.51 ± 0.03	23.21 ± 0.01	856E3 ± 2E3	5.25 ± 0.04	$37.15/23 = 1.62$
2017 11	2.48 ± 0.02	23.25 ± 0.01	2245E3 ± 3E3	5.24 ± 0.03	$84.68/23 = 3.68$
2017 12	2.54 ± 0.02	23.34 ± 0.01	2456E3 ± 3E3	5.24 ± 0.02	$92.30/23 = 4.01$
2018 03	2.48 ± 0.02	22.87 ± 0.01	2172E3 ± 3E3	5.14 ± 0.03	$106.96/23 = 4.65$
2018 04	2.48 ± 0.01	23.08 ± 0.01	3239E3 ± 3E3	5.24 ± 0.02	$91.90/23 = 4.00$
2018 05	2.53 ± 0.02	23.29 ± 0.01	3121E3 ± 3E3	5.25 ± 0.02	$127.22/23 = 5.53$
Barrel Y, single-ended (mirrored) readout					
2010 11	2.55 ± 0.06	26.62 ± 0.03	240E3 ± 1E3	6.32 ± 0.08	$56.39/27 = 2.09$
2010 12	2.86 ± 0.05	25.65 ± 0.02	291E3 ± 1E3	5.35 ± 0.08	$23.25/25 = 0.93$
2011 01	2.39 ± 0.05	26.20 ± 0.03	515E3 ± 1E3	6.86 ± 0.06	$77.64/28 = 2.77$
2011 02	2.66 ± 0.03	25.61 ± 0.01	826E3 ± 2E3	5.53 ± 0.04	$40.72/25 = 1.63$
2011 03	2.46 ± 0.06	25.62 ± 0.03	206E3 ± 1E3	5.73 ± 0.09	$39.53/25 = 1.58$
2012 02	2.38 ± 0.09	24.46 ± 0.05	86E3 ± 1E3	5.57 ± 0.13	$22.21/24 = 0.93$
2012 03	2.62 ± 0.03	24.25 ± 0.02	581E3 ± 1E3	5.19 ± 0.05	$36.10/24 = 1.50$
2012 04	2.57 ± 0.03	24.28 ± 0.01	777E3 ± 2E3	5.24 ± 0.04	$25.03/24 = 1.04$
2012 05	2.52 ± 0.03	24.27 ± 0.02	712E3 ± 1E3	5.31 ± 0.04	$36.08/24 = 1.50$
2012 06	2.59 ± 0.06	24.12 ± 0.03	188E3 ± 1E3	5.14 ± 0.09	$31.31/23 = 1.36$
2012 10	2.49 ± 0.04	23.81 ± 0.02	384E3 ± 1E3	5.25 ± 0.06	$23.01/23 = 1.00$
2012 11	2.47 ± 0.03	23.74 ± 0.02	618E3 ± 1E3	5.25 ± 0.04	$33.39/24 = 1.39$
2012 12	2.49 ± 0.04	23.68 ± 0.02	355E3 ± 1E3	5.26 ± 0.06	$29.09/24 = 1.21$
2013 01	2.54 ± 0.05	23.76 ± 0.03	243E3 ± 1E3	5.10 ± 0.08	$28.27/23 = 1.23$
2013 02	2.49 ± 0.03	23.62 ± 0.01	856E3 ± 2E3	5.21 ± 0.04	$33.54/23 = 1.46$
2013 03	2.47 ± 0.03	23.36 ± 0.01	873E3 ± 2E3	5.19 ± 0.04	$39.97/23 = 1.74$
2013 04	2.58 ± 0.04	23.43 ± 0.02	335E3 ± 1E3	5.02 ± 0.06	$22.80/23 = 0.99$
2013 05	2.49 ± 0.07	23.47 ± 0.03	150E3 ± 1E3	5.20 ± 0.10	$14.20/23 = 0.62$
2014 05	2.46 ± 0.05	22.95 ± 0.02	262E3 ± 1E3	5.02 ± 0.07	$18.01/22 = 0.82$
2014 06	2.45 ± 0.03	22.90 ± 0.01	703E3 ± 2E3	5.08 ± 0.05	$29.80/22 = 1.35$
2014 11	2.40 ± 0.03	22.71 ± 0.01	719E3 ± 2E3	5.03 ± 0.04	$40.06/22 = 1.82$
2014 12	2.42 ± 0.03	22.63 ± 0.01	809E3 ± 2E3	5.01 ± 0.04	$27.67/22 = 1.26$
2015 01	2.27 ± 0.07	22.65 ± 0.04	134E3 ± 1E3	5.29 ± 0.11	$17.36/22 = 0.79$
2015 02	2.33 ± 0.09	22.55 ± 0.05	74E3 ± 1E3	5.14 ± 0.12	$22.28/23 = 0.97$
2015 03	2.43 ± 0.03	22.66 ± 0.01	865E3 ± 2E3	5.06 ± 0.04	$20.61/22 = 0.94$
2015 05	2.34 ± 0.03	22.47 ± 0.02	509E3 ± 1E3	5.12 ± 0.05	$52.97/23 = 2.30$
2015 06	2.48 ± 0.11	22.44 ± 0.05	55E3 ± 1E3	4.79 ± 0.16	$16.58/21 = 0.79$
2016 02	2.26 ± 0.03	22.13 ± 0.02	564E3 ± 1E3	5.19 ± 0.05	$34.67/22 = 1.58$
2016 03	2.33 ± 0.03	21.96 ± 0.01	731E3 ± 2E3	4.95 ± 0.04	$39.31/22 = 1.79$
2016 04	2.39 ± 0.04	22.04 ± 0.02	325E3 ± 1E3	4.95 ± 0.06	$23.87/22 = 1.08$

Continued on next page

Table C.1 – continued from previous page

Year Month	σ_{LD}	μ_{LD}	N_{LD}	$\sigma_{\text{LD-Gaus}}$	χ^2/NDF
2016 05	2.30 ± 0.03	22.11 ± 0.01	$923\text{E}3 \pm 2\text{E}3$	5.09 ± 0.04	$38.61/22 = 1.75$
2016 10	2.31 ± 0.14	21.47 ± 0.07	$29\text{E}3 \pm 1\text{E}3$	4.83 ± 0.21	$16.41/21 = 0.78$
2016 11	2.32 ± 0.03	21.84 ± 0.02	$615\text{E}3 \pm 1\text{E}3$	4.98 ± 0.04	$36.53/22 = 1.66$
2016 12	2.30 ± 0.03	21.89 ± 0.02	$605\text{E}3 \pm 1\text{E}3$	5.04 ± 0.05	$44.76/22 = 2.03$
2017 01	2.30 ± 0.04	21.87 ± 0.02	$453\text{E}3 \pm 1\text{E}3$	5.01 ± 0.05	$31.91/22 = 1.45$
2017 02	2.36 ± 0.03	21.90 ± 0.01	$773\text{E}3 \pm 2\text{E}3$	4.95 ± 0.04	$42.15/22 = 1.92$
2017 03	2.31 ± 0.03	21.83 ± 0.01	$784\text{E}3 \pm 2\text{E}3$	5.00 ± 0.04	$40.68/22 = 1.85$
2017 04	2.29 ± 0.04	21.75 ± 0.02	$338\text{E}3 \pm 1\text{E}3$	4.95 ± 0.06	$28.64/21 = 1.36$
2017 10	2.34 ± 0.05	21.41 ± 0.02	$236\text{E}3 \pm 1\text{E}3$	4.84 ± 0.07	$26.66/21 = 1.27$
2017 11	2.22 ± 0.03	21.47 ± 0.01	$867\text{E}3 \pm 2\text{E}3$	5.00 ± 0.04	$39.20/21 = 1.87$
2017 12	2.28 ± 0.03	21.44 ± 0.01	$743\text{E}3 \pm 2\text{E}3$	4.92 ± 0.04	$32.53/21 = 1.55$
2018 03	2.25 ± 0.03	21.10 ± 0.02	$571\text{E}3 \pm 1\text{E}3$	4.82 ± 0.05	$47.88/21 = 2.28$
2018 04	2.27 ± 0.02	21.22 ± 0.01	$924\text{E}3 \pm 2\text{E}3$	4.88 ± 0.04	$26.28/21 = 1.25$
2018 05	2.26 ± 0.03	21.41 ± 0.01	$826\text{E}3 \pm 2\text{E}3$	4.96 ± 0.04	$48.03/21 = 2.29$
Barrel Z, double-ended readout					
2010 11	2.42 ± 0.02	16.44 ± 0.01	$3614\text{E}3 \pm 4\text{E}3$	4.89 ± 0.03	$53.18/19 = 2.80$
2010 12	2.28 ± 0.01	16.41 ± 0.01	$4635\text{E}3 \pm 4\text{E}3$	4.76 ± 0.02	$60.77/19 = 3.20$
2011 01	2.21 ± 0.02	16.44 ± 0.01	$5094\text{E}3 \pm 5\text{E}3$	5.43 ± 0.02	$29.08/20 = 1.45$
2011 02	2.07 ± 0.01	16.19 ± 0.01	$8130\text{E}3 \pm 6\text{E}3$	5.12 ± 0.01	$112.74/20 = 5.64$
2011 03	2.06 ± 0.02	16.16 ± 0.01	$2193\text{E}3 \pm 3\text{E}3$	5.10 ± 0.03	$31.04/20 = 1.55$
2012 02	2.07 ± 0.03	15.48 ± 0.01	$824\text{E}3 \pm 2\text{E}3$	4.91 ± 0.05	$23.18/18 = 1.29$
2012 03	2.02 ± 0.01	15.39 ± 0.01	$5968\text{E}3 \pm 5\text{E}3$	4.90 ± 0.02	$46.76/18 = 2.60$
2012 04	2.05 ± 0.01	15.36 ± 0.01	$8274\text{E}3 \pm 6\text{E}3$	4.90 ± 0.01	$51.82/18 = 2.88$
2012 05	2.04 ± 0.01	15.35 ± 0.01	$7706\text{E}3 \pm 6\text{E}3$	4.91 ± 0.02	$38.18/18 = 2.12$
2012 06	2.05 ± 0.02	15.30 ± 0.01	$2026\text{E}3 \pm 3\text{E}3$	4.88 ± 0.03	$34.70/18 = 1.93$
2012 10	2.05 ± 0.02	15.08 ± 0.01	$4183\text{E}3 \pm 5\text{E}3$	4.82 ± 0.02	$22.00/17 = 1.29$
2012 11	2.04 ± 0.01	15.04 ± 0.01	$6552\text{E}3 \pm 6\text{E}3$	4.81 ± 0.02	$46.96/17 = 2.76$
2012 12	2.03 ± 0.02	15.01 ± 0.01	$3775\text{E}3 \pm 5\text{E}3$	4.80 ± 0.02	$21.17/17 = 1.25$
2013 01	2.01 ± 0.02	15.01 ± 0.01	$2521\text{E}3 \pm 4\text{E}3$	4.81 ± 0.03	$13.74/17 = 0.81$
2013 02	2.02 ± 0.01	14.95 ± 0.01	$9119\text{E}3 \pm 7\text{E}3$	4.80 ± 0.01	$35.08/17 = 2.06$
2013 03	2.03 ± 0.01	14.88 ± 0.01	$7755\text{E}3 \pm 6\text{E}3$	4.78 ± 0.02	$54.00/17 = 3.18$
2013 04	2.00 ± 0.02	14.87 ± 0.01	$3585\text{E}3 \pm 4\text{E}3$	4.76 ± 0.02	$32.13/17 = 1.89$
2013 05	2.01 ± 0.02	14.87 ± 0.01	$1624\text{E}3 \pm 3\text{E}3$	4.82 ± 0.04	$24.34/17 = 1.43$
2014 05	1.98 ± 0.02	14.51 ± 0.01	$2786\text{E}3 \pm 4\text{E}3$	4.69 ± 0.03	$21.16/16 = 1.32$
2014 06	2.04 ± 0.01	14.49 ± 0.01	$7516\text{E}3 \pm 7\text{E}3$	4.58 ± 0.01	$209.43/17 = 12.32$
2014 11	2.04 ± 0.01	14.35 ± 0.01	$7692\text{E}3 \pm 6\text{E}3$	4.52 ± 0.01	$202.72/17 = 11.92$
2014 12	2.05 ± 0.01	14.32 ± 0.01	$8699\text{E}3 \pm 7\text{E}3$	4.51 ± 0.01	$199.83/17 = 11.76$
2015 01	2.03 ± 0.02	14.30 ± 0.01	$1359\text{E}3 \pm 3\text{E}3$	4.54 ± 0.03	$44.44/17 = 2.61$
2015 02	2.02 ± 0.03	14.33 ± 0.01	$754\text{E}3 \pm 2\text{E}3$	4.56 ± 0.05	$24.52/17 = 1.44$
2015 03	2.04 ± 0.01	14.30 ± 0.01	$8982\text{E}3 \pm 7\text{E}3$	4.52 ± 0.01	$317.27/17 = 18.66$
2015 05	2.03 ± 0.01	14.22 ± 0.01	$5307\text{E}3 \pm 5\text{E}3$	4.50 ± 0.02	$167.75/17 = 9.87$
2015 06	2.09 ± 0.04	14.22 ± 0.01	$578\text{E}3 \pm 2\text{E}3$	4.41 ± 0.05	$32.85/17 = 1.93$
2016 02	1.96 ± 0.01	13.92 ± 0.01	$6322\text{E}3 \pm 6\text{E}3$	4.58 ± 0.02	$23.84/15 = 1.59$
2016 03	1.93 ± 0.01	13.82 ± 0.01	$8019\text{E}3 \pm 7\text{E}3$	4.54 ± 0.02	$27.87/15 = 1.86$

Continued on next page

Table C.1 – continued from previous page

Year Month	σ_{LD}	μ_{LD}	N_{LD}	$\sigma_{\text{LD-Gaus}}$	χ^2/NDF
2016 04	1.96 ± 0.02	13.93 ± 0.01	3599E3 ± 5E3	4.54 ± 0.03	$15.80/15 = 1.05$
2016 05	1.97 ± 0.01	13.92 ± 0.01	10260E3 ± 8E3	4.55 ± 0.02	$26.79/15 = 1.79$
2016 10	1.95 ± 0.03	13.58 ± 0.01	650E3 ± 2E3	4.38 ± 0.05	$28.45/16 = 1.78$
2016 11	1.95 ± 0.01	13.77 ± 0.01	6831E3 ± 6E3	4.53 ± 0.02	$15.88/15 = 1.06$
2016 12	1.95 ± 0.01	13.80 ± 0.01	6519E3 ± 6E3	4.53 ± 0.02	$21.47/15 = 1.43$
2017 01	2.01 ± 0.01	13.78 ± 0.01	4673E3 ± 5E3	4.40 ± 0.02	$149.78/16 = 9.36$
2017 02	1.93 ± 0.01	13.75 ± 0.01	8087E3 ± 7E3	4.56 ± 0.02	$35.21/15 = 2.35$
2017 03	2.02 ± 0.01	13.77 ± 0.01	8308E3 ± 7E3	4.37 ± 0.01	$290.32/16 = 18.15$
2017 04	2.01 ± 0.02	13.72 ± 0.01	3610E3 ± 4E3	4.37 ± 0.02	$129.93/16 = 8.12$
2017 10	2.02 ± 0.02	13.51 ± 0.01	2390E3 ± 4E3	4.25 ± 0.03	$88.17/15 = 5.88$
2017 11	2.05 ± 0.01	13.56 ± 0.01	6726E3 ± 7E3	4.23 ± 0.02	$317.58/15 = 21.17$
2017 12	2.01 ± 0.01	13.55 ± 0.01	6957E3 ± 7E3	4.30 ± 0.02	$207.60/15 = 13.84$
2018 03	1.97 ± 0.01	13.28 ± 0.01	5988E3 ± 7E3	4.20 ± 0.02	$171.48/14 = 12.25$
2018 04	1.96 ± 0.01	13.38 ± 0.01	9098E3 ± 7E3	4.28 ± 0.01	$263.57/15 = 17.57$
2018 05	1.98 ± 0.01	13.49 ± 0.01	8636E3 ± 7E3	4.31 ± 0.02	$261.12/15 = 17.41$
Downstream, double-ended readout					
2010 03	2.11 ± 0.12	16.81 ± 0.05	68E3 ± 1E3	5.09 ± 0.16	$12.31/19 = 0.65$
2010 04	2.11 ± 0.04	16.76 ± 0.02	702E3 ± 2E3	5.12 ± 0.05	$28.33/20 = 1.42$
2010 05	2.00 ± 0.02	16.84 ± 0.01	2426E3 ± 3E3	4.73 ± 0.02	$28.93/19 = 1.52$
2010 06	2.14 ± 0.01	16.73 ± 0.01	4165E3 ± 4E3	4.65 ± 0.02	$53.43/19 = 2.81$
2010 11	2.04 ± 0.02	15.96 ± 0.01	1039E3 ± 2E3	4.49 ± 0.03	$31.15/18 = 1.73$
2010 12	1.99 ± 0.02	15.86 ± 0.01	1344E3 ± 2E3	4.61 ± 0.03	$20.50/18 = 1.14$
2011 01	1.89 ± 0.02	15.82 ± 0.01	2292E3 ± 4E3	5.46 ± 0.03	$38.87/19 = 2.05$
2011 02	1.81 ± 0.02	15.64 ± 0.01	3808E3 ± 4E3	5.07 ± 0.02	$24.94/18 = 1.39$
2011 03	1.81 ± 0.03	15.60 ± 0.02	976E3 ± 2E3	5.02 ± 0.04	$29.76/18 = 1.65$
2012 02	1.72 ± 0.04	15.09 ± 0.02	378E3 ± 1E3	4.88 ± 0.05	$22.16/18 = 1.23$
2012 03	1.76 ± 0.02	14.90 ± 0.01	2651E3 ± 3E3	4.78 ± 0.02	$27.63/17 = 1.63$
2012 04	1.77 ± 0.01	14.93 ± 0.01	3699E3 ± 4E3	4.83 ± 0.02	$22.54/18 = 1.25$
2012 05	1.75 ± 0.01	14.93 ± 0.01	3468E3 ± 4E3	4.85 ± 0.02	$25.43/18 = 1.41$
2012 06	1.74 ± 0.03	14.87 ± 0.02	894E3 ± 2E3	4.86 ± 0.04	$21.79/18 = 1.21$
2012 10	1.74 ± 0.02	14.64 ± 0.01	1747E3 ± 3E3	4.80 ± 0.03	$22.44/18 = 1.25$
2012 11	1.73 ± 0.02	14.68 ± 0.01	2881E3 ± 4E3	4.76 ± 0.02	$10.03/17 = 0.59$
2012 12	1.72 ± 0.02	14.63 ± 0.01	1700E3 ± 3E3	4.77 ± 0.03	$13.94/17 = 0.82$
2013 01	1.79 ± 0.03	14.59 ± 0.01	1147E3 ± 2E3	4.70 ± 0.03	$8.97/17 = 0.53$
2013 02	1.73 ± 0.01	14.58 ± 0.01	4132E3 ± 5E3	4.76 ± 0.02	$19.62/17 = 1.15$
2013 03	1.76 ± 0.01	14.42 ± 0.01	3537E3 ± 4E3	4.70 ± 0.02	$19.99/17 = 1.18$
2013 04	1.74 ± 0.02	14.49 ± 0.01	1618E3 ± 3E3	4.74 ± 0.03	$14.87/17 = 0.87$
2013 05	1.77 ± 0.03	14.50 ± 0.02	730E3 ± 2E3	4.64 ± 0.04	$34.03/17 = 2.00$
2014 05	1.72 ± 0.03	14.17 ± 0.01	1253E3 ± 3E3	4.64 ± 0.03	$16.00/16 = 1.00$
2014 06	1.72 ± 0.02	14.16 ± 0.01	3320E3 ± 4E3	4.66 ± 0.02	$16.99/16 = 1.06$
2014 11	1.72 ± 0.02	14.04 ± 0.01	3293E3 ± 4E3	4.60 ± 0.02	$9.55/16 = 0.60$
2014 12	1.72 ± 0.01	13.98 ± 0.01	3794E3 ± 4E3	4.58 ± 0.02	$15.58/16 = 0.97$
2015 01	1.65 ± 0.04	14.03 ± 0.02	617E3 ± 2E3	4.73 ± 0.05	$14.06/16 = 0.88$
2015 02	1.86 ± 0.05	13.95 ± 0.02	342E3 ± 1E3	4.41 ± 0.06	$21.07/16 = 1.32$

Continued on next page

Table C.1 – continued from previous page

Year Month	σ_{LD}	μ_{LD}	N_{LD}	$\sigma_{\text{LD-Gaus}}$	χ^2/NDF
2015 03	1.75 ± 0.01	14.00 ± 0.01	3952E3 $\pm$ 5E3	4.58 ± 0.02	$21.60/16 = 1.35$
2015 05	1.72 ± 0.02	13.92 ± 0.01	2448E3 $\pm$ 4E3	4.57 ± 0.02	$22.69/16 = 1.42$
2015 06	1.77 ± 0.05	13.90 ± 0.02	261E3 $\pm$ 1E3	4.48 ± 0.07	$14.98/16 = 0.94$
2016 02	1.76 ± 0.02	13.67 ± 0.01	2939E3 $\pm$ 4E3	4.49 ± 0.02	$30.32/16 = 1.90$
2016 03	1.69 ± 0.01	13.51 ± 0.01	3669E3 $\pm$ 4E3	4.47 ± 0.02	$37.71/17 = 2.22$
2016 04	1.71 ± 0.02	13.71 ± 0.01	1828E3 $\pm$ 3E3	4.53 ± 0.03	$13.02/16 = 0.81$
2016 05	1.71 ± 0.01	13.69 ± 0.01	4628E3 $\pm$ 5E3	4.53 ± 0.02	$29.42/16 = 1.84$
2016 10	1.71 ± 0.04	13.42 ± 0.02	313E3 $\pm$ 1E3	4.49 ± 0.06	$12.26/17 = 0.72$
2016 11	1.72 ± 0.01	13.53 ± 0.01	3204E3 $\pm$ 4E3	4.47 ± 0.02	$20.27/17 = 1.19$
2016 12	1.73 ± 0.01	13.60 ± 0.01	3010E3 $\pm$ 4E3	4.48 ± 0.02	$23.08/17 = 1.36$
2017 01	1.77 ± 0.02	13.60 ± 0.01	2111E3 $\pm$ 3E3	4.46 ± 0.02	$30.82/17 = 1.81$
2017 02	1.72 ± 0.01	13.59 ± 0.01	3691E3 $\pm$ 4E3	4.51 ± 0.02	$53.80/17 = 3.16$
2017 03	1.73 ± 0.01	13.55 ± 0.01	3881E3 $\pm$ 4E3	4.49 ± 0.02	$30.19/17 = 1.78$
2017 04	1.66 ± 0.02	13.54 ± 0.01	1673E3 $\pm$ 3E3	4.52 ± 0.02	$17.52/17 = 1.03$
2017 10	1.72 ± 0.03	13.27 ± 0.01	1098E3 $\pm$ 3E3	4.40 ± 0.04	$23.35/14 = 1.67$
2017 11	1.70 ± 0.02	13.25 ± 0.01	3405E3 $\pm$ 5E3	4.36 ± 0.02	$4.74/14 = 0.34$
2017 12	1.67 ± 0.02	13.26 ± 0.01	3239E3 $\pm$ 5E3	4.41 ± 0.02	$11.07/14 = 0.79$
2018 03	1.68 ± 0.02	12.99 ± 0.01	2812E3 $\pm$ 4E3	4.31 ± 0.02	$14.54/14 = 1.04$
2018 04	1.68 ± 0.02	13.11 ± 0.01	4117E3 $\pm$ 5E3	4.39 ± 0.02	$10.26/14 = 0.73$
2018 05	1.72 ± 0.02	13.23 ± 0.01	3903E3 $\pm$ 5E3	4.38 ± 0.02	$21.99/14 = 1.57$

C.2 — P0D

The fitting method of P0D is similar to ECAL, but has several minor differences:

11. The normalisation factor of functional form of Landau-Gaussian function is different. The denominator is absorbed into the normalisation parameter.

12. The lower bound and higher bound of fitting range is different. The lower bound is 50% of mean of entries, and the higher bound is 150% of the mean. The fitting examples for 2010-2018 are shown in Figures C.5, C.6, C.7 and C.8 for the Super-PØDules 0 through 3, respectively, and the associated fit parameters are shown in Table C.2.

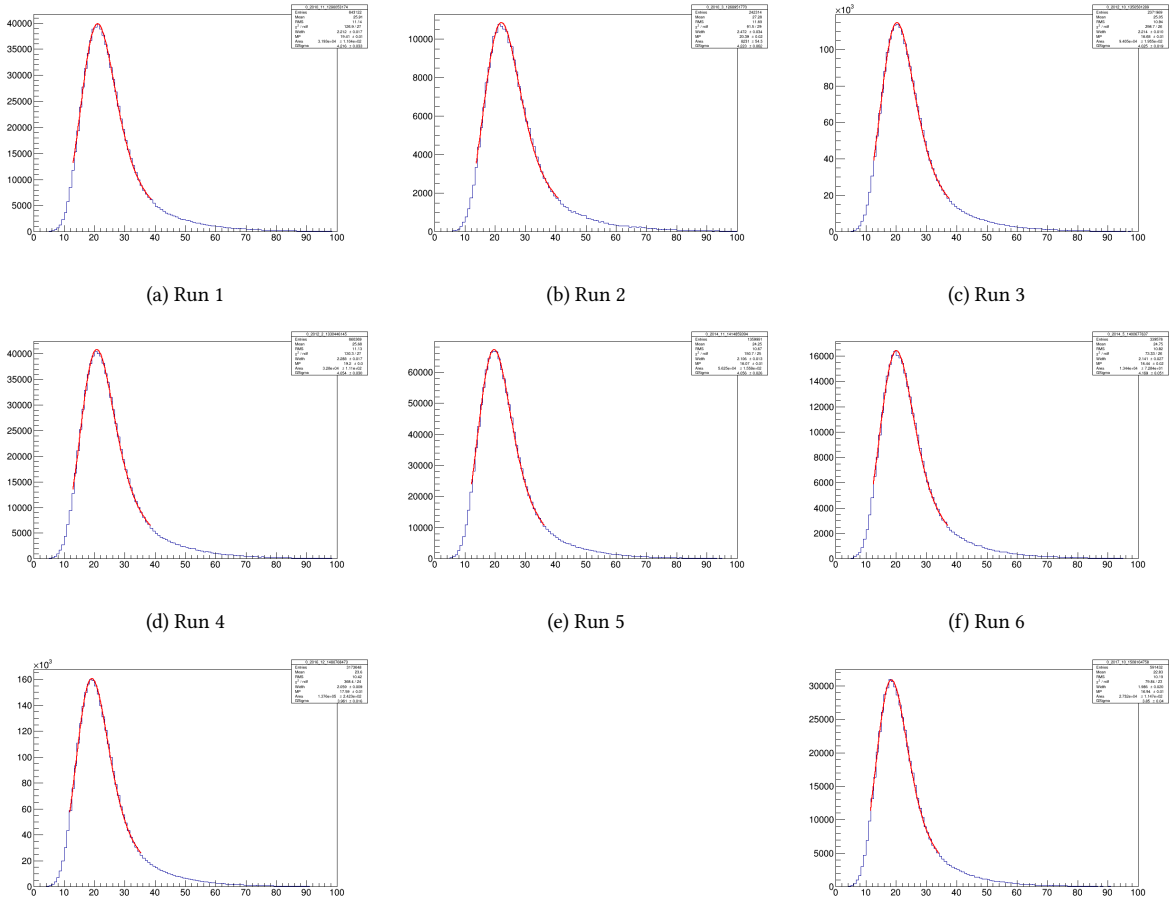

(a) Run 1 (b) Run 2 (c) Run 3

(d) Run 4 (e) Run 5 (f) Run 6

(g) Run 8 (h) Run 9

Figure C.5: P0D SuperP0Dule 0 Landau-Gaussian convolution fits.

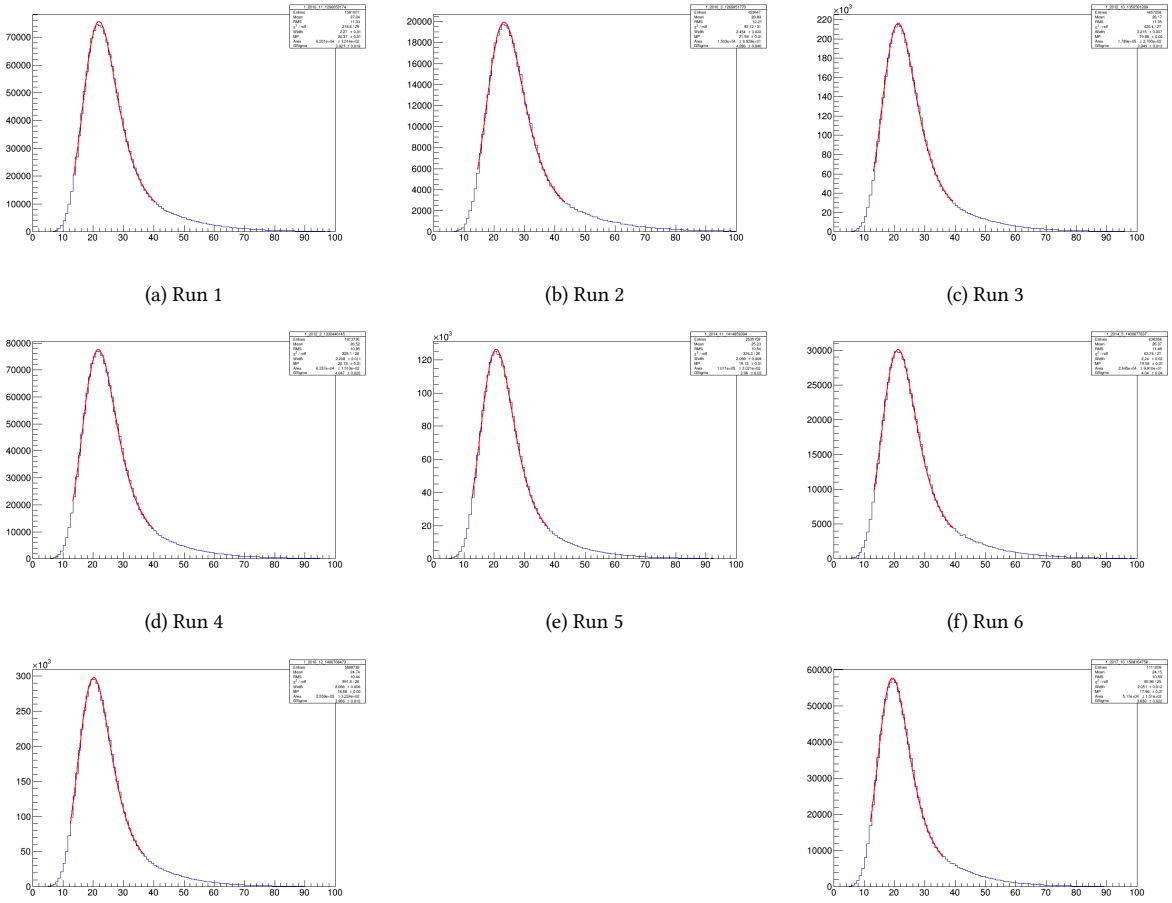

(a) Run 1 (b) Run 2 (c) Run 3

(d) Run 4 (e) Run 5 (f) Run 6

(g) Run 8 (h) Run 9

Figure C.6: P0D SuperP0Dule 1 Landau-Gaussian convolution fits.

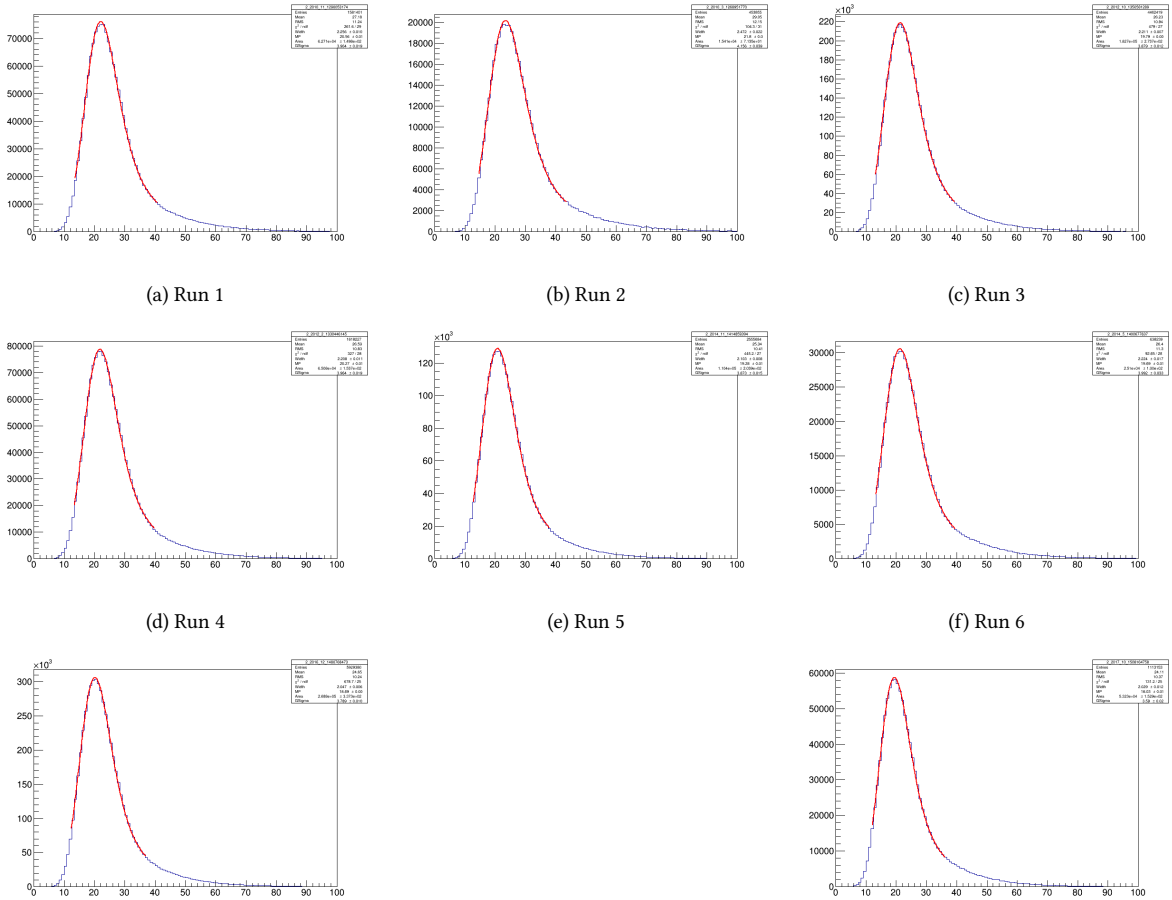

(a) Run 1 (b) Run 2 (c) Run 3

(d) Run 4 (e) Run 5 (f) Run 6

(g) Run 8 (h) Run 9

Figure C.7: P0D SuperP0Dule 2 Landau-Gaussian convolution fits.

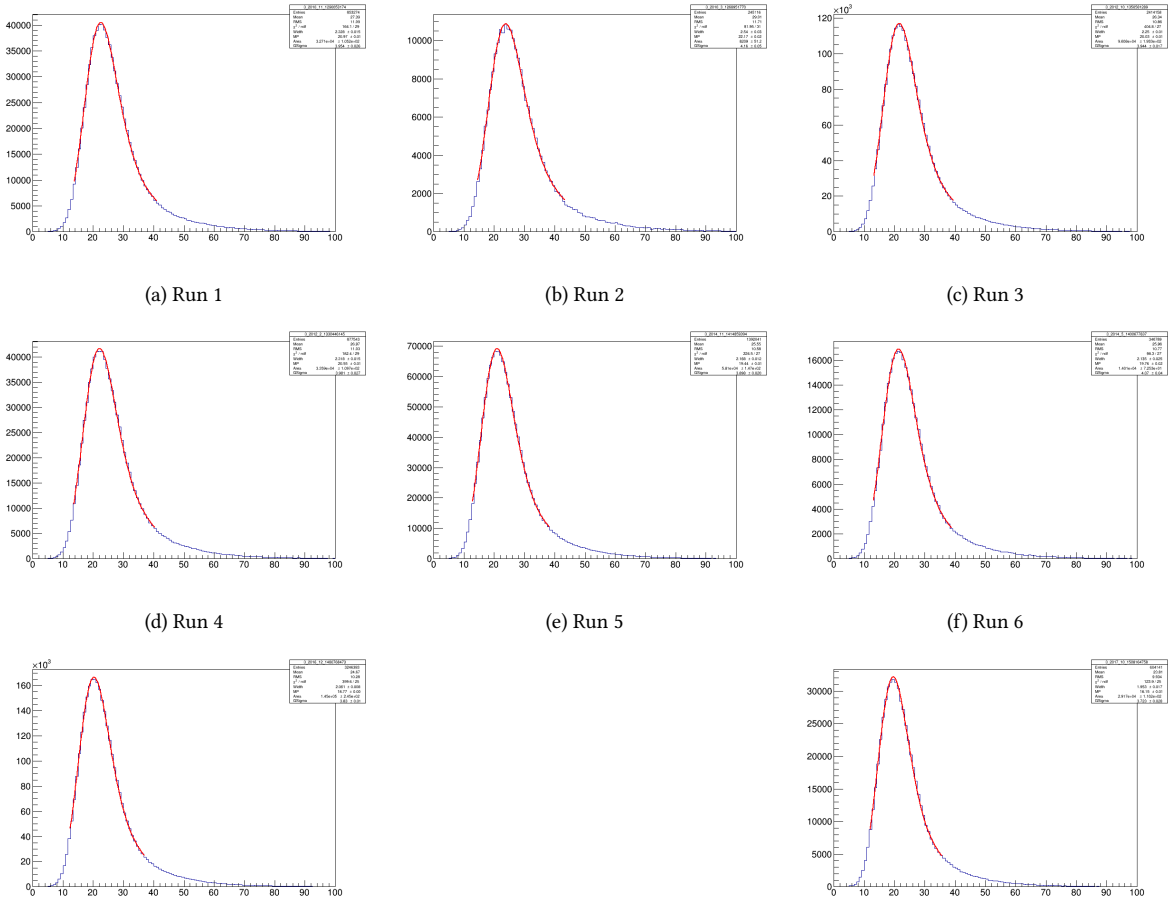

(a) Run 1 (b) Run 2 (c) Run 3

(d) Run 4 (e) Run 5 (f) Run 6

(g) Run 8 (h) Run 9

Figure C.8: P0D SuperP0Dule 3 Landau-Gaussian convolution fits.

Table C.2: P0D Landau-Gaussian convolution fit parameters.

T2K Run	σ_{LD}	μ_{LD}	N_{LD}	$\sigma_{\text{LD-Gaus}}$	χ^2/NDF
SuperP0Dule 0					
Run 1	2.472 ± 0.034	20.391 ± 0.020	$8\text{E}3 \pm 55$	4.223 ± 0.062	$91.496/29 = 3.155$
Run 2	2.212 ± 0.017	19.408 ± 0.011	$32\text{E}3 \pm 110$	4.216 ± 0.033	$126.895/27 = 4.700$
Run 3	2.288 ± 0.017	19.203 ± 0.010	$33\text{E}3 \pm 111$	4.054 ± 0.030	$130.264/27 = 4.825$
Run 4	2.214 ± 0.010	18.684 ± 0.006	$94\text{E}3 \pm 195$	4.025 ± 0.019	$298.731/26 = 11.490$
Run 5	2.141 ± 0.027	18.436 ± 0.018	$13\text{E}3 \pm 73$	4.169 ± 0.051	$73.327/26 = 2.820$
Run 6	2.106 ± 0.013	18.066 ± 0.009	$56\text{E}3 \pm 156$	4.056 ± 0.026	$150.704/25 = 6.028$
Run 8	2.059 ± 0.009	17.587 ± 0.005	$138\text{E}3 \pm 242$	3.961 ± 0.016	$368.355/24 = 15.348$
Run 9	1.986 ± 0.020	16.942 ± 0.013	$27\text{E}3 \pm 115$	3.850 ± 0.038	$79.841/23 = 3.471$
SuperP0Dule 1					
Run 1	2.454 ± 0.022	21.591 ± 0.015	$15\text{E}3 \pm 69$	4.286 ± 0.040	$92.123/31 = 2.972$
Run 2	2.270 ± 0.011	20.375 ± 0.007	$62\text{E}3 \pm 151$	3.921 ± 0.019	$218.619/29 = 7.539$
Run 3	2.208 ± 0.011	20.132 ± 0.007	$63\text{E}3 \pm 151$	4.047 ± 0.020	$225.096/28 = 8.039$
Run 4	2.215 ± 0.007	19.680 ± 0.004	$179\text{E}3 \pm 270$	3.941 ± 0.013	$420.412/27 = 15.571$

Continued on next page

Table C.2 – continued from previous page

T2K Run	σ_{LD}	μ_{LD}	N_{LD}	$\sigma_{\text{LD-Gaus}}$	χ^2/NDF
Run 5	2.240 ± 0.019	19.583 ± 0.012	$24\text{E}3 \pm 99$	4.040 ± 0.035	$63.736/27 = 2.361$
Run 6	2.099 ± 0.009	19.132 ± 0.006	$107\text{E}3 \pm 202$	3.960 ± 0.016	$324.187/26 = 12.469$
Run 8	2.068 ± 0.006	18.683 ± 0.004	$256\text{E}3 \pm 322$	3.906 ± 0.010	$591.762/26 = 22.760$
Run 9	2.051 ± 0.012	17.957 ± 0.008	$52\text{E}3 \pm 151$	3.638 ± 0.022	$95.956/25 = 3.838$
SuperP0Dule 2					
Run 1	2.472 ± 0.022	21.803 ± 0.014	$15\text{E}3 \pm 71$	4.156 ± 0.039	$104.314/31 = 3.365$
Run 2	2.256 ± 0.010	20.564 ± 0.007	$63\text{E}3 \pm 150$	3.904 ± 0.019	$261.606/29 = 9.021$
Run 3	2.208 ± 0.011	20.270 ± 0.007	$65\text{E}3 \pm 154$	3.964 ± 0.019	$326.973/28 = 11.678$
Run 4	2.211 ± 0.007	19.790 ± 0.004	$183\text{E}3 \pm 274$	3.879 ± 0.012	$478.973/27 = 17.740$
Run 5	2.224 ± 0.017	19.690 ± 0.012	$25\text{E}3 \pm 100$	3.992 ± 0.033	$92.647/28 = 3.309$
Run 6	2.103 ± 0.008	19.283 ± 0.006	$110\text{E}3 \pm 204$	3.873 ± 0.015	$445.228/27 = 16.490$
Run 8	2.047 ± 0.006	18.689 ± 0.004	$269\text{E}3 \pm 337$	3.789 ± 0.010	$678.723/25 = 27.149$
Run 9	2.029 ± 0.012	18.029 ± 0.008	$53\text{E}3 \pm 153$	3.590 ± 0.021	$131.224/25 = 5.249$
SuperP0Dule 3					
Run 1	2.540 ± 0.030	22.172 ± 0.019	$8\text{E}3 \pm 51$	4.160 ± 0.053	$81.953/31 = 2.644$
Run 2	2.328 ± 0.015	20.968 ± 0.010	$33\text{E}3 \pm 105$	3.954 ± 0.026	$164.101/29 = 5.659$
Run 3	2.318 ± 0.015	20.550 ± 0.010	$34\text{E}3 \pm 110$	3.981 ± 0.027	$182.407/29 = 6.290$
Run 4	2.250 ± 0.010	20.029 ± 0.006	$96\text{E}3 \pm 193$	3.944 ± 0.017	$404.763/27 = 14.991$
Run 5	2.135 ± 0.025	19.763 ± 0.016	$14\text{E}3 \pm 73$	4.070 ± 0.045	$98.300/27 = 3.641$
Run 6	2.168 ± 0.012	19.437 ± 0.008	$58\text{E}3 \pm 146$	3.898 ± 0.020	$224.522/27 = 8.316$
Run 8	2.061 ± 0.008	18.768 ± 0.005	$145\text{E}3 \pm 245$	3.830 ± 0.014	$399.573/25 = 15.983$
Run 9	1.953 ± 0.017	18.152 ± 0.011	$29\text{E}3 \pm 110$	3.723 ± 0.028	$123.880/25 = 4.955$

C.3 — FGD

The fitting method of FGD is similar to ECAL. The selected data is fitted as described in C.1. The fitting examples for 2010-2018 are shown in Fig. C.9, whereas the associated fit parameters are shown in Table C.3. The parameters from fit in x-axis range 15-35 are in rows starting with an arrow. The corresponding fits are shown in Fig. C.10.

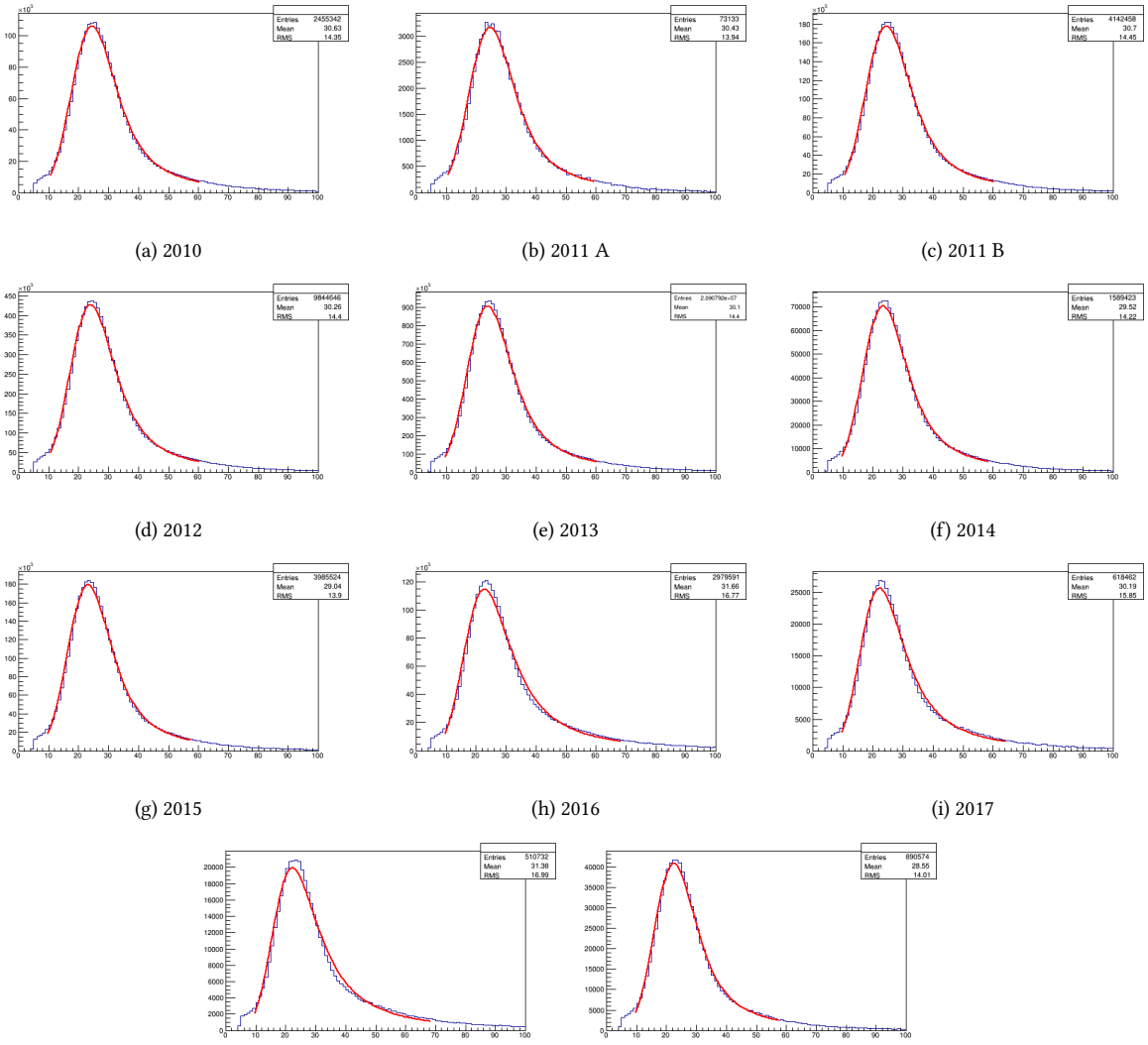

(a) 2010 (b) 2011 A (c) 2011 B

(d) 2012 (e) 2013 (f) 2014

(g) 2015 (h) 2016 (i) 2017

(j) 2018 A (k) 2018 B

Figure C.9: FGD Landau-Gaussian convolution fits.

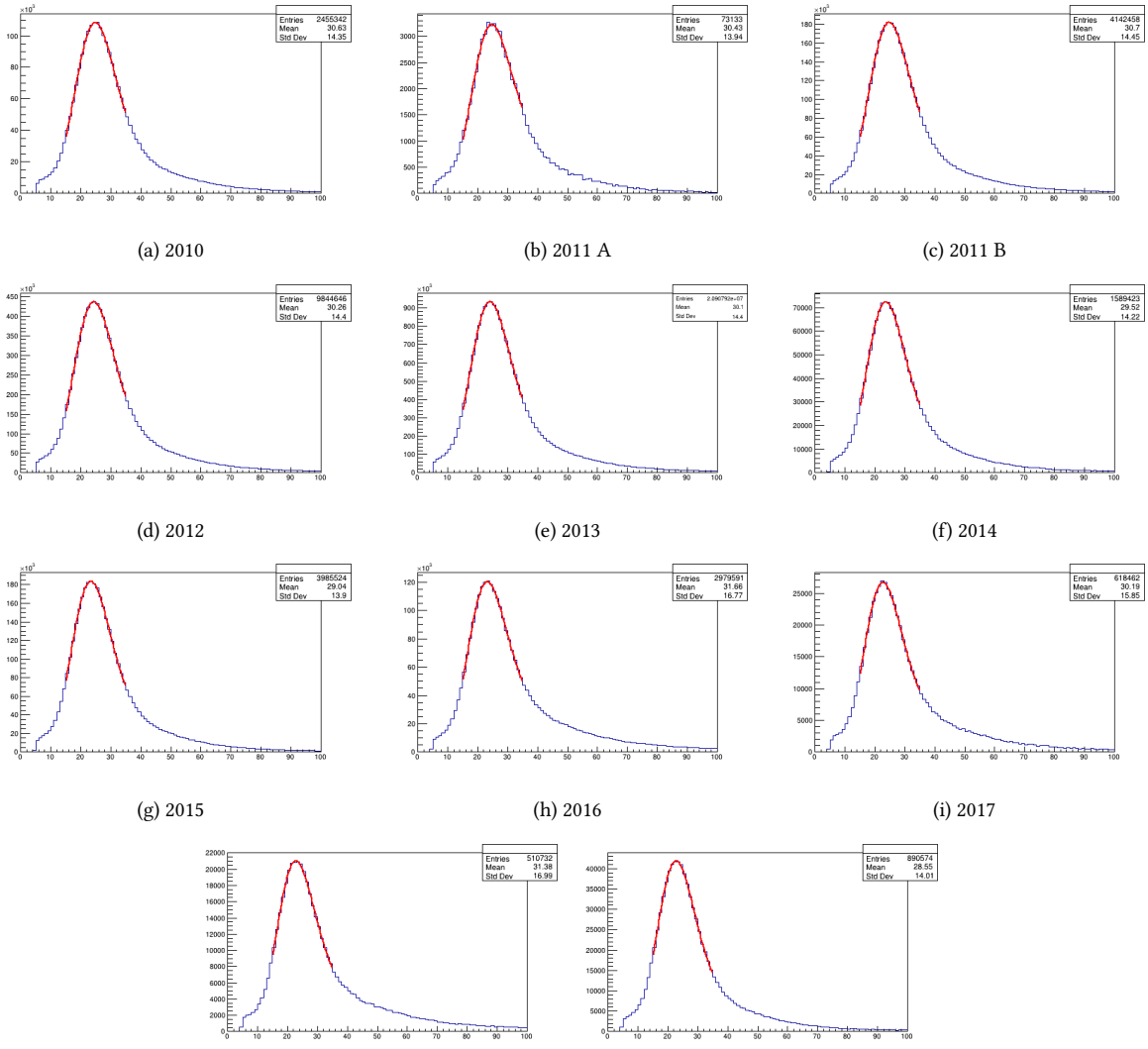

(a) 2010 (b) 2011 A (c) 2011 B

(d) 2012 (e) 2013 (f) 2014

(g) 2015 (h) 2016 (i) 2017

(j) 2018 A (k) 2018 B

Figure C.10: FGD Landau-Gaussian convolution fits (in x range: 15-35)

Year	σ_{LD}	μ_{LD}	N_{LD}	$\sigma_{\text{LD-Gaus}}$	χ^2/NDF
2010	2.879 ± 0.007	22.53 ± 0.01	$4.868\text{E}5 \pm 1.162\text{E}3$	5.125 ± 0.011	$4656/47 = 99.06$
$\rightarrow$	2.349 ± 0.045	22.73 ± 0.01	$4.444\text{E}5 \pm 5.306\text{E}3$	5.326 ± 0.045	$76.4/16 = 4.78$
2011 A	2.851 ± 0.040	22.62 ± 0.04	$1.429\text{E}4 \pm 1.978\text{E}2$	5.244 ± 0.066	$167.8/46 = 3.64$
$\rightarrow$	3.039 ± 0.226	22.85 ± 0.06	$1.608\text{E}4 \pm 1.165\text{E}3$	4.675 ± 0.260	$23.13/16 = 1.45$
2011 B	2.913 ± 0.005	22.51 ± 0.01	$8.220\text{E}5 \pm 1.540\text{E}3$	5.124 ± 0.009	$7789/47 = 165.72$
$\rightarrow$	2.495 ± 0.034	22.7 ± 0.00	$7.760\text{E}5 \pm 7.320\text{E}3$	5.187 ± 0.036	$46.14/16 = 2.88$
2012	2.916 ± 0.003	22.10 ± 0.00	$2.002\text{E}6 \pm 2.469\text{E}3$	4.998 ± 0.006	$17150/47 = 364.89$
$\rightarrow$	2.471 ± 0.021	22.28 ± 0.00	$1.862\text{E}6 \pm 1.104\text{E}4$	5.132 ± 0.023	$79.14/16 = 4.95$
2013	2.882 ± 0.002	21.90 ± 0.00	$4.183\text{E}6 \pm 3.310\text{E}3$	5.086 ± 0.004	$51980/48 = 1082.92$
$\rightarrow$	2.481 ± 0.013	22.11 ± 0.00	$4.020\text{E}6 \pm 1.500\text{E}4$	5.046 ± 0.014	$111.2/16 = 6.95$
2014	2.810 ± 0.010	21.47 ± 0.01	$3.238\text{E}5 \pm 9.426\text{E}2$	4.991 ± 0.013	$3655/46 = 79.45$
$\rightarrow$	2.455 ± 0.042	21.66 ± 0.01	$3.143\text{E}5 \pm 4.217\text{E}3$	4.916 ± 0.052	$35.2/16 = 2.2$
2015	2.739 ± 0.005	21.22 ± 0.01	$8.128\text{E}5 \pm 1.493\text{E}3$	5.006 ± 0.008	$7627/45 = 169.48$
$\rightarrow$	2.449 ± 0.026	21.41 ± 0.01	$7.946\text{E}5 \pm 6.649\text{E}3$	4.934 ± 0.033	$25.34/16 = 1.58$
2016	3.870 ± 0.010	21.33 ± 0.01	$7.246\text{E}5 \pm 2.190\text{E}3$	4.093 ± 0.012	$1447/56 = 25.84$
$\rightarrow$	2.943 ± 0.032	21.4 ± 0.00	$5.984\text{E}5 \pm 7.028\text{E}3$	4.533 ± 0.045	$38.17/16 = 2.39$
2017	3.447 ± 0.013	20.68 ± 0.01	$1.471\text{E}5 \pm 8.475\text{E}2$	4.215 ± 0.024	$2562/52 = 49.27$
$\rightarrow$	2.661 ± 0.059	20.83 ± 0.02	$1.248\text{E}5 \pm 2.735\text{E}3$	4.593 ± 0.086	$28.08/16 = 1.76$
2018 A	3.868 ± 0.014	20.92 ± 0.01	$1.332\text{E}5 \pm 1.021\text{E}3$	3.790 ± 0.030	$3586/56 = 64.03$
$\rightarrow$	2.723 ± 0.066	20.98 ± 0.02	$1.004\text{E}5 \pm 2.511\text{E}3$	4.525 ± 0.097	$19.82/16 = 1.24$
2018 B	2.762 ± 0.010	20.66 ± 0.01	$1.920\text{E}5 \pm 7.700\text{E}2$	4.709 ± 0.017	$2006/45 = 44.58$
$\rightarrow$	2.402 ± 0.046	20.86 ± 0.01	$1.838\text{E}5 \pm 2.946\text{E}3$	4.710 ± 0.060	$24.82/16 = 1.55$

Table C.3: FGD Landau-Gaussian convolution fit parameters. The rows start with arrow: parameters from fit in range 15-35.

C.4 — SMRD

For the data analysis in SMRD highland numuCCOuterDet package was used. Events had to pass standard selection cuts for high momentum negative(positive) events originating in SMRD. The selected data is fitted as described in C.1. The fitting examples for 2010-2018 are shown in Fig. C.11 and the associated fit parameters are shown in Table C.4.

T2K Run	σ_{LD}	μ_{LD}	N_{LD}	$\sigma_{\text{LD-Gaus}}$	χ^2/NDF
Run 1	9.358 ± 0.769	61.646 ± 0.445	$4.924\text{E}3 \pm 1.047E2$	12.348 ± 1.343	$93.651/86 = 1.089$
Run 2	10.183 ± 0.446	59.237 ± 0.265	$1.536\text{E}4 \pm 1.829\text{E}2$	12.559 ± 0.793	$95.843/92 = 1.042$
Run 3	10.417 ± 0.320	59.981 ± 0.188	$3.116\text{E}4 \pm 2.642\text{E}2$	11.722 ± 0.606	$73.736/89 = 0.828$
Run 4	10.421 ± 0.232	58.385 ± 0.133	$6.494\text{E}4 \pm 3.964\text{E}2$	11.119 ± 0.459	$85.319/84 = 1.016$
Run 5	9.839 ± 0.605	58.683 ± 0.355	$7.303\text{E}3 \pm 1.241\text{E}2$	11.111 ± 1.154	$116.205/87 = 1.336$
Run 6	10.046 ± 0.347	57.490 ± 0.209	$2.308\text{E}4 \pm 2.243\text{E}2$	10.927 ± 0.683	$87.254/85 = 1.026$
Run 7	10.057 ± 0.413	59.131 ± 0.230	$2.141\text{E}4 \pm 2.264\text{E}2$	12.279 ± 0.769	$59.421/86 = 0.691$
Run 8	10.511 ± 0.181	56.084 ± 0.114	$1.057\text{E}5 \pm 5.129\text{E}2$	10.145 ± 0.394	$82.851/79 = 1.048$
Run 9	9.676 ± 0.451	56.268 ± 0.277	$1.161\text{E}4 \pm 1.554\text{E}4$	10.939 ± 0.826	$74.435/86 = 0.866$

Table C.4: SMRD Landau-Gaussian convolution fit parameters.

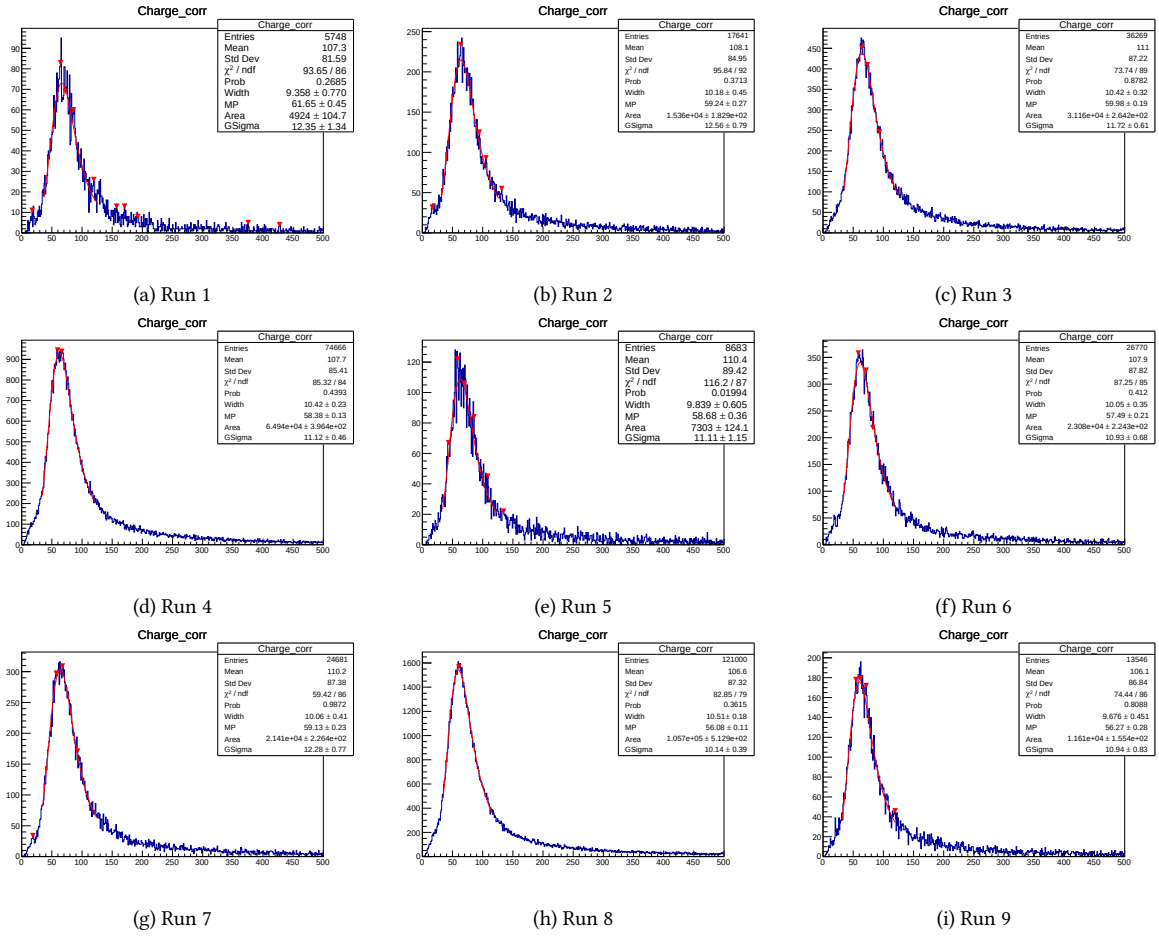

(a) Run 1 (b) Run 2 (c) Run 3

(d) Run 4 (e) Run 5 (f) Run 6

(g) Run 7 (h) Run 8 (i) Run 9

Figure C.11: SMRD Landau-Gaussian convolution fits.

Bibliography

[1] The average energy of disintegration of radium e. *Proceedings of the Royal Society of London. Series A, Containing Papers of a Mathematical and Physical Character*, 117:109–123, 12 1927.

[2] Matthew Walker. *Calibration Hardware Research and Development for SNO+*. PhD thesis, 05 2014.

[3] John N. Bahcall, Aldo M. Serenelli, and Sarbani Basu. New solar opacities, abundances, helioseismology, and neutrino fluxes. *The Astrophysical Journal*, 621(1):L85–L88, jan 2005.

[4] Takaaki KAJITA. Atmospheric neutrinos and discovery of neutrino oscillations. *Proceedings of the Japan Academy, Series B*, 86(4):303–321, 2010.

[5] T. Kajita, E. Kearns, and M. Shiozawa. Establishing atmospheric neutrino oscillations with super-kamiokande. *Nuclear Physics B*, 908:14–29, 2016. Neutrino Oscillations: Celebrating the Nobel Prize in Physics 2015.

[6] Y. Fukuda, T. Hayakawa, E. Ichihara, K. Inoue, K. Ishihara, H. Ishino, Y. Itow, T. Kajita, J. Kameda, S. Kasuga, K. Kobayashi, Y. Kobayashi, Y. Koshio, K. Martens, M. Miura, M. Nakahata, S. Nakayama, A. Okada, M. Oketa, K. Okumura, M. Ota, N. Sakurai, M. Shiozawa, Y. Suzuki, Y. Takeuchi, Y. Totsuka, S. Yamada, M. Earl, A. Habig, E. Kearns, S.B. Kim, M.D. Messier, K. Scholberg, J.L. Stone, L.R. Sulak, C.W. Walter, M. Goldhaber, T. Barszczak, W. Gajewski, P.G. Halverson, J. Hsu, W.R. Kropp, L.R. Price, F. Reines, H.W. Sobel, M.R. Vagins, K.S. Ganezer, W.E. Keig, R.W. Ellsworth, S. Tasaka, J.W. Flanagan, A. Kibayashi, J.G. Learned, S. Matsuno, V. Stenger, D. Takemori, T. Ishii, J. Kanzaki, T. Kobayashi, K. Nakamura, K. Nishikawa, Y. Oyama, A. Sakai, M. Sakuda, O. Sasaki, S. Echigo, M. Kohama, A.T. Suzuki, T.J. Haines, E. Blaufuss, R. Sanford, R. Svoboda, M.L. Chen, Z. Conner, J.A. Goodman, G.W. Sullivan, M. Mori, J. Hill, C.K. Jung, C. Mauger, C. McGrew, E. Sharkey, B. Viren, C. Yanagisawa, W. Doki, T. Ishizuka, Y. Kitaguchi, H. Koga, K. Miyano, H. Okazawa, C. Saji, M. Takahata, A. Kusano, Y. Nagashima, M. Takita, T. Yamaguchi, M. Yoshida, M. Etoh, K. Fujita, A. Hasegawa, T. Hasegawa, S. Hatakeyama, T. Iwamoto, T. Kinebuchi, M. Koga, T. Maruyama, H. Ogawa, A. Suzuki, F. Tsushima, M. Koshiba, M. Nemoto, K. Nishijima, T. Futagami, Y. Hayato, Y. Kanaya, K. Kaneyuki, Y. Watanabe, D. Kielczewska, R. Doyle, J. George, A. Stachyra, L. Wai, J. Wilkes, and K. Young. Study of the atmospheric neutrino flux in the multi-GeV energy range. *Physics Letters B*, 436(1-2):33–41, sep 1998.

[7] P. F. De Salas, D. V. Forero, S. Gariazzo, P. Martínez-Miravé, O. Mena, C. A. Ternes, M. Tórtola, and J. W. F. Valle. Chi2 profiles from Valencia neutrino global fit. `http://globalfit.astroparticles.es/`, 2021.

[8] Jeanne Wilson. Accelerator neutrino ii_hyper-k, June 2022.

[9] Mathew Muether. Accelerator neutrino ii_dune, June 2022.

[10] S. Assylbekov et al. The T2K ND280 off-axis pi–zero detector. *Nuclear Instruments and Methods in Physics Research Section A: Accelerators, Spectrometers, Detectors and Associated Equipment*, 686:48–63, 2012.

[11] P. A. Amaudruz et al. The T2K Fine-Grained Detectors. *Nuclear Instruments and Methods in Physics Research Section A: Accelerators, Spectrometers, Detectors and Associated Equipment*, 696:1–31, 2012.

[12] N. Abgrall, B. Andrieu, P. Baron, P. Bene, V. Berardi, J. Beucher, P. Birney, F. Blaszczyk, A. Blondel, C. Bojechko, M. Boyer, F. Cadoux, D. Calvet, M.G. Catanesi, A. Cervera, P. Colas, X. De La Broise, E. Delagnes, A. Delbart, M. Di Marco, F. Druillole, J. Dumarchez, S. Emery, L. Escudero, W. Faszer, D. Ferrere, A. Ferrero, K. Fransham, A. Gaudin, C. Giganti, I. Giomataris, J. Giraud, M. Goyette, K. Hamano, C. Hearty, R. Henderson, S. Herlant, M. Ieva, B. Jamieson, G. Jover-Mañas, D. Karlen, I. Kato, A. Konaka, K. Laihem, R. Langstaff, M. Laveder, A. Le Coguie, O. Le Dortz, M. Le Ross, M. Lenckowski, T. Lux, M. Macaire, K. Mahn, F. Masciocchi, E. Mazzucato, M. Mezzetto, A. Miller, J.-Ph. Mols, L. Monfregola, E. Monmarthe, J. Myslik, F. Nizery, R. Openshaw, E. Perrin, F. Pierre, D. Pierrepont, P. Poffenberger, B. Popov, E. Radicioni, M. Ravonel, J.-M. Reymond, J.-L. Ritou, M. Roney, S. Roth, F. Sánchez, A. Sarrat, R. Schroeter, A. Stahl, P. Stamoulis, J. Steinmann, D. Terhorst, D. Terront, V. Tvaskis, M. Usseglio, A. Vallereau, G. Vasseur, J. Wendland, G. Wikström, and M. Zito. Time projection chambers for the t2k near detectors. *Nuclear Instruments and Methods in Physics Research Section A: Accelerators, Spectrometers, Detectors and Associated Equipment*, 637(1):25–46, 2011.

[13] D. Allan et al. The Electromagnetic Calorimeter for the T2K Near Detector ND280. *Journal of Instrumentation*, 8:P10019, 2013.

[14] S. Aoki et al. The T2K Side Muon Range Detector (SMRD). *Nuclear Instruments and Methods in Physics Research Section A: Accelerators, Spectrometers, Detectors and Associated Equipment*, 698:135–146, 2013.

[15] N. Abgrall, A. Aduszkiewicz, Y. Ali, E. Andronov, T. Antićić, N. Antoniou, B. Baatar, F. Bay, A. Blondel, and et al. Measurements of $\pi^{\pm}$, $k^{\pm}$, k^{0}_{s} , λ and proton production in proton–carbon interactions at 31 gev/c with the na61/shine spectrometer at the cern sps. *The European Physical Journal C*, 76(2), Feb 2016.

[16] Tomislav Vladisavljevic. *Predicting the T2K Neutrino Flux and Measuring Oscillation Parameters*. PhD thesis, Oxford U., 2020.

[17] C. Vilela et al. Super-Kamiokande detector systematic uncertainty including the multi-ring ν_μCC1π^+-likesample. Technical Report T2K-TN448, T2K Collaboration, 2022.

[18] F. et al An. Improved measurement of the reactor antineutrino flux and spectrum at daya bay. *Chinese Physics C*, 41, 07 2016.

[19] D. Adey et al. Measurement of the electron antineutrino oscillation with 1958 days of operation at daya bay. *Physical Review Letters*, 121(24), dec 2018.

[20] K. Abe et al. The T2K Experiment. *Nucl. Instrum. Meth. A*, 659:106–135, 2011.

[21] Y. et al Abe. Indication of reactor $\overline{\nu}_e$ disappearance in the double chooz experiment. *Phys. Rev. Lett.*, 108:131801, Mar 2012.

[22] G. Bak, J. H. Choi, H. I. Jang, J. S. Jang, S. H. Jeon, K. K. Joo, K. Ju, D. E. Jung, J. G. Kim, J. H. Kim, J. Y. Kim, S. B. Kim, S. Y. Kim, W. Kim, E. Kwon, D. H. Lee, H. G. Lee, Y. C. Lee, I. T. Lim, D. H. Moon, M. Y. Pac, Y. S. Park, C. Rott, H. Seo, J. W. Seo, S. H. Seo, C. D. Shin, J. Y. Yang, J. Yoo, and I. Yu. Measurement of reactor antineutrino oscillation amplitude and frequency at reno. *Phys. Rev. Lett.*, 121:201801, Nov 2018.

[23] Y. Abe et al. Improved measurements of the neutrino mixing angle theta13 with the double chooz detector. *Journal of High Energy Physics*, 2014(10), oct 2014.

[24] K. et al Abe. Observation of electron neutrino appearance in a muon neutrino beam. *Phys. Rev. Lett.*, 112:061802, Feb 2014.

[25] DUNE Collaboration and B. Abi et al. The dune far detector interim design report volume 1: Physics, technology and strategies, 2018.

[26] Hyper-Kamiokande Proto-Collaboration, :, and K. Abe et al. Hyper-kamiokande design report, 2018.

[27] J. Chadwick. The intensity distribution in the magnetic spectrum of beta particles from radium (B + C). *Verh. Phys. Gesell.*, 16:383–391, 1914.

[28] W. Pauli. On the Earlier and more recent history of the neutrino. *Camb. Monogr. Part. Phys. Nucl. Phys. Cosmol.*, 1:1–25, 1991.

[29] Seth H. Neddermeyer and Carl D. Anderson. Note on the nature of cosmic-ray particles. *Phys. Rev.*, 51:884–886, May 1937.

[30] G. Danby, J-M. Gaillard, K. Goulianos, L. M. Lederman, N. Mistry, M. Schwartz, and J. Steinberger. Observation of high-energy neutrino reactions and the existence of two kinds of neutrinos. *Phys. Rev. Lett.*, 9:36–44, Jul 1962.

[31] Precision electroweak measurements on the z resonance. *Physics Reports*, 427(5-6):257–454, may 2006.

[32] K. Kodama, N. Ushida, C. Andreopoulos, N. Saoulidou, G. Tzanakos, P. Yager, B. Baller, D. Boehnlein, W. Freeman, B. Lundberg, J. Morfin, R. Rameika, J.C. Yun, J.S. Song, C.S. Yoon, S.H. Chung, P. Berghaus, M. Kubantsev, N.W. Reay, R. Sidwell, N. Stanton, S. Yoshida, S. Aoki, T. Hara, J.T. Rhee, D. Ciampa, C. Erickson, M. Graham, K. Heller, R. Rusack, R. Schwienhorst, J. Sielaff, J. Trammell, J. Wilcox, K. Hoshino, H. Jiko, M. Miyanishi, M. Komatsu, M. Nakamura, T. Nakano, K. Niwa, N. Nonaka, K. Okada, O. Sato, T. Akdogan, V. Paolone, C. Rosenfeld, A. Kulik, T. Kafka, W. Oliver, T. Patzak, and J. Schneps. Observation of tau neutrino interactions. *Physics Letters B*, 504(3):218–224, apr 2001.

[33] Bruce T. Cleveland, Timothy Daily, Jr. Raymond Davis, James R. Distel, Kenneth Lande, C. K. Lee, Paul S. Wildenhain, and Jack Ullman. Measurement of the solar electron neutrino flux with the homestake chlorine detector. *The Astrophysical Journal*, 496(1):505–526, mar 1998.

[34] John N. Bahcall, Neta A. Bahcall, and Giora Shaviv. Present status of the theoretical predictions for the ^{37}Cl solar-neutrino experiment. *Phys. Rev. Lett.*, 20:1209–1212, May 1968.

[35] J. N. Abdurashitov, V. N. Gavrin, S. V. Girin, V. V. Gorbachev, T. V. Ibragimova, A. V. Kalikhov, N. G. Khairnasov, T. V. Knodel, I. N. Mirmov, A. A. Shikhin, E. P. Veretenkin, V. M. Vermul, V. E. Yants, G. T. Zatsepin, T. J. Bowles, W. A. Teasdale, D. L. Wark, M. L. Cherry, J. S. Nico, B. T. Cleveland, R. Davis, K. Lande, P. S. Wildenhain, S. R. Elliott, and J. F. Wilkerson. Measurement of the solar neutrino capture rate with gallium metal. *Physical Review C*, 60(5), oct 1999.

[36] W. Hampel, J. Handt, G. Heusser, J. Kiko, T. Kirsten, M. Laubenstein, E. Pernicka, W. Rau, M. Wojcik, Y. Zakharov, R.v. Ammon, K.H. Ebert, T. Fritsch, D. Heidt, E. Henrich, L. Stielglitz, F. Weirich, M. Balata, M. Sann, F.X. Hartmann, E. Bellotti, C. Cattadori, O. Cremonesi, N. Ferrari, E. Fiorini, L. Zanotti, M. Altmann, F.v. Feilitzsch, R. Mößbauer, S. Wänninger, G. Berthomieu, E. Schatzman, I. Carmi, I. Dostrovsky, C. Bacci, P. Belli, R. Bernabei, S. d'Angelo, L. Paoluzi, M. Cribier, J. Rich, M. Spiro, C. Tao, D. Vignaud, J. Boger, R.L. Hahn, J.K. Rowley, R.W. Stoenner, and J. Weneser. Gallex solar neutrino observations: results for gallex iv. *Physics Letters B*, 447(1):127–133, 1999.

[37] T. K. Gaisser and M. Honda. Flux of atmospheric neutrinos. *Annual Review of Nuclear and Particle Science*, 52(1):153–199, 2002.

[38] Q. R. Ahmad, R. C. Allen, T. C. Andersen, J. D.Anglin, J. C. Barton, E. W. Beier, M. Bercovitch, J. Bigu, S. D. Biller, R. A. Black, I. Blevis, R. J. Boardman, J. Boger, E. Bonvin, M. G. Boulay, M. G. Bowler, T. J. Bowles, S. J. Brice, M. C. Browne, T. V. Bullard, G. Bühler, J. Cameron, Y. D. Chan, H. H. Chen, M. Chen, X. Chen, B. T. Cleveland, E. T. H. Clifford, J. H. M. Cowan, D. F. Cowen, G. A. Cox, X. Dai, F. Dalnoki-Veress, W. F. Davidson, P. J. Doe, G. Doucas, M. R. Dragowsky, C. A. Duba, F. A. Duncan, M. Dunford, J. A. Dunmore, E. D. Earle, S. R. Elliott, H. C. Evans, G. T. Ewan, J. Farine, H. Fergani, A. P. Ferraris, R. J. Ford, J. A. Formaggio, M. M. Fowler, K. Frame, E. D. Frank, W. Frati, N. Gagnon, J. V. Germani, S. Gil, K. Graham, D. R. Grant, R. L. Hahn, A. L. Hallin, E. D. Hallman, A. S. Hamer, A. A. Hamian, W. B. Handler, R. U. Haq, C. K. Hargrove, P. J. Harvey, R. Hazama, K. M. Heeger, W. J. Heintzelman,

J. Heise, R. L. Helmer, J. D. Hepburn, H. Heron, J. Hewett, A. Hime, M. Howe, J. G. Hykawy, M. C. P. Isaac, P. Jagam, N. A. Jelley, C. Jillings, G. Jonkmans, K. Kazkaz, P. T. Keener, J. R. Klein, A. B. Knox, R. J. Komar, R. Kouzes, T. Kutter, C. C. M. Kyba, J. Law, I. T. Lawson, M. Lay, H. W. Lee, K. T. Lesko, J. R. Leslie, I. Levine, W. Locke, S. Luoma, J. Lyon, S. Majerus, H. B. Mak, J. Maneira, J. Manor, A. D. Marino, N. McCauley, A. B. McDonald, D. S. McDonald, K. McFarlane, G. McGregor, R. Meijer Drees, C. Mifflin, G. G. Miller, G. Milton, B. A. Moffat, M. Moorhead, C. W. Nally, M. S. Neubauer, F. M. Newcomer, H. S. Ng, A. J. Noble, E. B. Norman, V. M. Novikov, M. O'Neill, C. E. Okada, R. W. Ollerhead, M. Omori, J. L. Orrell, S. M. Oser, A. W. P. Poon, T. J. Radcliffe, A. Roberge, B. C. Robertson, R. G. H. Robertson, S. S. E. Rosendahl, J. K. Rowley, V. L. Rusu, E. Saettler, K. K. Schaffer, M. H. Schwendener, A. Schülke, H. Seifert, M. Shatkay, J. J. Simpson, C. J. Sims, D. Sinclair, P. Skensved, A. R. Smith, M. W. E. Smith, T. Spreitzer, N. Starinsky, T. D. Steiger, R. G. Stokstad, L. C. Stonehill, R. S. Storey, B. Sur, R. Tafirout, N. Tagg, N. W. Tanner, R. K. Taplin, M. Thorman, P. M. Thornewell, P. T. Trent, Y. I. Tserkovnyak, R. Van Berg, R. G. Van de Water, C. J. Virtue, C. E. Waltham, J.-X. Wang, D. L. Wark, N. West, J. B. Wilhelmy, J. F. Wilkerson, J. R. Wilson, P. Wittich, J. M. Wouters, and M. Yeh. Direct evidence for neutrino flavor transformation from neutral-current interactions in the sudbury neutrino observatory. *Phys. Rev. Lett.*, 89:011301, Jun 2002.

[39] J. H. Christenson, J. W. Cronin, V. L. Fitch, and R. Turlay. Evidence for the 2π decay of the k_2^0 meson. *Phys. Rev. Lett.*, 13:138–140, Jul 1964.

[40] B Pontecorvo. Inverse $beta$ processes and nonconservation of lepton charge. *Zhur. Eksptl'. i Teoret. Fiz.*, 34, 1 1958.

[41] Ziro Maki, Masami Nakagawa, and Shoichi Sakata. Remarks on the unified model of elementary particles. *Prog. Theor. Phys.*, 28:870–880, 1962.

[42] Nicola Cabibbo. Unitary Symmetry and Leptonic Decays. *Phys. Rev. Lett.*, 10:531–533, 1963.

[43] Makoto Kobayashi and Toshihide Maskawa. CP Violation in the Renormalizable Theory of Weak Interaction. *Prog. Theor. Phys.*, 49:652–657, 1973.

[44] Ling-Lie Chau and Wai-Yee Keung. Comments on the Parametrization of the Kobayashi-Maskawa Matrix. *Phys. Rev. Lett.*, 53:1802, 1984.

[45] M. Tanabashi, K. Hagiwara, K. Hikasa, K. Nakamura, Y. Sumino, F. Takahashi, J. Tanaka, K. Agashe, G. Aielli, C. Amsler, M. Antonelli, D. M. Asner, H. Baer, Sw. Banerjee, R. M. Barnett, T. Basaglia, C. W. Bauer, J. J. Beatty, V. I. Belousov, J. Beringer, S. Bethke, A. Bettini, H. Bichsel, O. Biebel, K. M. Black, E. Blucher, O. Buchmuller, V. Burkert, M. A. Bychkov, R. N. Cahn, M. Carena, A. Ceccucci, A. Cerri, D. Chakraborty, M.-C. Chen, R. S. Chivukula, G. Cowan, O. Dahl, G. D'Ambrosio, T. Damour, D. de Florian, A. de Gouvêa, T. DeGrand, P. de Jong, G. Dissertori, B. A. Dobrescu, M. D'Onofrio, M. Doser, M. Drees, H. K. Dreiner, D. A. Dwyer, P. Eerola, S. Eidelman, J. Ellis, J. Erler, V. V. Ezhela, W. Fetscher,

B. D. Fields, R. Firestone, B. Foster, A. Freitas, H. Gallagher, L. Garren, H.-J. Gerber, G. Gerbier, T. Gershon, Y. Gershtein, T. Gherghetta, A. A. Godizov, M. Goodman, C. Grab, A. V. Gritsan, C. Grojean, D. E. Groom, M. Grünewald, A. Gurtu, T. Gutsche, H. E. Haber, C. Hanhart, S. Hashimoto, Y. Hayato, K. G. Hayes, A. Hebecker, S. Heinemeyer, B. Heltsley, J. J. Hernández-Rey, J. Hisano, A. Höcker, J. Holder, A. Holtkamp, T. Hyodo, K. D. Irwin, K. F. Johnson, M. Kado, M. Karliner, U. F. Katz, S. R. Klein, E. Klempt, R. V. Kowalewski, F. Krauss, M. Kreps, B. Krusche, Yu. V. Kuyanov, Y. Kwon, O. Lahav, J. Laiho, J. Lesgourgues, A. Liddle, Z. Ligeti, C.-J. Lin, C. Lippmann, T. M. Liss, L. Littenberg, K. S. Lugovsky, S. B. Lugovsky, A. Lusiani, Y. Makida, F. Maltoni, T. Mannel, A. V. Manohar, W. J. Marciano, A. D. Martin, A. Masoni, J. Matthews, U.-G. Meißner, D. Milstead, R. E. Mitchell, K. Mönig, P. Molaro, F. Moortgat, M. Moskovic, H. Murayama, M. Narain, P. Nason, S. Navas, M. Neubert, P. Nevski, Y. Nir, K. A. Olive, S. Pagan Griso, J. Parsons, C. Patrignani, J. A. Peacock, M. Pennington, S. T. Petcov, V. A. Petrov, E. Pianori, A. Piepke, A. Pomarol, A. Quadt, J. Rademacker, G. Raffelt, B. N. Ratcliff, P. Richardson, A. Ringwald, S. Roesler, S. Rolli, A. Romaniouk, L. J. Rosenberg, J. L. Rosner, G. Rybka, R. A. Ryutin, C. T. Sachrajda, Y. Sakai, G. P. Salam, S. Sarkar, F. Sauli, O. Schneider, K. Scholberg, A. J. Schwartz, D. Scott, V. Sharma, S. R. Sharpe, T. Shutt, M. Silari, T. Sjöstrand, P. Skands, T. Skwarnicki, J. G. Smith, G. F. Smoot, S. Spanier, H. Spieler, C. Spiering, A. Stahl, S. L. Stone, T. Sumiyoshi, M. J. Syphers, K. Terashi, J. Terning, U. Thoma, R. S. Thorne, L. Tiator, M. Titov, N. P. Tkachenko, N. A. Törnqvist, D. R. Tovey, G. Valencia, R. Van de Water, N. Varelas, G. Venanzoni, L. Verde, M. G. Vincter, P. Vogel, A. Vogt, S. P. Wakely, W. Walkowiak, C. W. Walter, D. Wands, D. R. Ward, M. O. Wascko, G. Weiglein, D. H. Weinberg, E. J. Weinberg, M. White, L. R. Wiencke, S. Willocq, C. G. Wohl, J. Womersley, C. L. Woody, R. L. Workman, W.-M. Yao, G. P. Zeller, O. V. Zenin, R.-Y. Zhu, S.-L. Zhu, F. Zimmermann, P. A. Zyla, J. Anderson, L. Fuller, V. S. Lugovsky, and P. Schaffner. Review of particle physics. *Phys. Rev. D*, 98:030001, Aug 2018.

[46] A. Gando, Y. Gando, T. Hachiya, A. Hayashi, S. Hayashida, H. Ikeda, K. Inoue, K. Ishidoshiro, Y. Karino, M. Koga, S. Matsuda, T. Mitsui, K. Nakamura, S. Obara, T. Oura, H. Ozaki, I. Shimizu, Y. Shirahata, J. Shirai, A. Suzuki, T. Takai, K. Tamae, Y. Teraoka, K. Ueshima, H. Watanabe, A. Kozlov, Y. Takemoto, S. Yoshida, K. Fushimi, T. I. Banks, B. E. Berger, B. K. Fujikawa, T. O'Donnell, L. A. Winslow, Y. Efremenko, H. J. Karwowski, D. M. Markoff, W. Tornow, J. A. Detwiler, S. Enomoto, and M. P. Decowski. Publisher's note: Search for majorana neutrinos near the inverted mass hierarchy region with kamland-zen [phys. rev. lett. 117, 082503 (2016)]. *Phys. Rev. Lett.*, 117:109903, Sep 2016.

[47] D. Q. Adams, C. Alduino, K. Alfonso, F. T. Avignone, O. Azzolini, G. Bari, F. Bellini, G. Benato, M. Biassoni, A. Branca, C. Brofferio, C. Bucci, A. Caminata, A. Campani, L. Canonica, X. G. Cao, S. Capelli, L. Cappelli, L. Cardani, P. Carniti, N. Casali, D. Chiesa, N. Chott, M. Clemenza, S. Copello, C. Cosmelli, O. Cremonesi, R. J. Creswick, A. D'Addabbo, D. D'Aguanno, I. Dafinei, C. J. Davis, S. Dell'Oro, S. Di Domizio, V. Dompè, D. Q. Fang, G. Fantini, M. Faverzani, E. Ferri, F. Ferroni, E. Fiorini, M. A. Franceschi, S. J. Freedman, B. K. Fujikawa, A. Giachero, L. Gironi, A. Giuliani, P. Gorla, C. Gotti, T. D. Gutierrez, K. Han, K. M. Heeger, R. G. Huang, H. Z. Huang, J. Johnston, G. Keppel, Yu. G. Kolomensky, C. Ligi, Y. G. Ma, L. Ma, L. Marini, R. H. Maruyama, Y. Mei, N. Moggi, S. Morganti, T. Napolitano, M. Nas-

tasi, J. Nikkel, C. Nones, E. B. Norman, V. Novati, A. Nucciotti, I. Nutini, T. O'Donnell, J. L. Ouellet, C. E. Pagliarone, L. Pagnanini, M. Pallavicini, L. Pattavina, M. Pavan, G. Pessina, V. Pettinacci, C. Pira, S. Pirro, S. Pozzi, E. Previtali, A. Puiu, C. Rosenfeld, C. Rusconi, M. Sakai, S. Sangiorgio, B. Schmidt, N. D. Scielzo, V. Sharma, V. Singh, M. Sisti, D. Speller, P. T. Surukuchi, L. Taffarello, F. Terranova, C. Tomei, M. Vignati, S. L. Wagaarachchi, B. S. Wang, B. Welliver, J. Wilson, K. Wilson, L. A. Winslow, L. Zanotti, S. Zimmermann, and S. Zucchelli. Improved limit on neutrinoless double-beta decay in ^{130}Te with cuore. *Phys. Rev. Lett.*, 124:122501, Mar 2020.

[48] P.F. De Salas, S. Gariazzo, O. Mena, C.A. Ternes, and M. Tórtola. Neutrino Mass Ordering from Oscillations and Beyond: 2018 Status and Future Prospects. *Front. Astron. Space Sci.*, 5:36, 2018.

[49] S. Gariazzo, M. Archidiacono, P. F. de Salas, O. Mena, C. A. Ternes, and M. Tórtola. Neutrino masses and their ordering: Global Data, Priors and Models. *JCAP*, 1803(03):011, 2018.

[50] L. Wolfenstein. Neutrino oscillations in matter. *Phys. Rev. D*, 17:2369–2374, May 1978.

[51] A Yu Smirnov. The MSW effect and matter effects in neutrino oscillations. *Physica Scripta*, T121:57–64, jan 2005.

[52] Carlo Giunti and Chung W. Kim. *Fundamentals of Neutrino Physics and Astrophysics.* 2007.

[53] K. Abe et al. Improved constraints on neutrino mixing from the T2K experiment with $\mathbf{3.13 \times 10^{21}}$ protons on target. *Phys. Rev. D*, 103(11):112008, 2021.

[54] K. Abe, Y. Haga, Y. Hayato, M. Ikeda, K. Iyogi, J. Kameda, Y. Kishimoto, Ll. Marti, M. Miura, S. Moriyama, M. Nakahata, T. Nakajima, S. Nakayama, A. Orii, H. Sekiya, M. Shiozawa, Y. Sonoda, A. Takeda, H. Tanaka, Y. Takenaga, S. Tasaka, T. Tomura, K. Ueno, T. Yokozawa, R. Akutsu, T. Irvine, H. Kaji, T. Kajita, I. Kametani, K. Kaneyuki, K. P. Lee, Y. Nishimura, T. McLachlan, K. Okumura, E. Richard, L. Labarga, P. Fernandez, F. d. M. Blaszczyk, J. Gustafson, C. Kachulis, E. Kearns, J. L. Raaf, J. L. Stone, L. R. Sulak, S. Berkman, S. Tobayama, M. Goldhaber, K. Bays, G. Carminati, N. J. Griskevich, W. R. Kropp, S. Mine, A. Renshaw, M. B. Smy, H. W. Sobel, V. Takhistov, P. Weatherly, K. S. Ganezer, B. L. Hartfiel, J. Hill, W. E. Keig, N. Hong, J. Y. Kim, I. T. Lim, R. G. Park, T. Akiri, J. B. Albert, A. Himmel, Z. Li, E. O'Sullivan, K. Scholberg, C. W. Walter, T. Wongjirad, T. Ishizuka, T. Nakamura, J. S. Jang, K. Choi, J. G. Learned, S. Matsuno, S. N. Smith, M. Friend, T. Hasegawa, T. Ishida, T. Ishii, T. Kobayashi, T. Nakadaira, K. Nakamura, K. Nishikawa, Y. Oyama, K. Sakashita, T. Sekiguchi, T. Tsukamoto, Y. Nakano, A. T. Suzuki, Y. Takeuchi, T. Yano, S. V. Cao, T. Hayashino, T. Hiraki, S. Hirota, K. Huang, K. Ieki, M. Jiang, T. Kikawa, A. Minamino, A. Murakami, T. Nakaya, N. D. Patel, K. Suzuki, S. Takahashi, R. A. Wendell, Y. Fukuda, Y. Itow, G. Mitsuka, F. Muto, T. Suzuki, P. Mijakowski, K. Frankiewicz, J. Hignight, J. Imber, C. K. Jung, X. Li, J. L. Palomino, G. Santucci, I. Taylor, C. Vilela, M. J. Wilking, C. Yanagisawa, D. Fukuda, H. Ishino, T. Kayano, A. Kibayashi, Y. Koshio, T. Mori, M. Sakuda, J. Takeuchi, R. Yamaguchi, Y. Kuno, R. Tacik, S. B. Kim, H. Okazawa, Y. Choi, K. Ito, K. Nishijima, M. Koshiba, Y. Totsuka, Y. Suda, M. Yokoyama, C. Bronner, R. G. Calland, M. Hartz, K. Martens, Y. Obayashi, Y. Suzuki, M. R. Vagins, C. M. Nantais,

J. F. Martin, P. de Perio, H. A. Tanaka, A. Konaka, S. Chen, H. Sui, L. Wan, Z. Yang, H. Zhang, Y. Zhang, K. Connolly, M. Dziomba, and R. J. Wilkes. Solar neutrino measurements in super-kamiokande-iv. *Phys. Rev. D*, 94:052010, Sep 2016.

[55] A. Gando et al. Reactor On-Off Antineutrino Measurement with KamLAND. *Phys. Rev. D*, 88(3):033001, 2013.

[56] Cong Guo and On behalf of the JUNO Collaboration. Prospects and status of the juno experiment. *Moscow University Physics Bulletin*, 77(2):365–368, Apr 2022.

[57] Angel Abusleme, Thomas Adam, Shakeel Ahmad, Sebastiano Aiello, Muhammad Akram, Nawab Ali, Fengpeng An, Guangpeng An, Qi An, Giuseppe Andronico, Nikolay Anfimov, Vito Antonelli, Tatiana Antoshkina, Burin Asavapibhop, João Pedro Athayde Marcondes de André, Didier Auguste, Andrej Babic, Wander Baldini, Andrea Barresi, Eric Baussan, Marco Bellato, Antonio Bergnoli, Enrico Bernieri, David Biare, Thilo Birkenfeld, Sylvie Blin, David Blum, Simon Blyth, Anastasia Bolshakova, Mathieu Bongrand, Clément Bordereau, Dominique Breton, Augusto Brigatti, Riccardo Brugnera, Riccardo Bruno, Antonio Budano, Max Buesken, Mario Buscemi, Jose Busto, Ilya Butorov, Anatael Cabrera, Hao Cai, Xiao Cai, Yanke Cai, Zhiyan Cai, Antonio Cammi, Agustin Campeny, Chuanya Cao, Guofu Cao, Jun Cao, Rossella Caruso, Cédric Cerna, Jinfan Chang, Yun Chang, Pingping Chen, Po-An Chen, Shaomin Chen, Shenjian Chen, Xurong Chen, Yi-Wen Chen, Yixue Chen, Yu Chen, Zhang Chen, Jie Cheng, Yaping Cheng, Alexander Chepurnov, Davide Chiesa, Pietro Chimenti, Artem Chukanov, Anna Chuvashova, Gérard Claverie, Catia Clementi, Barbara Clerbaux, Selma Conforti Di Lorenzo, Daniele Corti, Salvatore Costa, Flavio Dal Corso, Christophe De La Taille, Jiawei Deng, Zhi Deng, Ziyan Deng, Wilfried Depnering, Marco Diaz, Xuefeng Ding, Yayun Ding, Bayu Dirgantara, Sergey Dmitrievsky, Tadeas Dohnal, Georgy Donchenko, Jianmeng Dong, Damien Dornic, Evgeny Doroshkevich, Marcos Dracos, Frédéric Druillole, Shuxian Du, Stefano Dusini, Martin Dvorak, Timo Enqvist, Heike Enzmann, Andrea Fabbri, Lukas Fajt, Donghua Fan, Lei Fan, Can Fang, Jian Fang, Marco Fargetta, Anna Fatkina, Dmitry Fedoseev, Vladko Fekete, Li-Cheng Feng, Qichun Feng, Richard Ford, Andrey Formozov, Amélie Fournier, Haonan Gan, Feng Gao, Alberto Garfagnini, Alexandre Göttel, Christoph Genster, Marco Giammarchi, Agnese Giaz, Nunzio Giudice, Franco Giuliani, Maxim Gonchar, Guanghua Gong, Hui Gong, Oleg Gorchakov, Yuri Gornushkin, Marco Grassi, Christian Grewing, Maxim Gromov, Vasily Gromov, Minghao Gu, Xiaofei Gu, Yu Gu, Mengyun Guan, Nunzio Guardone, Maria Gul, Cong Guo, Jingyuan Guo, Wanlei Guo, Xinheng Guo, Yuhang Guo, Paul Hackspacher, Caren Hagner, Ran Han, Yang Han, Miao He, Wei He, Tobias Heinz, Patrick Hellmuth, Yuekun Heng, Rafael Herrera, Daojin Hong, YuenKeung Hor, Shaojing Hou, Yee Hsiung, Bei-Zhen Hu, Hang Hu, Jianrun Hu, Jun Hu, Shouyang Hu, Tao Hu, Zhuojun Hu, Chunhao Huang, Guihong Huang, Hanxiong Huang, Qinhua Huang, Wenhao Huang, Xingtao Huang, Yongbo Huang, Jiaqi Hui, Wenju Huo, Cédric Huss, Safeer Hussain, Antonio Insolia, Ara Ioannisian, Daniel Ioannisyan, Roberto Isocrate, Kuo-Lun Jen, Xiaolu Ji, Xingzhao Ji, Huihui Jia, Junji Jia, Siyu Jian, Di Jiang, Xiaoshan Jiang, Ruyi Jin, Xiaoping Jing, Cécile Jollet, Jari Joutsenvaara, Sirichok Jungthawan, Leonidas Kalousis, Philipp Kampmann, Li Kang, Michael Karagounis, Nar-

ine Kazarian, Amir Khan, Waseem Khan, Khanchai Khosonthongkee, Patrick Kinz, Denis Korablev, Konstantin Kouzakov, Alexey Krasnoperov, Svetlana Krokhaleva, Zinovy Krumshteyn, Andre Kruth, Nikolay Kutovskiy, Pasi Kuusiniemi, Tobias Lachenmaier, Cecilia Landini, Sébastien Leblanc, Frederic Lefevre, Liping Lei, Ruiting Lei, Rupert Leitner, Jason Leung, Demin Li, Fei Li, Fule Li, Haitao Li, Huiling Li, Jiaqi Li, Jin Li, Kaijie Li, Mengzhao Li, Nan Li, Nan Li, Qingjiang Li, Ruhui Li, Shanfeng Li, Shuaijie Li, Tao Li, Weidong Li, Weiguo Li, Xiaomei Li, Xiaonan Li, Xinglong Li, Yi Li, Yufeng Li, Zhibing Li, Ziyuan Li, Hao Liang, Hao Liang, Jingjing Liang, Jiajun Liao, Daniel Liebau, Ayut Limphirat, Sukit Limpijumnong, Guey-Lin Lin, Shengxin Lin, Tao Lin, Jiajie Ling, Ivano Lippi, Fang Liu, Haidong Liu, Hongbang Liu, Hongjuan Liu, Hongtao Liu, Hu Liu, Hui Liu, Jianglai Liu, Jinchang Liu, Min Liu, Qian Liu, Qin Liu, Runxuan Liu, Shuangyu Liu, Shubin Liu, Shulin Liu, Xiaowei Liu, Yan Liu, Alexey Lokhov, Paolo Lombardi, Claudio Lombardo, Kai Loo, Chuan Lu, Haoqi Lu, Jingbin Lu, Junguang Lu, Shuxiang Lu, Xiaoxu Lu, Bayarto Lubsandorzhiev, Sultim Lubsandorzhiev, Livia Ludhova, Fengjiao Luo, Guang Luo, Pengwei Luo, Shu Luo, Wuming Luo, Vladimir Lyashuk, Qiumei Ma, Si Ma, Xiaoyan Ma, Xubo Ma, Jihane Maalmi, Yury Malyshkin, Fabio Mantovani, Francesco Manzali, Xin Mao, Yajun Mao, Stefano M. Mari, Filippo Marini, Sadia Marium, Cristina Martellini, Gisele Martin-Chassard, Agnese Martini, Davit Mayilyan, Axel Müller, Ints Mednieks, Yue Meng, Anselmo Meregaglia, Emanuela Meroni, David Meyhöfer, Mauro Mezzetto, Jonathan Miller, Lino Miramonti, Salvatore Monforte, Paolo Montini, Michele Montuschi, Nikolay Morozov, Pavithra Muralidharan, Massimiliano Nastasi, Dmitry V. Naumov, Elena Naumova, Igor Nemchenok, Alexey Nikolaev, Feipeng Ning, Zhe Ning, Hiroshi Nunokawa, Lothar Oberauer, Juan Pedro Ochoa-Ricoux, Alexander Olshevskiy, Domizia Orestano, Fausto Ortica, Hsiao-Ru Pan, Alessandro Paoloni, Nina Parkalian, Sergio Parmeggiano, Teerapat Payupol, Yatian Pei, Nicomede Pelliccia, Anguo Peng, Haiping Peng, Frédéric Perrot, Pierre-Alexandre Petitjean, Fabrizio Petrucci, Luis Felipe Piñeres Rico, Oliver Pilarczyk, Artyom Popov, Pascal Poussot, Wathan Pratumwan, Ezio Previtali, Fazhi Qi, Ming Qi, Sen Qian, Xiaohui Qian, Hao Qiao, Zhonghua Qin, Shoukang Qiu, Muhammad Rajput, Gioacchino Ranucci, Neill Raper, Alessandra Re, Henning Rebber, Abdel Rebii, Bin Ren, Jie Ren, Taras Rezinko, Barbara Ricci, Markus Robens, Mathieu Roche, Narongkiat Rodphai, Aldo Romani, Bedřich Roskovec, Christian Roth, Xiangdong Ruan, Xichao Ruan, Saroj Rujirawat, Arseniy Rybnikov, Andrey Sadovsky, Paolo Saggese, Giuseppe Salamanna, Simone Sanfilippo, Anut Sangka, Nuanwan Sanguansak, Utane Sawangwit, Julia Sawatzki, Fatma Sawy, Michaela Schever, Jacky Schuler, Cédric Schwab, Konstantin Schweizer, Dmitry Selivanov, Alexandr Selyunin, Andrea Serafini, Giulio Settanta, Mariangela Settimo, Muhammad Shahzad, Vladislav Sharov, Gang Shi, Jingyan Shi, Yongjiu Shi, Vitaly Shutov, Andrey Sidorenkov, Fedor Šimkovic, Chiara Sirignano, Jaruchit Siripak, Monica Sisti, Maciej Slupecki, Mikhail Smirnov, Oleg Smirnov, Thiago Sogo-Bezerra, Julanan Songwadhana, Boonrucksar Soonthornthum, Albert Sotnikov, Ondrej Sramek, Warintorn Sreethawong, Achim Stahl, Luca Stanco, Konstantin Stankevich, Dušan Štefánik, Hans Steiger, Jochen Steinmann, Tobias Sterr, Matthias Raphael Stock, Virginia Strati, Alexander Studenikin, Gongxing Sun, Shifeng Sun, Xilei Sun, Yongjie Sun, Yongzhao Sun, Narumon Suwonjandee, Michal Szelezniak, Jian Tang, Qiang Tang, Quan Tang, Xiao Tang, Alexander Tietzsch, Igor Tkachev, Tomas Tmej, Konstantin Treskov, Andrea Triossi,

Giancarlo Troni, Wladyslaw Trzaska, Cristina Tuve, Stefan van Waasen, Johannes van den Boom, Guillaume Vanroyen, Nikolaos Vassilopoulos, Vadim Vedin, Giuseppe Verde, Maxim Vialkov, Benoit Viaud, Cristina Volpe, Vit Vorobel, Lucia Votano, Pablo Walker, Caishen Wang, Chung-Hsiang Wang, En Wang, Guoli Wang, Jian Wang, Jun Wang, Kunyu Wang, Lu Wang, Meifen Wang, Meng Wang, Meng Wang, Ruiguang Wang, Siguang Wang, Wei Wang, Wei Wang, Wenshuai Wang, Xi Wang, Xiangyue Wang, Yangfu Wang, Yaoguang Wang, Yi Wang, Yi Wang, Yifang Wang, Yuanqing Wang, Yuman Wang, Zhe Wang, Zheng Wang, Zhimin Wang, Zongyi Wang, Apimook Watcharangkool, Lianghong Wei, Wei Wei, Yadong Wei, Liangjian Wen, Christopher Wiebusch, Steven Chan-Fai Wong, Bjoern Wonsak, Diru Wu, Fangliang Wu, Qun Wu, Wenjie Wu, Zhi Wu, Michael Wurm, Jacques Wurtz, Christian Wysotzki, Yufei Xi, Dongmei Xia, Yuguang Xie, Zhangquan Xie, Zhizhong Xing, Benda Xu, Donglian Xu, Fanrong Xu, Jilei Xu, Jing Xu, Meihang Xu, Yin Xu, Yu Xu, Baojun Yan, Xiongbo Yan, Yupeng Yan, Anbo Yang, Changgen Yang, Huan Yang, Jie Yang, Lei Yang, Xiaoyu Yang, Yifan Yang, Haifeng Yao, Zafar Yasin, Jiaxuan Ye, Mei Ye, Ugur Yegin, Frédéric Yermia, Peihuai Yi, Xiangwei Yin, Zhengyun You, Boxiang Yu, Chiye Yu, Chunxu Yu, Hongzhao Yu, Miao Yu, Xianghui Yu, Zeyuan Yu, Chengzhuo Yuan, Ying Yuan, Zhenxiong Yuan, Ziyi Yuan, Baobiao Yue, Noman Zafar, Andre Zambanini, Pan Zeng, Shan Zeng, Tingxuan Zeng, Yuda Zeng, Liang Zhan, Feiyang Zhang, Guoqing Zhang, Haiqiong Zhang, Honghao Zhang, Jiawen Zhang, Jie Zhang, Jingbo Zhang, Peng Zhang, Qingmin Zhang, Shiqi Zhang, Tao Zhang, Xiaomei Zhang, Xuantong Zhang, Yan Zhang, Yinhong Zhang, Yiyu Zhang, Yongpeng Zhang, Yuanyuan Zhang, Yumei Zhang, Zhenyu Zhang, Zhijian Zhang, Fengyi Zhao, Jie Zhao, Rong Zhao, Shujun Zhao, Tianchi Zhao, Dongqin Zheng, Hua Zheng, Minshan Zheng, Yangheng Zheng, Weirong Zhong, Jing Zhou, Li Zhou, Nan Zhou, Shun Zhou, Xiang Zhou, Jiang Zhu, Kejun Zhu, Honglin Zhuang, Liang Zong, Jiaheng Zou, and (JUNO Collaboration). Feasibility and physics potential of detecting 8b solar neutrinos at juno *. *Chinese Physics C*, 45(2):023004, feb 2021.

[58] K. Abe, N. Akhlaq, R. Akutsu, A. Ali, C. Alt, C. Andreopoulos, M. Antonova, S. Aoki, T. Arihara, Y. Asada, Y. Ashida, E. T. Atkin, Y. Awataguchi, G. J. Barker, G. Barr, D. Barrow, M. Batkiewicz-Kwasniak, A. Beloshapkin, F. Bench, V. Berardi, L. Berns, S. Bhadra, A. Blanchet, A. Blondel, S. Bolognesi, T. Bonus, B. Bourguille, S. B. Boyd, A. Bravar, D. Bravo Berguño, C. Bronner, S. Bron, A. Bubak, M. Buizza Avanzini, S. Cao, S. L. Cartwright, M. G. Catanesi, A. Cervera, J. Chakrani, D. Cherdack, G. Christodoulou, M. Cicerchia, J. Coleman, G. Collazuol, L. Cook, D. Coplowe, A. Cudd, G. De Rosa, T. Dealtry, C. C. Delogu, S. R. Dennis, C. Densham, A. Dergacheva, F. Di Lodovico, S. Dolan, D. Douqa, T. A. Doyle, J. Dumarchez, P. Dunne, A. Eguchi, L. Eklund, S. Emery-Schrenk, A. Ereditato, A. J. Finch, G. Fiorillo, C. Francois, M. Friend, Y. Fujii, R. Fukuda, Y. Fukuda, K. Fusshoeller, C. Giganti, M. Gonin, E. A. G. Goodman, A. Gorin, M. Grassi, M. Guigue, D. R. Hadley, P. Hamacher-Baumann, D. A. Harris, M. Hartz, T. Hasegawa, S. Hassani, N. C. Hastings, Y. Hayato, A. Hiramoto, M. Hogan, J. Holeczek, N. T. Hong Van, T. Honjo, F. Iacob, A. K. Ichikawa, M. Ikeda, T. Ishida, M. Ishitsuka, K. Iwamoto, A. Izmaylov, N. Izumi, M. Jakkapu, B. Jamieson, S. J. Jenkins, C. Jesús-Valls, J. J. Jiang, P. Jonsson, C. K. Jung, P. B. Jurj, M. Kabirnezhad, H. Kakuno, J. Kameda, S. P. Kasetti, Y. Kataoka, Y. Katayama, T. Ka-

tori, E. Kearns, M. Khabibullin, A. Khotjantsev, T. Kikawa, H. Kikutani, S. King, J. Kisiel, T. Kobata, T. Kobayashi, L. Koch, A. Konaka, L. L. Kormos, Y. Koshio, A. Kostin, K. Kowalik, Y. Kudenko, S. Kuribayashi, R. Kurjata, T. Kutter, M. Kuze, L. Labarga, J. Lagoda, M. Lamoureux, D. Last, M. Laveder, M. Lawe, S.-K. Lin, R. P. Litchfield, S. L. Liu, A. Longhin, L. Ludovici, X. Lu, T. Lux, L. N. Machado, L. Magaletti, K. Mahn, M. Malek, S. Manly, L. Maret, A. D. Marino, L. Marti-Magro, T. Maruyama, T. Matsubara, K. Matsushita, C. Mauger, A. Maurel, K. Mavrokoridis, E. Mazzucato, N. McCauley, J. McElwee, K. S. McFarland, C. McGrew, A. Mefodiev, G. D. Megias, L. Mellet, M. Mezzetto, A. Minamino, O. Mineev, S. Mine, M. Miura, L. Molina Bueno, S. Moriyama, Th. A. Mueller, D. Munford, L. Munteanu, Y. Nagai, T. Nakadaira, M. Nakahata, Y. Nakajima, A. Nakamura, H. Nakamura, K. Nakamura, Y. Nakano, S. Nakayama, T. Nakaya, K. Nakayoshi, C. E. R. Naseby, T. V. Ngoc, V. Q. Nguyen, K. Niewczas, Y. Nishimura, K. Nishizaki, E. Noah, T. S. Nonnenmacher, F. Nova, J. Nowak, J. C. Nugent, H. M. O'Keeffe, L. O'Sullivan, T. Odagawa, T. Ogawa, R. Okada, K. Okumura, T. Okusawa, R. A. Owen, Y. Oyama, V. Palladino, V. Paolone, M. Pari, W. C. Parker, J. Parlone, S. Parsa, J. Pasternak, M. Pavin, D. Payne, G. C. Penn, D. Pershey, L. Pickering, C. Pidcott, G. Pintaudi, C. Pistillo, B. Popov, K. Porwit, M. Posiadala-Zezula, A. Pritchard, B. Quilain, T. Radermacher, E. Radicioni, B. Radics, P. N. Ratoff, M. Reh, C. Riccio, E. Rondio, S. Roth, A. Rubbia, A. C. Ruggeri, C. A. Ruggles, A. Rychter, L. S. M. Lakshmi, K. Sakashita, F. Sánchez, G. Santucci, C. M. Schloesser, K. Scholberg, M. Scott, Y. Seiya, T. Sekiguchi, H. Sekiya, D. Sgalaberna, A. Shaikhiev, A. Shaykina, M. Shiozawa, W. Shorrock, A. Shvartsman, K. Skwarczynski, M. Smy, J. T. Sobczyk, H. Sobel, F. J. P. Soler, Y. Sonoda, R. Spina, S. Suvorov, A. Suzuki, S. Y. Suzuki, Y. Suzuki, A. A. Sztuc, M. Tada, M. Tajima, A. Takeda, Y. Takeuchi, H. K. Tanaka, Y. Tanihara, M. Tani, N. Teshima, N. Thamm, L. F. Thompson, W. Toki, C. Touramanis, T. Towstego, K. M. Tsui, T. Tsukamoto, M. Tzanov, Y. Uchida, M. Vagins, S. Valder, D. Vargas, G. Vasseur, C. Vilela, W. G. S. Vinning, T. Vladisavljevic, T. Wachala, J. Walker, J. G. Walsh, Y. Wang, L. Wan, D. Wark, M. O. Wascko, A. Weber, R. Wendell, M. J. Wilking, C. Wilkinson, J. R. Wilson, K. Wood, C. Wret, J. Xia, Y.-h. Xu, K. Yamamoto, C. Yanagisawa, G. Yang, T. Yano, K. Yasutome, N. Yershov, M. Yokoyama, T. Yoshida, Y. Yoshimoto, M. Yu, R. Zaki, A. Zalewska, J. Zalipska, K. Zaremba, G. Zarnecki, M. Ziembicki, M. Zito, and S. Zsoldos. Improved constraints on neutrino mixing from the t2k experiment with 3.13×10^{21} protons on target. *Phys. Rev. D*, 103:112008, Jun 2021.

[59] H. de Kerret et al. Double Chooz θ_{13} measurement via total neutron capture detection. *Nature Phys.*, 16(5):558–564, 2020.

[60] C. D. Shin et al. Observation of reactor antineutrino disappearance using delayed neutron capture on hydrogen at RENO. *JHEP*, 04:029, 2020.

[61] M. A. Acero, P. Adamson, L. Aliaga, N. Anfimov, A. Antoshkin, E. Arrieta-Diaz, L. Asquith, A. Aurisano, A. Back, C. Backhouse, M. Baird, N. Balashov, P. Baldi, B. A. Bambah, S. Bashar, K. Bays, R. Bernstein, V. Bhatnagar, D. Bhattarai, B. Bhuyan, J. Bian, J. Blair, A. C. Booth, R. Bowles, C. Bromberg, N. Buchanan, A. Butkevich, S. Calvez, T. J. Carroll, E. Catano-Mur, B. C. Choudhary, A. Christensen, T. E. Coan, M. Colo, L. Cremonesi, G. S. Davies, P. F. Derwent, P. Ding, Z. Djurcic, M. Dolce, D. Doyle,

D. Dueñas Tonguino, E. C. Dukes, H. Duyang, R. Ehrlich, M. Elkins, E. Ewart, G. J. Feldman, P. Filip, J. Franc, M. J. Frank, H. R. Gallagher, R. Gandrajula, F. Gao, A. Giri, R. A. Gomes, M. C. Goodman, V. Grichine, M. Groh, R. Group, B. Guo, A. Habig, F. Hakl, A. Hall, J. Hartnell, R. Hatcher, H. Hausner, M. He, K. Heller, J. Hewes, A. Himmel, A. Holin, J. Huang, B. Jargowsky, J. Jarosz, F. Jediny, C. Johnson, M. Judah, I. Kakorin, D. M. Kaplan, A. Kalitkina, R. Keloth, O. Klimov, L. W. Koerner, L. Kolupaeva, S. Kotelnikov, R. Kralik, Ch. Kullenberg, M. Kubu, A. Kumar, C. D. Kuruppu, V. Kus, T. Lackey, K. Lang, P. Lasorak, J. Lesmeister, S. Lin, A. Lister, J. Liu, M. Lokajicek, S. Magill, M. Manrique Plata, W. A. Mann, M. L. Marshak, M. Martinez-Casales, V. Matveev, B. Mayes, D. P. Méndez, M. D. Messier, H. Meyer, T. Miao, W. H. Miller, S. R. Mishra, A. Mislivec, R. Mohanta, A. Moren, A. Morozova, W. Mu, L. Mualem, M. Muether, S. Mufson, K. Mulder, D. Naples, N. Nayak, J. K. Nelson, R. Nichol, E. Niner, A. Norman, A. Norrick, T. Nosek, H. Oh, A. Olshevskiy, T. Olson, J. Ott, J. Paley, R. B. Patterson, G. Pawloski, O. Petrova, R. Petti, D. D. Phan, R. K. Plunkett, J. C. C. Porter, A. Rafique, F. Psihas, V. Raj, M. Rajaoalisoa, B. Ramson, B. Rebel, P. Rojas, P. Roy, V. Ryabov, O. Samoylov, M. C. Sanchez, S. Sánchez Falero, P. Shanahan, A. Sheshukov, P. Singh, V. Singh, E. Smith, J. Smolik, P. Snopok, N. Solomey, A. Sousa, K. Soustruznik, M. Strait, L. Suter, A. Sutton, S. Swain, C. Sweeney, A. Sztuc, R. L. Talaga, B. Tapia Oregui, P. Tas, T. Thakore, R. B. Thayyullathil, J. Thomas, E. Tiras, J. Tripathi, J. Trokan-Tenorio, A. Tsaris, Y. Torun, J. Urheim, P. Vahle, Z. Vallari, J. Vasel, P. Vokac, T. Vrba, M. Wallbank, T. K. Warburton, M. Wetstein, D. Whittington, D. A. Wickremasinghe, S. G. Wojcicki, J. Wolcott, W. Wu, Y. Xiao, A. Yallappa Dombara, A. Yankelevich, K. Yonehara, S. Yu, Y. Yu, S. Zadorozhnyy, J. Zalesak, Y. Zhang, and R. Zwaska and. Improved measurement of neutrino oscillation parameters by the NOvA experiment. *Physical Review D*, 106(3), aug 2022.

[62] K. Abe et al. Measurement of the charged-current electron (anti-)neutrino inclusive cross-sections at the T2K off-axis near detector ND280. *JHEP*, 10:114, 2020.

[63] K. Abe et al. Simultaneous measurement of the muon neutrino charged-current cross section on oxygen and carbon without pions in the final state at T2K. *Phys. Rev. D*, 101(11):112004, 2020.

[64] K. Abe et al. Measurements of $\overline{\nu}_\mu$ and $\overline{\nu}_\mu + \nu_\mu$ charged-current cross-sections without detected pions or protons on water and hydrocarbon at a mean anti-neutrino energy of 0.86 GeV. *PTEP*, 2021(4):043C01, 2021.

[65] K. Abe et al. T2K measurements of muon neutrino and antineutrino disappearance using 3.13×10^{21} protons on target. *Phys. Rev. D*, 103(1):L011101, 2021.

[66] Benjamin Quilain and Akihiro Minamino. The WAGASCI detector as an off-axis near detector of the T2K and Hyper-Kamiokande experiments. *Journal of Physics: Conference Series*, 888:012166, 9 2017.

[67] M. Antonova et al. Baby MIND: a magnetized segmented neutrino detector for the WAGASCI experiment. *Journal of Instrumentation*, 12(07):C07028–C07028, 7 2017.

[68] J. Timmer. The UA1 Detector. In *3rd Moriond Workshop: Antiproton-Proton Physics*, 1983.

[69] D. G. Michael et al. The Magnetized steel and scintillator calorimeters of the MINOS experiment. *Nucl. Instrum. Meth. A*, 596:190–228, 2008.

[70] T.T. Böhlen, F. Cerutti, M.P.W. Chin, A. Fassò, A. Ferrari, P.G. Ortega, A. Mairani, P.R. Sala, G. Smirnov, and V. Vlachoudis. The fluka code: Developments and challenges for high energy and medical applications. *Nuclear Data Sheets*, 120:211–214, 2014.

[71] C. Zeitnitz and T.A. Gabriel. The geant-calor interface and benchmark calculations of zeus test calorimeters. *Nuclear Instruments and Methods in Physics Research Section A: Accelerators, Spectrometers, Detectors and Associated Equipment*, 349(1):106–111, 1994.

[72] K. Abe, N. Abgrall, H. Aihara, T. Akiri, J. B. Albert, C. Andreopoulos, S. Aoki, A. Ariga, T. Ariga, S. Assylbekov, D. Autiero, M. Barbi, G. J. Barker, G. Barr, M. Bass, M. Batkiewicz, F. Bay, S. W. Bentham, V. Berardi, B. E. Berger, S. Berkman, I. Bertram, D. Beznosko, S. Bhadra, F. d. M. Blaszczyk, A. Blondel, C. Bojechko, S. Boyd, A. Bravar, C. Bronner, D. G. Brook-Roberge, N. Buchanan, R. G. Calland, J. Caravaca Rodríguez, S. L. Cartwright, R. Castillo, M.-G. Catanesi, A. Cervera, D. Cherdack, G. Christodoulou, A. Clifton, J. Coleman, S. J. Coleman, G. Collazuol, K. Connolly, A. Curioni, A. Dabrowska, I. Danko, R. Das, S. Davis, M. Day, J. P. A. M. de André, P. de Perio, G. De Rosa, T. Dealtry, C. Densham, F. Di Lodovico, S. Di Luise, J. Dobson, T. Duboyski, F. Dufour, J. Dumarchez, S. Dytman, M. Dziewiecki, M. Dziomba, S. Emery, A. Ereditato, L. Escudero, L. S. Esposito, A. J. Finch, E. Frank, M. Friend, Y. Fujii, Y. Fukuda, V. Galymov, A. Gaudin, S. Giffin, C. Giganti, K. Gilje, T. Golan, J. J. Gomez-Cadenas, M. Gonin, N. Grant, D. Gudin, P. Guzowski, D. R. Hadley, A. Haesler, M. D. Haigh, D. Hansen, T. Hara, M. Hartz, T. Hasegawa, N. C. Hastings, Y. Hayato, C. Hearty, R. L. Helmer, J. Hignight, A. Hillairet, A. Himmel, T. Hiraki, J. Holeczek, S. Horikawa, K. Huang, A. Hyndman, A. K. Ichikawa, K. Ieki, M. Ieva, M. Ikeda, J. Imber, J. Insler, T. Ishida, T. Ishii, S. J. Ives, K. Iyogi, A. Izmaylov, B. Jamieson, R. A. Johnson, J. H. Jo, P. Jonsson, K. K. Joo, G. V. Jover-Manas, C. K. Jung, H. Kaji, T. Kajita, H. Kakuno, J. Kameda, Y. Kanazawa, D. Karlen, I. Karpikov, E. Kearns, M. Khabibullin, F. Khanam, A. Khotjantsev, D. Kielczewska, T. Kikawa, A. Kilinski, J. Y. Kim, J. Kim, S. B. Kim, B. Kirby, J. Kisiel, P. Kitching, T. Kobayashi, G. Kogan, A. Konaka, L. L. Kormos, A. Korzenev, K. Koseki, Y. Koshio, K. Kowalik, I. Kreslo, W. Kropp, H. Kubo, Y. Kudenko, S. Kumaratunga, R. Kurjata, T. Kutter, J. Lagoda, K. Laihem, A. Laing, M. Laveder, M. Lawe, K. P. Lee, C. Licciardi, I. T. Lim, T. Lindner, C. Lister, R. P. Litchfield, A. Longhin, G. D. Lopez, L. Ludovici, M. Macaire, L. Magaletti, K. Mahn, M. Malek, S. Manly, A. Marchionni, A. D. Marino, J. Marteau, J. F. Martin, T. Maruyama, J. Marzec, P. Masliah, E. L. Mathie, C. Matsumura, K. Matsuoka, V. Matveev, K. Mavrokoridis, E. Mazzucato, N. McCauley, K. S. McFarland, C. McGrew, T. McLachlan, M. Messina, C. Metelko, M. Mezzetto, P. Mijakowski, C. A. Miller, A. Minamino, O. Mineev, S. Mine, A. Missert, M. Miura, L. Monfregola, S. Moriyama, Th. A. Mueller, A. Murakami, M. Murdoch, S. Murphy, J. Myslik, T. Nagasaki, T. Nakadaira, M. Nakahata, T. Nakai, K. Nakajima, K. Nakamura, S. Nakayama, T. Nakaya, K. Nakayoshi, D. Naples, T. C. Nicholls, C. Nielsen, K. Nishikawa, Y. Nishimura, H. M. O'Keeffe, Y. Obayashi, R. Ohta, K. Okumura, W. Oryszczak, S. M. Oser, M. Otani, R. A. Owen, Y. Oyama, M. Y. Pac, V. Palladino, V. Paolone, D. Payne, G. F. Pearce,

O. Perevozchikov, J. D. Perkin, E. S. Pinzon Guerra, P. Plonski, E. Poplawska, B. Popov, M. Posiadala, J.-M. Poutissou, R. Poutissou, P. Przewlocki, B. Quilain, E. Radicioni, P. N. Ratoff, M. Ravonel, M. A. Rayner, M. Reeves, E. Reinherz-Aronis, F. Retiere, P. A. Rodrigues, E. Rondio, B. Rossi, S. Roth, A. Rubbia, D. Ruterbories, R. Sacco, K. Sakashita, F. Sánchez, E. Scantamburlo, K. Scholberg, J. Schwehr, M. Scott, D. I. Scully, Y. Seiya, T. Sekiguchi, H. Sekiya, M. Shibata, M. Shiozawa, S. Short, Y. Shustrov, P. Sinclair, B. Smith, R. J. Smith, M. Smy, J. T. Sobczyk, H. Sobel, M. Sorel, L. Southwell, P. Stamoulis, J. Steinmann, B. Still, R. Sulej, A. Suzuki, K. Suzuki, S. Y. Suzuki, Y. Suzuki, T. Szeglowski, M. Szeptycka, R. Tacik, M. Tada, S. Takahashi, A. Takeda, Y. Takeuchi, H. A. Tanaka, M. Tanaka, M. M. Tanaka, I. J. Taylor, D. Terhorst, R. Terri, L. F. Thompson, A. Thorley, S. Tobayama, W. Toki, T. Tomura, Y. Totsuka, C. Touramanis, T. Tsukamoto, M. Tzanov, Y. Uchida, K. Ueno, A. Vacheret, M. Vagins, G. Vasseur, T. Wachala, A. V. Waldron, C. W. Walter, J. Wang, D. Wark, M. O. Wascko, A. Weber, R. Wendell, G. Wikström, R. J. Wilkes, M. J. Wilking, C. Wilkinson, Z. Williamson, J. R. Wilson, R. J. Wilson, T. Wongjirad, Y. Yamada, K. Yamamoto, C. Yanagisawa, T. Yano, S. Yen, N. Yershov, M. Yokoyama, T. Yuan, A. Zalewska, L. Zambelli, K. Zaremba, M. Ziembicki, E. D. Zimmerman, M. Zito, and J. Żmuda. T2k neutrino flux prediction. *Phys. Rev. D*, 87:012001, Jan 2013.

[73] R. Brun, F. Bruyant, M. Maire, A. C. McPherson, and P. Zanarini. GEANT3. 9 1987.

[74] N Abgrall et al. Na61/shine facility at the cern sps: beams and detector system. *Journal of Instrumentation*, 9(06):P06005, jun 2014.

[75] S. Bolognesi et al. Niwg model and uncertainties for 2019-2020 oscillation analysis. Technical Report T2K-TN344, T2K Collaboration, 2019.

[76] S. Bolognesi et al. Niwg model and uncertainties for 2017 oscillation analysis. Technical Report T2K-TN315, T2K Collaboration, 2017.

[77] K. Abe, R. Akutsu, A. Ali, et al. Search for CP Violation in Neutrino and Antineutrino Oscillations by the T2K Experiment with 2.2×10^{21} Protons on Target. *Phys. Rev. Lett.*, 121:171802, 10 2018.

[78] Abe, K. and others. Improved constraints on neutrino mixing from the T2K experiment with $\mathbf{3.13 \times 10^{21}}$ protons on target. 1 2021.

[79] O. Benhar, A. Fabrocini, S. Fantoni, and I. Sick. Spectral function of finite nuclei and scattering of GeV electrons. *Nucl. Phys. A*, 579:493–517, 1994.

[80] A. M. Ankowski, O. Benhar, and M. Sakuda. Improving the accuracy of neutrino energy reconstruction in charged-current quasielastic scattering off nuclear targets. *Phys. Rev. D*, 91:033005, 2 2015.

[81] K. Abe, J. Amey, C. Andreopoulos, et al. Characterization of nuclear effects in muon-neutrino scattering on hydrocarbon with a measurement of final-state kinematics and correlations in charged-current pionless interactions at t2k. *Phys. Rev. D*, 98:032003, 8 2018.

[82] X.-G. Lu, M. Betancourt, T. Walton, F. Akbar, L. Aliaga, O. Altinok, D. A. Andrade, M. Ascencio, L. Bellantoni, A. Bercellie, A. Bodek, A. Bravar, H. Budd, T. Cai, M. F. Carneiro, J. Chaves, D. Coplowe, H. da Motta, S. A. Dytman, G. A. Díaz, J. Felix, L. Fields, R. Fine, A. M. Gago, R. Galindo, H. Gallagher, A. Ghosh, R. Gran, D. A. Harris, S. Henry, S. Jena, D. Jena, J. Kleykamp, M. Kordosky, T. Le, E. Maher, S. Manly, W. A. Mann, C. M. Marshall, K. S. McFarland, A. M. McGowan, B. Messerly, J. Miller, A. Mislivec, J. G. Morfín, J. Mousseau, D. Naples, J. K. Nelson, C. Nguyen, A. Norrick, Nuruzzaman, A. Olivier, V. Paolone, C. E. Patrick, G. N. Perdue, M. A. Ramírez, R. D. Ransome, L. Ren, D. Rimal, P. A. Rodrigues, D. Ruterbories, H. Schellman, J. T. Sobczyk, C. J. Solano Salinas, H. Su, M. Sultana, E. Valencia, D. Wark, A. Weber, J. Wolcott, M. Wospakrik, and B. Yaeggy. Measurement of Final-State Correlations in Neutrino Muon-Proton Mesonless Production on Hydrocarbon at $<E_{\nu}> = 3$ GeV. *Phys. Rev. Lett.*, 121:022504, 7 2018.

[83] S. Dolan. Exploring Nuclear Effects in Neutrino-Nucleus Interactions Using Measurements of Transverse Kinematic Imbalance from T2K and MINERvA. 10 2018.

[84] D. Dutta et al. A Study of the quasielastic (e,e-prime p) reaction on C-12, Fe-56 and Au-97. *Phys. Rev. C*, 68:064603, 2003.

[85] M. Leuschner et al. Quasielastic proton knockout from O-16. *Phys. Rev. C*, 49:955–967, 1994.

[86] P. Guèye, M. Bernheim, J. F. Danel, et al. Coulomb distortion measurements by comparing electron and positron quasielastic scattering off $^{12}\mathrm{C}$ and $^{208}\mathrm{Pb}$. *Phys. Rev. C*, 60:044308, 9 1999.

[87] C.H. Llewellyn Smith. Neutrino reactions at accelerator energies. *Physics Reports*, 3(5):261–379, 1972.

[88] K.S. Kuzmin, V.V. Lyubushkin, and V.A. Naumov. Quasielastic axial-vector mass from experiments on neutrino–nucleus scattering. *The European Physical Journal C*, 54(4):517–538, 04 2008.

[89] V. Bernard, L. Elouadrhiri, and U.-G Meißner. Axial structure of the nucleon. *Journal of Physics G: Nuclear and Particle Physics*, 28(1):R1–R35, 11 2001.

[90] A. Chappell. *CP violation and neutrino mass ordering at the T2K experiment.* PhD thesis, University of Warwick, 04 2019.

[91] P.A. Rodrigues, J. Demgen, E. Miltenberger, L. Aliaga, et al. Identification of nuclear effects in neutrino-carbon interactions at low three-momentum transfer. *Physical Review Letters*, 116(7), 02 2016.

[92] K. Abe, N. Akhlaq, R. Akutsu, et al. Simultaneous measurement of the muon neutrino charged-current cross section on oxygen and carbon without pions in the final state at t2k. *Physical Review D*, 101(11), 7 2020.

[93] T. Katori and M. Martini. Neutrino–nucleus cross sections for oscillation experiments. *Journal of Physics G: Nuclear and Particle Physics*, 45(1):013001, 12 2017.

[94] J.E. Amaro and E. Ruiz Arriola. Axial-vector dominance predictions in quasielastic neutrino-nucleus scattering. *Physical Review D*, 93(5), 03 2016.

[95] A. S. Meyer, M. Betancourt, R. Gran, and R. J. Hill. Deuterium target data for precision neutrino-nucleus cross sections. *Physical Review D*, 93(11), 06 2016.

[96] B. Bhattacharya, R. J. Hill, and G. Paz. Model-independent determination of the axial mass parameter in quasielastic neutrino-nucleon scattering. *Physical Review D*, 84(7), 10 2011.

[97] B. Bhattacharya, G. Paz, and A. J. Tropiano. Model-independent determination of the axial mass parameter in quasielastic antineutrino-nucleon scattering. *Physical Review D*, 92(11), 12 2015.

[98] J. Nieves, I. Ruiz Simo, and M. J. Vicente Vacas. Inclusive charged-current neutrino-nucleus reactions. *Physical Review C*, 83(4), 04 2011.

[99] M. Martini, M. Ericson, G. Chanfray, and J. Marteau. Unified approach for nucleon knock-out and coherent and incoherent pion production in neutrino interactions with nuclei. *Physical Review C*, 80(6), 12 2009.

[100] R. González-Jiménez, G. D. Megias, M. B. Barbaro, J. A. Caballero, and T. W. Donnelly. Extensions of superscaling from relativistic mean field theory: The susav2 model. *Physical Review C*, 90(3), 09 2014.

[101] I Ruiz Simo, J E Amaro, M B Barbaro, A De Pace, J A Caballero, and T W Donnelly. Relativistic model of 2p-2h meson exchange currents in (anti)neutrino scattering. *Journal of Physics G: Nuclear and Particle Physics*, 44(6):065105, 4 2017.

[102] D. Rein and L. M. Sehgal. Neutrino Excitation of Baryon Resonances and Single Pion Production. *Annals Phys.*, 133:79–153, 1981.

[103] Ch. Berger and L. M. Sehgal. Lepton mass effects in single pion production by neutrinos. *Physical Review D*, 76(11), 12 2007.

[104] K. S. Kuzmin, V. V. Lyubushkin, and V. A. Naumov. Extended rein–sehgal model for tau lepton production. *Nuclear Physics B - Proceedings Supplements*, 139:158–161, 02 2005.

[105] Krzysztof M. Graczyk and Jan T. Sobczyk. Lepton mass effects in weak charged current single pion production. *Physical Review D*, 77(5), 03 2008.

[106] O. Lalakulich, E. A. Paschos, and G. Piranishvili. Resonance production by neutrinos: The second resonance region. *Phys. Rev. D*, 74:014009, 07 2006.

[107] K. M. Graczyk and J. T. Sobczyk. Form factors in the quark resonance model. *Phys. Rev. D*, 77:053001, 03 2008.

[108] K. Iwamoto et al. Inelastic single pion signal study in ν_e appearance using modified decay electron cut. Technical Report T2K-TN233, T2K Collaboration, 2016.

[109] S. Ahmad, A. M. Sajjad, and S. K. Singh. Neutrino induced charged current 1 pi+ production at intermediate energies. *Phys. Rev. D*, 74:073008, 2006.

[110] G. M. Radecky et al. Study of Single Pion Production by Weak Charged Currents in Low-energy Neutrino d Interactions. *Phys. Rev. D*, 25:1161–1173, 1982. [Erratum: Phys.Rev.D 26, 3297 (1982)].

[111] T. Kitagaki et al. Charged Current Exclusive Pion Production in Neutrino Deuterium Interactions. *Phys. Rev. D*, 34:2554–2565, 1986.

[112] C. Wilkinson, P. Rodrigues, S. Cartwright, L. Thompson, and K. McFarland. Reanalysis of bubble chamber measurements of muon-neutrino induced single pion production. *Phys. Rev. D*, 90(11):112017, 2014.

[113] A. A. Aguilar-Arevalo, C. E. Anderson, A. O. Bazarko, S. J. Brice, et al. Measurement of neutrino-induced charged-current charged pion production cross sections on mineral oil at Enu = 1 GeV. *Physical Review D*, 83(5), 03 2011.

[114] M. Kabirnezhad. Single pion production in electron-nucleon interactions. *Phys. Rev. D*, 102(5):053009, 2020.

[115] D. Rein and L. M. Sehgal. Coherent $\pi 0$ production in neutrino reactions. *Nuclear Physics B*, 223(1):29–44, 1983.

[116] A. Higuera, A. Mislivec, L. Aliaga, O. Altinok, et al. Measurement of Coherent Production of $\pi^{\pm}$ in Neutrino and Antineutrino Beams on Carbon from E_{ν} of 1.5 to 20 GeV. *Phys. Rev. Lett.*, 113:261802, 12 2014.

[117] Ch. Berger and L. M. Sehgal. Partially conserved axial vector current and coherent pion production by low energy neutrinos. *Physical Review D*, 79(5), 03 2009.

[118] D. Rein. Diffractive Pion Production in Neutrino Reactions. *Nucl. Phys. B*, 278:61–77, 1986.

[119] M. Glück, E. Reya, and A. Vogt. Dynamical parton distributions revisited. *Eur. Phys. J. C*, 5:461–470, 1998.

[120] Arie Bodek and Un-ki Yang. A Unified model for inelastic e - N and nu - N cross-sections at all Q**2. *AIP Conf. Proc.*, 792(1):257–260, 2005.

[121] M. Derrick, P. Gregory, L. G. Hyman, K. Jaeger, et al. Properties of the hadronic system resulting from $\overline{\nu}_{\mu} p$ interactions. *Phys. Rev. D*, 17:1–15, 01 1978.

[122] T. Yang, C. Andreopoulos, H. Gallagher, K. Hofmann, and P. Kehayias. A hadronization model for few-gev neutrino interactions. *The European Physical Journal C*, 63(1):1–10, 08 2009.

[123] T. Sjostrand. High-energy physics event generation with PYTHIA 5.7 and JETSET 7.4. *Comput. Phys. Commun.*, 82:74–90, 1994.

[124] M. Tanabashi, K. Hagiwara, K. Hikasa, et al. Review of particle physics 2018 with 2019 update. *Phys. Rev. D*, 98:030001, 8 2018.

[125] Roger D. Woods and David S. Saxon. Diffuse surface optical model for nucleon-nuclei scattering. *Phys. Rev.*, 95:577–578, 07 1954.

[126] E. S. Pinzon Guerra, S. Bhadra, S. Berkman, et al. Measurement of σ_{ABS} and σ_{CX} of π^+ on carbon by the Dual Use Experiment at TRIUMF (DUET). *Phys. Rev. C*, 95:045203, 4 2017.

[127] T. Feusels et al. Tuning of the NEUT Cascade Model using $\pi^{\pm}$-A Scattering External Data to Improve Final State Interaction and Secondary Interaction Systematic Uncertainties. Technical Report T2K-TN325, T2K Collaboration, 2017.

[128] P. Perio et al. Pion Hadronic Secondary Interactions in Super-Kamiokande. Technical Report T2K-TN105, T2K Collaboration, 2012.

[129] J. Tena-Vidal, C. Andreopoulos, A. Ashkenazi, et al. Neutrino-nucleon cross-section model tuning in genie v3, 2021.

[130] C. L. McGivern, T. Le, B. Eberly, L. Aliaga, O. Altinok, et al. Cross sections for ν_μ and $\overline{\nu}_\mu$ induced pion production on hydrocarbon in the few-GeV region using MINERvA. *Phys. Rev. D*, 94:052005, 09 2016.

[131] M. Day and K. S. McFarland. Differences in quasielastic cross sections of muon and electron neutrinos. *Physical Review D*, 86(5), 09 2012.

[132] E. Wang, L. Alvarez-Ruso, Y. Hayato, K. Mahn, and J. Nieves. Photon emission in neutral current interactions at the t2k experiment. *Physical Review D*, 92(5), 09 2015.

[133] E. Wang, L. Alvarez-Ruso, and J. Nieves. Photon emission in neutral-current interactions at intermediate energies. *Physical Review C*, 89(1), 01 2014.

[134] M. Dunkman et al. Updated Recommendation of the 2014-5 Oscillation Parameters. Technical Report T2K-TN256, T2K Collaboration, 2015.

[135] P. Bartet et al. ν_μCC event selections in the ND280 tracker using Run 2++3+4 data. Technical Report T2K-TN212, T2K Collaboration, 2015.

[136] M. Hartz et al. Constraining the Flux and Cross Section Models with Data from the ND280 Detector for the 2014/15 Oscillation Analysis. Technical Report T2K-TN220, T2K Collaboration, 2015.

[137] M. Munteanu et al. Constraining the Flux and Cross Section Models with Data from ND280 using FGD1 and FGD2 for the 2020 Oscillation Analysis. Technical Report T2K-TN395, T2K Collaboration, 2020.

[138] R. Barlow and C. Beeston. Fitting using finite monte carlo samples. *Computer Physics Communications*, 77(2):219 – 228, 1993.

[139] J.S. Conway. Incorporating Nuisance Parameters in Likelihoods for Multisource Spectra. pages 115–120. 6 p, 03 2011. Comments: Presented at PHYSTAT 2011, CERN, Geneva, Switzerland, January 2011, to be published in a CERN Yellow Report.

[140] C. Bojechko et al. CC-multiple-pion ν_μ event selections in the ND280 tracker using Run 1+2+3+4 data. Technical Report T2K-TN152, T2K Collaboration, 2013.

[141] C. Andreopoulos et al. T2K 3.010×10^{20}-POT 3-Flavour Muon-Neutrino Disappearance Analysis. Technical Report T2K-TN141, T2K Collaboration, 2013.

[142] Lakshmi S.M. et al. Super-Kamiokande ν_μ multi-ring samples for 2021 Oscillation Analysis. Technical Report T2K-TN447, T2K Collaboration, 2022.

[143] L. Xiaoyue et al. FiTQun Event Selection Optimization. Technical Report T2K-TN319, T2K Collaboration, 2017.

[144] J. Hignight et al. Super-Kamiokande event displays for T2K Run1-4 analysis candidates. Technical Report T2K-TN148, T2K Collaboration, 2013.

[145] D. Barrow et al. Super-Kamiokande Data Quality, MC, and Systematics in Run 10. Technical Report T2K-TN399, T2K Collaboration, 2020.

[146] K. Abe, J. Adam, H. Aihara, T. Akiri, C. Andreopoulos, Aoki, and Others. Measurements of neutrino oscillation in appearance and disappearance channels by the T2K experiment with 6×10^{20} protons on target. *Phys. Rev. D*, 91:072010, 4 2015.

[147] Andreopoulos, C. and others. T2K Neutrino and Anti-Neutrino 3-Flavour Joint Analysis of Run 1-7c) data sets with ν_e CC1π^+ -like samples. Technical Report T2K-TN306, T2K Collaboration, 2016.

[148] JOACHIM KOPP. Efficient numerical diagonalization of hermitian 3 × 3 matrices. *International Journal of Modern Physics C*, 19(03):523–548, 2008.

[149] William H. Press, Saul A. Teukolsky, et al. *Numerical Recipes in C: The Art of Scientific Computing, Third Edition.* Cambridge University Press, 2007.

[150] S. S. Wilks. The large-sample distribution of the likelihood ratio for testing composite hypotheses. *Ann. Math. Statist.*, 9(1):60–62, 03 1938.

[151] K. Abe, J. Amey, C. Andreopoulos, et al. Measurement of neutrino and antineutrino oscillations by the T2K experiment including a new additional sample of ν_e interactions at the far detector. *Phys. Rev. D*, 96:092006, 11 2017.

[152] L. Berns et al. Five Sample Joint Oscillation Analysis with T2K Run1–10 Data. Technical Report T2K-TN397, T2K Collaboration, 2020.

[153] Gary J. Feldman and Robert D. Cousins. A Unified approach to the classical statistical analysis of small signals. *Phys. Rev.*, D57:3873–3889, 1998.

[154] J. Nieves, I. Ruiz Simo, and M.J. Vicente Vacas. The nucleon axial mass and the miniboone quasielastic neutrino–nucleus scattering problem. *Physics Letters B*, 707(1):72–75, 01 2012.

[155] C. Andreopoulos et al. T2K Neutrino and Anti-Neutrino 3-Flavour Joint Analysis of Run 1-9 (1.49×10^{21}-POT ν 1.63×10^{21}-POT $/\bar{\nu}$) data sets. Technical Report T2K-TN360, T2K Collaboration, 2019.

[156] C F Barnaby and J C Barton. Ageing of Plastic Sscintillators. *Journal of Scientific Instruments*, 39, 4 1962.

[157] V Senchishin et al. New radiation stable and long-lived plastic scintillator for the SSC. 11 1993. FNAL-TM-1866.

[158] A. Artikov et al. Properties of the Ukraine polystyrene-based plastic scintillator UPS 923A. *Nuclear Instruments and Methods in Physics Research Section A: Accelerators, Spectrometers, Detectors and Associated Equipment*, 555(1):125–131, 2005.

[159] T. Zhou, Huihai He, and X. Sheng. The long-term stability of plastic scintillator for electromagnetic particle detectors. *Proceedings of the 32nd International Cosmic Ray Conference, ICRC 2011*, 4:346–349, 1 2011.

[160] Matthew Loyd et al. Accelerated aging test of new plastic scintillators. *Nuclear Instruments and Methods in Physics Research. Section A, Accelerators, Spectrometers, Detectors and Associated Equipment*, 949, 10 2019.

[161] Eric D Sword. Humidity-Induced Damage in Polyvinyl Toluene and Polystyrene Plastic Scintillator. 1 2017.

[162] M. Loyd. *Investigation of Environmental Degradation of Plastic Scintillators*. PhD thesis, Univeristy of Tennessee, 2019.

[163] N.P. Zaitseva et al. Plastic scintillators stable for operating in wide ranges of humidity and temperature variations. *Nuclear Instruments and Methods in Physics Research Section A: Accelerators, Spectrometers, Detectors and Associated Equipment*, 954:161709, 2020. Symposium on Radiation Measurements and Applications XVII.

[164] R. P. Kambour. A review of crazing and fracture in thermoplastics. *Journal of Polymer Science: Macromolecular Reviews*, 7(1):1–154, 1973.

[165] Richard J. Cameron et al. Fogging in Polyvinyl Toluene Scintillators. *IEEE Transactions on Nuclear Science*, 62(1):368–371, 2015.

[166] E. Yousif and R. Haddad. Photodegradation and photostabilization of polymers, especially polystyrene: review. *Springerplus*, 2:398, 2013.

[167] P. A. Amaudruz et al. The T2K Fine-Grained Detectors. *Nuclear Instruments and Methods in Physics Research Section A: Accelerators, Spectrometers, Detectors and Associated Equipment*, 696:1–31, 2012.

[168] D. Allan et al. The Electromagnetic Calorimeter for the T2K Near Detector ND280. *Journal of Instrumentation*, 8:P10019, 2013.

[169] H. Pernegger and M. Friedl. Convoluted Landau and Gaussian Fitting Function. https://root.cern/doc/master/langaus8C.html.

[170] L. Aliaga, L. Bagby, B. Baldin, A. Baumbaugh, A. Bodek, R. Bradford, W.K. Brooks, D. Boehnlein, S. Boyd, H. Budd, and et al. Design, calibration, and performance of the minerva detector. *Nuclear Instruments and Methods in Physics Research Section A: Accelerators, Spectrometers, Detectors and Associated Equipment*, 743:130–159, Apr 2014.

[171]

[172] G. DeZoort et al. Performance of Wavelength-Shifting Fibers for the Mu2e Cosmic Ray Veto Detector. 11 2015. arXiv:1511.06225v1 [physics.ins-det].

[173] E. C. Dukes et al. Performance of Wavelength-Shifting Fibers for the Mu2e Cosmic Ray Veto Detector. *Journal of Instrumentation*, 13(12):P12028–P12028, 12 2018.

[174] Hamamatsu Photonics K.K. MPPC Technical Note. https://www.hamamatsu.com/resources/pdf/ssd/mppckapd9008e.pdf.

[175] K. Abe et al. T2K ND280 Upgrade - Technical Design Report. 1 2019. CERN-SPSC-2019-001 (SPSC-TDR-006).

[176] Ko Abe et al. Sensitivity of the T2K accelerator-based neutrino experiment with an Extended run to 20×10^{21} POT. 7 2016. arXiv:1607.08004v1 [hep-ex].

[177] K. Abe et al. Hyper-Kamiokande Design Report. 5 2018. arXiv:1805.04163v2 [physics.ins-det].

[178] N. Abgrall, A. Aduszkiewicz, M. Ajaz, et al. Measurements of $\pi^{\pm}$ differential yields from the surface of the T2K replica target for incoming 31 GeV/c protons with the NA61/SHINE spectrometer at the CERN SPS. *The European Physical Journal C*, 76(11), 11 2016.

[179] N. Abgrall, A. Aduszkiewicz, T. Anticic, et al. Measurement of production properties of positively charged kaons in proton-carbon interactions at 31 gev/c. *Physical Review C*, 85(3), 03 2012.

[180] P. Dunne and Others. XsecResponse software repository, 2021.